DEVELOPMENT OF CONTACT-RESONANCE HIGH-SPEED ATOMIC FORCE MICROSCOPY

Quantitative Stiffness Measurements for Stiff Materials

by

Namid R. Shatil

A dissertation submitted to the University of Bristol in accordance with the requirements for award of the degree of Doctor of Philosophy in the Department of Engineering Mathematics, Faculty of Engineering.

2018

52,500 words

ABSTRACT

The ability to characterise material properties at sub-micron length scales is imperative for understanding phenomena such as corrosion and fatigue. Atomic force microscopy (AFM) is one tool to achieve this; it creates topographic maps of materials with nanometre spatial resolution. The high-speed AFM (HS-AFM), developed at the University of Bristol, captures these topographic images at frame-rate speeds, orders of magnitudes faster than conventional AFMs. However, alongside the topography of a sample, it has long been thought that the AFM is capable of the characterisation of non-topographic properties. In this thesis, we develop the means for stiffness measurements and combine it with the high–speed AFM to create a valuable tool for material characterisation at sub-micron length scales.

The quantification of non-topographic measurements is complicated by uncertainties in the AFM probe, the influence of hydrodynamic forces, as well as lateral forces, on the cantilever and the scan speed of the HS-AFM. We achieve several important results by investigating each of these influencing factors in turn, such as our new calibration method to measure the effective stiffness of a probe and our custom-built FEM solver that calculates the influence of hydrodynamic effects on a probe as it is brought towards a sample. Both results are used in our development of a method for quantified stiffness measurements.

Stiffness measurements of a material can be achieved with AFM by utilising a shift in the resonant frequency of the AFM probe as it comes into contact with a sample. We describe the theory that underpins this technique, as well as showing a new method to estimate two critical parameters of the system, the tip height and offset. We then give experimental evidence that our findings can be used to quantify the Young's moduli of stiff materials, specifically for steel and gold samples, and highlight the existence of sources of error intrinsic to the method. Finally, we implement our findings on the HS-AFM to calculate the Young's moduli of graphene flakes on a silicon substrate. This demonstrates the sensitivity of our work, which is capable of video-rate mapping of the elastic properties of materials that are sub-micron in height. The quantification of stiffness at these length scales is expected to enable important results in material science applications, such as to predict life of system components, and to be of value to the nuclear industry, as well as the wider material science community.

DECLARATION

I declare that the work in this dissertation was carried out in accordance with the requirements of the University's Regulations and Code of Practice for Research Degree Programmes and that it has not been submitted for any other academic award. Except where indicated by specific reference in the text, the work is the candidate's own work. Work done in collaboration with, or with the assistance of, others, is indicated as such. Any views expressed in the dissertation are those of the author.

Bristol, September, 2018

Namid R. Shatil

ACKNOWLEDGEMENTS

First and foremost, I would like to thank both of my academic supervisors, Oliver Payton and Martin Homer, without whom this work would not have been possible. Thank you to Ollie for bringing me into the world of atomic force microscopy and offering me an opportunity to work on this project, and thanks to Martin for all of his comments and suggestions over the years that have considerably raised the quality of my academic writing. Most of all, thank you both for your unwavering support and motivation throughout my time as a PhD student.

Much of this work has benefited from collaborations and discussions with my peers at the University of Bristol. Thank you to Alan Champneys, a great source of support and guidance during my yearly reviews. A special thanks to the HS-AFM research group: Loren Picco, Freddie Russell-Pavier, Stacey Moore. Every chapter of my thesis has been improved by your friendly discussions, guidance during experiments and optimism on results. Thanks too to members of the Interface Analysis, Peter Martin for his SEM imaging work used in Chapter 1, Tomas Martin and Tom Scott.

The work in Chapter 5 would not have been possible without the input of Jason Killgore at NIST, who was a gracious host during my time in Boulder and has always been on hand to answer any questions that came up afterwards. Thanks to the groups in Auckland and Christchurch, New Zealand. My first conference at NMC15 and the workshop on Mount Cook were both incredible experiences and greatly enriched by discussions with you all.

Thanks to all past and present members of the Buncaer: Alex, Aaron, Ana, Antos, Andy, Bharat, Charlotte, Choi, Chintu, Dan (Hewitt and Ward), Espen, Ed, Fahad, Frank, Gabor, Harry, Hui, Kekko, Keren, Lewis, Matt, Neej, Noah, Nico, Oscar, Plinio, Simon (Godwin and Webb), Sophie, Tom (Dobra and Strain), Yanni, Zohar, and anyone else that I have (no doubt) undeservedly forgotten. You've filled my time at the University of Bristol with interesting discussions, solid advice and laughter.

Away from my University work, thanks to all of my friends from Bristol who have been a great source of strength over the years, to the Floutier family who gave me a much needed push to pursue this PhD when I was just starting out, to members of 4BP who have always encouraged my with kind words and laughter, to the 'as you were' crew for the many cheesy pies and gags over the years, to Emily and James for being amazing housemates and to Em again for the early days of Cotham Hill.

I would like to especially thank my dad, mum, brother and sister. Thanks to dad who has gone through this himself and could pass on his personal lessons, and to mum for always being on hand with words of kindness and encouragement. Most of all, I would like to thank Tals for constantly encouraging me and without whose love and support, this would have been a lot harder.

CONTENTS

LIST OF FIGURES

LIST OF TABLES

NOMENCLATURE

L	Length of an AFM probe
b	Width of an AFM probe
h_{T}	Total thickness of an AFM probe
L_2	Length offset of the tip
θ	Cantilever tilt
h	Tip height
h_{Au}	Thickness of the reflective layer on an AFM probe (typically gold)
E	Young's Modulus of a material
I	Second moment of area
EI	Flexural Rigidity
M	Mass of an AFM probe
M_{e}	Effective mass
μ	Areal mass density
k_{c}	Static spring constant of an AFM probe
k_n	Effective stiffness of an AFM probe
k^*	Contact stiffness
$k_\perp$	Perpendicular contact stiffness
$w(x,t)$	Flexural deflection
$\phi_n(x)$	Spatial Mode
f_R	Resonant frequency of a simple harmonic oscillator
f_n	Resonant frequency of the n^{th} mode
ω_n	Angular resonant frequency of the n^{th} mode
ω_{vac}	Angular resonant frequency of an AFM probe oscillating in vacuum
Q_n	Quality factor of the n^{th} mode
A_n	Oscillatory amplitude of the n^{th} mode
A_{white}	Amplitude of background white noise
α_n	Spatial wavenumber of the n^{th} eigenmode of an oscillating beam
$\alpha_{\text{ contact}}$	Spatial wavenumber of an oscillating beam in contact with a surface
$\alpha_{\text{ free}}$	Spatial wavenumber of an oscillating beam free from a surface
ρ_{f}	Density of fluid
μ_{f}	Viscosity of fluid
$\mathbf{u}$	Fluid velocity
p	Fluid pressure
σ	Fluid stress
Re_{f}	Oscillatory Reynolds number
λ	Measure of the characteristic flow inertia
D	Hydrodynamic Drag
R	Radius of a circular cantilever (or half-width of a rectangular cantilever)

$\Gamma(\omega)$	Hydrodynamic Function
γ_{f}	Hydrodynamic damping
m_{f}	Added mass due to hydrodynamic drag
H	Tip-sample separation distance
Ω	Fluid domain
Ω_{far}	Far field of fluid domain
$\partial\Omega_c$	Boundary of an oscillating body
a	Contact area
R_{tip}	Radius of the tip
E^*	Reduced modulus
ν	Poisson ratio
μ_c^T	Modified Tabor Parameter
w_{adhesion}	Adhesion energy
γ_{m}	Surface tension of meniscus layer
δ_H	Penetration depth given Hertzian mechanics
δ_{c}	Penetration depth
$\delta_{\mathrm{adhesion}}$	Adhesive penetration depth
F_N	Normal load
F_C	Capillary force
F_T	Total contact force
f'	Reference frequency for Lock-in Amplifier
A'	Amplitude measured by Lock-in Amplifier
ϕ'	Phase measured by Lock-in Amplifier

ACRONYMS

AFM Atomic Force Microscopy

AFAM Atomic Force Acoustic Microscopy

UAFM Ultrasonic Atomic Force Microscopy

SEM Scanning Electron Microscope

CR Contact Resonance

DRFT Dual Resonance Frequency Tracking

DART Dual A/C Resonance Tracking

HS-AFM High Speed Atomic Force Microscopy

CR-HSAFM Contact Resonance High Speed Atomic Force Microscopy

OBD Optical Beam Deflection

LDV Laser Doppler Vibrometer

LIA Lock-In Amplifier

DHO Damped Harmonic Oscillator

MAC Multiple Asperity Contact

SS Stainless Steel

1 INTRODUCTION

1.1 THE ATOMIC FORCE MICROSCOPE

The quest for an increased understanding of life at the nanometre length scale can be traced back to 1959, when Richard Feynman delivered his famous talk titled "There's Plenty of Room at the Bottom" [1]. He encouraged an exploration of the world at nanoscale resolution and called for a microscope to be developed with one hundred times better resolution than any scanning electron microscopes (SEM) available at the time. He postulated that such a microscope would resolve, by observation, many of the mysteries in biology, chemistry, and physics. Fifty years after Feynman's challenge came the atomic force microscope (AFM), capable of producing topographic images of materials at subatomic resolution [2, 3].

The breakthrough in new microscopy techniques began with Gerd Binnig and his colleagues working at IBM [4]. In 1986, Binnig and Roher won the Nobel Prize for the invention of the scanning tunnel microscope (STM), yet six months earlier another new microscope had already been born. Developed with the help of Quate and Gerber during Binnig's sabbatical year in Stanford University, this new microscope was described in their landmark paper of the same name, *Atomic Force Microscope* [5].

AFMs and STMs differ in how they utilise the mechanical interactions between a probe and a sample. While the STM reacts to the current caused by the interaction between the voltage biased tip and sample, an AFM measures the total interaction force which causes the probe to deflect, as shown in Figure 1.1. Usually made up of a cantilevered beam with a sharp tip at the free end, the probe behaves like the tonearm of a record player where each dimension has been shrunk down to a thousandth of the size; a length of 300 µm compared with 300 mm, for example.

Measurement of the deflection or displacement of the scanning AFM cantilever creates a topographic map of the sample with nanometre resolution in height. However, the small lengthscales of these micro-mechanical cantilevers (with length in the hundreds of microns and tips with radii in the tens of nanometres) have enabled the AFM to image individual atoms [2]. To put this in perspective, if an atom (approximately 5 Å) were scaled up to the size of a snooker ball (approximately 5 cm), imaging individual atoms with an AFM is analogous to being able to look from the Earth and see individual snooker balls on the Moon (approximately 384 400 km away).

The overarching concept of an AFM has remained relatively unchanged since its first inception over thirty years ago. Topographic images are still created by inferring the forces on the tip from measurement of the deflection of the cantilever. Many AFMs also include a feedback loop which controls the force as the cantilever moves across the

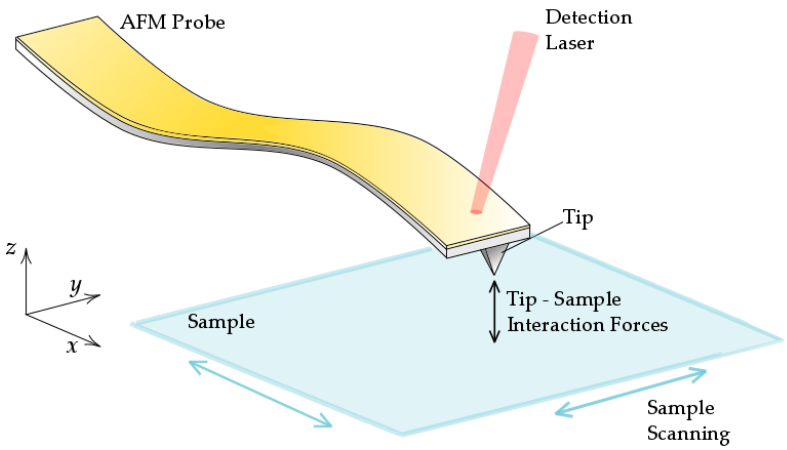

Figure 1.1: Example of how an AFM utilises a cantilevered probe to measure a sample, by monitoring the movement of the tip, through some detection system that typically utilises a detection laser, as it is exposed to tip-sample interaction forces.

surface, tracing out the surface contours. This highlights four of the crucial components for AFM design [6]: the force sensors, the feedback loop, the piezo-electric transducers that move the stage (or probe) relative to a sample, and the cantilevered probe. Each of these can be altered and combined in various ways to create a wide range of operational modes of AFM.

The many different changes to AFM operation have led not only to different experimental configuration but different images, sample preparation procedures, imaging conditions, and information about the sample. For example, the interaction between tip and sample contains additional non-topographic information about the sample. In this thesis, we will outline the steps undertaken to develop a high-speed AFM (HS-AFM) capable of non-topographic stiffness measurements. This is achieved by relating a change in the resonant frequency of an AFM probe to the stiffness of a sample and results in a tool capable of real-time (8 frames per second) quantitative stiffness mapping of large areas (μm^2).

1.2 MICRO-MECHANICAL CANTILEVERS

The original conception of an AFM used a scanning tunnelling microscope (STM) as a force sensor by sandwiching an AFM probe between the sample below and an STM above [4]. This approach is difficult to implement in practice and most AFM users now opt for methods that are either more straightforward or that provide extra information about the displacement or deflection of the AFM probe. These include differential interferometers [7], laser Doppler vibrometers (LDV) [8], crystal oscillators [9], piezo-resistive cantilevers [10], and the optical beam deflection (OBD) method [11]. The OBD method is one of the most widely used [12], as the hardware is often more economical than using LDVs or piezo-resistive cantilevers. The OBD method directs a laser at the free end of the cantilevered probe which is then reflected off the back of the probe and onto a detector. A thin layer of gold, typically tens of nanometres in thickness, is often added to the

cantilever to boost reflectivity and this can significantly alter the dynamic behaviour of the probe, as we show in Chapter 2. The cantilevered probe is the means by which the AFM measures both the topographic and non-topographic sample properties. Hence, it is important that the micro-mechanical AFM probe is well calibrated. In Chapter 2, we introduce our method for calibrating both the resonant frequency and the effective stiffness, a measure of the increased stiffness of the probe at higher frequencies, by taking into account the gold layer and the hydrodynamics of the system.

As the AFM cantilever moves and bends in response to changes in the sample, the laser beam makes corresponding movements in the detector, tracking the motion of the cantilever. As the laser spot moves proportionally to the cantilever's lateral (or torsional for adapted force sensors) bending, the detector will record changes in the laser position as a voltage which relates to the inclination of the beam (rather than the displacement) [13]. The voltage is converted to a cantilever deflection using the so-called inverse optical lever sensitivity value, InvOLS. This value is found by conducting force-distance measurements, described in Section 1.3, on a hard surface, in order to relate the voltage measured by the photodetector to the known movement of the cantilever. However, the measurement of deflection, rather than displacement, and the InvOLS value, can introduce inaccuracies in the position of the tip, leading to alternative methods being used [6]. For example, an LDV directly measures the displacement (rather than deflection) of the cantilever, and also gives information about the dynamics of the probe, as an LDV is capable of directly tracking single locations along the cantilever's length [14, 15]. For example, the displacement of the cantilever along its length can be compared to the normalised eigenmode shape in order to confirm the validity of models that describe the flexural motion of the probe. We demonstrate this in Section 2.5 for the Euler-Bernoulli model of a cantilevered probe.

The movement of the cantilever offers another possible design parameter for AFM devices. The original concept of the AFM aimed to keep the cantilever fixed at a constant net repulsive or attractive force [5]. Known as *contact mode* or *static mode*, for many years this was the most popular technique for AFM users. Most measurements were taken in water or solvent due to the large lateral forces that come from 'dragging' the tip along the surface [4]. Furthermore, the large forces led to the possibility of either substantial wear to the tip or to the deformation of soft samples. This can be mitigated by decreasing the scan speeds, which corresponds to longer experiment time [6]. In order to minimise the lateral forces and increase scan speed, *tapping mode* and *intermittent-contact mode* AFM were introduced [16–18]. Both methods excite the cantilevers with large amplitudes of oscillation (relative to the tip size) so that tip-sample contact is not constantly maintained. This can lead to a range of nonlinear behaviours of the cantilever motion [19, 20] necessitating complex control loops [21]. *Non-contact mode* AFMs are increasingly popular and have been used to image biological objects [16, 22], as well as both soft [23] and stiff [24] materials.

We can further differentiate between the two types of contact mode AFM: *constant-force contact mode* and *constant-height contact mode* [6]. Conventionally, most contact mode AFMs have operated in constant-force mode, which seeks to maintain a constant force

on the cantilever tip [25]. This is achieved by using a feedback loop that keeps the deflection of the probe fixed at a certain value by moving either the stage underneath the cantilever or the cantilever itself. On the other hand, this feedback loop can be turned off so that the height of the cantilever is monitored directly. In this constant-height mode, the stage adjusts to keep the distance between tip and sample fixed and the stage movement is taken to be a direct representation of the sample topography. This method has proved valuable for the HS-AFM developed at the University of Bristol, where any active control mechanism can suppress maximum attainable speeds [26]. Instead the feedback loop is replaced with a passive control mechanism which is believed to come from a thin (typically several nanometres) meniscus layer that sits between the sample and the probe induced by the high speed of the AFM tip relative to the sample [27]. It lubricates the movement of the tip, preventing damage to either the tip or the sample, and avoiding the large lateral forces of the original contact mode. Several design features allow it to reach scan speeds much faster ($1\,\mathrm{mm\,s^{-1}}$) than many other conventional AFM techniques, such as the inclusion of LDV force sensors and a high speed piezo scan stage, as shown in Figure 1.2.

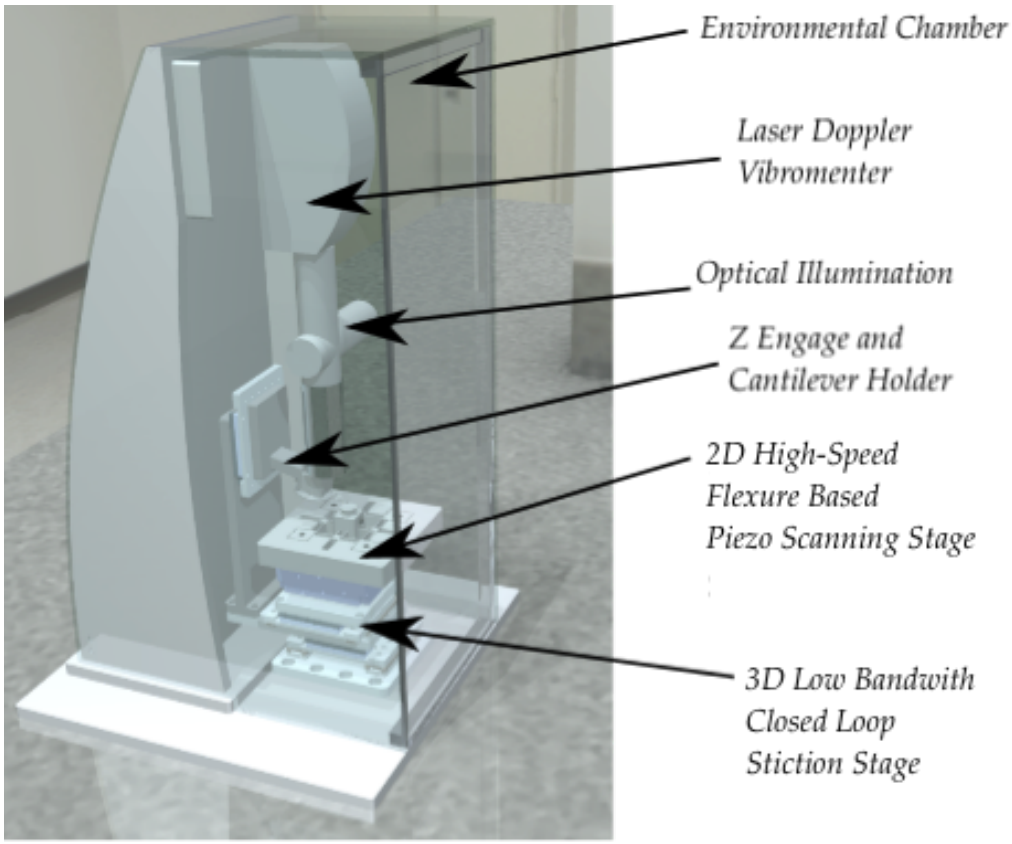

Figure 1.2: The HS–AFM design with pertinant features highlighted such as the use of LDV detection system and high–speed scanning stage.

1.2.1 *AFM at High Speed*

The ability to utilise AFM techniques to build topographic maps at sub-micron and even sub-nanometre resolution has improved our understanding of processes occuring at these lengthscales [28–30]. Traditionally, AFM has focussed on biological samples due to the relatively small sizes of biological objects and a lower requirement for data-collection times [31]. This is partly due to the slow scan speeds of conventional AFMs. For example, most commercial AFMs operate at low scan rates that can take up to ten minutes per image [32]. However, research is increasingly focussed on extending the operational capabilities of AFM to include larger sample sizes, ranging from several microns to centimetre frame sizes, for the benefit of material sciences. This requires implementing improvements to the restrictive imaging speeds of AFMs. We review some of these improvements below

Faster imaging speeds will lead to the ability to observe natural processes in real time, whilst increasing sample throughput [31, 33]. There are a number of ways in which speed can be improved. First, the individual components of an AFM may be optimised to improve performance, including the AFM probe, the detection system, the control loop, and the scan stage. For example, some groups have focused on optimising the cantilevered AFM probe, through miniaturisation of the cantilever dimensions and the utilisation of lighter materials [33–35]. As the spring constant of a beam can be defined in material terms, any decrease in length scales will have a corresponding effect on the spring constant, allowing for softer samples to be imaged faster. However, this must be weighed against corresponding drops in resonant frequency; the optimum cantilever has both a high resonant frequency and low spring constant. This is to protect the cantilever against unwanted forces that cause unstable cantilever behaviour such as uncontrolled contact with the sample surface [4], as we will show in Chapter 2. Other methods include utilising smaller and faster actuators [36, 37], a more rigid scanning stage [38, 39] and modern control methods [40, 41] all of which have improved the rate at which samples are imaged and leading to an HS-AFM capable of imaging over one hundred lines per second [33], the first example of an AFM with video rate imaging [42].

The HS-AFMs, developed by Ando et al, were the first to image dynamic phenomena in real time at the nanoscale [33]. A significant result reported was on the motion of single molecule which gave new insight into molecule motility [43]. Since then, video-rate AFM imaging has led to unparalled access to many of the mechanisms used by biological processes, including diffusion on live cell surfaces and membranes [44, 45], DNA-protein interactions [46], self-assembly processes [47], as well as a host of other dynamic events (see, for example [48] for more details). Furthermore, the HS-AFM of Ando et al. is now being used to consider non-biological samples such as photoresistors [49], with the aim of aiding the future development of nano-lithography techniques. However, the HS-AFM developed by Ando et al. suffers from several limitations. The use of optimised components and highly specialised control loops makes this brand of HS-AFM expensive to reproduce and offers a steep learning curve for new practictioners.

Furthermore, there is an upper-bound for the image volume that this HS-AFM can image, 1 mm^3, due to physical limitations in the control loops and components [31, 50].

The ability to image large areas is paramount for extending the usability of AFM beyond images several microns in diameter [48]. For example, the ability to characterise material properties with nanometre resolution across several millimetres will offer a rich data source for the validation of theories of crack propagation and corrosion [51, 52]. However, for samples that are several millimetres in diameter, highly optimised video-rate AFMs is often too slow for the analysis of large areas. One such method that circumnavigates the internal restrictions to AFM speeds has been the implementation of cantilever arrays to raster material surfaces. For example, the IBM 'milipede' utilised an array of 1,024 AFM probes to achieve a thousand-fold increase in scan rates [53, 54]. Similarly, Seong et al. [55] and Somnath et al. [56] achieved AFM images over areas of hundreds of square microns by using 30 heat-sensitive AFM probes. The use of cantilever arrays is an ongoing area of study, where issues such as cantilever coupling are yet to be resolved [57].

The HS-AFM developed at Bristol University is capable of frame-rate imaging that can capture dynamic phenomena, such as the dissolution of crystalline features [58], as well as imaging large areas (20 mm^2) with high resolution (90 megapixels with a pixel size of 10 nm) and low data acquisition times (under four minutes to collect) [59].

This HS-AFM operates in a low-wear constant-contact regime that comes from interaction of the tip with a meniscus water layer, caused by increasing the tip-velocity to within the HS-AFM range of 250 μm/s to 1,000 μm/s [60]. This is currently the fastest contact mode AFM in the world, in terms of tip velocity, and is capable of scan rates in excess of 1,200 fps and of imaging macro-scale (mm^2) sample areas [31]. Imaging with high-speed tip velocity has been shown to significantly reduce lateral forces compared to dynamic modes [26], allowing large areas to be mapped out orders of magnitude faster than a conventional AFM without depreciation of the tip (as observed through worsening image quality). This feature is crucial in removing some of the uncertainty in contact resonance measurements, as we observe in Chapter 5.

The meniscus layer that enables the high speeds of the HS-AFM is one example of the sensitivity of the probe to its surrounding environment. In Chapter 2, we utilise the hydrodynamics of the surrounding fluid (e.g. ambient air) to discern the cantilever properties. However, we assume that the probe is free of the influence of the sample. In Chapter 3, we consider the influence of the surface on the hydrodynamics of the system and how this changes the fluid loading on the surface of the probe. This work highlights that the hydrodynamics of the system can have a substantial effect on the frequency response of an AFM probe and needs to be accounted for when conducting frequency based measurements, as we do in Chapter 5 and Chapter 6.

1.3 TIP-SAMPLE INTERACTION

An AFM probe will be exposed to a range of forces as the distance between the probe and sample decreases. Furthermore, the amplitude of an oscillating AFM probe will dictate the contact regime within which an AFM probe will operate. For example, AFM probes that are excited to high amplitude relates to intermittent-contact and tapping mode AFM, as the tip of the probe makes contact with the sample for a small section of the oscillation period [61]. Alternatively, an AFM probe may be kept a distance away from the sample and forced to oscillate, representing non-contact mode AFM [61]. This mode is generally used for soft samples, where the tip contact forces would otherwise be expected to cause damage to the sample. In this thesis, we will be primarily concerned with an AFM probe that undergoes small amplitude oscillations, such that the tip remains in permanent contact with the sample once contact is made. The forces on an AFM probe as it comes into contact with a sample surface are typically captured on force-distance curves, which describe how the interaction between the tip and sample varies with distance [61, 62]. In Figure 1.3, we show a schematic example force-distance curve.

The probe initially begins far away from the surface, where it is uninfluenced by the surface forces (I.). As the distance decreases, the attractive surface forces overcome the probe's spring elastic force causing the probe to snap-to-contact (STC) (II.). The snap-to-contact event gives information about the relative strength of the attractive forces in the system, shown as the minimum of the blue curve in Figure 1.3. The probe is then pushed into the surface (III.) until a maximum contact force has been applied (IV.). Following this, the probe is brought away from the surface by the stage motors (V.). If significant sample deformation occurs, a hysterisis will occur between the approach and retract curves, as highlighted in Figure 1.3. This may occur due to plastic deformation of either sample or AFM tip, or visco-elastic behaviour of the sample such that material creep prevents the sample from immediately returning to its underformed state. We discuss visco-elastic material phenomena in more detail in Chapter 5. For many AFMs that are operated in ambient conditions, a meniscus bridge will form between the sample and probe (VI.). This introduces additional adhesive forces into the system, as marked in Figure 1.3, and prevents the probe from returning to its initial position until the probe's spring elastic force overcomes the additional forces. When the elastic forces are sufficently high, the probe will snap-from-contact (SFC) and return to its intial position.

The interaction forces that act on the AFM probe can broadly be separated into long-range and short-range forces. The long-range forces, often effective at separations of order 100 nm, can be caused by environmental factors such as electrostatic charge between tip and sample or liquid adhesion (depending on the operating conditions of the AFM) [63]. When considerations of electrostatic charge and liquid adhesion are removed, the long-range forces will comprise of van der Waals forces which are weak interaction forces operating between molecules. Long-range forces are typically attractive and are the main contributing factors for the snap-to-contact event [62]. Other attractive forces include Coulomb forces due to the relative conductivity of tip and sample.

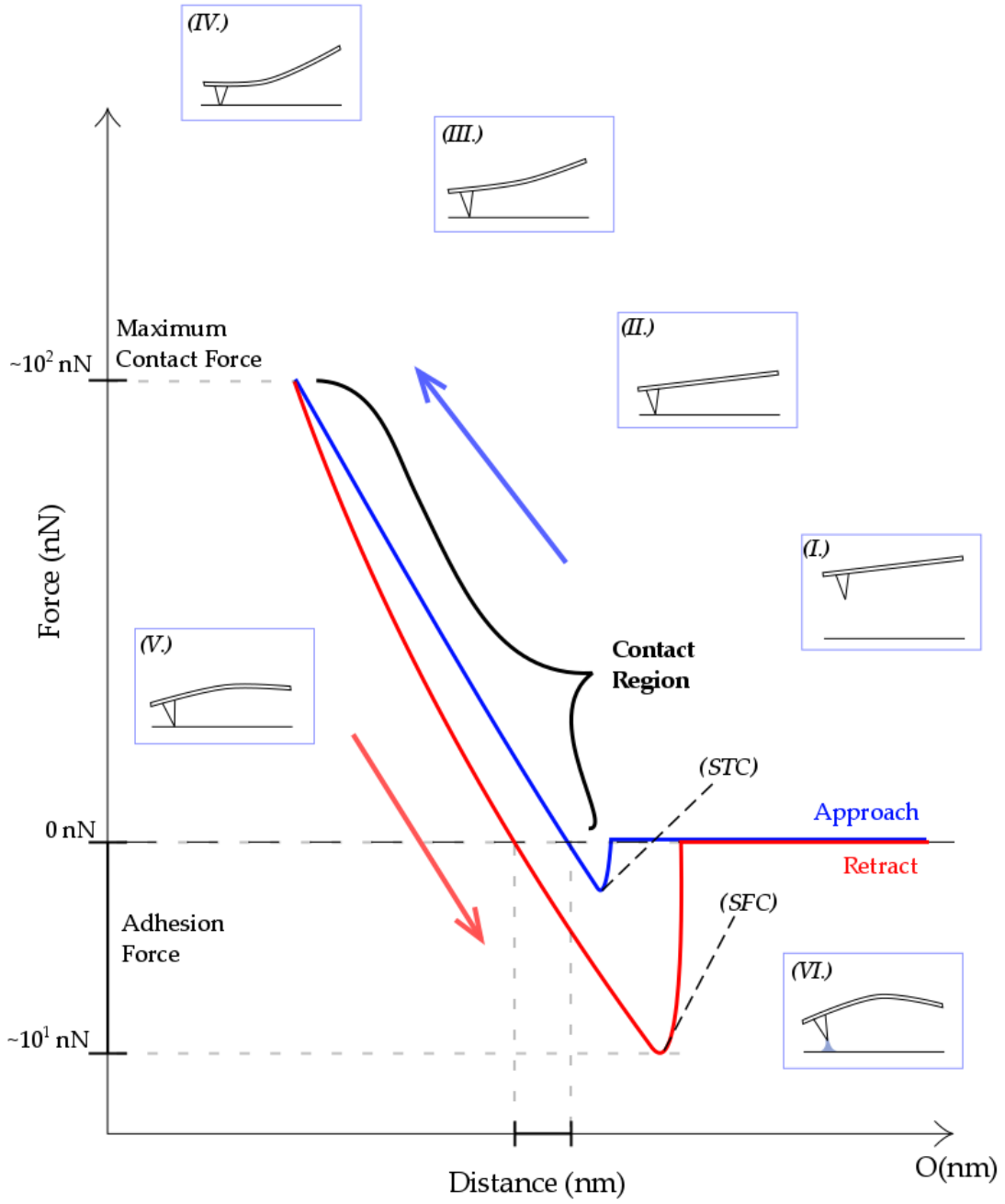

Figure 1.3: Schematic force-distance curve for an AFM probe based on theoretical descriptions set out in [62]. The cantilever begins at a free position (I.) under zero load and is moved towards a sample until the cantilever snaps to contact (II.). While in contact the cantilever is pushed into the surface (III.) until it reaches a pre–described maximum penetration distance (IV.) where it begins to retract away (V.). The cantilever will continue to retract away (VI.) until the surface forces are weaker than the cantilever's spring elastic forces which cause the probe to snap for contact.

Both STC and SFC events are caused by a combination of short–range and long–range interaction forces. The STC event is caused predominantly by van der Waals and elastic forces, while SFC typically involves a combination of adhesion and capillary forces. The van der Waals potential is a result of the combination of different potentials that act between molecules. These include two potentials which are specifically related to the polar molecules (known as the polar or entropic contribution) and the dispersion contribution which is quantum-mechanical in nature and acts between every molecule [64]. As such, the van der Waals force will be present in all AFM measurements. However, the van der Waals force is a greater consideration for non-contact mode AFM. This is because contact mode AFM assumes that contact has been made such that the long range electrostatic or van der Waals forces have less influence on the oscillating cantilever than the short-range forces. Information about the van der Waals force, such as the Hamaker constant (which includes physical and chemical information on the interaction between two bodies) can be gained by considering the snap-to-contact force or the adhesion in the system, as described in [62]. We will not consider such methods here. Instead, we focus on the interaction between a tip that is assumed to be in contact with the sample.

When the probe is brought close to the sample, a tip-sample separation distance of several nm, short-range forces will dominate [61]. These short range interaction forces typically comprise of both Pauli and ionic forces; for tens or hundreds of atoms, continuum models are typically used. This is the transition into models based on continuum contact mechanics. The contact region, in which the short-range force dominates, is marked in Figure 1.3. In this thesis, we shall be concerned with AFM probes that oscillate with small amplitudes such that we assume they remain within this contact region once the tip has made contact with the sample. Specifically, we shall relate the resonant frequency of an oscillating AFM probe to the material properties of the sample under the assumption that the tip of the probe and sample remain in contact.

In order to model the contact event occuring within this region, one approach has been to use Kelvin-Voigt elements [65], such that, for samples that are predominantly elastic, the contact event is approximated by a *contact stiffness* [66]. The contact stiffness, which we will define and study in Chapter 4, is an idealisation of the tip-sample interaction during a contact event between an oscillating sensor and sample. Alternatively, if the material displays viscoelastic behaviour such as creep, then a dashpot can be introduced which describes the interaction damping between sensor and sample [67]. The interaction damping is a measure of viscous contributions from the sample as well as viscous contributions from the surrounding medium. In Chapter 5 we will describe how to relate a contact stiffness to material properties such as Young's modulus. The use of springs and dashpots in order to describe the contact stiffness and interaction damping of a material is particularly popular among non-destructive and non-topographic techniques that consider the change in resonant behaviour (the resonant frequency and Q factor) of an AFM probe when it is in contact with the sample [68–71]. These techniques are broadly known as *contact-resonance AFM*, where contact resonance describes the change in resonant frequency due to a contact event. In this thesis, we shall show how contact resonance AFM techniques can be combined with HS-AFM.

1.4 CONTACT RESONANCE AFM

The probe of an AFM is akin to a tiny finger, gently moving across some unknown surface. The AFM probe qualitatively describes changes in the topography of surface features and, like a finger, the probe also has the potential to take measurements of non-topographic properties such as the stiffness and hardness of a sample [66]. One method, known as *contact-resonance atomic force microscopy* (CR-AFM) [65], extends the operational potential of AFM to include stiffness maps of a material. This is achieved by exciting the AFM probe and measuring the change in the resonant frequencies of the probe that results from contact between an oscillating sensor and surface. In Chapter 6, we discuss this technique as well as its extension in more detail and only give an overview of the technique here.

We assume that an idealised contact stiffness is descriptive of a single instance of the contact between a quasi-static sensor and sample, the so-called contact event. In Chapter 4, we describe the contact resonance technique which calculates an idealised contact stiffness, by measuring the change in resonant frequency of an AFM probe. We demonstrate that the tilt of the cantilever, which results in additional lateral stiffness contributions, should be included in order to measure the stiffness of stiff materials with a soft cantilever and that, by doing so, we are able to estimate the important sensor parameters of tip height and tip offset. For the lower modes of a soft cantilever, these parameters are crucial in relating a shift in frequency to a sample material property. However, as we show in Chapter 5, the higher modes reduce the importance of these parameters owing to an increased stiffening of the AFM cantilever.

The contact resonance method connects the idealised contact stiffness to a material property, such as Young's Modulus, through a model of the contact mechanics. However, as we show in Chapter 5, the assumptions inherent to these models of contact mechanics can cease to hold under typical operating conditions of an AFM when measuring stiff materials. For example, we show that low-resolution measurements on stainless steel (Grade 316) and gold lead to inconclusive values for the Young's modulus, ranging over several orders of magnitude. One possible cause for this is that the tip has been exposed to substantial wear, such as a change in the geometry and radius of the tip, and this has altered some of the assumptions implicit in a given theory of the contact mechanics between sensor and sample [72]. Alternatively, this may be caused by experimentation errors, changes to the contact event or additional adhesion on the sample. We discuss these causes in detail in Chapter 5 whilst highlighting the effectiveness of higher modes for contact resonance measurements.

With the development of HS–AFM, capable of imaging at high resolution in real time, the possibility of combining contact resonance with imaging is a promising prospect; the stiffness of large sample areas can be mapped to sub-nanometre resolution, orders of magnitude faster than any current technique, whilst simultaneously giving a topographical image of the surface in real time in a non-destructive fashion. This is a significant improvement on the widely used method of stiffness mapping at the nanoscale, nano-indentation, which causes irreversible damage to the sample, as shown in Figure 1.4.

1.5 MATERIAL CHARACTERISATION

The characterisation of material properties is critical in the engineering design process and during the assessment of service components. It encompasses areas such as material sciences, life sciences, physics, engineering, and any industry that involves some form of structural design. It is often critical in predicting component life [73]. This is particularly true within the nuclear power industry, where understanding plant material behaviour under extreme conditions is crucial for extending lifetimes of existing nuclear reactors, as well as for the development of materials in the next generation of reactors [74]. Nuclear plant reactor components are exposed to extreme conditions, which can cause significant damage due to stress concentrations in the component materials [75]. This can become a critical safety issue, if left unchecked [76].

It is well known that cracks initiate at levels of high stress concentrations on a sample surface and then spread to micro-structural barriers, often through grain boundaries [77, 78]. As such, the microstructure of a sample leads to macro-scale mechanical size effects when the sample is observed at nanometre length-scales [79]. Specifically, metallic materials have inhomogeneous microstructures that reflect their intrinsic crystalline properties [80]. They will contain combinations of grains with perfect crystallography as well as others that have defective crystalline structure caused by inclusions and grain boundaries [81]. These grain boundaries affect the nucleation and propagation of cracks, and, hence, the ability to identify and measure stress concentration near grain boundaries is expected to aid the prediction of material life and fatigue [82].

However, in-service inspection may not provide sufficient detail on the level of stress within a material component. Moreover, if a component has been damaged, it may prove too difficult to extract large sections of the in-use material for macro-testing without incurring prohibitive costs. Nanoscale testing resolves this with a reduction in the amount of material required for testing. AFM-based techniques are the only ones capable of quantitatively measuring material properties at nanometre length scales without also causing substantial damage to the sample but are prohibitevely slow to use. Hence, the realisation of a high-speed AFM for assessing the design life of structural and functional material components in these facilities is expected to be beneficial for ensuring reliable operation and safety.

At the nano-scale, characterisation of material impurities, carbide formations, phase segregation, and grain boundaries is still a significant open challenge [83–86]. With the advent of miniaturisation, a range of techniques has been developed to meet the growing demand for characterisation of material properties, such as stiffness, at nanometre resolution [87–90]. For example, nanoindentation measures the stiffness of materials by measuring the distance that a rigid indentator (typically made of diamond or diamond coated) is able to penetrate into a material under different loads. However, this technique causes substantial damage to the sample, as shown in Figure 1.4, and can generate strain-fields that are typically microns in radius [91]. Furthermore, the technique is low-resolution as measurements on a material comprise of the analysis of tens of measurement points [92]. On the other hand, the atomic force microscope (AFM) is

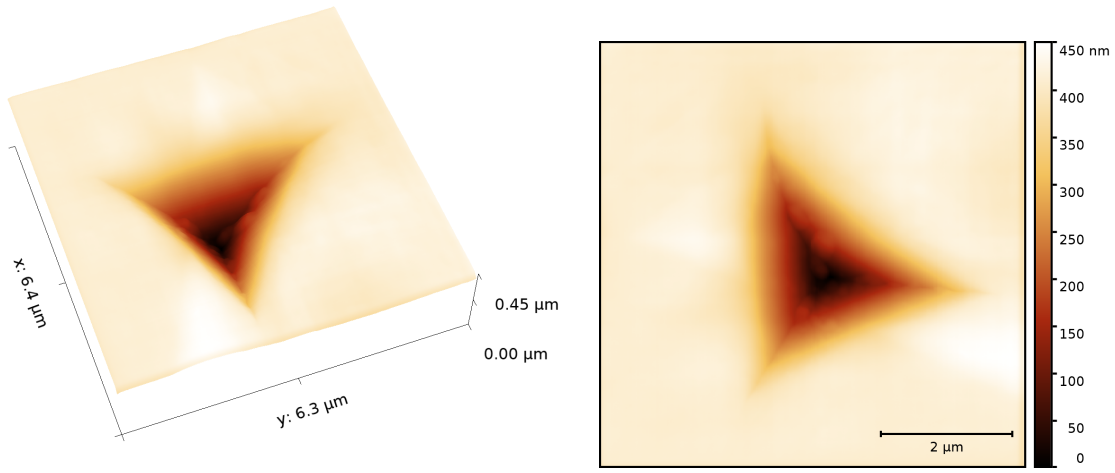

(a) (b)

Figure 1.4: The after effects of a nanoindentation measurement conducted on a sample of nickel, that has caused irreversible damage over a μm^2 area; here a triangular-shaped hole that is around 450 nm deep.

able to measure the topography of large areas with increasingly high resolution and scan speeds. Furthermore, contact resonance AFM has nanometre lateral resolution and is entirely non-destructive [66].

As discussed, the HS–AFM operates in a low tip-wear regime which is thought to be caused by a super-lubrication effect of a meniscus layer that exists on a sample surface. As such, it is ideally suited to CR measurements which are particularly sensitive to tip degradation. In this thesis, we will outline the steps undertaken to combine non-topographic measurements with high speed atomic force microscopy (HS-AFM), to achieve non–destructive, high–resolution, stiffness measurements at nanometre length-scales. We demonstrate this in Chapter 6 with non-topographic feature detection and quantified stiffness measurements on a sample of stainless steel and of graphene (monolayers and flakes) deposited on a silicon substrate.

1.6 SUMMARY

The parallel development and eventual combination of HS-AFM with the contact resonance method has the potential to vastly improve material characterisation, in terms of both measurement time and resolution. As this combination matures, the aim is to be able to simultaneously describe viscoelasticity, stiffness, hardness and other properties whilst 'seeing' the sample in real time. In order to do this, we must first resolve the problem of how to gain quantitative, rather than qualitative, measurements. The custom built HS-AFM in the University of Bristol has a unique capability to do this. This thesis sets out the work that has been done in the development of contact resonance HS-AFM. The research and key findings are as follows:

- *Chapter 2* – We begin by introducing the concept of an effective stiffness, a measure of the increase in stitffness of a cantilever at high mode number, and use our own

calibration method to calculate both effective stiffness and resonant frequencies. The output from this work is published in [93]. This method relies on knowledge of the hydrodynamics of the system which we investigate in more detail in Chapter 3.

- *Chapter 3* – We create our own procedure for calculating the hydrodynamic loading on an oscillating cantilever using FEM open-source software. We apply our solver to the specific case of a cantilever oscillating near to a surface at high frequency. We find that the added mass on the cantilever caused by the hydrodynamic drag is small at high frequencies but that the damping can be considerable.

- *Chapter 4* – We introduce the method of acoustic measurements as applied to AFM and detail the theoretical steps undertaken to relate a change in resonant frequency to an idealised contact stiffness, representing the contact event between a quasi-static probe and surface. We show that higher modes are required for stiff materials and that this leads to a self consistent means for the estimation of two key parameters, tip height and tip offset.

- *Chapter 5* – We describe the contact mechanics theories that connect a contact stiffness, introduced in Chapter 4, to a material property (such as a Young's modulus) and highlight the key theoretical assumptions. We verify the relationship between contact mechanics and contact stiffness by taking repeated contact resonance measurements on a stiff sample over varying normal loads. We find that the calculated material properties can range over several orders of magnitude and discuss potential sources of uncertainty.

- *Chapter 6* – By combining CR with HS-AFM, we demonstrate that considerations of the tip, discussed in Chapter 5, are reduced due to the low-tip wear regime of the HS-AFM. We apply CR-HSAFM to a sample of steel with carbide features, and also to graphene monolayers and flakes deposited on a silicon substrate. This culminates in a device capable of non-topographic feature detection, quantified stiffness measurements, measurements across μm^2 areas with low variation and a thousand–fold increase in pixel count compared to existing CR-AFM devices.

2

CALIBRATION METHODS

The work in this chapter has been published in Ref. [93]. The power spectra, I.-V. described in Section 2.5 were taken using the HS-AFM located at the University of Bristol, with support from Dr. Loren Picco. The SEM images in Figure 2.11 were taken by Dr. Peter Martin at the Interface Analysis Centre, University of Bristol.

2.1 INTRODUCTION

In this chapter, we describe and evaluate methods for calibrating an AFM cantilevered probe. This enables us to estimate the key parameters which will inform both experimental investigations as well as analytic models. We are primarily interested in calibrating the effective stiffness of the cantilever for high mode number, but also discuss the importance of features such as the reflective layer on one side of the AFM probe, and the AFM tip. We begin by discussing the effective stiffness and its importance. We then describe existing calibration methods and their limitations in finding the effective stiffness at high mode number. We address the shortcomings in existing methods by developing a new method for the calibration of micro-mechanical cantilevers which is applicable at any mode number, and subsequently describe and apply our method on a commercial AFM probe.

2.2 PRELIMINARY DEFINITIONS

AFM probes are typically long and thin micro-mechanical cantilevers, often with rectangular geometry. While many are rectangular, there are also many cantilevers with irregular geometry such as V-shaped, U-shaped or picketed. In this work, we will focus on rectangular geometry, though the approach can be extended to include other cantilever considerations. In Figure 2.1, we show the typical dimensions of an AFM probe (not drawn to scale).

In general, the cantilevers are manufactured such that the length is much larger than the width and the width is much larger than the thickness. In this section, we are concerned with cantilevers that match these length proportions and are rectangular in their cross-sectional area and in their geometry. For a rectangular cantilever, with uniform cross section and undergoing small deflections perpendicular to the centroid of the long axis and its width, the second moment of area, I, is given as [94]

$$I = \frac{bh_{\mathrm{T}}^3}{12}, \tag{2.1}$$

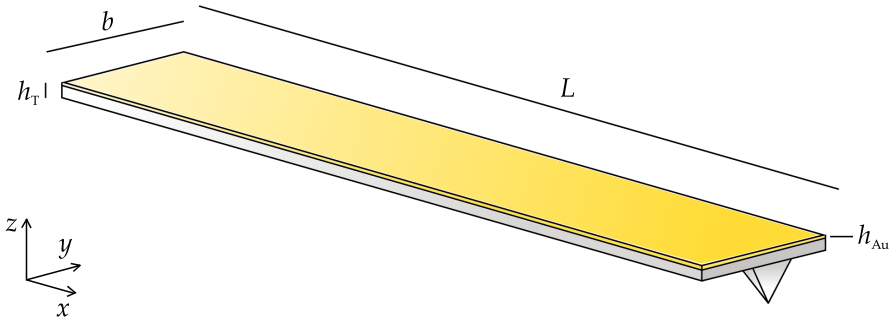

Figure 2.1: The AFM probe has length, L, that is considerably larger than width, b, and width that is considerably larger than the total thickness of the probe, h_T. The probe typically contains a reflective layer, with thickness h_{Au}, on the top side of the beam, used to boost the signal of the detection system.

where b is the cantilever width and h_T is the total cantilever thickness.

The second moment of area, also described as the area moment of inertia or second area moment, is used to describe the propensity of the cross-section of the cantilever to resist bending; a large second moment of area implies that a cantilever is less likely to deflect and has high stiffness. As the thickness of the cantilever is much lower than the cantilever width, the second moment of area is typically low. Given a point load, F_N, at the free end, $x = L$, of the cantilever (and clamped at $x = 0$), the cantilever's deflection at $x = L$, according to Euler-Bernoulli theory, is given by [95]

$$w(L) = \frac{3F_N EI}{L^3}, \tag{2.2}$$

where E is the Young's Modulus of the cantilever and L is its length. Hooke's law states that the spring constant, k_c, of a structure, forced to extend by x due to a load, F_N, is given by

$$k_c = \frac{F_N}{x}. \tag{2.3}$$

By applying Hooke's law to the above consideration of a point load at the cantilever's free end, we introduce the following definition [96],

DEFINITION 1: **Static Stiffness.** The static stiffness, k_c, of a rectangular cantilever under static load at the free end, is

$$k_c = \frac{3EI}{L^3}. \tag{2.4}$$

where E is the Young's modulus of the cantilever.

Knowledge of the stiffness of the beam gives us a means to approximate the cantilever as a single lumped-parameter model described by a point-mass with an effective mass, $m_e M$, where m_e is the effective mass factor and M is the cantilever mass, and spring constant k_c. The effective mass represents the mass of the moving section of the beam (the free end) which is no longer distributed. It can be found using Rayleigh's method, which assumes that, for a suspended structure moving at its maximum velocity, the potential energy at its maximum displacement will be equal to the kinetic energy [97].

It is commonly presented as a geometric correction factor which multiples the mass of the system. For a rectangular cantilever with high aspect ratio (such that the thickness is much less than the width), we have $m_e/M \approx 0.2427$ [97, 98].

The static stiffness is a measure of the cantilever's stiffness to contact point load; the theory above is in the absence of any oscillatory motion and relates only to the static behaviour of the system. However, in this thesis we will be concerned with the dynamic behaviour of an oscillating AFM probe. Given the effective mass, derived above, we introduce a further definition for the effective spring constant of the point-mass model.

DEFINITION 2: **Effective Stiffness.** The effective stiffness, k_n, of a cantilever, oscillating at its n^{th} resonant frequency in vacuo[1], $\omega_{\text{n,vac}}$, is [99]

$$k_n = M m_e \mu L \omega_{n,\text{vac}}^2, \tag{2.5}$$

where $\mu = \rho b h$ is the areal mass, for a cantilever of uniform density ρ, and m_e is the effective mass factor.

This is also referred to as the modal [100] stiffness of a cantilever. The effective stiffness is a measure of the stiffness of the cantilever at its n^{th} resonant frequency and is useful for achieving our aim of quantifying the stiffness of materials at the nanoscale. The effective stiffness gives practical information for non-topographic measurements. For example, material properties of a surface in contact with the cantilever can be found via a shift in the resonant behaviour of the cantilever [66]. Changes in resonant frequency occur according to the material under investigation, due to the tip-sample interaction, which we investigate in detail in Chapter 5. In order to avoid damaging the sample or tip, soft cantilevers are typically used in practice and excited to high frequencies; the higher modes of the cantilever are used to imitate a stiff cantilever whilst avoiding damage to the sample surface [101]. The ability to calibrate the effective stiffness of the beam allows the user to stiffness-match the cantilever to the sample, identifying modes that will give greatest sensitivity to the sample's material properties.

Here, we are focused on oscillating cantilevers and their effective stiffness. We discuss existing means for calibrating a cantilever's stiffness in Section 2.3, describing how a cantilever's static stiffness can be calibrated and why these methods cannot easily be extended to consider the effective stiffness of the cantilever. We then present two existing methods for calibrating the effective stiffness of a cantilever, in Section 2.3. Finally, we introduce our own method for calibrating the effective stiffness of a cantilever in Section 2.4 before demonstrating our own method in Section 2.5.

1 We will us *in vacuo* to refer to a cantilever oscillating in an idealised vacuum without hydrodynamic influences.

2.3 CALIBRATION METHODS

At the heart of all AFM operations is the mechanical movement of the AFM probe. One of the first requirements identified by Binnig for successful scanning was finding a probe with the right sample sensitivity [5]. He understood that the probe must be soft enough to react to weak tip-sample interaction forces, and must also have a resonant frequency that would be unaffected by environmental vibrations. This led to the use of long thin cantilevers [102]. AFMs are able to build topographic images of samples by measuring the deflection of the probe due to the tip-sample interaction forces. In order to relate the movement of the cantilever to an interaction force, the spring constant of these cantilevers must be known to high accuracy. Due to the thinness of the cantilevers and uncertainties within the fabrication process, manufacturers give values of the static spring constant that vary by as much as 25% [6]. Similar uncertainties are found in the thickness, density and Young's modulus of the cantilever, as well as the position and geometry of the probe tip [103]. These discrepancies can cause dramatic reduction in the quality and resolution of AFM images. Hence, the ability to calibrate cantilevers is an active and important area of research. Furthermore, the effective stiffness, (2.5), is not included as standard by manufactures of microcantilevers. This creates a significant obstacle in quantifying non-topographic properties of a sample, as we explain in Chapter 5.

In Chapter 5 we demonstrate that the effective stiffness of a soft (low static spring constant) AFM probe is an indicator for the sensitivity of the resonant mode, found by 'stiffness-matching' the effective stiffness to the expected contact stiffness (which we define and discuss in Chapter 4). By doing so, we are able to neglect considerations of difficult to measure cantilever parameters, such as the tip offset and height, and increase confidence in our measurements. Furthermore, the use of soft cantilevers for measuring material properties of stiff materials allows for contact resonance measurements, as introduced in Chapter 4 to be combined with high-speed AFM (HS-AFM), which we undertake in Chapter 6. Hence, the effective stiffness of the cantilever, found here, is a crucial parameter for later work in this thesis.

The cantilevers used as AFM probes are often made from silicon or silicon nitride with a reflective top layer of gold or aluminium used to increase the strength of a laser detection signal. The micro-fabrication process and mixing of materials introduces significant uncertainty to several of the properties of the cantilever; in particular, the thickness of the cantilever and reflective layer, as well as the density and Young's Modulus of the combined cantilever and reflective layer [104, 105]. However, the static spring constant of the cantilever is crucial for imaging and the effective stiffness allows for measurement of non-topographic sample information. Therefore, methods have been proposed to calibrate the spring constants of a cantilever, without reference to the physical geometry and material properties of the cantilever itself. Many of these methods introduce a calibration device such as a reference cantilever or an additional mass [106–108].

For methods that use a reference cantilever, the tip of the uncalibrated test cantilever is lowered onto the top side of a cantilever with known properties, and the spring constant,

as defined in Section 2.2, is found from the relationship between the test cantilever and its optical beam sensitivity, according to [107]

$$k_{\text{test}} = k_{\text{ref}}\left(\frac{S_c}{S_h} - 1\right)\left(1 - \tan(\theta)\left(\frac{3D}{2L_{\text{test}}}\right)\right)\left(\frac{L_{\text{ref}}}{L_{\text{ref}} - \Delta L}\right)^3. \tag{2.6}$$

Here, k_{ref} and L_{ref} are the spring constant and length of the reference cantilever respectively, S_c and S_h are the optical lever sensitivities[2] of the test cantilever when it is against the reference cantilever and a hard surface respectively, D is the distance between test cantilever and reference cantilever (generally taken to be the imaging tip of the test cantilever), θ is the angle of inclination of the test cantilever with respect to the reference cantilever and ΔL is the distance of the end of the reference cantilever to the tip. The relationship includes a correction term to account for the position along the reference cantilever's length and the inclined angle that the test cantilever makes with the reference cantilever. In practice, it is difficult to accurately locate the test cantilever's positioning, though work has been done to resolve this as well as extending this method to account for non-conventional cantilever shapes [32, 107]. However, this method still requires signicant experimental work in order to calibrate the cantilever.

Alternatively, calibration can be achieved by adding or removing mass to/from the cantilever, and measuring the change in resonant behaviour. One of the earliest examples of such a method is the Cleveland method [109]. The Cleveland method uses the fact that there is a linear relationship between the volume of added mass and the resulting shift in resonant frequency. In fact, a single added mass has been shown to be enough to derive the spring constant of a cantilever. Alternatively, a small amount of mass can be removed from the tip of the cantilever, using methods such as focused ion beam milling [110]. However, these methods require that the frequency shift be as high as possible, while the mass removed remains small in relation to the mass of the cantilever. High frequency fast-scan cantilevers have proven to be good candidates for these methods as a small change in mass results in large frequency shifts.

Overall, methods that rely on a calibration device such as a reference cantilevers or changes to the cantilevers mass are experimentally challenging. They require significant time taken before measurements can be carried out, due to the involvement of a reference cantilever, or introducing a change to the cantilever such as added mass. Furthermore, they are only applicable to the static spring constant as they do not consider the resonant behaviour of the cantilever. To achieve higher mode calibration of the effective stiffness, we must appeal to indirect methods.

Indirect methods consider the surrounding environment of the cantilever to find the spring constant, such as the thermal method which uses the equipartition theory to calibrate the cantilever's spring constant [111]. The equipartition theory states that, for a system in thermal equilibrium, the energy of the system is shared out equally across all degrees of freedom. This implies that every degree of freedom will have, on average, thermal energy, $\frac{1}{2}k_{\text{B}}T$, where k_{B} is the Boltzmann constant and T is the temperature

2 See Chapter 1 for discussion of the optical lever sensitivities of an AFM probe.

of the surrounding thermal bath [111]. These include translational degrees of freedom (given by the kinetic energy $k = \frac{1}{2}mv^2$ for some velocity, v), and vibrational degrees of freedom ($V = \frac{1}{2}kx^2$, for a stiffness k and displacement x). Here, we are concerned with the vibration of an oscillating cantilever and its potential energy (which is a vibrational degree of freedom, as described above). For an oscillating cantilever, driven purely by thermal excitations, the equipartion theory relates the potential energy according to,

$$\frac{1}{2}k_{\mathrm{B}}T = \frac{1}{2}k_n\langle x\rangle^2, \tag{2.7}$$

where $\langle\cdot\rangle$ denotes an average across time such that $\langle x\rangle^2$ is the mean squared fluctuations of the cantilever. The mean squared fluctuations are found by measuring the RMS amplitude of a free thermally excited cantilever. For example, a cantilever left in air at room temperature with a spring constant of 0.005 Nm^{-1}, will experience thermal fluctuations of the order of 3Å [111]. Using the optical beam deflection method[3], the frequency response of the cantilever due to thermal fluctuations can be measured and the resonant frequency peaks isolated to give the power spectral density (PSD) of the cantilever at each resonant frequency. The integral of the PSD is then equal to $\langle x\rangle^2$ and the effective stiffnesses are found by

$$k_n = \frac{k_{\mathrm{B}}T}{\langle x\rangle^2}. \tag{2.8}$$

There are several complications with this method. First, the optical beam deflection (OBD) method does not directly measure the deflection of the cantilever but rather the inclination [112]. This must be accounted for in the method and corrections have been proposed in order to do so [112, 113]. Secondly, the spot size and location of the laser beam used in OBD can have substantial effects on results [35]. Both of these restrictions can be circumnavigated by using a different detection system, such as laser Doppler vibrometry (LDV) [114]. Large spot diameters for OBD boost the signal strength while increasing the area of detection. However, as the mode number of the cantilever increases, the distance between nodes and antinodes decreases. This causes a corresponding increase in alternating positive and negative slopes which lowers the detection sensitivity as the spot size is spread across multiple changing gradients. This results in a lower OBD detection signal at higher modes. Detection systems that use LDV avoid this, allowing for the direct measurement of the displacement of the cantilever, much lower intrinsic noise, and precision of results that are independent of the laser spot size [114]. Furthermore, LDV methods can take repeated measurements of the displacement of the cantilever at several points along its length which can be used to build the mode shape of each eigenmode. We demonstrate this in Section 2.5.

However, the thermal method is only applicable to thermally excited cantilevers. The dependence of the thermal method on thermal excitations limits the frequency range and hence the maximum mode number that it can be applied to. Measuring the resonant frequencies for a cantilever driven only by energy from its ambient environment is challenging as the amplitude of the first mode is typically of the order of angstroms, and

3 For more discussion on the optical beam deflection method, see Chapter 1.

decreases with higher mode number. Despite this limitation, the thermal method is still capable of estimating the effective stiffness of a cantilever. Therefore, we use the thermal method as a benchmark for the new calibation method we propose in this chapter, utilising it at the first few modes.

We note previous studies that adapt the thermal method to consider the effect of cantilever features on calibration. For example, the thermal method was used to show that the tip mass causes the mode shape to deviate from that of a tipless cantilever and that this deviation increases with eigenmode number [115]. It was also shown that non-rectangular geometry of the cantilever can have a dramatic influence on the behaviour of the excited cantilever, due to the existence of non-flexural modes (such as torsional and shear modes). The specific case of approximating V-shaped cantilevers as a rectangular beam has also been shown to lead to significant errors [116]. However, we will be focused primarily with rectangular cantilevers with negligible tip mass, which are expected to be well calibrated by the thermal method and include calculation of the thermal method as a benchmark for our own calibration technique. We use measurements of the mode shape, Section 2.5, to validate this.

The thermal method gives a means to calibrate a cantilever that is thermally excitated. In practice, AFM cantilevers are often driven at the clamped end by piezo-electric actuators [6]. This ensures that the resonant peaks are easily identified and gives a larger range of modes that can be detected. However, the thermal method is formulated by considering the response of a cantilever due to thermal fluctuations caused by its surrounding environment which acts as a thermal bath with temperature, T. If the additional energy from actuation that is imparted to the cantilever is considered, then a different calibration method is needed which applies for both actuated and thermally excited cantilevers. One very widely used technique was proposed by John Sader. Known as the Sader method [117], this calibration method benefits from its ease of implementation and wide applicability. Like the thermal method, it avoids the need for knowledge of difficult to measure properties of the cantilever but it uses a mathematical description of the surrounding fluid dynamics to do so, rather than a result from statistical physics.

The Sader method describes the dynamic deflection of a cantilever immersed in viscous fluid and excited by an external driving force. This force can be from either thermal or direct actuation. The theory assumes that the osillation amplitude of the cantilever is small with respect to the width of the beam such that convective acceleration can be neglected, a good approximation for the motion of a typical AFM probe. Then, the flow can be described by an oscillatory version of incompressible Stokes flow, mathematically equivalent to Brinkman flow for porous media [118],

$$-i\rho_{\mathrm{f}}\omega\mathbf{u} = -\nabla p + \mu_{\mathrm{f}}\nabla^2\mathbf{u}, \qquad \nabla\cdot\mathbf{u} = 0, \tag{2.9}$$

where ω is the frequency of oscillation of the cantilever, $\mathbf{u}$ is the velocity field, p is the pressure field, ρ_{f} is the fluid density, μ_{f} is the fluid viscosity and ∇^2 is the Laplacian of the flow. We consider this flow in detail in Chapter 3.

Given by the fluid flow outlined above, the hydrodynamic loading on the cantilever can be calculated. This loading, represented by a hydrodynamic function, $\Gamma(\omega)$, is due to the additional inertial mass and drag caused by the oscillatory motion of the beam in a surrounding fluid. This problem was previously considered by E. O. Tuck [119], who derived a boundary-integral formulation for the fluid loading on an infinitely thin oscillating boundary. Tuck showed how the asymptotic form of the hydrodynamic loading function is well-approximated by the hydrodynamic loading function on an oscillating cylinder, for which a closed-form analytical result was already given by Stokes in 1851 [120]. Sader then calculated a correction factor, approximating the analytic result for the cylindrical case to that of the infinitely thin case treated by Tuck. What results is a straightforward means to calculate the hydrodynamic loading on a cantilever using only the knowledge of its length, width, and the oscillatory Reynolds number of the flow, avoiding the need for difficult measurements.

We note that, though it sets out specifically to avoid the need to make unnecessary additional measurements, the Sader method can be inverted to provide the areal mass, $\mu = \rho h b$, which is given as

$$\mu = \frac{\pi \rho_f b}{4} \left[Q \Gamma_i(\omega) - \Gamma_r(\omega) \right], \tag{2.10}$$

where subscripts r and i reflect the real and imaginary parts of the hydrodynamic loading function, $\Gamma(\omega)$, Q is the quality factor, and ρ_f is the density of the surrounding fluid. Once the hydrodynamic loading has been calculated through the correction factor introduced in [117], the Sader method calibrates the spring constant of the cantilever by considering the shift in the n^{th} resonant frequency due to the fluid loading. This is given by

$$\omega_{\text{vac},n} = \omega_R \left(1 + \frac{\pi \rho_f b}{4 \rho h} \Gamma_r(\omega_n) \right)^{\frac{1}{2}}. \tag{2.11}$$

Combining (2.10), (2.11) and (2.5), gives the final result, namely that the effective stiffness for the n^{th} mode of a cantilever is[4],

$$k_n = 0.1906 \rho_f b^2 Q L \Gamma_i(\omega_n) \omega_n^2. \tag{2.12}$$

The Sader method has been shown to calculate the spring constant of the fundamental mode of a cantilever to within 5% of the manufacturers value and to within 10% of the Cleveland method [106]. However, the success of the Sader method at higher modes of the micro-mechanical cantilever is contingent on the fluid theory that describes the flow. This becomes increasingly difficult to verify experimentally as the mode number increases. When applied to the first mode, the fluid theory assumes that the Reynolds number of the flow is small and considers (in its simplest form) only two-dimensional flow across the cantilever width. At high mode number, often greater than two or three, the Reynolds number increases and flow along the length has been shown to dominate [121]. We investigate how the contributions of the surrounding fluid change at high

4 The 0.1906 is a result of the effective mass factor, $m_e = 0.2427$, in (2.5) multiplied by $\pi/4$ in (2.10)

mode number for an oscillating cantilever free and near to the wall in Chapter 3. Here, we mention only that our method for the calibration of the effective stiffness at higher modes circumnavigates these difficulties by focussing on estimating material properties of the cantilever instead.

2.4 A NOVEL CALIBRATION METHOD FOR HIGHER MODES

Current calibration methods have developed in such a way that it is possible to quickly and reliably calculate the effective spring constant of the fundamental mode of a micro-mechanical cantilever. However, the ability to quantify non-topographic properties of a sample requires good knowledge not only of the spring constant of the cantilever but also of the effective stiffness at higher modes, as we demonstrate in Chapter 5. Furthermore, material properties of the cantilever, such as the density and thickness of composite layers are of additional benefit to both numerical and analytic models, see for example [122]. Here, we describe our new method of calibration. We show how considerations of the composite structure of the AFM probe, along with results about the fluid dynamics at the first mode can be used to find the effective stiffness of the cantilever at arbitrary mode number. Our method also estimates the thickness of the reflective top layer of an AFM probe, which can be some tens of nanometres, as well as the idealised resonant frequencies of the cantilever were it to oscillate in a vacuum. These additional results are a benefit to the broader MEMS community as they offer a straightforward means to predict the resonant peaks in the response of the cantilever using only measurements from the first mode.

The method is achieved as follows: The resonant frequencies of the Euler-Bernoulli beam can be calculated provided the material properties of the beam are known, namely the flexural rigidity EI and the areal mass density μ, as described in Section 2.4.1. However, as the material properties of micro-mechanical cantilevers are often not known to high accuracy, considerations of the fluid dynamics at the first mode are use to infer these properties. This gives a means for calculating the areal mass density, μ, while the flexural rigidity relies on considerations of the beam composite structure (a result of the introduction of a gold layer, commonly used to boost the reflectivity of AFM probes), described in Section 2.4.2. A further uncertainty comes from the unknown thickness of this reflective layer, h_{Au}, as well as the total thickness of the beam, h_{T}, as shown in Figure 2.1. These two unknown thicknesses are found by solving two simultaneous nonlinear equations: the equation for the flexural rigidity of a composite beam and the shift in resonant frequency due to fluid damping. Once the two thicknesses are found, the flexural rigidity can then be found which then leads to a calculation for the resonant frequencies of the beam in vacuo. Finally, these resonant frequencies in vacuo are combined with (2.5) to find the effective stiffness for each resonant mode, as described in Section 2.4.3.

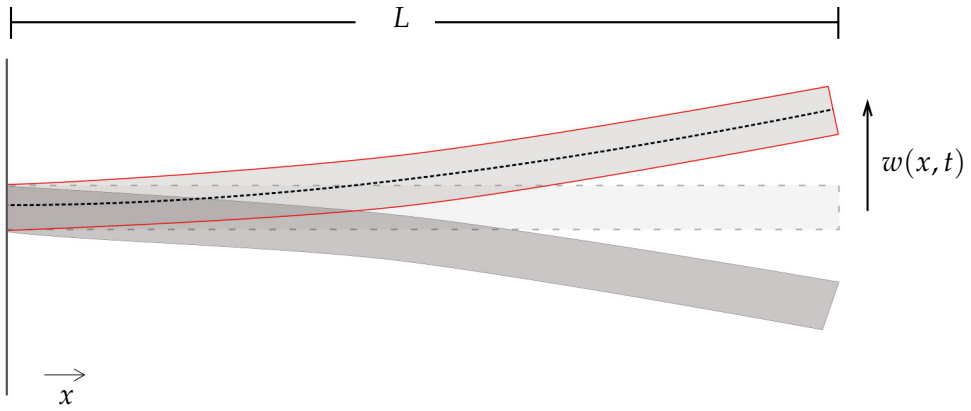

Figure 2.2: The Euler-Bernoulli beam theory modelsl the flexural bending, $w(x,t)$, of a beam.

2.4.1 *The Euler-Bernoulli Beam*

We begin by outlining a model for the motion of the cantilever itself. A common model for describing the AFM probe is the Euler-Bernoulli beam equation [66, 70], which describes how small, time-varying deflections occur due to flexural bending. Though the Euler-Bernoulli beam ignores shear deformation and rotary inertia, it can be adapted to incorporate them either individually or together to give the Timoshenko beam equation [123]. The Timoshenko model has been shown to give accurate predictions of the resonance frequency of stocky beams[5] at high mode number [123]. This condition is satisfied by beams which are oscillating at frequencies with wavelengths, λ_n, similar to the total thickness of the beam, h_T [123]. We will show later that this assumes a frequency far higher than the standard operation of an AFM. As such, we expect the Timoshenko beam theory to give little improvement in accuracy and here focus exclusively on the Euler-Bernoulli beam theory.

The Euler-Bernoulli beam theory, reproduced from [124] describes the motion of a homogenous, non-rotational beam with constant cross-sectional area which is subject to oscillatory forcing at a single frequency, ω,

$$EI\frac{\partial^4 w}{\partial x^4}(x,t) + \rho A\frac{\partial^2 w}{\partial t^2}(x,t) + \gamma_\mathrm{c}\frac{\partial w}{\partial t}(x,t) = F(x,t)e^{i\omega t}, \tag{2.13}$$

where A is the cross-sectional area, $w(x,t)$ is the position of the neutral axis (the axis that undergoes no strain) in the x-direction as shown in Figure 2.2, γ_c is the intrinsic damping of the cantilever, $F(x,t)e^{i\omega t}$ is the force per unit length acting on the beam and ω is the angular frequency, $\omega = 2\pi f$, for some vibrational frequency, f.

By neglecting damping and considering the unforced case, we can write (2.13) as

$$EIw''''(x,t) + \rho A\ddot{w}(x,t) = 0, \tag{2.14}$$

5 Stocky refers to those beams that have thicknesses similar to widths resulting in non-neglibile internal shear forces.

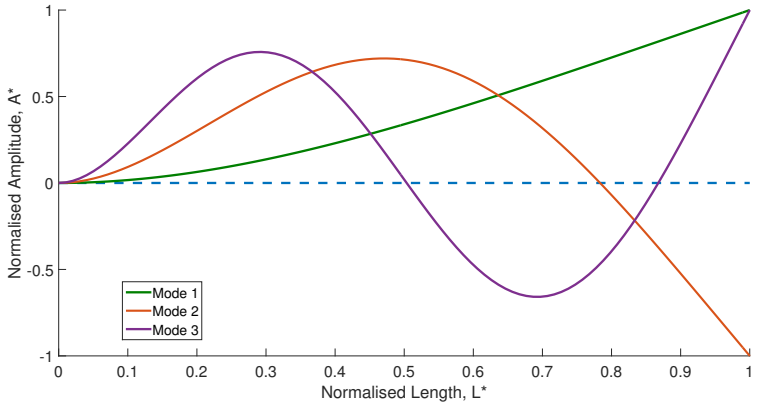

Figure 2.3: The first three spatial mode shapes of the Euler-Bernoulli beam with cantilevered boundary conditions, (2.17) - (2.18), with amplitude normalised according to (2.21) and length $L^* = x/L$.

where dash represents spatial derivative and dot represents time derivative. The first spatial derivative, $w'(x,t)$, describes the slope or curvature of the deflection, $EIw''(x,t)$ describes the moment around which bending occurs at position x, and $EIw'''(x,t)$ describes the shear force at position x.

Following a separation of variables approach, we write the solution of (2.14) as an infinite sum of spatial terms, $\phi_n(x)$, temporal terms, $T_n(t)$, and constant terms, C_n,

$$w(x,t) = \sum_{n=1}^{\infty} C_n \phi_n(x) T_n(t).$$

When substituted back into (2.14), this gives two ordinary differential equations. The eigenfunctions $\phi_n(x)$ describe the mode shapes of the beam and once normalised, can be used to give its spatial deflection. As the PDE is fourth order, we expect solutions of the form

$$\phi_n(x) = A_1 \sin(\alpha_n x) + A_2 \cos(\alpha_n x) + A_3 \sinh(\alpha_n x) + A_4 \cosh(\alpha_n x), \tag{2.15}$$

where A_i, $i = 1, ..., 4$, are constant coefficients, found from the boundary conditions, and α_n is the n^{th} eigenvalue, also known as the wave number or the frequency parameter. Combining (2.14) and (2.15) gives the dispersion relation,

$$\alpha_n^4 - \frac{\rho A}{EI}\omega_n^2 = 0. \tag{2.16}$$

Any solution to the dispersion relation (2.16) must satisfy the characteristic equation of the cantilever in question. The characteristic equation will differ based on the various spatial boundary conditions possible. As the PDE is of fourth order in space, we have four boundary conditions; typically two at each end of the beam.

For a cantilever clamped at one end and free to oscillate at the other, the boundary conditions are, at the clamped end ($x = 0$),

$$w(0,t) = 0, \qquad w'(0,t) = 0, \tag{2.17}$$

and at the free end ($x = L$) we have,

$$w''(L,t) = 0, \qquad w'''(L,t) = 0, \tag{2.18}$$

which ensures that there is no bending moment or shearing force at the free end.

The characteristic equation of the beam, also known as the frequency equation, is then found by seeking non-trivial solutions of (2.15) that satisfy boundary conditions (2.17 – 2.18) namely,

$$\cos(\alpha_n L)\cosh(\alpha_n L) + 1 = 0, \tag{2.19}$$

where the solutions $\alpha_n L$ for $n = \{1, 2, ...\}$, give the set of eigenvalues α_n of the vibrational eigenmodes. The roots of (2.19) are well approximated by $\frac{\pi}{2}(2n-1)$ as $n \to \infty$. Combining the characteristic equation with the dispersion relation gives a set of n eigenmodes with corresponding eigenfrequencies, ω_n. The associated spatial modes are given by,

$$\begin{aligned}\phi_n(x) = \left(\cos\left(\frac{\alpha_n x}{L}\right) - \cosh\left(\frac{\alpha_n x}{L}\right)\right) - \\ \frac{\cos(\alpha_n) + \cosh(\alpha_n)}{\sin(\alpha_n) + \sinh(\alpha_n)}\left(\sin\left(\frac{\alpha_n x}{L}\right) - \sinh\left(\frac{\alpha_n x}{L}\right)\right),\end{aligned} \tag{2.20}$$

illustrated in Figure 2.3 for $n = 1, ..., 3$. These spatial eigenmodes, $\phi_n(x)$, can be normalised according to

$$\int_0^L \phi_n^2(x)\mathrm{d}x = 1, \tag{2.21}$$

such that they provide an orthonormal basis for the solution set of the cantilever's displacement.

Given this expression for the eigenvalues of the cantilevered probe, we briefly return to the Timoshenko beam theory. Assuming that the eigenvalues will be similar, we can restate the condition for Timoshenko beam theory; the wavelength, $\lambda_n = \frac{2\pi}{\alpha_n}L \approx \frac{4L}{(2n-1)}$, of a resonant frequency must be of a similar size to the thickness of the beam. Given this condition, we restate it in terms of the n^{th} mode,

$$n \sim \frac{1}{2}\left(\frac{4L}{h} - 1\right). \tag{2.22}$$

In practice, AFM probes have length to thickness ratios, L/h, equivalent to order 10^2. This would require mode numbers as high as the 200th mode before the Timoshenko beam theory is expected to yield significant increases in accuracy. This justifies our focus on the Euler-Bernoulli theory.

Once the solutions to the characteristic equation are found, the dispersion equation (2.16), gives the angular resonance frequency for each mode,

$$\omega_{n,\text{vac}} = \alpha_n^2 \sqrt{\frac{EI}{\mu}}. \tag{2.23}$$

This represents the angular resonant frequency for a beam that is oscillating without any fluid damping; the *in vacuo* resonant response of the cantilever. We will make use of this relation in what follows.

2.4.2 *Flexural Rigidity of a Composite Beam*

The micromechanical beams used as AFM probes are rarely constructed from single materials. Instead, they include a reflective layer, used to boost the signal strength of the detection system, which introduces significant difficulty in estimating the resonant behaviour of the cantilever. For example, the Bruker MSNL-B (Bruker Nano Inc., CA, USA) cantilever (that we consider later when demonstrating our method) is made mostly of silicon nitride (SiNi) with a gold (Au) layer on the top side of the probe. The gold layer has a density of 19 320 kg/m^3 and a Young's Modulus of 80 GPa, while the SiNi body has a density of 3100 kg/m^3 and a Young's Modulus between 280 GPa to 290 GPa [125, 126]. The thickness of the top layer will have significant influence over the structural and mechanical properties of the entire beam and must be accounted for if the beam is to be calibrated at higher modes. Staying with properties of the MSNL-B, a 50 nm layer of gold on the top layer will cause a change in flexural rigidity of the whole beam by approximately three orders of magnitude (EI $\sim 10^{-11}$ to EI $\sim 10^{-14}$), calculated using (2.29) below.

While the gold layer will have different thermal, magnetic, and chemical properties to the rest of the beam, we focus only on the mechanical properties; the combined density and the flexural rigidity. Both can be calculated by considering the AFM probe as a composite cantilever and using classical results from the theory of composite structures. The density is given by the rule of mixtures for composite materials [127],

$$\rho_\text{T} V_\text{T} = \rho_\text{A} V_\text{A} + \rho_\text{B} V_\text{B}, \tag{2.24}$$

such that the product of the total density, ρ_T, and volume, V_T, is equal to the sum of the product of the constituent parts of the composite, denoted here by subscripts[6] A and B. We assume that the width and the length are equal for both sections. Hence, we can rewrite (2.24) as,

$$\mu = b(\rho_T h_T) = b(\rho_A h_A + \rho_B h_B), \tag{2.25}$$

where we now consider only width, b, height, h, and the density, ρ, of both the constituent parts and the total beam. We define the product of the thickness, width, and density of the total beam as the areal mass density, μ. Finally, since we consider only a

6 Note that we will later consider the specific case of a beam with gold top layer such that $h_B = h_{\text{Au}}$.

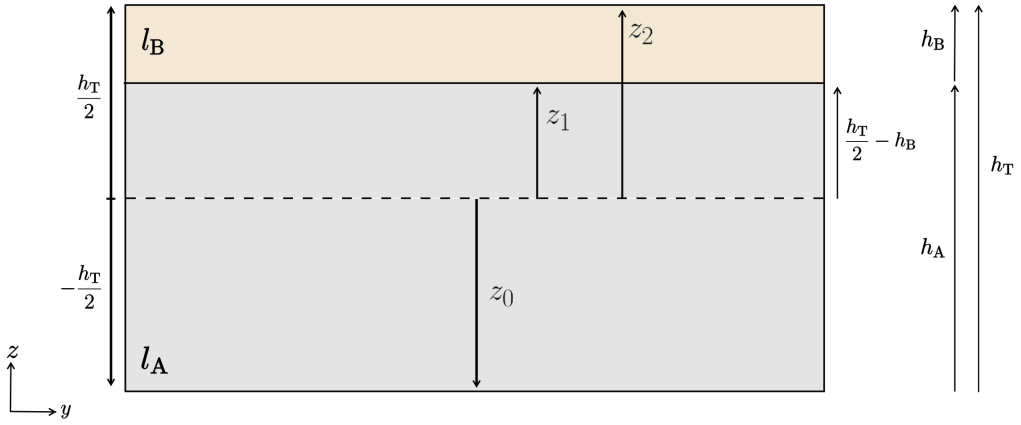

Figure 2.4: An illustration of a two layer composite, where z_1 is the distance from the neutral axis to the first layer, h_B. The composite structure was considered when calculating the flexural rigidity of the beam, (2.29).

two layer composite, we rewrite this equation in terms of only the top layer and the total layer,

$$\mu = b\left(\rho_A(h_T - h_B) + \rho_B h_B\right). \tag{2.26}$$

We now consider the flexural rigidity of the AFM probe, found through another classical result; laminated beam theory [127]. This theory assumes that the composite layers are perfectly bonded, are linearly elastic, and that there is no rotation in the plane cross-sections. These assumptions are consistent with a typical AFM probe. The combined flexural rigidity, EI, of the composite beam is given by

$$EI = \frac{b}{3}\sum_{k=1}^{N} E_k(z_k^3 - z_{k-1}^3). \tag{2.27}$$

where, b is the total width of the beam, N is the total number of layers, E_k is the Young's modulus and z_k is the distance from the neutral axis of the k^{th} layer. For our specific case of an AFM probe with two layers, as shown in Figure 2.4, we have

$$EI = \frac{b}{3}\left[E_A\left(\left(\left(\frac{h_T}{2} + \frac{h_T}{2} - h_B\right)^3\right)^3\right) + E_B\left(\left(\frac{h_T}{2}\right)^3 - \left(\frac{h_T}{2} - h_B\right)^3\right)\right]. \tag{2.28}$$

Substituting $H = h_T - 2h_B$, this further simplifies to,

$$EI = \frac{b}{24}\left[E_A(h_T^3 + H^3) + E_B(h_T^3 - H^3)\right]. \tag{2.29}$$

We make use of both of these equations in what follows.

2.4.3 *Combining the Sader Method with Composite Beam Theory*

We now show how a combination of the Euler-Bernoulli equations for the cantilever, considerations of the fluid dynamics of the surrounding environment, and the results from composite beam theory lead to a new calibration method for the higher modes of the cantilever.

Our method is straightforward to implement, without the need for additional reference materials or changes to be made to the cantilever. It follows four steps, which only require measurements to be taken of the first mode,

1. We consider the resonant frequency of the cantilever in vacuo, given by (2.23) and the equation for the shift in frequency when the cantilever is in ambient conditions, given by (2.11).

2. We then consider the material properties of the cantilever whilst taking into account the thickness of the reflective layer, through (2.26 – 2.29).

3. The unknown thickness of the reflective layer and total thickness of the beam can be found by solving two nonlinear simultaneous equations, (2.32 – 2.33). The first is the rule of mixtures for composite materials and the second combines the equation for the flexural rigidity of the beam with the equations for the shift in resonant frequency due to fluid damping.

4. Finally, the two thicknesses are used to find the flexural rigidity of the beam which, in turn, gives the resonant frequencies in vacuo and the effective stiffness of the beam at each resonant frequency.

Before we describe our method in more detail, we note again the equation for effective stiffness, (2.5),

$$k_n = m_e \mu L \omega_{n,\mathrm{vac}}^2. \tag{2.30}$$

Our approach to the problem of higher mode calibration is to discern the material properties that are avoided by most other calibration techniques in order to find the resonant frequency in vacuo, $\omega_{n,\mathrm{vac}}$, at any mode number. Given the resonant frequency in vacuo, we can find the effective spring constant at any desired mode. Furthermore, the shift in resonant frequency from $\omega_{n,\mathrm{vac}}$ can also be used to estimate the influence of the surrounding fluid on the cantilever.

As described above, the resonant frequency in vacuo is given by the dispersion relation of the Euler-Bernoulli beam equation, (2.23). We note that this assumes an AFM probe with rectangular geometry, with negligible tip mass, and constant height variation. To account for these changes, it is possible to adapt the Euler-Bernoulli beam equation via, for example, a finite difference (FD) approach or through a change at the boundary conditions [122, 128]. However, we will later show that this is not necessary for the cantilever we chose to investigate.

When the cantilever is excited in ambient conditions, there is a resulting shift in the n^{th} resonant angular frequency $\omega_{n,\mathrm{R}}$, due to the influence of the surrounding fluid. This

causes an additional inertial term, $\Gamma_r(\omega_{n,R})$, and drag term, $\Gamma_i(\omega_{n,R})$, which lower the resonant frequencies of the cantilever. As we have seen, considerations of the fluid dynamics were taken advantage of by Sader [117], which used them to circumnavigate the need to measure the areal mass density, μ, through the relation

$$\mu = \frac{\pi b^2 \rho_f}{4} \left(Q_1 \Gamma_i(\omega_1) + \Gamma_r(\omega_1) \right), \tag{2.31}$$

where Q_1 and ω_1 are the measured Q-factor and angular resonance at the first mode in ambient conditions. The Sader method also gives the shift in frequency due to presence of the surrounding fluid, given as (2.11). Thus, we can calculate the the areal mass density of the probe using (2.31). Once found, we are able to use the dispersion relation, (2.23), to find the higher resonant frequencies in vacuo. These resonant frequencies serve three purposes. First, they can be used to verify or identify resonant frequencies in the frequency sweep of a microcantilever. Second, the ratio of the calculated resonant frequencies in vacuo and the measured resonant frequencies can be used to estimate the hydrodynamic loading on the cantilever at any mode. Finally, when combined with (2.5), they give the effective stiffness of the cantilever at arbitrary mode number using only the first resonant frequency. However, in order to find these resonant frequencies, the flexural rigidity must also be known. As discussed, this will be influenced by the presence of the reflective gold layer on the cantilever and must be accounted for.

The flexural rigidity of the cantilever can be found by taking into account the additional reflective layer, included on most AFM probes to boost the detection signal. However, this also requires knowledge of the thickness of the reflective layer which is typically tens of nanometres thick. Instead, we calculate this layer using the above equations, without resorting to additional measurements of the cantilever. First, we assume the cantilever is a two-layer composite beam and use the results from composite beam theory, described above in (2.26) and (2.29). By combining the dispersion equation for the beam, (2.23), with the shift in frequency due to hydrodynamic effects, (2.11), and the flexural rigidity of a composite beam, (2.29), we have an equation for the two unknown thicknesses, h_T and h_{Au}, in terms of readily measureable quantities,

$$\frac{b}{24}\left[E_{SiNi}(h_T^3 + H^3) + E_{Au}(h_T^3 - H^3)\right] = \mu\left[\left(\frac{L}{\alpha_1}\right)^4 \omega_{1,R}^2 \left(1 + \left(\frac{\pi b^2 \rho_f}{4\mu}\right)\Gamma_r(\omega_{1,R})\right)\right], \tag{2.32}$$

where subscript SiNi denotes the bulk silicon nitride material of the Bruker MSNL-B cantilever we consider in Section 2.5 and Au denotes the gold reflective top layer. The rule of mixture for composite materials gives a second equation,

$$b\left(\rho_{SiNi}(h_T - h_{Au}) + \rho_{Au} h_{Au}\right) = \mu, \tag{2.33}$$

so that (2.32) and (2.33) can be solved numerically as two simultaneous equations for the two unknown thicknesses given knowledge of the cantilever's length, width, quality factor, and resonant frequency of the first mode, as well as the viscosity and density of

the surrounding fluid. Once these thicknesses are found, they can be used to find the unknown flexural rigidity of the AFM probe, (2.29), and the angular resonant frequency in vacuo, (2.23), of the n^{th} mode. Finally, these resonant frequencies are used with (2.5) to find the effective stiffness at any mode.

2.5 MEASUREMENTS

We demonstrate our method for the calibration of cantilevers, by taking five frequency sweeps of different MSNL-B (Bruker Nano Inc., USA) type rectangular cantilevers which feature a gold layer. These peaks were taken with the custom-built AFM at the University of Bristol, using a Polytec CLV 2534 laser Doppler Vibrometer to measure the displacement of the cantilever and a three axis stiction drive stage system (Smaract, Germany) controlled through custom software (Bristol Nanodynamics ltd., UK) for independent x-y-z motion of the cantilever under the focussed LDV laser. However, we note that all that is required in order to implement our method is the length, width, quality factor, and resonant frequency of the first mode of the cantilever as well as the density and viscosity of the surrounding fluid, rather than any specific hardware considerations. However, we utilise the LDV laser to validate that the beam is well described by the Euler-Bernoulli beam model.

The first three frequency sweeps, I. - III., were taken when the cantilever was excited by thermal fluctuations from the ambient environment, and these successfully captured the first four resonance frequency peaks, shown in Figure 2.5a. Our ability to capture the effective stiffness of the cantilever will be supported by our ability to correctly identify the cantilever's resonant frequencies in vacuo. However, as shown in Figure 2.5a, it is difficult to identify the higher modes of the thermally excited cantilever due to the small amplitude of higher resonant peaks. This prevents us from identifying how succesful our method is at calculating the resonant frequency of the beam in vacuo which is expected to be near to the measured resonant frequency. Hence, we use a different means for identifying the resonant peaks of thermally excited cantilevers.

2.5.1 *Mode Identification*

Our method for higher mode calibration does not depend on measurements of the higher modes of a micro-mechanical cantilever, but rather gives a means of identification using only the resonant behaviour at the first mode. In order to correctly demonstrate our method, we must have a means for higher mode identification so that we can compare against other calibration means such as the Sader method and the thermal method.

As discussed above, an AFM cantilever that is driven by thermal excitations will have significant noise at high frequencies. This makes it difficult to identify the higher mode resonant peaks. This can be seen in Figure 2.5a, where the first four resonant peaks can be visually identified yet the amplitude of the higher modes is not much more than the noise level. However, the ability to identify resonant peaks is necessary for both the

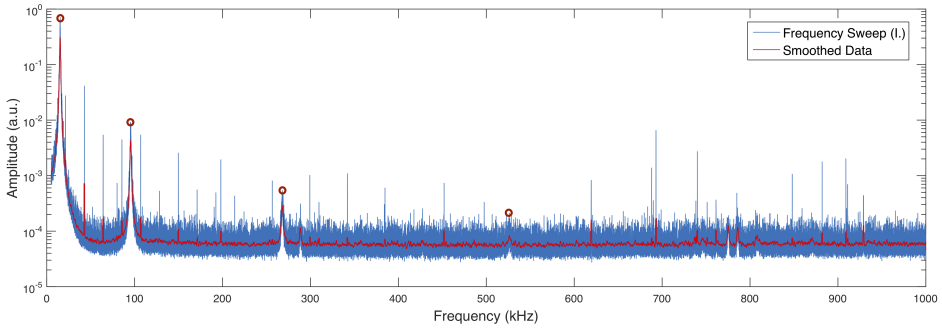

(a) Power spectrum of a thermally driven cantilever (I.).

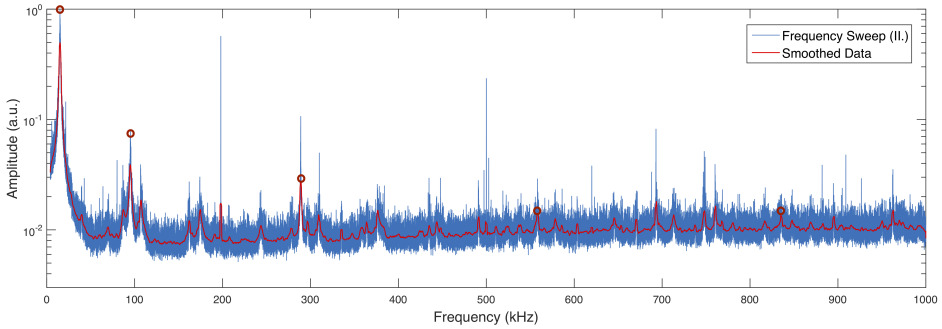

(b) Power spectrum of a thermally driven cantilever (II.).

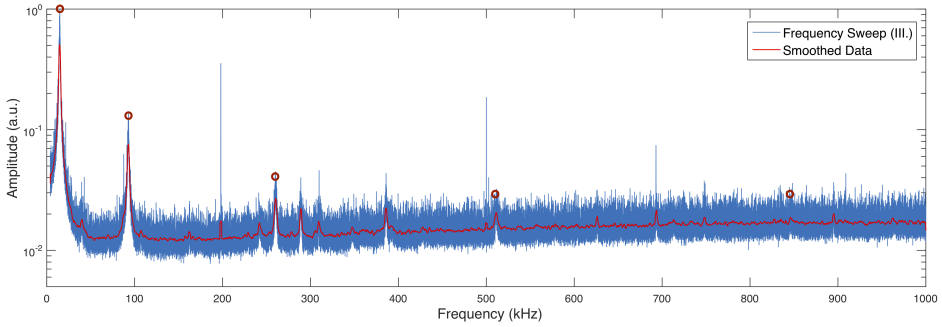

(c) Power spectrum of a thermally driven cantilever (III.).

Figure 2.5: The average power spectra (I. - III.) from incremental measurements along the length of a thermally excited Bruker MSNL-B cantilever for the first four modes of the cantilever in power spectrum I. (a) and first five in power spectra II.-III. (b-c). A moving window average filter (red) was applied to find the resonant peaks of the raw data (blue). Modes, shown as red circles, were identified visually (for I.) and using mode-shapes identified in Figure 2.6 (for II.-III.).

Sader method and the thermal method to find the effective stiffness. Furthermore, our ultimate aim of quantified non-topographic material measurements utilises the frequency shift away from a free resonance due to the tip-sample interaction, as described in Chapter 4. Therefore, an inability to identify resonant frequencies, or an incorrectly identified resonant frequency, will lead to signifcant errors in subsequent measurements.

In order to identify the resonant peaks of the thermally excited cantilever and validate our method, we adjust the methodology of [15] and use a laser Doppler vibrometer to take repeated measurements of the displacement along the length, x, of the cantilever. This gives us a set of points containing the frequency response of the cantilever at intervals across the length, shown in Figure 2.6. We choose to measure the cantilever at 0.5 µm intervals on the 120 µm cantilever, so as to build an image of the spatial mode-shapes as a function of frequency. Figure 2.6 shows the displacement of the beam at a specific frequency and position on the cantilever. Bright yellow areas show high amplitudes and shades of blue show low amplitudes. The resonant frequencies are then identified by visual inspection, where we look for an appropriate pattern of nodes and antinodes along the length. The resonant frequencies are found to be 15.0 kHz, 92.9 kHz, 260 kHz, 511 kHz, 847 kHz for the first five bending modes. These results demonstrate that the highest amplitude signal for the first mode occured near to the free end ($x/L \approx 1$). On the other hand, we note that there are two additional bandings in Figure 2.6. The first, at 347 kHz, is likely to be due to the torsional resonance of the beam. The second, at 742 kHz, is unexpected due to the number of nodes and antinodes but may also be a torsional mode. These additional peaks highlight the complexity of the micro-mechanical cantilever's resonant behaviour.

One of the underlying assumptions of our method is that the micro-mechanical cantilever does not violate any of the assumptions of the Euler-Bernoulli beam theory. We can now justify this, using the measurements of the frequency response of the beam at intervals along its length. If the beam follows the assumptions of the Euler-Bernoulli beam theory, we expect the displacement to be described by the spatial mode shapes (2.20) at each resonant frequency. Hence, we plot the amplitude of the beam, at resonant frequencies noted above, together with the normalised mode-shapes for a cantilevered beam, using the eigenfunction, (2.20) normalised by (2.21). The results are shown in Figure 2.7. We see very good agreement with the analytic model of the beam and our measurements of the deflection. This gives us confidence that the cantilever under investigation behaves according to the theoretical assumptions and that we do not need to extend our model to account for additional features such as the tip mass or height changes.

The resonant behaviour of the cantilever in the neighbourhood of each resonance is expected to behave like a harmonic oscillator. Having selected the peaks, using the method above, the response of a simple harmonic oscillator (SHO) can be fitted to the measured thermal noise spectra of the cantilever. The response of a SHO, R_{SHO}, with white noise is

$$R_{\text{SHO}}(\omega) = A_{\text{white}} + \frac{A_n \omega^4}{(\omega^2 - \omega_n^2) + \left(\frac{\omega \omega_{n,\text{R}}}{Q_n}\right)^2}, \tag{2.34}$$

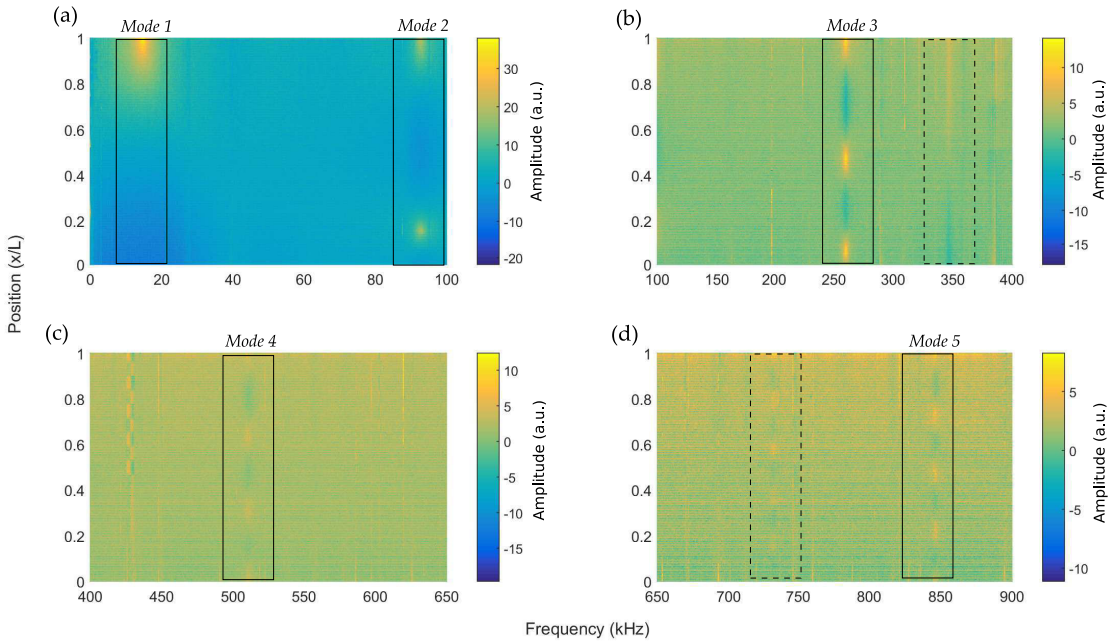

Figure 2.6: Plots over frequency ranges containing (a) the first (15.0 kHz) and second (92.9 kHz), (b) third (260 kHz, (c) fourth (511 kHz) and (d) fifth (847 kHz) modes, respectively. The modes are identified as the plan-view deflection of the beam with nodes represented as breaks in the yellow bands at the frequencies stated above and marked as solid boxes. Note the existence of two spurious mode shapes at 347 kHz (b) and 742 kHz (d), denoted as dashed boxes.

where A_{white} is the amplitude of the white noise and ω is the sampled frequency. Curve fits were performed using the MatLab curve fitting toolbox [7], where the free variables were the resonance frequency, $\omega_{n,\text{R}}$, quality factor, $Q_{n,\text{R}}$, white noise, A_n, and the amplitude, A, for a given input frequency, ω. These fits gave the resonant parameters for our method. Examples of these fits are shown in Figure 2.8. In order to have a greater range of resonant frequencies, additional frequency sweeps, IV. – V., were taken by exciting the cantilever at its base with piezo-electric actuators and a lock-in amplifier (Zurich Instruments HS2Li). These sweeps were capable of capturing eleven of the resonant frequencies, shown in Figure 2.9b up to the fifth mode and in Figure 2.10. The noise, even at high frequencies, was low enough for us to visually identify the resonant peaks without difficulty. This is aided by the high resolution of the LDV detection system, which is able to detect amplitudes up to $\pm 15\,\text{pm}$.

Having identified the resonant peaks for all five frequency sweeps, we proceed to calculate the effective stiffness of the beam using the thermal method and Sader method, outlined in Section 2.3 as well as our own method, outlined in Section 2.4. A comparison of these methods is shown in Table 2, Table 3, and Table 4. Our method of calibration also calculates both the thickness of the reflective layer and the cantilever as a whole. In order to validate these calculations, we obtain estimates of the material properties of the cantilever by taking images with a scanning electron microscope (SEM), shown in

7 MATLAB and Statistics Toolbox Release 2014b, The MathWorks, Inc., United States.

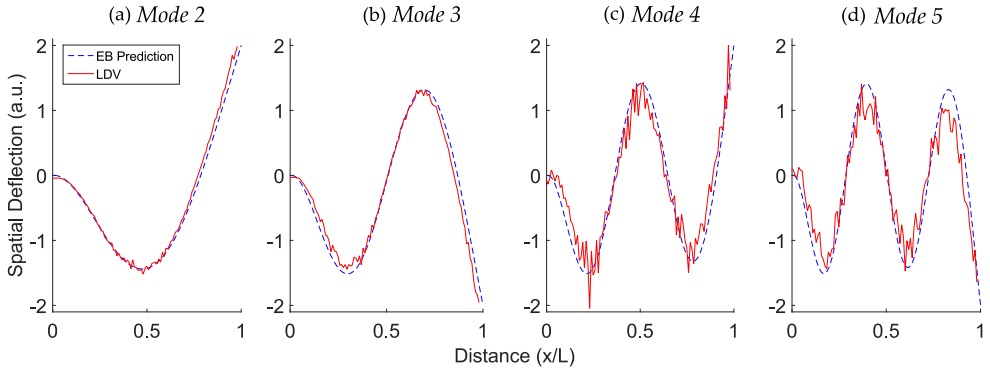

Figure 2.7: The deflection of the cantilever measured by the LDV (red, solid line) compared to the analytic model (blue, dashed line) for modes 2-5.

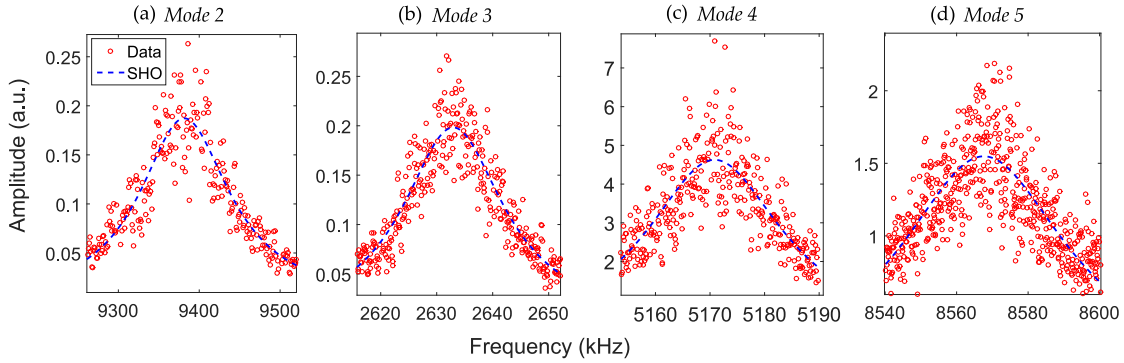

Figure 2.8: Demonstration of the used SHO fits for modes 2-5 of frequency sweep IV, using equation (2.34), to give the Q factor and resonant frequency for each mode of the cantilever.

Figure 2.11. These images showed the tip height, off-set, the total length and width of the cantilever (used in the calculations for our calibration method and the Sader method) and an approximation for both the total thickness of the cantilever and the individual thickness of the gold layer.

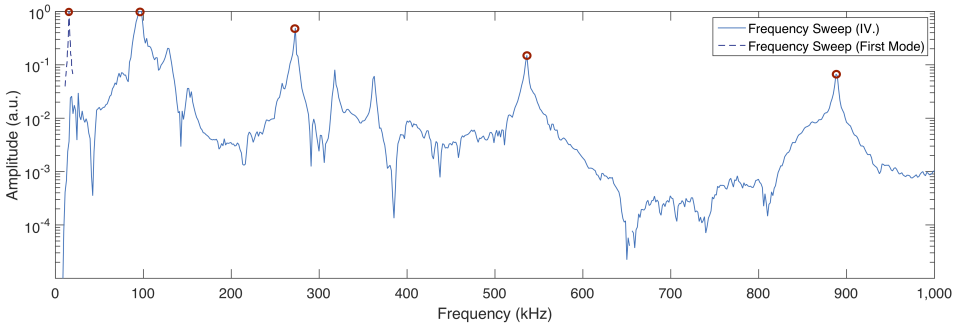

(a) Power spectrum (IV.) of a driven Bruker MSNL-B cantilever for the first five modes of the cantilever. The first mode (dashed line) was measured with the AC mode of the lock-in amplifier switched off as the AC mode corresponds to a high-pass (15 kHz) filter.

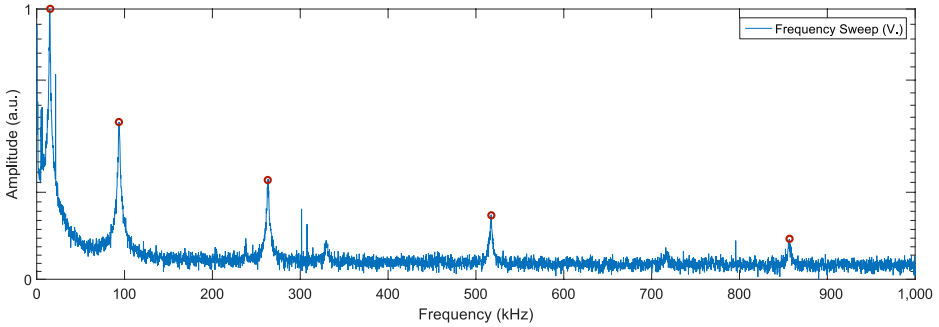

(b) Power spectrum (V.) of a driven Bruker MSNL-B cantilever for the first five modes of the cantilever.

Figure 2.9: Power spectra of the cantilever when driven, where modes are shown as red circles.

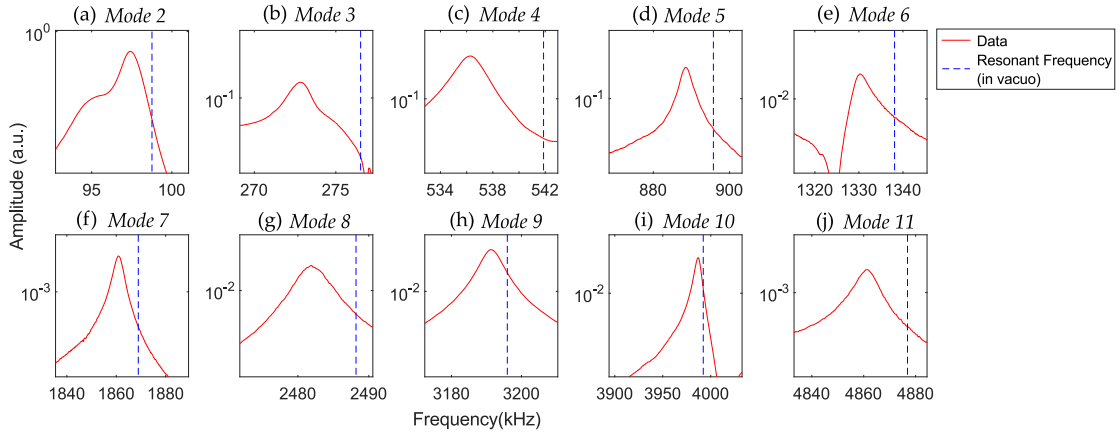

Figure 2.10: The second to eleventh modes of power spectrum IV., starting in the top left (mode 2) and moving from left to right to the bottom right (mode 11). The blue dashed line marks the calculation of resonant frequency in vacuo for each mode. Details of the resonant frequency (measured and in vacuo) and the calculated effective stiffness is shown in Table 3.

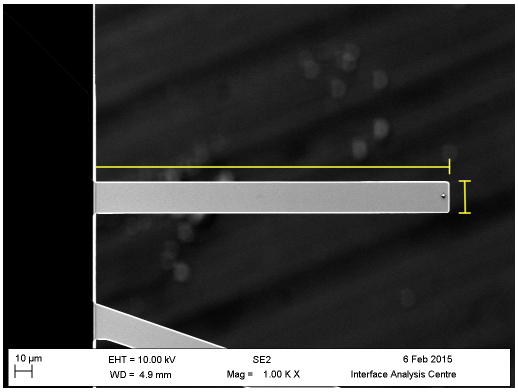

(a) Image showing the length of the cantilever, measured to be 207.0 µm ± 0.5 µm.

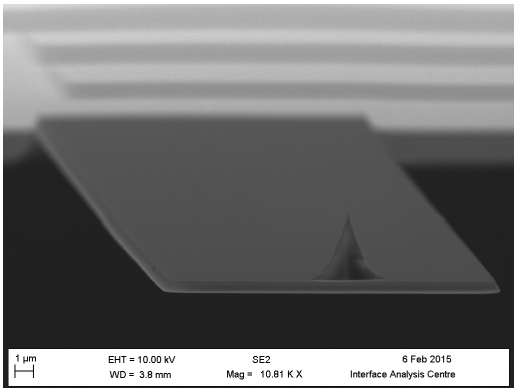

(b) An image showing the tip height and width which was found to be less than 1% of the total mass of the cantilever.

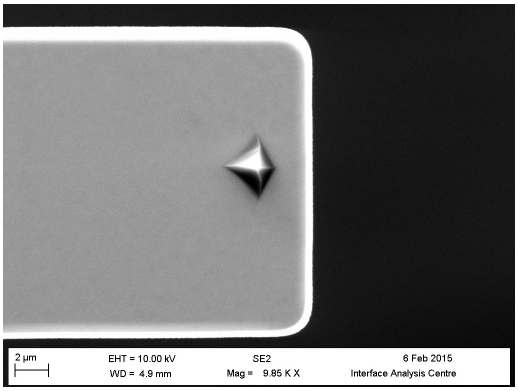

(c) An image showing the width of the cantilever, measured to be 19.0 µm ± 0.5 µm. Note the slight asymmetry of the cantilever tip position.

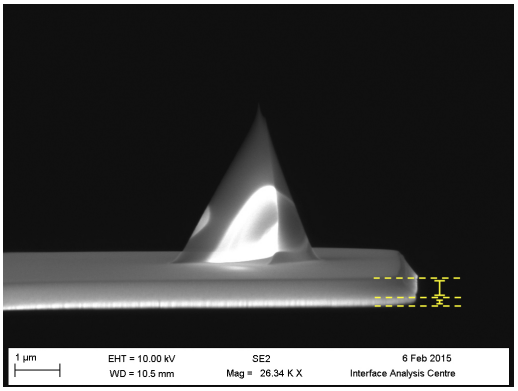

(d) An image showing the cantilever thickness, measured to be 0.50 µm ± 0.05 µm.

Figure 2.11: SEM images of the MSNL 10B Bruker Cantilever.

2.6 RESULTS AND DISCUSSION

The results of applying our method, described in Section 2.4, together with results from the Sader and thermal methods are shown in Table 1, Table 2, Table 3, and Table 4.

	h_T (μm)	h_{Au} (nm)	Q -	$f_{1,R}$ (kHz)	$f^*_{1,vac}$ (kHz)	k_1 (Nm^{-1})
Manufacturers	0.55	45	-	15	-	0.02
(Uncertainty)	(± 0.05)	(±5)	-	(±5)	-	(±0.02)
I. (Thermal)	0.547	37	21	15.1	18.2	0.0212
II. (Thermal)	0.524	29	19	14.7	18.1	0.0194
III. (Thermal)	0.553	36	21	15.1	18.2	0.0215
IV. (Driven)	0.549	36	21	14.9	18.1	0.0217
V. (Driven)	0.524	20	18	15.7	21	0.0187

Table 1: The thicknesses, h_T and h_{Au}, Q-factor, Q, measured resonant frequency, $f_{1,R}$, and estimated resonant frequency, $f^*_{1,vac}$, found using (2.23) and ignoring the influence of the additional gold layer, as well as the effective spring constant of the first mode, k_1, found using our method for frequency sweeps I.–V.

As shown in Table 1, our method for calibration calculates the thickness of the cantilever to within 10% of that given by the manufacturer in all cases; the gold layer is given as 45 nm ± 5 nm and the total thickness is given as 0.55 μm ± 0.05 μm. For all five measurements taken, we find that the mean total thickness as 0.52 μm and the mean thickness of the gold layer to be 34 nm. In three cases (I., III. and IV.), we are within 20% of the manufacturers value for the thickness of the gold layer. However, we consistently calculate a value lower than that provided by the manufacturer and cannot say with certainty whether this is a product of our method, or anomalies within the fabrication process. Furthermore, we find a consistent value for the resonant frequency of the cantilever in vacuo for the first mode, as well as for the effective spring constant. However, we are primarily interested in the effective stiffness of the higher modes, so turn our attention to the cases where the cantilever was thermally excited beyond the first mode.

The results of the thermally excited frequency sweeps are shown in Figure 2.5. For the first frequency sweep, I., shown in Figure 2.5a, we were only able to visually identify the first four modes. For the first frequency sweep, we failed to record the conversion factor from Volts to displacement so are unable to calculate the thermal method due to the lack of information about the thermal fluctuations. The conversion factor was recorded for all subsequent data collection allowing RMS amplitude data to be gathered from the lock-in amplifier. For the first measurement of the frequency sweep, we apply both the Sader method and our own method for calibration. For frequency sweeps II.-III., we were able to identify five of the resonant frequencies, as discussed in Section 2.5 and summarised in Section 2.4.3, and use the thermal method, Sader method and our own method to calibrate the cantilever. All results are shown in Table 2. We found that our method gives consistent values for the effective spring constant across repeated measurements.

Mode	II.	III.	σ
1	0.0747	0.0944	0.0139
2	1.74	2.20	0.324
3	9.03	15.1	4.27
4	36.1	38.9	1.98
5	51.4	66.6	10.8

(a) The Thermal Method, as described in Section 2.3.

Mode	I.	II.	III.	IV.	V.	σ
1	0.0198	0.0179	0.020	0.020	0.0171	0.0014
2	0.357	0.585	0.970	0.789	0.897	0.259
3	3.61	7.88	10.0	5.64	8.03	2.46
4	4.49	70.3	47.2	21.8	25.4	25.4
5	-	166	169	41.8	63.9	66.9

(b) The Sader Method, as described in Section 2.3

Mode	I.	II.	III.	IV.	V.	σ
1	0.0212	0.0194	0.0215	0.0217	0.0187	0.0013
2	0.835	0.764	0.843	0.853	0.736	0.0527
3	6.54	5.99	6.61	6.69	5.77	0.413
4	25.1	23.0	25.4	25.7	22.2	1.586
5	68.7	62.8	169	69.4	70.2	4.33

(c) Our own method, as described in Section 2.4.

Table 2: (a) The effective stiffness of the cantilever found using the thermal method for the first five modes of power spectra II.-III., (b) the effective stiffness of the cantilever found using the Sader method for the first five modes of power spectra I.-V. (Note that the fifth mode of power spectrum I. could not be identified which prevented the Sader method from being applied) and (c) the effective stiffness of the cantilever found using our own method for the first five modes of power spectra I.-V. All units are in Nm^{-1}

We also found that the thermal method calculates a higher effective stiffness than both Sader method and our own.

It is not possible to use the thermal method to calibrate a cantilever that is excited by piezo-electric actuators, as discussed in Section 2.4. Therefore, we compare only our method to the Sader method when the cantilever is driven directly (IV. and V.). We find good agreement between our method and the Sader method, emphasising that our method is equally applicable to direct and indirect actuation. Furthermore, we found that the variation in effective stiffness increases significantly with mode number for the Sader method due to the need to fit harmonic oscillator equations at each mode for the resonant frequency and Q factor. Instead, our method requires only the measured resonance and Q factor of the first mode which it uses to find the effective stiffness with low variation across experimental set-ups. This again emphasises the robustness of our method which is less exposed to experimental factors such as noise at higher modes.

Mode	f_R (kHz)	$f_{R,vac}$ (kHz)	$f^*_{R,vac}$ (kHz)	k_n (Nm^{-1})	k_{Sader} (Nm^{-1})
1	15.7	15.8	21.0	0.0187	0.0171
2	97.4	98.8	132	0.785	0.897
3	273	277	368.7	6.16	8.02
4	536	542	722	23.6	25.4
5	888	896	1,194	64.5	63.9
6	1,330	1,338	1,784	144	99
7	1,861	1,867	2,492	281	191
8	2,482	2,489	3,317	498	472
9	3,191	3,196	4,261	822	646
10	3,987	3,992	5,322	1282	1057
11	4,861	4,877	6,502	1914	1510

Table 3: The measured resonant frequency, f_R, the calculated resonant frequency in vacuo, $f_{R,vac}$, and the calculated resonant frequency without accounting for the gold layer, $f^*_{R,vac}$, for modes 1 to 11 with units kHz. The effective stiffness found using our own method, k_n, and the Sader method, k_{Sader} are included, where units are in Nm^{-1}.

We next consider the resonant frequency of the cantilever in vacuo. When the gold layer was ignored from our calculations, the frequency of resonance in vacuo, $\omega_{n,vac}$, was estimated to be as much as 35% higher than the measured resonance as shown in Table 3. This emphasises that the gold layer has a significant effect and cannot be ignored from calibration considerations. When we took the gold layer into consideration, we found that the resonant frequencies in vacuo, calculated using the method described in Section 2.4.3, agreed with the measured resonant frequencies to within 2%. This agreement continued through all our measurements at arbitrary mode number. For example, Figure 2.10 shows the estimated resonant frequency in vacuo of the cantilever, dashed blue line, for modes two to ten of power spectrum V. We note that the relative error for the measured resonant frequency of the tenth mode is less than 0.002 demonstrating that our method is useful for both calculating the effective stiffness of the cantilever and quickly finding the location of the higher resonant peaks. This will be relied upon in Chapter 4, where we utilise a shift in resonant frequency to infer material properties.

Given the estimates for the thicknesses and the resonant frequency in vacuo, we can also estimate the additional loading of the cantilever due to surrounding fluid effects by using (2.11) . We found that this gave an overestimate of the fluid loading compared to that predicted by the Tuck-Sader hydrodynamic function for an oscillating thin beam [117, 119], and that there was a large spread of potential values, shown in Figure 2.12. We include the variation across all measurements for modes one to five. However, only frequency sweep (IV.) gave information for modes six to ten and hence, no variation is calculatable. The Tuck-Sader beam was derived under the premise of low oscillatory Reynold's number, ($Re_f \ll 1$), yet all higher modes have Re_f significantly greater than unity. Therefore, we expect that the fluid dynamics should be reconsidered for thin beams oscillating at high frequencies. Despite this, the actual shift in resonant frequency

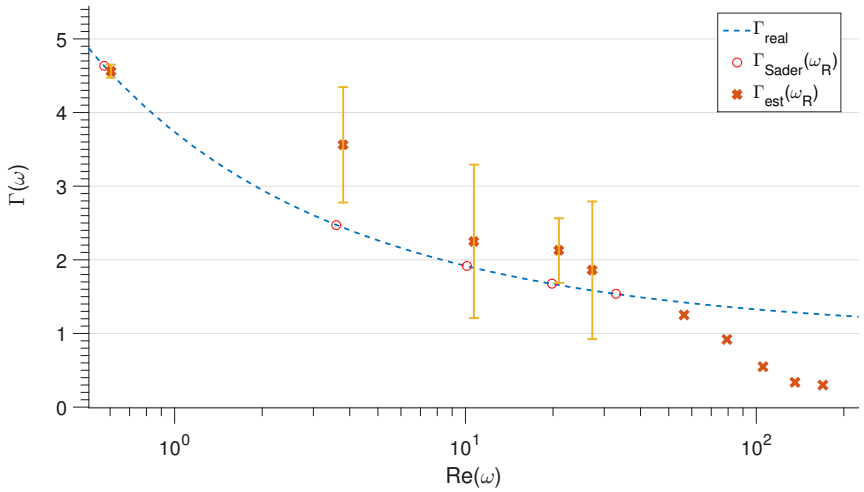

Figure 2.12: The real component of the hydrodynamic function representing interial mass from surrounding fluid on the oscillating cantilever. Orange crosses represent the loading calculated using (2.11) with errorbars representing variance across experiments I.-V. In frequency sweep, V., eleven modes of the cantilever were measured, shown in Figure 2.10, which predicted a decrease in hydrodynamic loading compared to the Sader correction for rectangular beams [117].

from that calculated is less than 2% at the first mode and less than 1% from the fifth mode onwards. This corresponds to less than 5% difference in the effective stiffness and gives a means for identifying the resonant frequencies of the cantilever using a few easily measured properties. This gives us further confidence that our method does indeed accurately predict the effective stiffness of a micro-mechanical cantilever at any mode, as well as providing a means for estimating the thickness of the reflective layer and for identifying higher mode frequencies using only resonant information measured at the first mode and the easy to measure properties (length, width, dnesity of fluid and viscosity of fluid) .

As can be seen in Table 4 and Figure 2.13, our method for the calibration of the effective stiffness has the lowest variation of all three calibration methods investigated. The effective stiffness is a modal property that can be influenced by a number of experimental variables: changes in thickness of the reflective layer, the location and size of the tip, anomalies in the manufacturing process, debris that accumulates on the cantilever or environmental conditions such as humidity. It is therefore encouraging to see such low variation for the calculated effective stiffness considering that it is derived from only the first resonant peak of the AFM probe. Furthermore, the effective stiffness is useful for interpreting and modelling the coupled tip-sample interaction which is influenced by environmental factors such as the surrounding hydrodynamics which do influence the cantilever in a different manner depending on whether the cantilever is oscillating free or close to the sample. We consider the influence of the hydrodynamics of the system when a cantilever oscillates near to the sample in Chapter 3. Hence, it is advantageous that our method gives the effective stiffness of the beam in vacuo, and this will be made use of in Chapter 5.

Mode	k_n	σ_n	k_{Sader}	σ_{Sader}	k_{Thermal}	σ_{Thermal}
1	0.0205	0.0013	0.019	0.0014	0.0846	0.014
2	0.806	0.0527	0.719	0.249	1.97	0.324
3	6.32	0.413	7.03	2.46	12.0	4.27
4	24.3	1.59	33.8	25.4	37.4	1.98
5	66.3	4.33	110	66.9	59.0	10.8

Table 4: Predicted effective spring constant (mean, standard deviation) of modes 1–5, found using our method, (k_n, σ_n), the Sader method, $(k_{\text{Sader}}, \sigma_{\text{Sader}})$, and the thermal method, $(k_{\text{Thermal}}, \sigma_{\text{Thermal}})$. All units are Nm^{-1}.

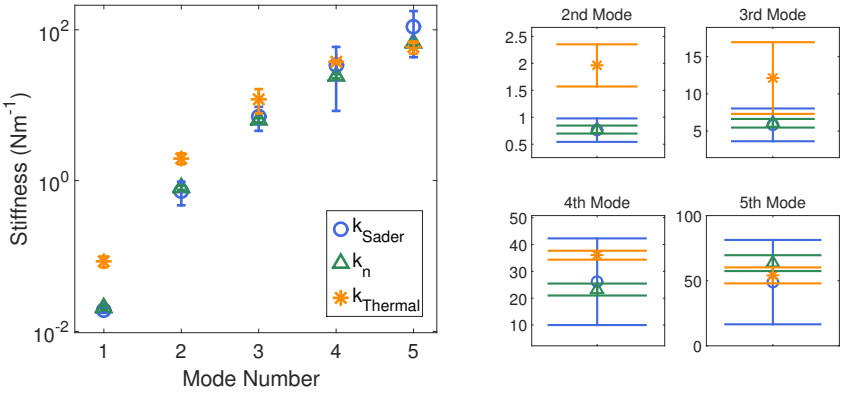

(a) Comparison between our method, the Sader method, and the thermal method.

(b) A zoom in on the effective stiffness and variation for modes 2-5.

Figure 2.13: Values of the effective stiffness, k_n, found using our own calibration method and compared against the thermal method and the Sader method.

2.7 CONCLUSIONS

The AFM probe is the tool that is used to extract non-topographic information about the sample. When the probe is excited to high frequencies, it undergoes a stiffening which makes the probe more similar to stiff materials, such as metals. In order to relate the behaviour of the probe back to a quantifiably material property, we require its free resonant frequencies. Furthermore, knowledge of the probes effective stiffness at higher modes can be used to 'stiffness-match' a specific frequency to the material under investigation. In Chapter 5 and Chapter 6, we will rely on the process of stiffness matching in choosing the resonant mode of the cantilever. These considerations combine to create a requirement for a method to calibrate the properties of a micromechanical cantilever that can be applied at arbitrary mode number. In this chapter, we have presented a new method to achieve this, which requires only the first resonant frequency and Q factor, as well as easily–measured dimensions of the beam (length and width) and the properties of the fluid. It is able to find the effective stiffness of the cantilever with less variation

than other methods and does so by calculating the material properties of the beam, giving further additional information about the probe.

Furthermore, it provides additonal information about the probe such as the expected higher frequencies of the cantilever in vacuo. Knowledge of these resonant frequencies holds a double purpose: it allows us to calculate a frequency shift that is independent of fluid considerations, as we do in Chapter 5 and it allows us to check that we are measuring the correct mode, as we show in Chapter 6). Our interest in using the in vacuo resonant frequencies is motivated by our belief that the hydrodynamics of the first few mode will influence our measurements of the resonant frequencies of a micro-mechanical cantilever, including when near to a sample surface. We next turn to explicitly setting out the influence of the hydrodynamics of the system.

3

FLUID DYNAMICS AROUND AN AFM PROBE

3.1 INTRODUCTION

In this chapter we consider the hydrodynamics of fluid surrounding an oscillating micro-mechanical cantilever, common to both atomic force microscopes (AFMs) and microelectromechanical systems (MEMS). The hydrodynamics of an AFM were used as a calibration tool in Chapter 2, where we showed that considerations of hydrodynamics can be used to infer the effective stiffness and material properties of an AFM probe. However, knowledge of the influence of the surrounding fluid can assist us in other ways. For example, we show in Chapter 5 that knowledge of the hydrodynamic loading on an AFM probe near to the surface can improve acoustic measurements of viscoelastic material properties.

Furthermore, as we show in Section 3.5, the resonant frequencies of the higher modes are less susceptible to the hydrodynamics of the system. This motivates our calculation of the frequency shift of modal pairs of resonant frequencies in Chapter 4 and later relied upon in Chapter 5 and Chapter 6. In this chapter, we introduce our solver for calculating hydrodynamic drag on an micro-mechanical oscillating body. We present our results for the hydrodynamics on a 2D cross-section of a cantilever oscillating free from a surface and demonstrate how the introduction of a surface influences the hydrodynamic loading. We explicitly compute (using an open-source finite element method solver) how the hydrodynamic changes as the distance between sample and oscillating body decreases, which, to the best of our knowledge, has not been demonstrated before.

We begin, Section 3.2, by discussing past research on the hydrodynamics around oscillating bodies and their respective limitations. In Section 3.3, we set out the governing equations for the hydrodynamics of the system and reformulate these equations to be solved numerically by the finite element method (FEM). Having made the governing equations amenable to numerical solutions, we calculate the hydrodynamic drag on the surface of the cantilever using our FEM solver. In Section 3.4.1, we present results on the hydrodynamics of fluid aound a 2D cross-section of the cantilever, free from the surface, with cylindrical and then rectangular cross-section. Our findings are compared to existing results in the literature and found to agree well. Having gained confidence in the case of a cantilever oscillating far from a sample, we turn our attention to the influence of the surface on the hydrodynamics of the system in Section 3.4.2 and compare our results to those that exist in the literature. We offer a discussion of how our findings impact AFM measurements, including our own in Chapter 5 and Chapter 6. Finally, we present possible extensions to this work in Section 3.7 before making our concluding remarks in Section 3.8 .

3.2 HYDRODYNAMICS OF AN OSCILLATING BODY

The AFM probe is the tool with which the sample surface is related to discernable topographic and non-topographic features. However, the interaction between sample and surface does not uniquely influence the motion of the probe. As discussed in Chapter 2, the probe will be exposed to hydrodynamic effects which can cause a change in the resonant frequency of the sensor. An increased knowledge of the hydrodynamics of the system can lead to new techniques for measuring material properties (see, for example, [129]), or highlight assumptions that require revisiting, such as that the flow along the length of the cantilever gives non-negligible contributions to the total load (as shown in [121]). Moreover, the influence of the surrounding fluid on a micro-mechanical cantilever encodes additional information about the coupled sensor-sample system such as the presence of viscous damping within a sample [130]. Ultimately, a better understanding will dictate operational limits for AFM measurements, marking the regions where hydrodynamic effects must be accounted for and those where they may be neglected. We utilise this in Chapter 6 to justify the use of the higher modes of an AFM probe, as discussed in Section 3.5. Hence, our results highlight the extent to which the hydrodynamics play a role in contact resonance measurements and contribute to the development of contact resonance applied to high speed AFM (CR-HSAFM) as a tool for stiffness measurements of stiff materials at the nanoscale.

3.2.1 *Early Studies on the Hydrodynamics of AFM Probes*

In 1850, the hydrodynamics of an oscillating body were considered by Stokes [120]. He examined the hydrodynamics forces on a sphere undergoing small periodic oscillations within a viscous fluid. The small amplitudes of the body meant that nonlinear inertial effects were neglected, and a combination of analytic and experimental observations led Stokes to put forward a closed form expression for the viscous drag on an oscillating sphere in a fluid medium. In 1969, the question of hydrodynamic forces on oscillating bodies was again considered by E. O. Tuck [119]. Tuck examined the specific problem of hydrodynamic drag on the cross-section of an infinite cylinder undergoing small amplitude oscillations in 2D flow. He reposed the problem as an integral equation, solved using the boundary element technique. He went on to analyse the hydrodynamics of an oscillating body with infinitesimal thickness, and showed how the hydrodynamic drag varies in the limit of high and low oscillatory frequency.

As discussed in Chapter 2, the formulation put forward by Tuck was utilised in the method for the calibration of micromechanical cantilevers by Sader [117]. Here, a correction factor was derived from the work of Tuck [119] that accounted for the rectangular geometry of a conventional AFM probe. The flexural deflection of the probe was then decomposed into the resonant modes, weighted by the influence of the fluid damping. Sader showed that the thermal spectrum of the probe near to a resonant frequency is well approximated by a damped harmonic oscillator, provided that the dissipative effects

from the fluid are small. A closed form expression was derived to relate experimental values of the amplitude, resonant frequency and quality factor, as well as the length and width of the beam, to the spring constant of the beam. In Chapter 2, we made use of the hydrodynamic damping for our own method of calibration [93], which goes the further step of estimating the material properties in order to calculate the effective stiffness of a cantilever at higher modess.

Prior to the analysis of Sader [117], Elmer and Dreier [131] studied a body oscillating in fluid flow and demonstrated that a change in resonant frequency will occur due to the presence of the fluid. However, their investigation was limited to a 1D beam and neglected viscous effects. Chon et al. [132] compared the full viscous case, the invisid case, and the response of a simple harmonic oscillator (SHO) against experimental data for an oscillating body in both air and water. They found that both viscous and SHO models outperformed the inviscid model (in air and water) demonstrating that viscous effects cannot be neglected[1]. Following the increase in attention during the 1990s, subsequent work has continued to investigate how the hydrodynamics of an oscillating cantilever can be used to find out information about other cantilever types and motion. The Sader method [117] has been extended to both the torsional motion of a cantilever [133], and the general case of a sensor with arbitrary cross-sectional geometry [134]. The extension to sensors with unconventional geometries was achieved through a general scaling law where the hydrodynamics was calculated through a comparison to beams of similar shape and sizes [114]. This has lead to the establishment of an online repository which contains experimental information on the hydrodynamics for beams with various geometries [135]. In this thesis, we will only be concerned with cantilevers with rectangular geometry and high aspect ratio, of the type used in Chapter 2 and shown in Figure 2.11. However, extensions to our results are possible, provided that the material properties are known to high accuracy. Instead, we utilise the previously reported results of the hydrodynamic loading on an AFM probe, with conventional geometry and oscillating free from a surface, to verify our own fluid solver.

There is a high level of interest in the hydrodynamics of oscillating bodies which continues to be an active area of research within the MEMS community today [129, 135, 136]. However, many past investigations into the hydrodynamics of oscillating cantilevers have been restricted to considerations at low frequencies, representing the first mode of the cantilever. In Chapter 5 and Chapter 6, we will use the change in resonant frequency of a cantilever, oscillating near to a sample, to discern the stiffness of a sample. We have already shown in Chapter 2, that $k_n > k_c$ for $n > 1$, such that higher resonant frequencies approximate a stiffer cantilever. This motivates the use of higher modes for stiffness measurements on stiff materials. However, we are required to also know the extent to which the surrounding fluid dynamics will affect the resonant frequencies of an AFM probe in order to rule out additional uncertainties due to the surrounding fluid environment. We create our own fluid solver in order to achieve this and verify the influence of a surface on a rectangular cantilever, oscillating at high frequencies.

1 We will only consider a body oscillating in air in this thesis but include numerical results that covers considerations of other fluid regimes, such as water.

Past results have also appraised how the presence of an additional surface, either deformable or non-deformable, will influence the hydrodynamics of a sensor-sample system [118, 137, 138]. However, these results utilised semi-analytic boundary element formulations, or commercial packages. Instead we choose to calculate the hydrodynamic loading on an AFM probe using open-source finite element method (FEM) packages. This has the advantages of not requiring commercial licenses to run whilst verifying previous boundary element method formulations. In Section 3.4, we show that the hydrodynamic loading calculated by our solver can reproduce results previously achieved using commerical solvers, such as results reported by [137] and [138]. In this chapter, we will describe the governing equations of the flow and the necessary steps undertaken which lead to calculation of the fluid loading on the probe. However, we envisage further extensions to the work in this chapter to include other considerations of the hydrodynamics of the sensor-sample coupled system. We briefly discuss other work that has focused on such extensions.

3.2.2 *Extensions to Models of the Hydrodynamics*

The interaction of a cantilever with a surface is of interest to both AFM practitioners and theoreticians. This is because AFM probes (and other MEMS devices) are extremely sensitive to small (typically sub-pN) forces. Understanding how the hydrodynamics couples to a probe-sample system will aid experimental techniques and build confidence in empirical results. One of the shortcomings of existing fluid theories (which we do not resolve here) is that only two dimensional flow around a cross-section of an AFM probe is considered, ignoring length-wise contributions. Numerical simulations have been carried out previously to address this. For example, Basak et al. [139] demonstrated an underestimation of the damping when comparing the computational results of a full three dimensional model to previous semi-analytic results, as well as showing that changes to the cantilever geometry, such as the introduction of slots or reduction in cantilever thickness, maximise the signal of the resonant frequency. The influence of the geometry of a micromechanical probe was also examined by Green et al. [137], who showed that the assumption of the dominance of spanwise fluid gave good agreement with experimental work (provided that the thickness of the probe was less than the width).

The full three dimensional problem of an oscillating cantilever was treated semi-analytically by Clarke [118], who utilised a slender-body approximation (which makes use of the slender geometry of an object to approximate nearby field effects) to account for the flow around a rectangular cantilever with high aspect ratio. Clarke then showed how a surface, modelled as a non-deformable wall, will influence the hydrodynamics of the system. The governing equations of the fluid were treated asymptotically for varying frequencies of oscillation and distance between sample and probe, as well as numerically through an integral equation formulation of the governing equations and subsequent application of this formulation with the boundary element method. We discuss how our

own results, as presented here, relate to Clarke's description of the fluid-sensor-sample in Section 3.7. Green and Sader [137] also considered the introduction of a surface and demonstrated that the influence of the surrounding fluid is weak when the cantilever is oscillating with small amplitudes and at distances from the surface greater than the total width of the cantilever (such that the cantilever can be approximated as oscillating in an infinite fluid region). However, for cases where the separation distance is less than the width of the probe, dissipative effects were shown to be significant. The hydrodynamics of the fluid surrounding both wall and cantilever were calculated through a boundary element method for oscillatory Reynolds number, a modification of the Reynolds number for describing the oscillatory behaviour of fluid [117], in the range of 10^{-3} to 10^{3}.

The work of Green and Sader is an example of how the additional hydrodynamics, caused by the introduction of a sample surface, can influence AFM measurements. However, the variation in hydrodynamic loading at high frequencies as the tip-sample separation is reduced is not explicitly considered. The influence of the surface at high frequencies is what we demonstrate in Section 3.4. Similar considerations have been undertaken by Tung et al. [140] who compared the hydrodynamic function found in [137] and the full three dimensional numerical solution of Basak et al. [139]. Tung et al. [138] showed that the formulation gave good agreement, with less than 3% error in the calculated natural frequencies of submerged cantilevers, when compared against measured frequencies from experimental results. We will compare our own fluid solver to these results in Section 3.5. Meanwhile, Hosaka et al. [141] approximated the motion of an oscillating cantilever as a series of coupled spheres and investigated the coupled hydrodynamics around this idealisation. Their work highlighted the dominance of squeeze-film damping on a micro-cantilever ocillating near to a wall. Our results in Section 3.4 may indicate similar effects, though further experimental investigations are required. Later work by Korayem et al. [142] has built on this approach, where simulations of the coupled-sphere approach evaluate the influence of both the viscosity of the surrounding fluid as well as the beam geometry. It was shown that the increased viscosity due to the sensor-sample interaction can greatly reduce the quality factor of the corresponding resonant behaviour of the beam. Both of these methods demonstrate that length-wise contributions can influence the hydrodynamics and resonant modes of a micromechanical cantilever. We do not consider length-wise contributions here but demonstrate how to include such extensions in Section 3.7.

The treatment of the hydrodynamics of the beam by Clarke [118] were later used to infer the properties of soft materials due to the deformation of a sample caused by the hydrodynamic interaction between sensor and sample by Clarke et al. [129]. They highlighted the theoretical possibility of non-contact measurements of the elastic properties of deformable samples, such as biological objects, through a tipless cantilever. However, they pointed towards potential problems in their approach due to the difficulty in quantifying the separation gap between probe and sample deformations. The utilisation of the hydrodynamics of the system to infer sample properties was also studied by Tung

et al. [138]. Here, the interaction damping[2] between an AFM probe and the surface was corrected to account for the hydrodynamics of the system. This led to an improvement in the measurement of the loss tangent (a measure of the viscoelastic damping of a material) of polystrene when compared to those found in the literature, as well as highlighting the sensitivity of the first mode for measurements that include damping considerations. In Chapter 5, we will apply our own solver, outlined in Section 3.3, to calculate the loss tangent of stainless steel (grade 316).

All of the results on the hydrodynamic loading on oscillating bodies, as described above, have assumed that the body is oscillating with small amplitudes. However, the influence of nonlinear hydrodynamics has also been studied. This occurs for bodies that have large finite amplitude, as described by the Keulgar-Carpenter number [143],

$$KC = \frac{2\pi A}{b}, \tag{3.1}$$

where A is the amplitude of oscillation and b is the width of the oscillating body. This nondimensional parameter captures the importance of drag forces over inertial forces for an oscillatory flow field. For a conventional AFM probe, of the type considered in this thesis, the KC number is typically of the order of 10^{-3}. However, for objects that are exposed to larger oscillation amplitudes, or are significantly smaller in width, then changes in the hydrodynamics have been shown to be dramatic. For example, Porfiri et al. [144] calculated the change in hydrodynamics for an oscillating beam with relatively large amplitude (greater than 1 µm) and worked out a correction factor for the hydrodynamic function given in [117],

$$\Phi(\omega, \mathrm{KC}) = \Gamma(\omega) - i0.879\mathrm{Re}^{0.75}\left(\frac{\mathrm{KC}}{2\pi}\right)^2, \tag{3.2}$$

where $\Gamma(\omega)$ is the hydrodynamic loading function, described in Section 3.3.1 and $i = \sqrt{-1}$. This correction factor holds for $20 \leq \mathrm{Re} \leq 2000$ and $\mathrm{KC} < 11.42\mathrm{Re}^{0.625}$. Further extension to this work has investigated the influence of a wall, and shows that the added mass was relatively unaffected while the convection-driven nonlinearities can drastically increase [145]. Both these studies were for KC = $O(-1)$ which are beyond the operation range that we will examine here. For further extensions to the study of thin laminae exposed to nonlinear hydrodynamics, see, for example, [146, 147].

The interest and ongoing research into the fluid dynamics of an AFM probe emphasises the impact of the interaction between fluid and cantilever. However, there are a number of assumptions common to each study: the 2D approximation of the flow, the geometry of the probe, the degree to which compressibility and nonlinearities within the flow are present, and how the existence of a sensor couples with the sample. The hydrodynamic function, which describes the effect of the fluid on the probe, is often limited to calculation based on tabulated results due to the use of commercial software or technical difficulties in recreating the codebase of a solver, as most have occured through the

2 See Chapter 1 for more details on interaction damping

implementation of boundary element solvers or commercial CFD packages. However, the problem of how the hydrodynamics influences an oscillating body is of importance to the operation of an AFM. Hence, an understanding of how limiting the assumptions are to the approach or the freedom to attempt extensions to past investigations would be an asset to the AFM and MEMS community. Here we show that the hydrodynamics of an AFM probe can be calculated using open-source FEM solver and that this solver is amenable to extensions including changes to the geometry and introduction of changes to the domain.

3.3 FLOW AROUND AN AFM PROBE

The fluid dynamics on an oscillating microbeam is an active field of research. Many important results have been gained by building custom-made optimised solvers or utilising commerically available software [119, 129, 139]. Here we seek to reproduce existing numerical results using our own solver that is designed using an open-source FEM package, FEniCS [148–151]. We begin by examing the case of the hydrodynamic drag on an oscillating cylinder in 2D flow for which an analytic solution exists. We then consider flow around an oscillating rectangular beam which is more typical to AFM probes. First, we describe the equations that govern the fluid flow around an oscillating probe far from a surface.

3.3.1 *Governing Equations*

Before setting out the governing equations for the fluid, we highlight a number of our assumptions. As set out in Section 2.2 and shown in Figure 2.1, typical AFM probes have width, b^*, smaller than the total length, L^*, and thickness, h_T^*, smaller than the total width; $h_T^* \ll b^* \ll L^*$, where the asterix is used to denote dimensional quantities in the context of this chapter. As the width is far smaller than the length, we assume that the fluid flow will vary more rapidly across the width of the cantilever than along its length, and take the width of the beam to be the characteristic length scale for the flow. As discussed in Section 3.1, the assumption that the width is the characteristic lengthscale may not hold at high frequencies. However, here we examine only the 2D case where $\mathbf{x}^* = (x_1^*, x_2^*)$ and offer further extensions to this work in Section 3.7. We further assume that the amplitude of oscillation for the n^{th} mode is small, $A_n^* \sim 1\,\text{nm}$, such that we may neglect nonlinear fluid inertial terms, and that the cross-section and material properties of the beam are uniform through its length, such that a 2D cross-section is representative of the rest of the beam. We neglect considerations of the tip and begin by neglecting the influence from any other structures, including the sample surface. We go on to discuss the influence of a 'wall' in Section 3.4.2. Finally, we assume the material damping in the beam is negligible.

We are concerned with calculating the hydrodynamic drag, D, on a cantilever that is oscillating in the x_2^* direction only, with amplitude of oscillation for the n^{th} mode,

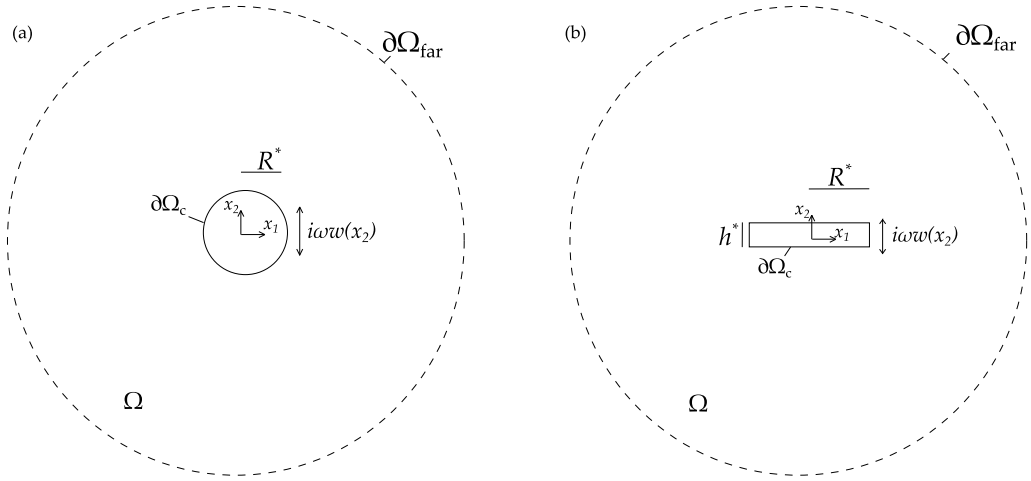

Figure 3.1: Schematic of a body, $\partial\Omega_c$ with cylindrical (a) and rectangular (b) geometry oscillating with flexural deflection, $i\omega w(x_2)$ and radius (or half-width) R^* in a domain of fluid, Ω.

A_n^*. This is described by the Euler-Bernoulli equation, (2.13), introduced in Section 2.4.1, where both the cantilever's flexural deflections, with respect to its neutral axis, and the hydrodynamic drag are assumed to be oscillatory (i.e. real$(w^*(x_2)\exp i\omega t)$, and real$(D^*(x_2^*)\exp i\omega t)$, where real denotes the real part to be taken). The external forcing in (2.13) is now given by the hydrodynamic drag per unit length, $F(x,t)e^{i\omega t} = D^*$, found by integrating the fluid stresses over the boundary of the oscillating body, $\partial\Omega_c$ [129],

$$D^*(x_2^*) = \int_{\partial\Omega_c} \mathbf{f}^* \cdot \hat{\mathbf{j}} \mathrm{d}l(x_2^*). \tag{3.3}$$

where $\hat{\mathbf{j}}$ is the unit vector in the x_2^* direction, and $\mathbf{f}^* = \sigma^* \cdot \mathbf{n}$ is the hydrodynamic traction on the surface of the cantilever, $\partial\Omega_c$, for stress tensor, $\sigma^* = -p^*\mathbf{I} + \mu_f^*\nabla\mathbf{u}^* + \mu_f^*(\nabla\mathbf{u}^*)^T$ and unit normal, $\mathbf{n}$. We non-dimensionalise the flexural deflection by the oscillation amplitude, A_n^*, and the spatial variables, (x_1^*, x_2^*), by the cantilever radius (or half width for rectangular cross-section) $R^* = b^*/2$,

$$w^*(\mathbf{x}) = A^* w \qquad x_1^* = R^* x_1, \qquad x_2^* = R^* x_2. \tag{3.4}$$

We also non-dimensionalise the temporal variables by the resonant angular frequency of the fundamental mode, ω_1, given by the dispersion relation (2.16) in Section 2.4.1.

$$t^* = \frac{t}{\omega_1^*}, \qquad \omega^* = \omega_1^* \omega, \tag{3.5}$$

where t^* is time and ω^* is the angular frequency of the oscillating cantilever.

We make the following assumptions on the flow: that the surrounding fluid is Newtonian and incompressible with dynamic viscosity μ_f^* and density ρ_f^*. We non-dimen-

	L (μm)	h_T (μm)	b (μm)	ω_1 (μm)	Q (kHz)	k_c (N m^{-1})
MSNL-B	120	0.5	20	$15(2\pi)$	20	0.02

Table 5: We show example dimensions and resonant behaviour for cantilevers used in Chapter 2. All measurements throughout were performed in air, with viscosity $\mu_f = 18.1\,\mu\text{Pa s}$ and density, $\rho_f = 1.225\,\text{kg/m}^3$.

sionalise the fluid velocity, $\mathbf{u}^*(\mathbf{x}) = (u_1^*(\mathbf{x}), u_2^*(\mathbf{x}))$, pressure, p^*, and stress tensor, σ^*, according to,

$$\mathbf{u}^* = (A^*\omega_1^*)\mathbf{u}, \qquad p^* = \left(\frac{\mu^*\omega_1^*A^*}{R^*}\right)p, \qquad \sigma^* = \left(\frac{\mu^*\omega_1^*A^*}{R^*}\right)\sigma. \tag{3.6}$$

Having non-dimensionalised our system, the governing equations of this flow are given by the Navier-Stokes equations for incompressible fluid [152]

$$\rho_f\left(\frac{\partial \mathbf{u}}{\partial t} + (\mathbf{u}\cdot\nabla)\mathbf{u}\right) = -\nabla p + \mu_f\nabla^2\mathbf{u}, \qquad \nabla\cdot\mathbf{u} = 0. \tag{3.7}$$

AFM probes typically oscillate with nanometre or sub-nanometre amplitudes, several orders of magnitude smaller than either the width or length of the probe (typically tens or hundreds of microns respectively). These small amplitudes ($A^* \sim 1\times10^{-9}\,\text{m}$) counteract the high frequencies of the cantilever ($\omega_1^* \sim 1\times10^5\,\text{Hz}$), reducing the characteristic velocity of the flow, ($U \sim 1\times10^{-4}\,\text{m s}^{-1}$). For the characteristic velocity under consideration, the Mach number (the ratio of the characteristic velocity to the speed of sound) will be approximately 10^{-6}. This supports our previous assumption of incompressibility above.

Assuming that the width is the characteristic length scale of the flow, we calculate the dimensionless oscillatory Reynolds number, Re_f as

$$\text{Re}_f = \frac{\omega^*\rho_f^*(R^*)^2}{\mu_f^*}, \tag{3.8}$$

The oscillatory Reynolds number describes the frequency dependent flow inertia. For a typical AFM probe in ambient air with properties listed in Table 5, we find the oscillatory Reynolds number to be in the range of 10^{-1} to 10^1 for the first ten modes[3]. This implies that the inertial acceleration force on the beam, due to the surrounding fluid is small in relation to the viscous surface forces. Hence, we drop the $(\mathbf{u}\cdot\nabla)\mathbf{u}$ term. All experiments in this thesis are conducted in air. However, for certain samples such as biological objects, fluid cells that contain different fluid mediums such as water are used to minimise the force on the sample. We note that for water at 298 K, density $\rho_f = 997\,\text{kg/m}^3$ and viscosity $\mu_f = 0.89\,\text{mPa}$, the oscillatory Reynolds number covers a range of 10^1 to 10^3 for the first ten modes. Therefore, the inertial acceleration terms may

3 For further details about the resonant frequencies of this cantilever, see Table 3

become significant. As stated, we will not consider such extensions here but include our numerical analysis up to $\mathrm{Re}_{\mathrm{f}}^{*} = 10^3$ such that the influence of different fluid mediums is included (though we continue to neglect inertial acceleration terms). Hence, we rewrite the governing equations for the flow around the cantilever, (3.7), as

$$\rho_{\mathrm{f}} \frac{\partial \mathbf{u}}{\partial t} = -\nabla p + \mu_{\mathrm{f}} \nabla^2 \mathbf{u}, \qquad \nabla \cdot \mathbf{u} = 0. \tag{3.9}$$

Given the oscillatory nature of the cantilevers motion, the velocity component of the fluid will be imparted with a harmonic component. Due to the linearity of equation (3.9), the vorticity, hydrodynamic pressure, and stress also become oscillatory. We rewrite these quantities as

$$\mathbf{u}(\mathbf{x}, t) = \mathbf{u}(\mathbf{x}, \omega) e^{-i\omega t}, \qquad p(\mathbf{x}, t) = p(\mathbf{x}, \omega) e^{-i\omega t}, \qquad \boldsymbol{\sigma}(\mathbf{x}, t) = \boldsymbol{\sigma}(\mathbf{x}, \omega) e^{-i\omega t}. \tag{3.10}$$

Combining (3.10) with (3.9), we have

$$\lambda^2 \mathbf{u} = -\nabla p + \nabla^2 \mathbf{u}, \qquad \nabla \cdot \mathbf{u} = 0 \tag{3.11}$$

where $\lambda^2 = \mathrm{iRe}_f$ is a measure of the characteristic flow inertia. Equation (3.11) is mathematically equivalent to what is known as Brinkman flow [153]. This is previously discussed in Chapter 2, specifically (2.13). We note that when $\lambda = 0$, this equation reduces to steady Stokes flow (or creeping flow) and for $\lambda = 1$, we have Darcy flow which is commonly used to describe flow through a porous medium. Hence, our results will correspond to applications of Brinkman flow for porous medium, see for example [154]. We will examine the fluid that is contained in the domain, Ω, around the boundary of the oscillating body, $\partial\Omega_c$. On the boundary, we have the no-slip condition

$$\mathbf{u}(\mathbf{x}) = i\omega w(\mathbf{x_2}), \qquad \text{for} \quad \mathbf{x} \in \partial\Omega_c, \tag{3.12}$$

while in the far field, the velocity of the flow returns to zero,

$$\mathbf{u}(\mathbf{x}) = 0, \qquad \text{for} \quad \mathbf{x} \to \infty. \tag{3.13}$$

Given these assumptions, we proceed to solve (3.11) to find the forcing on the cantilever boundary due to the surrounding fluid. The hydrodynamic drag, given in (3.3) is represented by a dimensionless hydrodynamic function,

$$\Gamma(\mathrm{Re}_{\mathrm{f}}) = \frac{D}{\pi \lambda^2}. \tag{3.14}$$

The real component of the hydrodynamic function corresponds to the additional inertial mass while the imaginary components correspond to the viscous damping terms. We repeat our assumption that the internal dissipation of the cantilever due to internal friction is negligible such that the damping terms are imparted entirely forms the fluid. The hydrodynamic function, $\Gamma(\mathrm{Re}_{\mathrm{f}})$, will dictate how the drag changes as we vary the

oscillatory Reynolds number. The additional inertial mass due to the surrounding fluid, m_f, is given by [121],

$$m_f = C_f \Gamma_r(\mathrm{Re}), \tag{3.15}$$

while the damping coefficient, γ_f, is,

$$\gamma_f = C_f \omega \Gamma_i(\mathrm{Re}), \tag{3.16}$$

and where $C_f = \rho_f \pi b^2 L/4$ contains (easily measured) properties of the cantilever and fluid. Given the formulation of the governing equations above, we proceed to solve them using the finite element method.

3.3.2 *The Finite Element Method*

Finite element methods (FEM) achieve computational solutions by decreasing a complex problem into many small, interconnected regions. These subregions are known as finite elements. FEM is only able to calculate approximate solutions. However, these approximate solutions can achieve high accuracy through increased discretisation of the solution space. In order to solve a differential equation using FEM, the equations to be solved must be reformulated into weak variational form, where 'weak' refers to the continuity enforced on the dependent field variable. The weak form of the equations is achieved by composing the field variables with trial functions (also called interpolation functions) and integrating over the problem domain. This leads to a discretised system of equations, often consisting of well-behaved linear equations (provided the underlying PDE is linear). Here, we describe the steps needed to solve the specific problem of (3.11) using FEM. For further information on FEM see, for example, [155–158].

We first repeat the governing equations of the problem,

$$\lambda^2 u + \nabla p - \nabla^2 u = f, \qquad \forall x \in \Omega \tag{3.17}$$

$$\nabla \cdot u = 0, \qquad \forall x \in \Omega, \tag{3.18}$$

with boundary conditions

$$\mathbf{u}(\mathbf{x}) = i\omega w(\mathbf{x_2}), \qquad \text{for} \quad \mathbf{x} \in \partial\Omega_c, \tag{3.19}$$

$$\mathbf{u}(\mathbf{x}) = 0, \qquad \text{for} \quad \mathbf{x} \to \infty. \tag{3.20}$$

We must express (3.17) and (3.18) in weak variational form in order to utilise the FEM method. We introduce two test functions, v and q which belong in the function space $\hat{V}$ and $\hat{Q}$, respectively. We shall specify the function space explicitly later in this section. We require two such functions because we seek solutions for both the unknown velocity, u, and pressure, p. We will choose both test functions such that they are exactly zero on

the boundary. We then multiply the first equation (3.17) by v, before integrating over the domain, Ω,

$$\lambda^2 \int_\Omega u \cdot v \mathrm{d}x + \int_\Omega (\nabla p) \cdot v \mathrm{d}x - \int_\Omega (\nabla^2 u) v \mathrm{d}x = \int_\Omega f \cdot v \mathrm{d}x. \tag{3.21}$$

Using integration by parts and the divergence theorem, we can rewrite (3.21) as,

$$\lambda^2 \int_\Omega (u \cdot v) \mathrm{d}x + \int_\Omega (\nabla u \cdot \nabla v) \mathrm{d}x + \int_\Omega p(\nabla v) \mathrm{d}x = \int_\Omega (f \cdot v) \mathrm{d}x. \tag{3.22}$$

We then multiply the continuity equation, (3.18) by our other test function, q, and again integrate over the domain,

$$\int_\Omega q(\nabla \cdot v) \mathrm{d}x = 0. \tag{3.23}$$

Subtracting (3.23) from (3.22) gives us the weak variational form of (3.17 – 3.18),

$$\lambda^2 \int_\Omega (u \cdot v) \mathrm{d}x + \int_\Omega (\nabla u \cdot \nabla v) \mathrm{d}x + \int_\Omega p(\nabla \cdot v) \mathrm{d}x - \int_\Omega q(\nabla \cdot v) \mathrm{d}x = \int_\Omega (f \cdot v) \mathrm{d}x. \tag{3.24}$$

Henceforth, we write the inner-product as (A, B) where A and B are the elements of our function spaces. Then, (3.24) in its weak variational form becomes

$$a(u, v) + b(p, v) + b(q, u) = L(f, v), \tag{3.25}$$

where,

$$a(\cdot, \cdot) = \lambda^2(\cdot, \cdot) + (\nabla \cdot, \nabla \cdot) \tag{3.26}$$

$$b(\cdot, \cdot) = (\cdot, \nabla \cdot) \tag{3.27}$$

$$L(\cdot, \cdot) = (\cdot, \cdot). \tag{3.28}$$

Given the weak variational form, (3.25) – (3.28), we consider the case where u and p are complex valued, $u = u_\mathrm{r} + u_\mathrm{i}$ and $p = p_\mathrm{r} + p_\mathrm{i}$, where superscripts r and i denote the real and imaginary parts of the functions. Similarly, we have complex valued test functions given by , $v = v_\mathrm{r} + v_\mathrm{i}$ and $q = q_\mathrm{r} + q_\mathrm{i}$. We proceed to separate our complex PDE into two real valued PDEs according to the real and imaginary parts of each of the functions,

$$(u_\mathrm{r} + u_\mathrm{i}, v_\mathrm{r} + v_\mathrm{i}) = \int_\Omega u_\mathrm{r} v_\mathrm{r} \mathrm{d}x + \int_\Omega u_\mathrm{i} v_\mathrm{i} \mathrm{d}x + i \left(\int_\Omega u_\mathrm{r} v_\mathrm{i} \mathrm{d}x - \int_\Omega u_\mathrm{i} v_\mathrm{r} \mathrm{d}x \right). \tag{3.29}$$

Noting that $\lambda^2 = i\omega \mathrm{Re}_\mathrm{f}$, we rewrite (3.29) as

$$\bar{a}(u_\mathrm{r} + u_\mathrm{i}, v_\mathrm{r} + v_\mathrm{i}) + b(p_\mathrm{r} + p_\mathrm{i}, v_\mathrm{r} + v_\mathrm{i}) + b(q_\mathrm{r} + q_\mathrm{i}, u_\mathrm{r} + u_\mathrm{i}) = L(f_\mathrm{r} + f_\mathrm{i}, v_\mathrm{r} + v_\mathrm{i}), \tag{3.30}$$

where $\bar{a}(\cdot,\cdot) \in \mathbb{R}$, such that

$$\bar{a}(u_r + u_i, v_r + v_i) = \lambda^2(u_r + u_i, v_r + v_i) + (\nabla u_r + u_i, \nabla v_r + v_i) \tag{3.31}$$

$$= (i\omega \mathrm{Re}_f)(u_r + u_i, v_r + v_i) + (\nabla u_r + u_i, \nabla v_r + v_i) \tag{3.32}$$

$$= \int_\Omega \nabla u_r \cdot \nabla v_r \mathrm{d}x + \int_\Omega \nabla u_i \cdot \nabla v_i \mathrm{d}x + \ldots \tag{3.33}$$

$$\lambda^2 \left(- \int_\Omega u_r v_i \mathrm{d}x + \int_\Omega u_i v_r \mathrm{d}x) \right) \tag{3.34}$$

As discussed, FEM requires that the solution space is discretised into N subregions known as finite elements. These finite elements allow the differential equations to be reformulated as a linear system of equations. The classic definition of a finite element is the following triplet,

- a geometric simplex, K, which defines the shape of the element,
- a polynomial function space, P, which acts on K,
- the set of $n = \dim(P)$ functionals, L_j, which define the degrees of freedom for the problem.

A wide range of finite elements can be built from different simplices and function spaces. The choice of each depends on the complexity of the domain or differential equations to be solved. We will predominantly be concerned with relatively straightforward geometries such that conventional finite elements are expected to suffice. Hence, we implement our numeric solution using piecewise linear finite elements. These finite elements have a geometric simplex which is triangular in 2D with a function space of linear polynomials, $P^1(K)$. To facilitate working with the function space, we equip it with a nodal basis, $\{N_j\}_{j=1}^n$, for the n functionals $L_j(\cdot)$, $j = 1, 2, 3, ..., n$. We then introduce shape functions, ϕ_j, for the functionals in $L_j(\cdot)$, such that

$$L_j(\phi_j) = \delta_{i,j} \quad \text{for} \quad i, j = 1, 2, 3, ..., n. \tag{3.35}$$

where $\delta_{i,j}$ is the kronecker delta function.

The set of these shape functions forms the nodal basis for the functionals. When combined with the field variables, they convert the differential equations into a system of algebraic equations. Having reformulated (3.11) as a weak variational problem, (3.25), and specified the finite element for the problem (piecewise linear) we solve (3.17 – 3.18) using a suitable linear solver. This completes the FEM method for the above case of oscillatory Brinkman flow, (3.17 – 3.18). We summarise the procedure below.

1. Discretise the domain, Ω, and boundary, $\partial\Omega_c$, using Lagrange finite elements.
2. Introduce test functions for the weak formulation given by (3.30).
3. Prepare the system of linear equations to be solved.
4. Solve the linear system for both velocity and pressure in the domain, Ω.

Having solved for the velocity and pressure in the domain, we calculate the hydrodynamic drag on the boundary according to (3.14). In order to solve (3.30), we make use of FEniCS [148–151], an open-source package that is built on Python and C++ architecture and designed to solve PDEs using the finite element method. Our mesh generation is performed with gmsh [159], while FEniCS is used for matrix assembly and the solution of the linear systems.

3.4 RESULTS

We have set out our governing equations, (3.17) and (3.18), along with boundary conditions, (3.12) and (3.13), and reformulated them such that they are amenable to FEM numerical solution, (3.30). In Section 3.4.1, we reproduce past results on the hydrodynamics of an oscillating cylinder and rectangular beam free from a surface using our FEM solver. We show that our solver is able to recreate these results with high accuracy and, in Section 3.4.2, we extend our solver to account for the hydrodynamics of a cylinder and rectangular beam osillating near to a surface. For discussion on these results, see Section 3.5.

3.4.1 *Hydrodynamics around a Body Oscillating Free From a Surface*

We are interested in the hydrodynamic drag on the surface of the cantilever. First, we validate our numerical scheme for an infinite cylinder oscillating in a viscous fluid, such that our problem is reduced to two-dimensional flow around the two-dimensional circular cross-section. In Figure 3.2, we show an example discretisation. The outer circle, $\partial\Omega_{\text{far}}$, represents the far flow field, where we specify that the fluid velocity is zero, $\mathbf{u}_\infty = 0$. As we are focused on the hydrodynamic drag on the cylinder caused by the surrounding fluid, we refine the mesh around the inner circle representing the cylinder, $\partial\Omega_c$. Having discretised the boundary, we pass our mesh file to our FEM solver to compute the complex velocity and pressure at each element, as described in Section 3.3.2. The total domain has a radius of 35, whereas the cantilever surface $\partial\Omega_c$ has a radius of 1. To improve our confidence in the traction calculated on the inner boundary, we refine the mesh such that each element has a characteristic length of 10^{-3}, whereas the outer boundary, $\partial\Omega_{\text{far}}$ comprises elements with a characteristic length of 5. This results in $62,000$ elements in the entirety of the domain.

In Figure 3.2, we show example outputs for the oscillatory velocity field of the real and imaginary components of the fluid velocity. We first show the total domain, where we can see that our discretisation approach is large enough that the velocity has become zero by the outer boundary. This gives us confidence that we are well-approximating a semi-infinite domain, as no transients of the fluid velocity remain. We then examine the velocity profile centered around the inner boundary. We see that the real component of the fluid velocity reaches its maximum at the upper and lower regions of the boundary, which is oscillating in the x_2 direction only. This demonstrates that our solver correctly

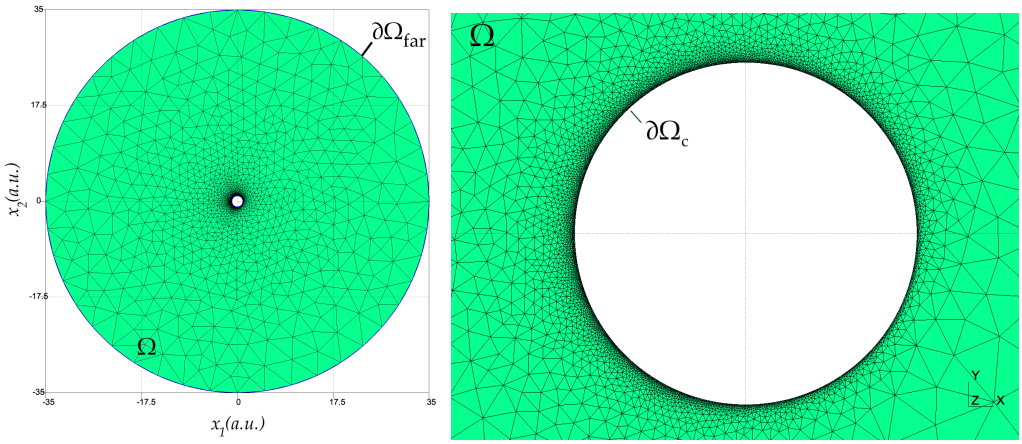

Figure 3.2: Mesh for a body with cylindrical cross-section.

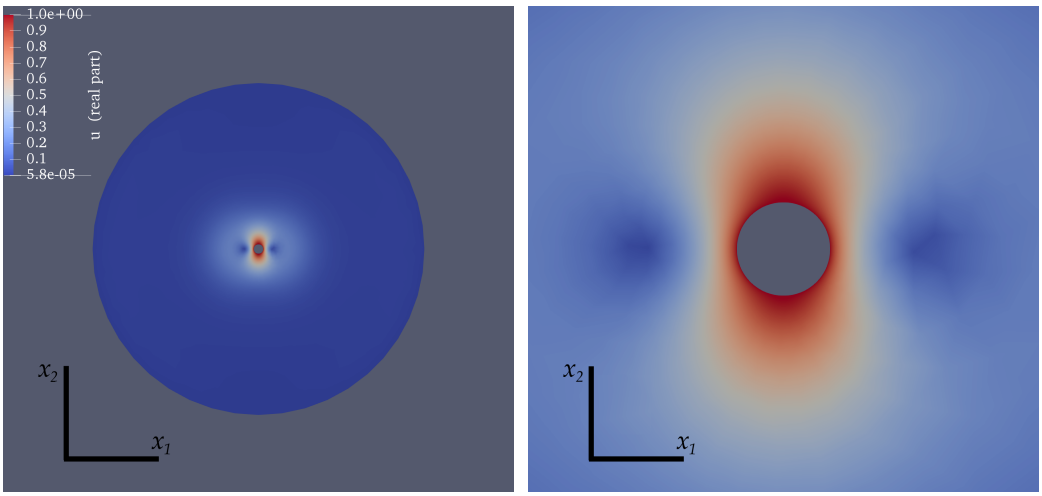

(a) (b)

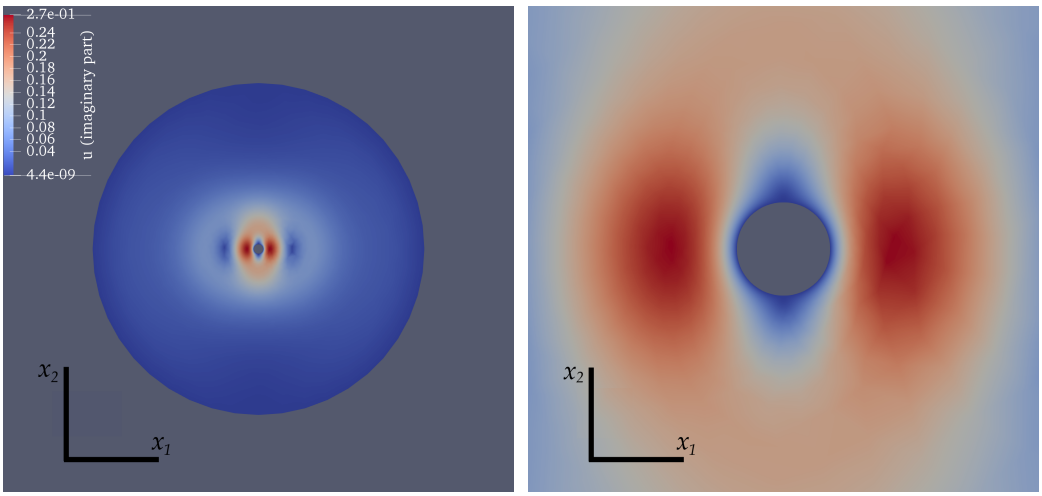

(c) (d)

Figure 3.3: The velocity profile for flow around an oscillating body with cylindrical cross section. In (a-b) we show the real components of the velocity profile for the entire domain (a) and a magnified section including the object (b). In (c-d) we show the imaginary components of the velocity profile for the entire domain (c) and a section around the object (d).

captures the fluid displacement due to the displacement of the oscillating body in the x_2 direction.

We next turn our attention to the case of an oscillating body with rectangular geometry. This case has previously been handled using boundary element methods, [117, 119]. We aim to recreate these results using our FEM solver. An example rectangular mesh is shown in Figure 3.4. We follow the same procedure as that done with a circular boundary, using a coarse mesh at the outer limits where the variation in the fluid flow is expected to be minimal. On the inner boundary, representing the probe, we refine the mesh to improve our calculations of the traction. The radius of the domain is again chosen to be 35 and the half-width of the rectangular inner boundary chosen to be 1. In order to match the geometry of typical AFM probes, we set the non-dimensionalised height of the inner boundary to be 0.05. As with the cylindrical case, we refine the mesh on the inner boundary, this time specifying that each element has a characteristic length of 1.25×10^{-3}, such that the height of the boundary contains 40 elements on each side, and the outer boundary, $\partial\Omega_{\text{far}}$ comprises elements with a characteristic length of 5. This results in approximately $52,500$ elements in the entirety of the domain, provided that they have the same radius (which we have specified here).

In Figure 3.5, we show the velocity profile for real and imaginary components of the fluid over the entire domain, with an expanded focus for both real and imaginary velocity profile around the inner boundary in Figure 3.5. We see that the real component of the fluid velocity is reduced for the rectangular geometry, shown as a reduction in the magnitude of the velocity. In Figure 3.6, we show the hydrodynamic pressure across half the length of the beam. We observe a spike in the pressure, localised at the end of the probe where there exist corners, and which rapidly decay towards the centre. This has been previously observed, see for example [119], and highlights the difference in the drag effects between the two geometries.

We next examine what happens with increased frequency of the oscillating probe, and examine how both real and imaginary components (relating to the the additional mass and damping caused by the fluid, respectively) vary with frequency. We consider an oscillatory Reynold's number in the range of 10^{-1} to 10^{3}, as shown in Figure 3.7. The FEM solver outputs both real and imaginary components of the fluid velocity at each element and calculates the traction on the boundary surface according to (3.14). We see a drop in both added mass and damping as we increase the frequency of the system, in good agreement with both the analytic solution found by Stokes [120] and the correction factor that was calculated by Sader [117] and based on the work of Tuck [119]. Furthermore, when comparing the hydrodynamic drag calculated on both cylindrical and rectangular geometries, as shown in Figure 3.3 and Figure 3.4, we see very good qualitative agreement with the analysis of Tuck showing a reduction in both real and imaginary components of the drag for rectangular, or 'thin', geometries, as shown in Figure 3.7c and Figure 3.7d. Hence, we have shown that the hydrodynamics of an oscillating body free from a surface can be calculated using our FEM solver. We have reproduced several important results including the oscillatory drag on a cylindrical body and a rectangular body with low aspect ratio.

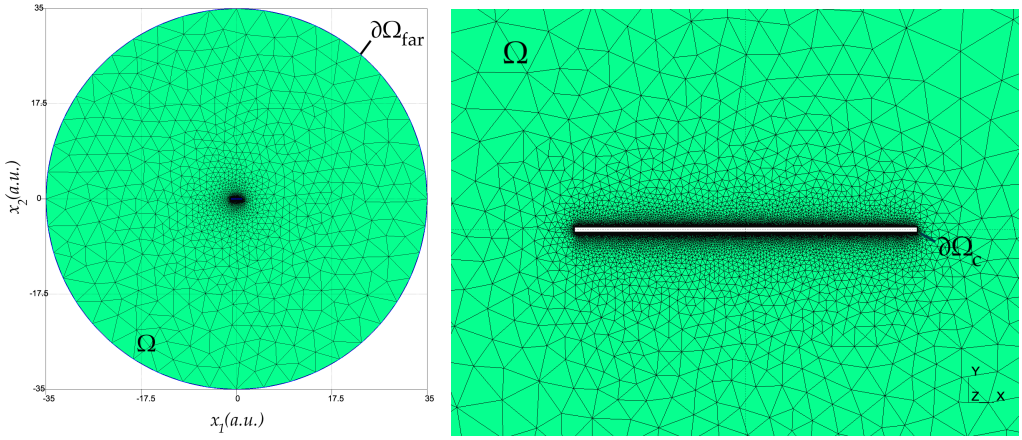

Figure 3.4: Mesh for a body with rectangular cross-section.

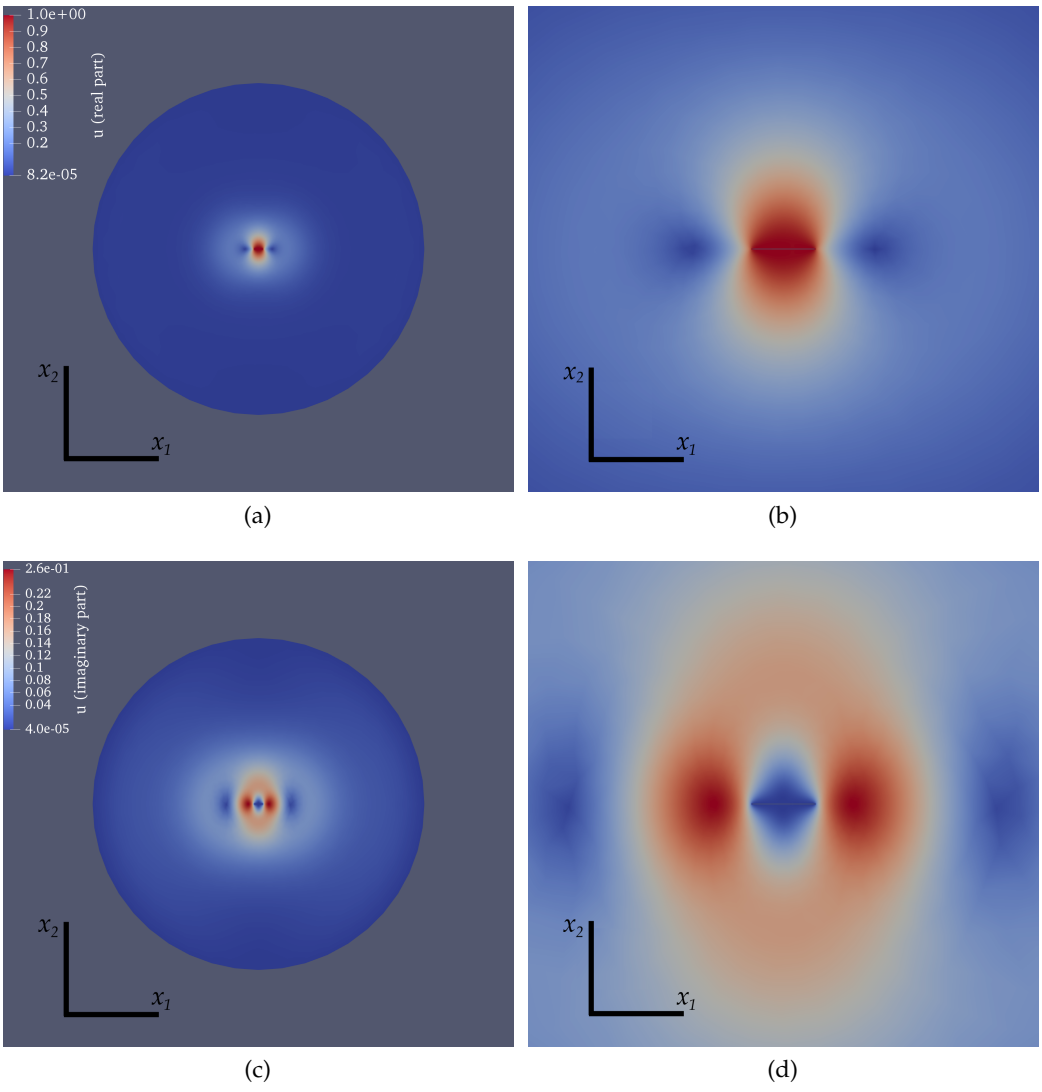

Figure 3.5: The velocity profile for flow around an oscillating body with rectangular cross section. In (a-b) we show the real components of the velocity profile for the entire domain (a) and a magnified (with same magnification as in Figure 3.5) section including the object (b). In (c-d) we show the imaginary components of the velocity profile for the entire domain (c) and a section around the object (d).

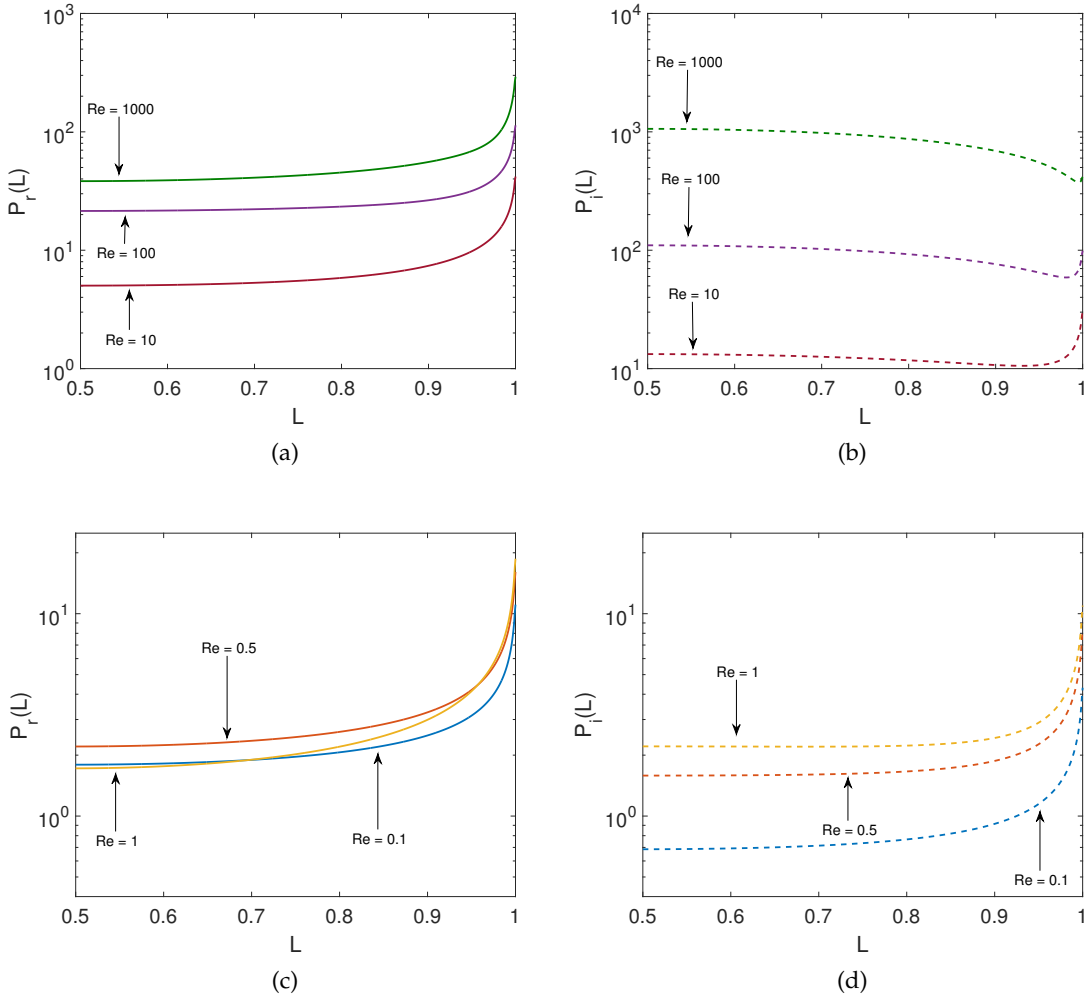

Figure 3.6: The pressure distribution across one half of a body with thin rectangular cross-section. We show the real (a) and imaginary (b) components for low frequencies, $\mathrm{Re}(\omega) = 0.1$, 0.5, 1, as well as the real (c) and imaginary (d) components for high frequencies, $\mathrm{Re}(\omega) = 10$, 100, 1000. We see siginifcant blow up at the corners $L = 1$, as reported in [119].

3.4.2 *Influence of the Surface on Hydrodynamics*

We now turn our attention to the influence of a surface, $\partial\Omega_{\text{surface}}$, on the hydrodynamics of an object oscillating in viscous fluid. The surface is assumed to be semi-infinite and a distance H^* from the oscillating body, as shown in Figure 3.8. We are specifically interested in how the drag and inertial mass on the body vary as the separation distance decreases. We examine the same cylindrical and rectangular geometries, as described in Section 3.4.1, but now prescribe a no-slip condition on the surface,

$$\mathbf{u}(\mathbf{x}) = 0, \qquad \text{for} \quad \mathbf{x} \in \partial\Omega_{\text{surface}}. \tag{3.36}$$

We continue as in Section 3.3.2, changing only the mesh file to include the additional surface boundary, where we set (3.36) to hold.

We choose the cylindrical and rectangular bodies to both have $R = 1$ and specify that the length of the surface, $\partial\Omega_{\text{surface}}$, is 70. We specify that the characteristic size of finite elements on the outer circular boundary, $\partial\Omega_{\text{far}}$ to be 5, on the surface to be 1 and on the cylindrical body to be 10^{-3}. We also create a semi-circular region with a radius of 10 which has smaller elements, 0.1, in order to properly capture the influence of the surface on the oscillating body. This results in a total domain of 66,000 elements. An example mesh file, where $H = 5$, is shown in Figure 3.9, where we have increased the size of the elements to aid visibility. We normalise the distance between the cantilever and the surface, H^*, by the radius (or half width when rectangular) of the probe such that $H^* = R^*H$. As described in [137], we expect the probe to be insensitive to the influence of the surface when the distance between surface and probe is greater than the width of the probe, $H > 2$, where we expect the drag on the oscillating body to return to that of a body far from a surface, as described in Section 3.4.1. Hence, we begin by considering the cases where $H = 5, 2$ and 1 to see how closely our solver matches the hydrodynamics for the free case.

In Figure 3.10, we compare the hydrodynamic function, $\Gamma(\text{Re}_f)$, calculated on the body using (3.14), as the body is moved closer to the surface. In Figure 3.10a, we show the change in hydrodynamic drag for a body with circular cross-section and, in Figure 3.10b, we show a probe with rectangular cross-section. In both inset figures, we show the relative error in calculated $\Gamma(\text{Re}_f)$ for when $H = 5$ to that of a probe oscillating far from a surface as given by Stokes [120] and Sader [117], respectively. For $H > 2$, the relative error for both geometries is approximately less than 1×10^{-2} for almost all frequencies, supporting our assumption that the surface has little influence on the body for large distances. However, for $H \leq 2$, we see significant influence on the probe due to the presence of the surface, in line with the observations of [137]. The damping, denoted by dashed lines, increases for decreased surface-body separation though this diminishes with increasing frequency. On the other hand, the additional mass, denoted as solid lines, decreases for low frequencies ($\text{Re}_f(\omega) \lesssim 1$) and increases for large frequencies ($\text{Re}_f(\omega) > 1$).

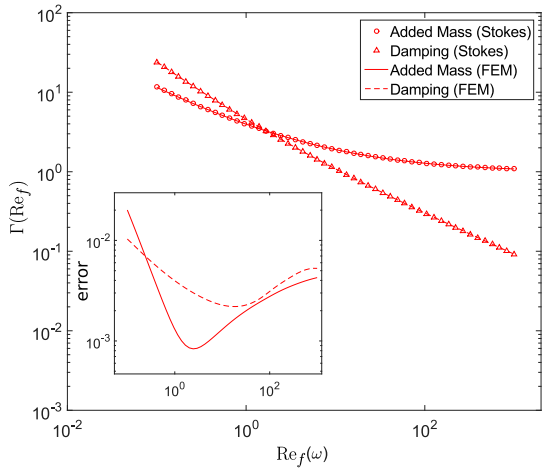

(a) Comparison with Stokes (Circular) [120].

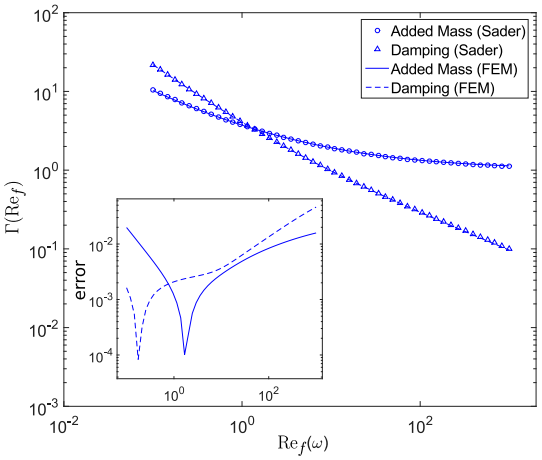

(b) Comparison with Sader (Rectangular) [117].

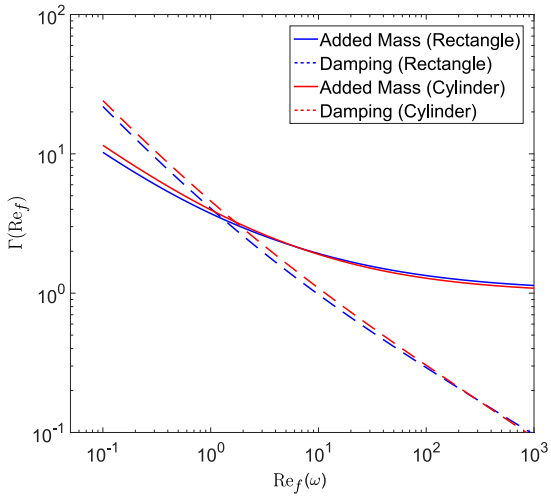

(c) Comparison for different geometries.

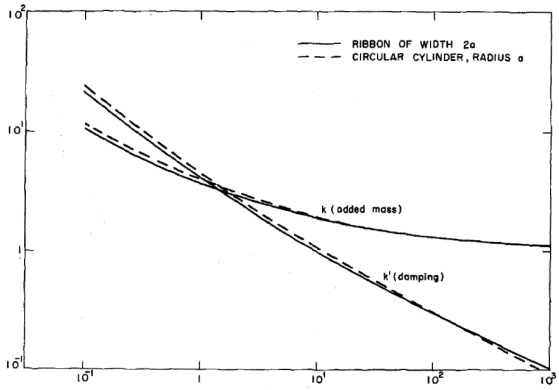

(d) Comparison calculated by Tuck [119]

Figure 3.7: A comparison of the results of our FEM solver for(a) the drag on a cylindrical object compared against the analytic solution found in [120] and (b) the drag on a rectangular object compared against the analytic solution found in [117]. We show the relative error in our calculation inset in both (a) and (b), while in (c) we compare the drag calculated for both geometries which gives qualitative agreement with the results of Tuck [119], reproduced in (d).

In Figure 3.12, we show the real and imaginary components of the fluid velocity for $H = 10$, 5, 2, and 1. Here, we have chosen $\mathrm{Re}_f(\omega_1) = 0.6$, which corresponds to the first resonant frequency for a conventional AFM probe (with properties described in Table 5) oscillating in air. This mode is most influenced by the introduction of a surface, as shown in Figure 3.10. In Figure 3.12, we can see a reduction in both the real and imaginary components of the fluid velocity as we decrease the distance between probe and surface.

We next examine the case of a body with rectangular cross-section that is brought towards a surface. We study the same distance regime explored for the cylindrical case, shown in Figure 3.10a, and observe a decrease in the influence of the wall on the rectangular body for these distances and at all frequencies, as shown in Figure 3.10b. We posit that this is due to the difference in surface area between the two bodies such that less fluid is displaced for the rectangular case, as described in Section 3.4.1. However, the qualitative change in the drag remains the same as in Figure 3.10a. We see a large increase in the damping terms on the cantilever for low frequencies ($\mathrm{Re}_f(\omega) < O(2)$), but find that this has a reduced effect at high frequencies ($\mathrm{Re}_f(\omega) > O(2)$) when compared to the cylindrical case. Similarly, we find a decrease in the fluid inertial mass for

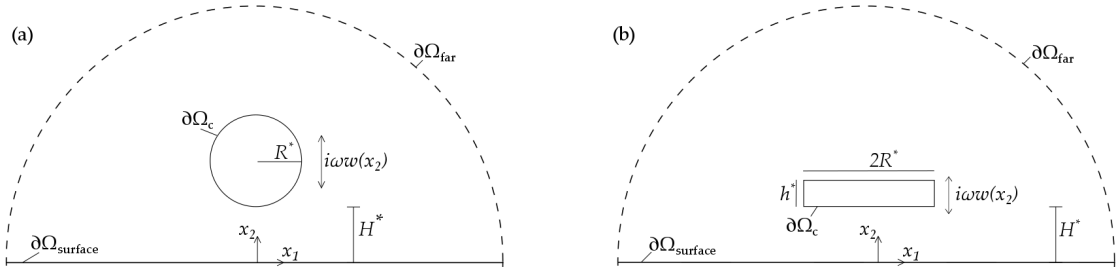

Figure 3.8: Schematic showing the oscillating body with (a) cylindrical cross-section and (b) rectangular geometry which is a total distance H^* from the surface.

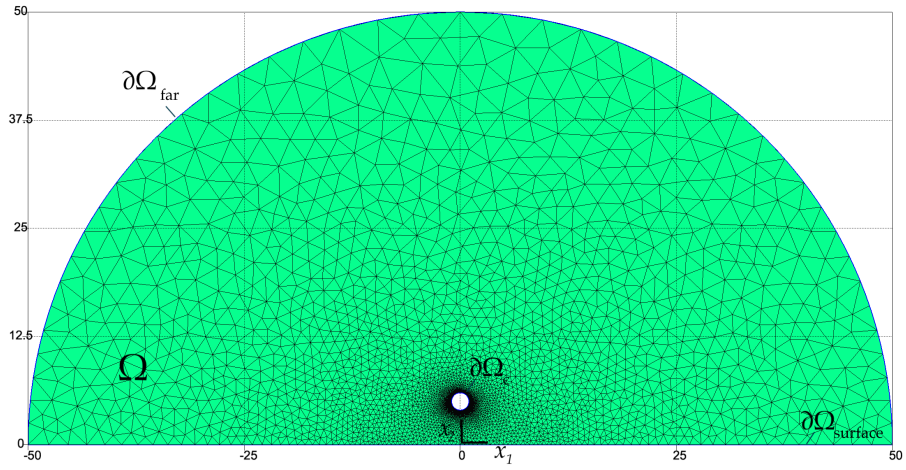

(a) $H = 5$

Figure 3.9: The mesh used for a probe with cylindrical geometry which is brought closer to the wall. We refine the around the probe geometry and the lower plane which represents a surface.

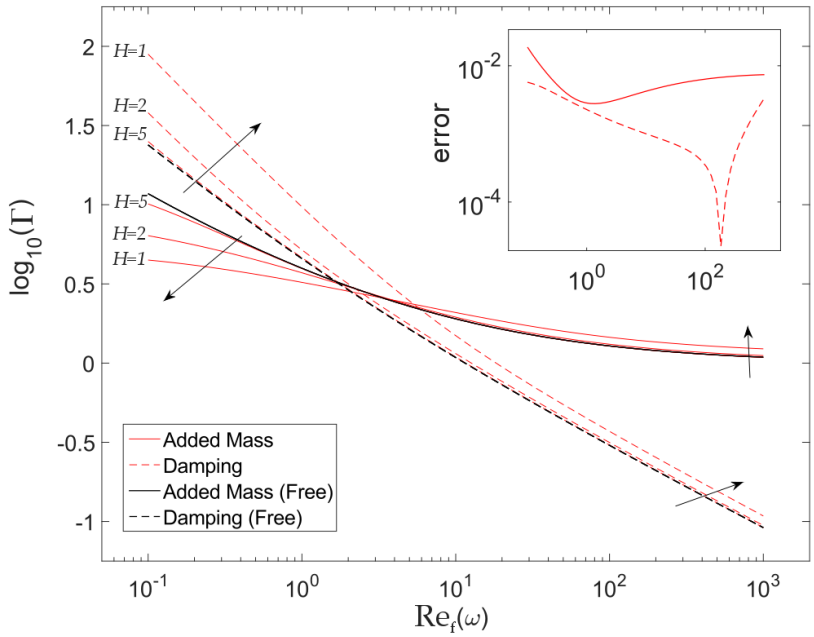

(a) Cylindrical

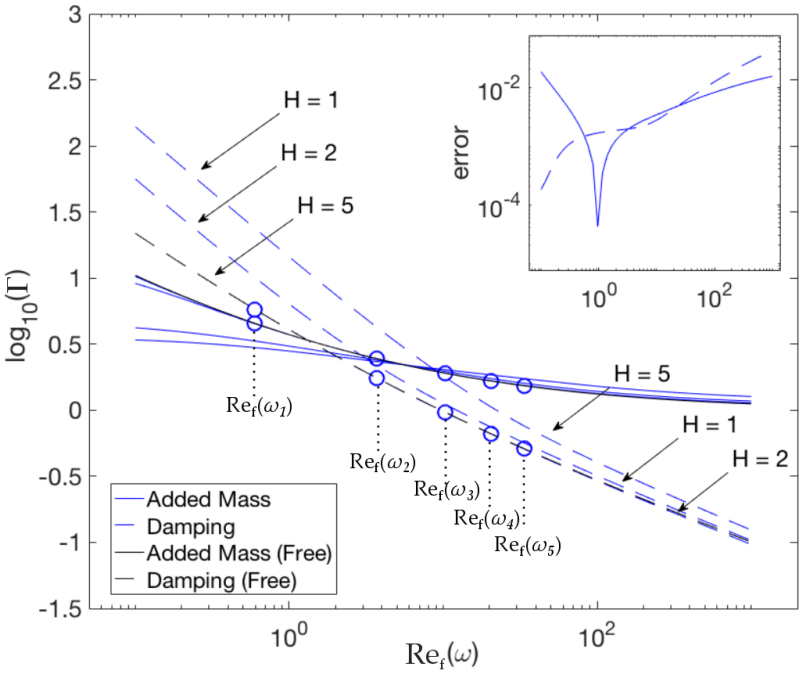

(b) Rectangular

Figure 3.10: Influence of the wall on the hydrodynamic drag terms, added mass and damping, as a function of oscillation frequency where (a) demonstrates the effect on a probe with cylindrical geometry and (b) shows a probe with rectangular geometry. We see that, for both geometries, there is not much change from the hydrodynamics calculated in Section 3.4.1 until the distance one or two times the width of the probe, $H = 1, 2$, as discussed in [137]. We have highlighted the resonant frequencies for a cantilever with properties given in Table 5; $\mathrm{Re_f}(\omega_1) = 0.6, \mathrm{Re_f}(\omega_2) = 3.7, \mathrm{Re_f}(\omega_3) = 10.4, \mathrm{Re_f}(\omega_4) = 20.4$ and $\mathrm{Re_f}(\omega_5) = 33.8$.

low frequencies ($\mathrm{Re_f}(\omega) < O(2)$) and an increase for high frequencies ($\mathrm{Re_f}(\omega) > O(2)$), though this is also reduced when compared against the cylindrical case. We show the resonant frequencies for cantilevers with the properties given in Table 5 as open circles. These are discussed further in Section 3.6.

In Chapter 5 and Chapter 6, we shall consider the shift in frequency of the n^{th} mode in contact with a sample to the n^{th} free mode of an AFM probe (opposed to the first free mode, or fundamental mode, as is conventionally done in contact resonance (CR) measurements[66]). Conventional contact mode AFMs[4] will have a distance between probe and sample of $H = 0.25 - 0.6$. Hence, we are interested in tip-sample separations less than unity for applications to CR-AFM. Hence, we solve for $H = 1, 0.9, \ldots, 0.6$ and also $H = 0.5, 0.3, 0.2$, and 0.1. These results are shown in Figure 3.11. For a beam which is approximately 20 µm in width, the minimum distance for the rectangular case, $H = 0.1$, would equate to 1 µm which is a less than the tip height for many conventional AFM probes.

In Figure 3.11a, we show the change in drag for a cylindrical probe as it is brought close to a surface. We find that there is a significant increase in the hydrodnamic drag for all frequencies as well as a considerable increase in the inertial mass for a body oscillating at high resonant frequencies ($\mathrm{Re}(\omega) > O(1)$). We find that at low frequencies ($\mathrm{Re}(\omega) \leq O(1)$), the inertial mass decreases as in Figure 3.11a and that this is relatively insensitive to probe-sample separation. For all frequencies, there is a far larger increase in the damping term (dashed lines) than the added mass on the cantilever. For small separation distances, $H < 0.6$, we see a noticable increase in the hydrodynamic damping term, as shown in Figure 3.11d. There is also an increase in the inertial mass term but less pronounced than that of the damping term (which increases by almost two orders of magnitude for $\mathrm{Re_f}(\omega) \lessapprox 10^2$).

The rectangular probe is shown for the same distances as the cylindrical probe, with separation distances $H = 1, 0.9, \ldots, 0.6$ in Figure 3.11b, and for small separation distances in Figure 3.11c. We see a substantial increase in drag with sensor-sample separation when compared to that of the cylindrical case, as shown in Figure 3.11b. Furthermore, for small distances, shown in Figure 3.11c, we see an increase in the damping on the probe that can be as large as three orders of magnitude (an order of magnitude larger than that observed for the cyldrical case) and that this increase exists for all frequencies. Additionally, we see an increase in the inertial mass term for low tip-sample separation distances ($H \sim 0.1$) and all frequencies, though this less pronounced than the increase in fluid damping. In Table 6, we give our calculated values for the real and imaginary components of drag of the first five resonant frequencies of an AFM probe, with properties described in Table 5 and marked as open circles in Figure 3.11b.

We have shown that our solver is able to capture a change in the hydrodynamic drag as an oscillating body is moved towards a surface, assuming that span-wise fluid flow will dominate such that the dimensionality of the problem can be reduced to two dimensional flow around the cross-section of an infinitely long beam. We have examined both

4 We discuss the distinction between contact mode and tapping mode AFM in Chapter 1.

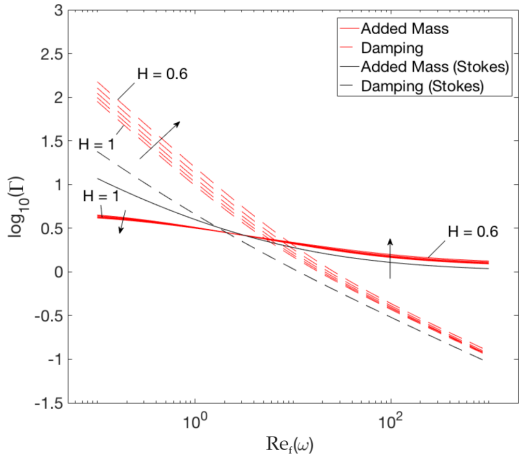

(a) Circular Geometry

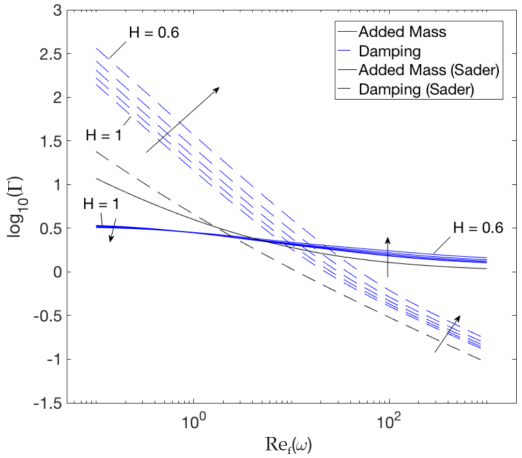

(b) Rectangular Geometry

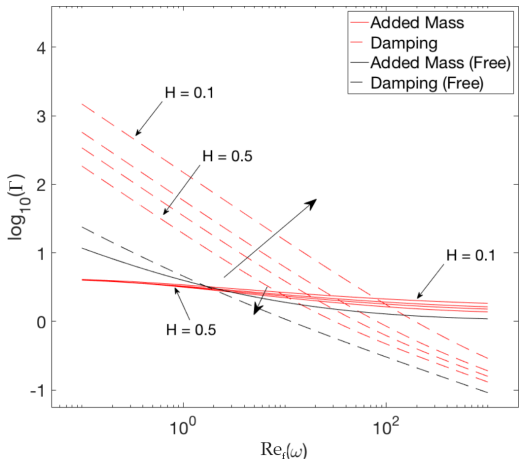

(c) Circular Geometry

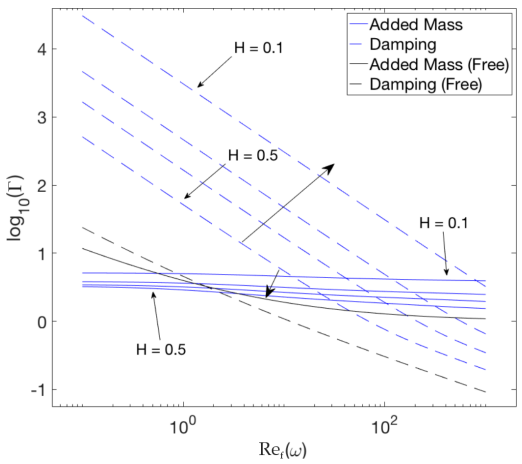

(d) Rectangular Geometry

Figure 3.11: Added mass and damping as a function of oscillation frequency for different probe–sample separations. Both (a) and (b) are for $H = 1, 0.9, ..., 0.6$, where arrows show decreasing H. We show the additional tip-sample separations for the rectangular case in (c) where $H = 0.5, 0.3, 0.2, 0.1$.

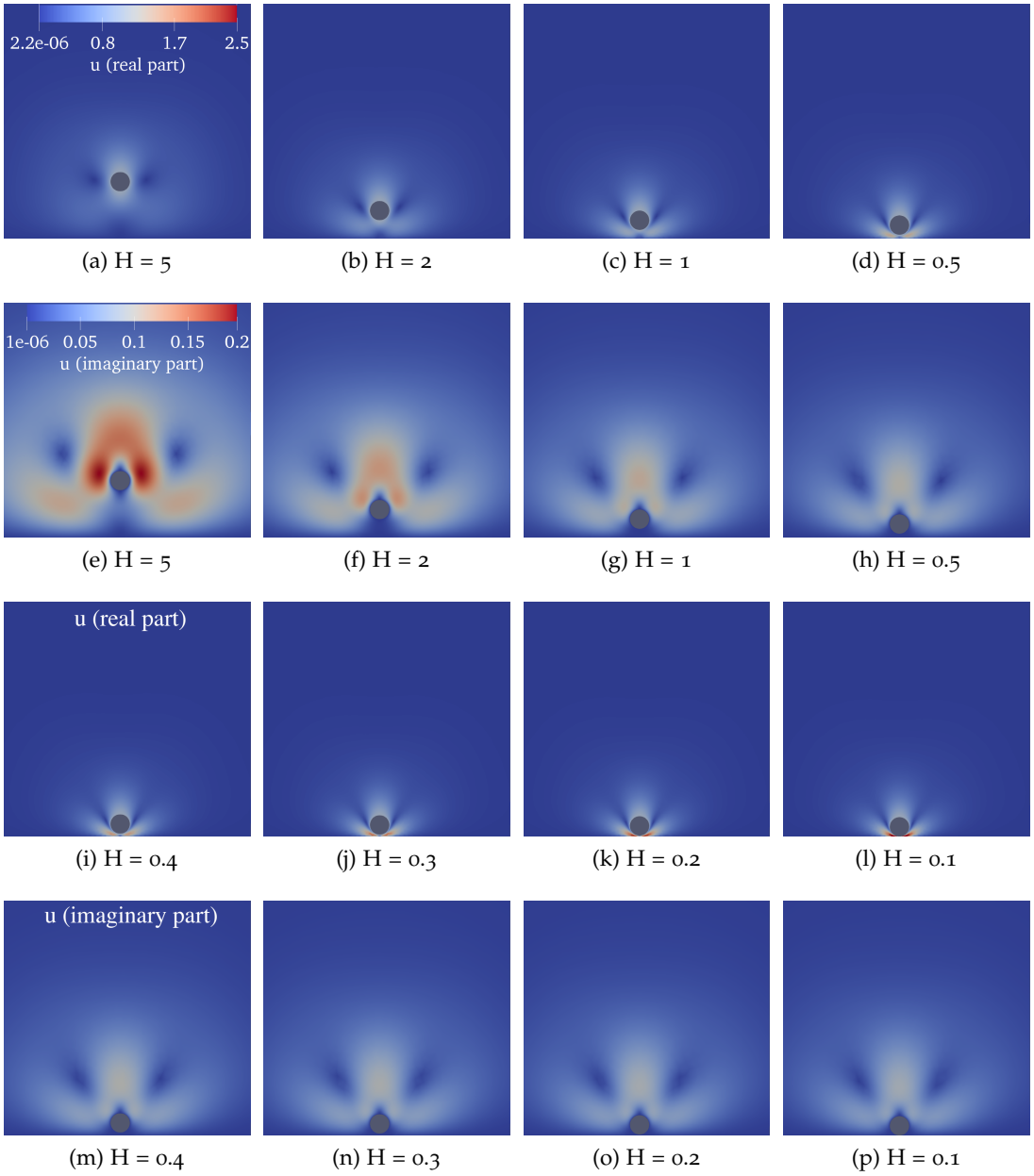

(a) H = 5 (b) H = 2 (c) H = 1 (d) H = 0.5

(e) H = 5 (f) H = 2 (g) H = 1 (h) H = 0.5

(i) H = 0.4 (j) H = 0.3 (k) H = 0.2 (l) H = 0.1

(m) H = 0.4 (n) H = 0.3 (o) H = 0.2 (p) H = 0.1

Figure 3.12: We show the velocity profile for a probe with cylindrical geometry which is brought closer to the wall. We refine the mesh around the probe geometry and the lower plane which represents a surface.

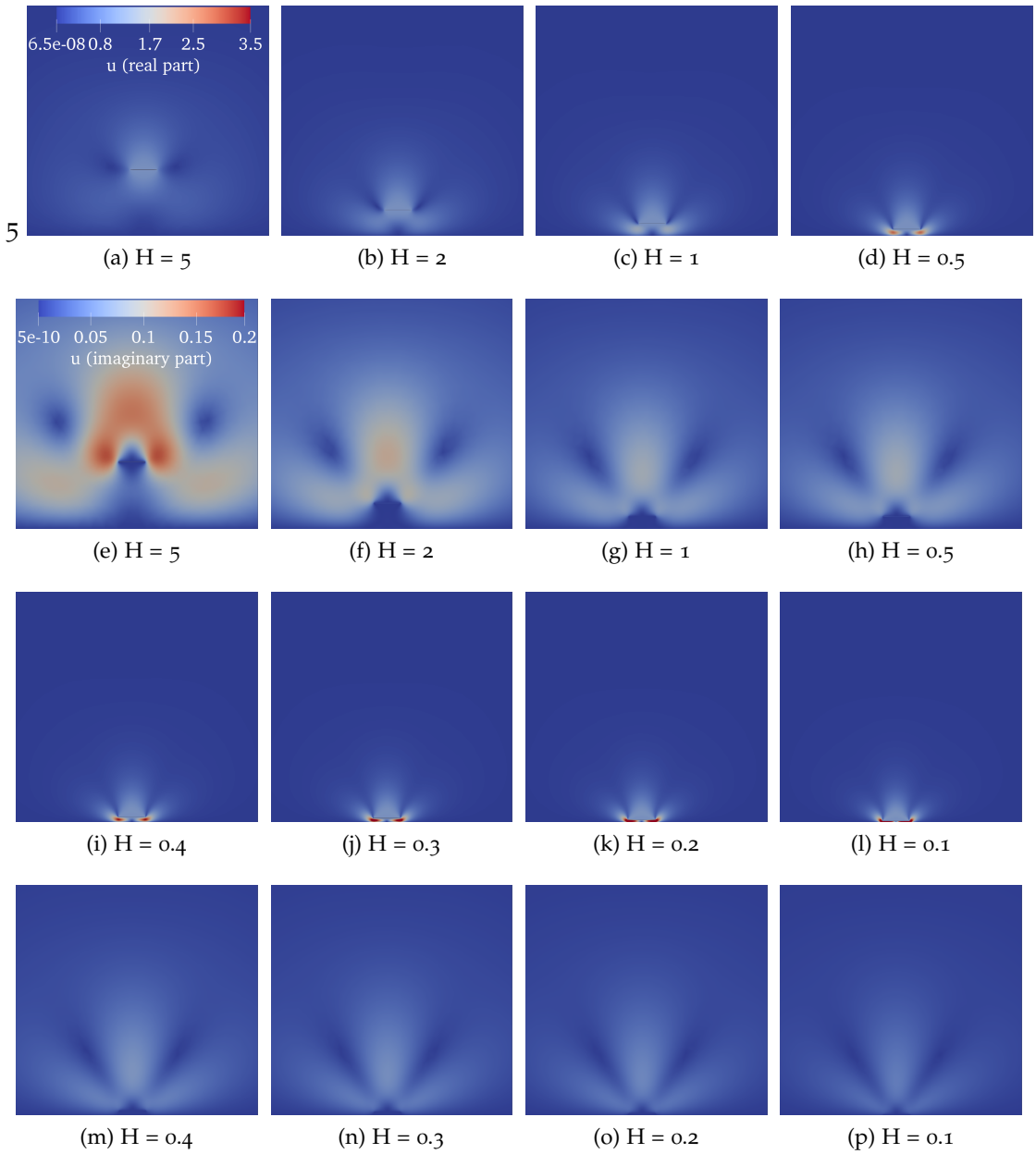

(a) H = 5 (b) H = 2 (c) H = 1 (d) H = 0.5

(e) H = 5 (f) H = 2 (g) H = 1 (h) H = 0.5

(i) H = 0.4 (j) H = 0.3 (k) H = 0.2 (l) H = 0.1

(m) H = 0.4 (n) H = 0.3 (o) H = 0.2 (p) H = 0.1

Figure 3.13: We show the real components of the velocity profile of a probe with rectangular geometry, oscillating near to a surface, such that $\mathrm{Re}(\omega_1) = 3$ and $\omega_1 = (2\pi)15\,\mathrm{kHz}$. We refine the around the probe geometry and the lower plane which represents a surface.

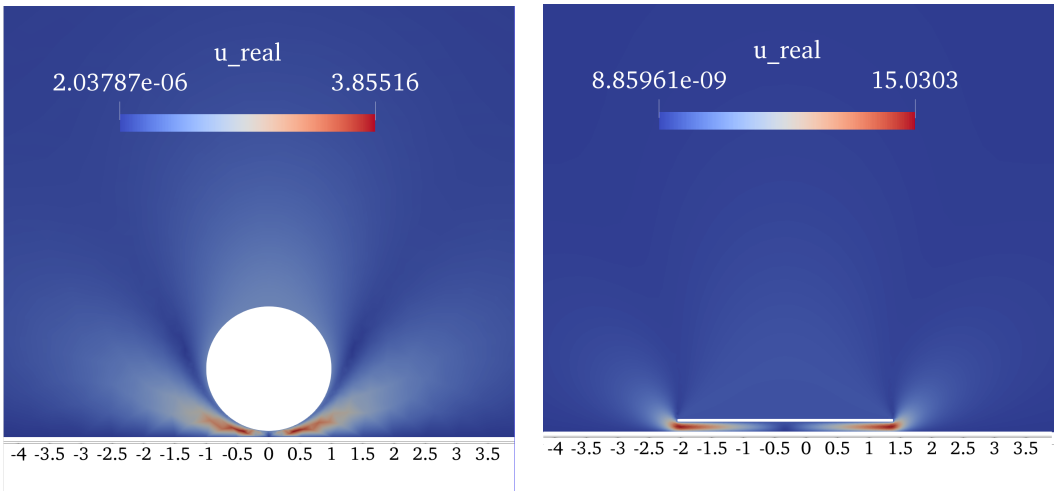

Figure 3.14: A magnification of the last figure showing the real part of the fluid velocity in Figure 3.12 and Figure 3.13, respectively. Both figures show the same region in the domain but with updated scalebar to highlight the difference in magnitude of the fluid velocity for differing geometries.

cross-sectional geometries, cylindrical and rectangular, over a range of realistic separation distances and find that hydrodynamics of the system remain relatively unaffected by the influence of the wall for distances greater than the width, supporting the work of [137]. However, for smaller separations, we find significant increase (by several orders of magnitude) in the damping on the body, particularly at low frequencies. This has implications for contact mode AFM probes which oscillate within this separation regime. For both geometries, we find that there is an initial reduction in the inertial term of the hydrodynamic drag for low frequencies ($\mathrm{Re}(\omega) \leq O(1)$). For all higher frequencies of oscillation, the added mass is relatively unaffected by wall effects until the separation distance is small **(**$H \leq 0.6$**)**, where there is a signicant increase in the added inertia for high frequencies ($\mathrm{Re}(\omega) \leq O(1)$).

We show the velocity profile for the cylindrical beam in Figure 3.12 and rectangular beam in Figure 3.13. This highlights the qualitative difference in the hydrodynamics of the two geometries that we have chosen to investigate. The magnitude of the real part of the velocity is larger for almost all separation distances, for the specific case where both cylindrical and rectangular body are brought close to the wall ($H = 0.1$) in Figure 3.14. It can be seen that a body with rectangular geometry captures more fluid in the space between the bottom boundary and the wall than a body with cylindrical geometry. This demonstrates that our solver is capturing the full interaction between the two boundaries and points to the possibility of a 'squeeze-film' damping effect that occurs when a shape with rectangular geometry oscillates near to a wall, as has been discussed elsewhere in [118, 142]. However, further investigations are required to validate this. We next turn to the implications of these results for AFM operation, with specific attention given to how they will alter the resonant frequency and Q factor of an oscillating AFM probe.

	$H = 2$	$H = 1$	$H = 0.5$	$H = 0.3$	$H = 0.2$	$H = 0.1$
$\Gamma(\mathrm{Re_f}(\omega_1))$	$3.3 + 10i$	$3 + 24i$	$3 + 86i$	$3.3 + 280i$	$3.7 + 770i$	$5 + 5{,}100i$
$\Gamma(\mathrm{Re_f}(\omega_2))$	$2.4 + 2.2i$	$2.3 + 4.3i$	$2.5 + 14i$	$2.9 + 45i$	$3.4 + 130i$	$4.8 + 830i$
$\Gamma(\mathrm{Re_f}(\omega_3))$	$2 + 1.1i$	$2 + 1.8i$	$2.3 + 5.3i$	$2.6 + 16i$	$3.1 + 45i$	$4.6 + 300i$
$\Gamma(\mathrm{Re_f}(\omega_4))$	$1.7 + 0.75i$	$1.9 + 1.1i$	$2.1 + 2.8i$	$2.5 + 8.4i$	$3 + 23i$	$4.4 + 150i$
$\Gamma(\mathrm{Re_f}(\omega_5))$	$1.6 + 0.56i$	$1.7 + 0.76i$	$2 + 1.8i$	$2.4 + 5.2i$	$2.9 + 14i$	$4.3 + 91i$

Table 6: Calculated hydrodynamic function, $\Gamma(\mathrm{Re}(\omega_n))$, calculated by (3.14), for the first five modes, n = 1, ..., 5 of the rectangular cantilever with properties given in Table 5. Note that increase in viscous damping as the sample-probe distance decreases. The resonant frequencies $f_n = \omega_n/(2\pi)$ are given in Chapter 2.

3.5 DISCUSSION

In Section 3.4.2, we considered the influence of the wall on an oscillating cantilevered probe over a range of driving frequencies and wall-probe distances. We are primarily concerned with the behaviour of the probe as it is brought towards a rigid surface, and the additional contribution to viscous drag due to the surrounding fluid. We have demonstrated that the probe will be unaffected by the surface when the separation distance is greater than the width of the probe, in line with what was discussed in [137]. However, for distances smaller than the width, the influence of the surface becomes significant, as shown in Figure 3.11.

We now turn to the validity of our solver when considering surface influences. Past work [137, 140] has considered the introduction of a surface on the hydrodynamics of an oscillating AFM probe (with rectangular geometry only) through a semi-analytic BEM approach and provided tabulated values for the hydrodynamic function over varying probe-surface distances. In [137], the hydrodynamics of 2D flow around a cross-section of a rectangular beam was calculated over the distances, $H = 2$, 1, 0.6, 0.4, 0.2. Meanwhile, [140] calculated the same 2D function and compared it against the 3D work given in [139] and experimental work of [132], where they found good agreement. In [140], the hydrodynamic function is also given in tabulated results and can be calculated for arbitrary frequency and probe-surface distances. We compare the tabulated values of [140] against our own for the case of $H = 2$ in Figure 3.15, where we expect the hydrodynamics to match the hydrodynamics of the free probe. Hence, we include the relative error for the respective solvers when compared to the free hydrodynamics (described in Section 3.4.1). We find that our FEM solver calculates the drag with equal or improved accuracy when compared against the tabulated results of [137, 140] for how well it approximates the hydrodynamic drag on a free oscillating rectangular probe.

In Figure 3.16, we compare our 2D solver to the hydrodynamic drag calculated from the tabulated results of [137, 140] over the range of separation distances $H = 2$, 1, 0.6, 0.4, 0.2. We find good qualitative agreement with the hydrodynamic drag calculated by [140], which has also been validated against [137] and the full three dimensional solver introduced in [139]. To reiterate, both [137, 140] utilise a boundary element method to

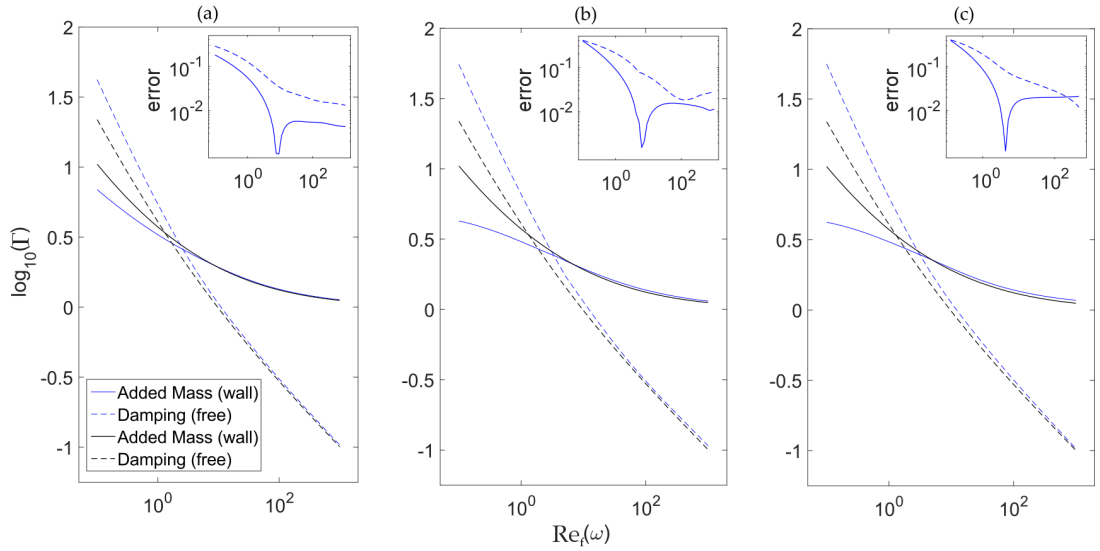

Figure 3.15: The hydrodynamic drag on a rectangular cantilever for $H = 2$, calculated using the tabulated results of (a) [137], (b) [140], and, (c), our own FEM solver. Inset is the relative error when compared against the hydrodynamic drag on a rectangular cantilever oscillating far from a surface given in [117].

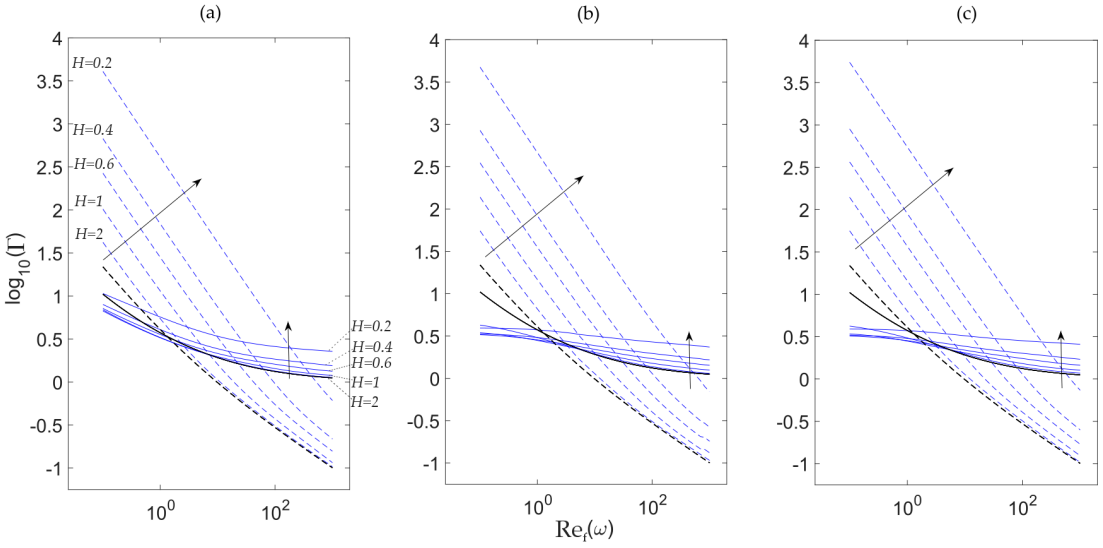

Figure 3.16: The hydrodynamic drag D on a rectangular probe calculated over the range of separation distances $H = 2, 1, 0.6, 0.4, 0.2$. In (a) we show drag calculated using the tabulated results of [137], and, in (b), the tabulated results of [140]. We find good qualitative agreement with both [137] and [140] for our own calculation of the hydrodynamic drag (c).

solve for the hydrodynamic drag, whereas we have used a finite element method solver. To the best of our knowledge, this is the first validation of the work by [137] that has not employed BEM techniques. This demonstrates that our FEM solver is able to reproduce existing hydrodynamic results. However, our solver is amenable to extensions (in a way that BEM is not) including considerations of three-dimensionality and biphasic flow as we discuss in Section 3.7. Furthermore, as we have developed our solution using open-source libraries, the work can easily be built upon by others in the AFM and MEMS community to study, for example how the influence of multiple oscillating bodies near to a surface as occurs for cantilever arrays [160, 161].

3.6 IMPLICATIONS FOR AFM

Our findings are directly relatable to the operation of an oscillating AFM probe. For an oscillating beam in a vacuum, discussed in Chapter 2, the dispersion relation describes how the n^{th} resonant angular frequency, $\omega_n = 2\pi f_n$, relates to the beam's material properties and boundary conditions

$$\omega_n = \alpha_n^2 \sqrt{\frac{EI}{\mu}}. \tag{3.37}$$

where α_n is the boundary-specific wavenumber of the n^{th} eigenmode, EI is the flexural rigidity and ρA is the areal mass density as described in Chapter 2. We rewrite (3.37) in terms of the static spring constant, defined in (2.4), and the mass of the beam $m_c = \rho A L$, giving

$$\omega_n = \alpha_n^2 \sqrt{\frac{k_c}{3m_c}}. \tag{3.38}$$

As discussed in Section 3.3.1, the presence of fluid surrounding the cantilever will introduce additional inertial and damping terms, described by the complex-valued hydrodynamic function, Γ, where the real part represents the additional inertial forces due to the presence of the fluid and the imaginary part denotes viscous fluid damping. Hence, when the cantilever is oscillating in a fluid, the dispersion relation will also contain additional inertial effects from the presence of the fluid, m_f, such that the total mass is

$$m_T = m_f + m_c. \tag{3.39}$$

For an oscillating cantilever that is initially free from any surface contributions and then brought towards the surface to a separation distance of H, the ratio of the cantilever free resonant frequency, $f_{R,\,\text{free}}$, to the resonant frequency when the cantilever is brought close to the surface, $f_{R,\,\text{contact}}$, is

$$\Delta f_n = \frac{f_{n,\text{contact}}}{f_{n,\text{free}}} = \left(\frac{\alpha_{n,f_{\text{contact}}}}{\alpha_{n,f_{\text{free}}}} \right)^2 \sqrt{\Delta m}, \tag{3.40}$$

where $\Delta m = m_{\mathrm{T,\,free}}/m_{\mathrm{T,\,contact}}$ and where we refer to the contact and free wavenumber, resonant frequency and total mass via their subscript. The change in mass due to additional hydrodynamic influence of the surface, Δm, can be found using the definition of the hydrodynamic function, (3.15 – 3.16),

$$\Delta m = m_c \left(\frac{1 + c\Gamma_{\mathrm{r,\,free}}(\omega_{n,\mathrm{free}})}{1 + c\Gamma_{\mathrm{r}}(\omega_{n,\mathrm{contact}}, H)} \right), \tag{3.41}$$

where $\Gamma_{\mathrm{r,\,free}}(\omega_n)$ denotes the hydrodynamic function for an probe oscillating far from a surface, $\Gamma_{\mathrm{free}}(\omega) = \lim_{H\to\infty} \Gamma(\omega, H)$, where the subscript r denotes the real part of the hydrodynamic function and $c = \pi\rho_{\mathrm{f}} L b^2/(4m_{\mathrm{c}})$.

The hydrodynamic function also introduces additional viscous damping, γ, to the system. Note that, in a vacuum, γ will be predominantly composed of the intrinsic damping of the probe when oscillating free from a surface. The damping on the cantilever causes a change in the quality factor of the resonance,

$$Q_n = \frac{m_c \omega_n}{\gamma}, \tag{3.42}$$

where the hydrodynamic damping is given by the imaginary component of the hydrodynamic function, according to (3.16). We again consider the ratio of the Q factor for the cantilever oscillating free from a surface to that of the cantilever oscillating nearby,

$$\Delta Q = \frac{Q_{n,\mathrm{contact}}}{Q_{n,\mathrm{free}}} = \Delta m \Delta\gamma, \tag{3.43}$$

and where,

$$\Delta\gamma = \Delta f_n \frac{\Gamma_{\mathrm{i,\,free}}(\omega_{n,\mathrm{free}})}{\Gamma_i(\omega_{n,\mathrm{contact}}, H)}. \tag{3.44}$$

In Figure 3.17, we plot the change in the square root of the added mass (Figure 3.17a) and the damping scaled by the shift in frequency Δf_n (Figure 3.17b), for the first five modes of a MSNL-B cantilever, with properties described in Table 5 and resonant frequencies marked as circles on Figure 3.10b, and where $H = 2, 1, 0.5, 0.3$ and 0.2. We have chosen to plot $\sqrt{\Delta m/m_c}$ as this represents a potential error when calculating material properties using a shift in resonant frequency. Similarly, we plot $\Delta\gamma/\Delta f_n$ as this corresponds to the change in calculated damping when measuring the shift in Q, though we note that both Δf_n and Δm will also be influenced by the added mass, as shown in (3.40) and (3.43). It can be seen that both the damping and added mass are less affected by the influence of a surface as the mode number increases, owing to the decreased sensitivity to the influence of the wall at higher oscillatory Reynolds numbers. This gives further motivation for using the higher modes of a micro-mechanical cantilever to measure material properties, as discussed in Chapter 1. We also see that for $H = 0.2$, which is approximately equal to the tip height of conventional contact-mode AFMs, there is a decrease in both the scaled influence of the added mass, Figure 3.17a, and of damping, Figure 3.17b. For $n > 2$, this is less than 1% for the added mass. However, for the scaled damping, this is between $25\% - 35\%$ demonstrating that the viscous damping

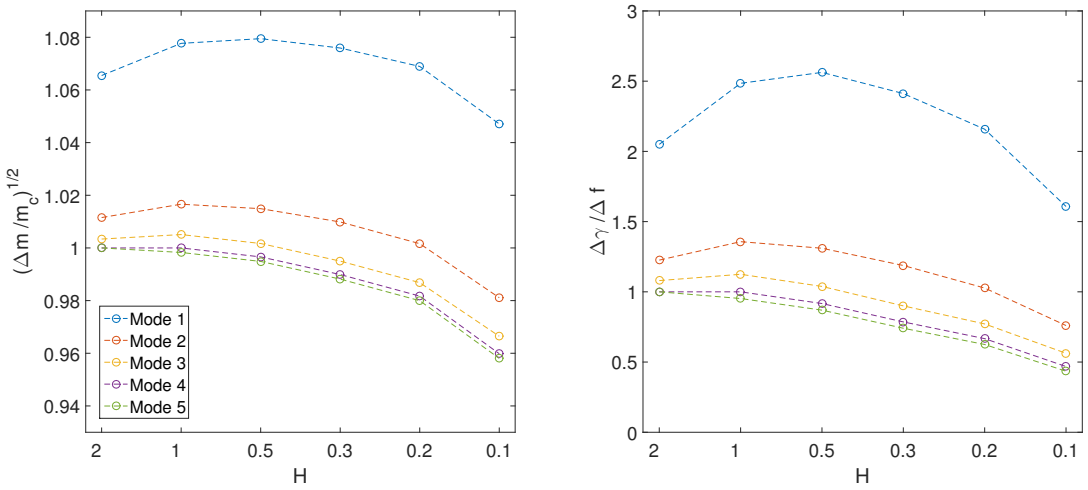

(a) Added Mass (b) Damping

Figure 3.17: The influence of (a) the hydrodynamic inertial effects, scaled by the mass of the cantilever according to (3.41) and (b) the hydrodynamic damping, scaled by the shift in resonant frequency according to (3.44), for the first five resonance frequencies, $\mathrm{Re}_f(\omega_1) = 0.6, \mathrm{Re}_f(\omega_2) = 3.7, \mathrm{Re}_f(\omega_3) = 10.4, \mathrm{Re}_f(\omega_4) = 20.4$ and $\mathrm{Re}_f(\omega_5) = 33.8$.

term should be accounted for when calculating the damping in the system, through the Q factor of the resonant peak of an AFM probe.

To the best of our knowledge, the change in the hydrodynamics with respect to a change in height has not been considered explicitly before using the finite element method. Instead, previous investigations have examined how the hydrodynamics is influenced by different fluids [140]. In this thesis, we will show how the resonant frequency and Q factor, can give additional non-topographic information about the sample. Hence, the correction factors that are shown in Figure 3.17 are expected to influence the accuracy of acoustic measurements of viscoelastic properties, as described in Chapter 5, when they are not accounted for. Given the need for improved confidence and accuracy in measurement techniques, we expect the above discussion to be of relevance to any method that considers the resonant properties of a probe in fluid environment. We give examples of this in Chapter 5.

3.7 FURTHER CONSIDERATIONS

We have demonstrated a new solver for calculating the hydrodynamics on an oscillating body immersed in fluid. Our solver is versatile in that it can be adapted to different geometries and frequencies, as discussed in Section 3.4.1. We have been able to reproduce boundary element results, including those found in [119] and [117], by calculating the velocity and pressure in the fluid as well as calculating the hydrodynamic drag on the boundary of an oscillating body. This can be accomplished in approximately 15 s for a domain with 30,000 finite elements (2.7 GHz Intel Core i5 laptop with 16 GB of RAM). Having treated the case of a body that is oscillating in a fluid, we then consider how the

introduction of the surface will influence the system. Again, we find good agreement with past literature such as [137, 140].

Thus far, we have treated only the two dimensional case of a body oscillating free and near to a plane surface. However, our solver is conceived such that a full three dimensional version is implementable. In Figure 3.18, we show example meshes that can be used to implement our solver for the full 3D case. In order to run this script, we must account for the velocity profile of the beam across the length which is found by considering the n^{th} mode shape as described in Section 2.5. Once the velocity profile of the beam has been accounted for, the script is run as before where only the dimensionality of the elements must be changed. The increase in dimension causes a corresponding increase in the number of elements that we are required to solve for. In Section 3.4, we 30,000 to 60,000 finite elements. The extension of this solver to three dimensions would require an increase in the number of elements to retain accuracy. As such, we believe it conducive to run a parallelised version of our solver on a high performance computing (HPC) system. Future work will seek to implement this in order to resolve some of the issues of the two dimensional flow approximation, such as the discrepancies when back-calculating the hydrodynamic function in Figure 2.12 and considerations of the length-wise fluid contributions [121].

As discussed in Section 3.1, Clarke [118] calculated the change in hydrodynamic drag in the limit of high and low oscillations and proble-sample separation distances. In [118], the parameter space for different fluid regimes was constructed for the tip-sample separation, H, and characteristic flow inertia, λ as introduced in (3.11). For moderate separations, $H = O(1)$ and low frequencies, $\lambda \ll 1$, the viscous terms become neglible and the governing equations of the flow reduce to the steady Stokes equation [118]. However, as the surface distance becomes small, $H \ll 1$, the flow between the wall and surface can separate due to the disparity in length scales between the radius of the surface and the separation distance. This leads to a lubrication regime which requires a relevant change in the governing equations of the flow. We have not dealt with either of these cases here.

Instead, we have examined the cases where the separation is significantly greater than the reciprocal of the characteristic flow inertia $H \gg \lambda^{-1}$. This returns the result of Stokes and Tuck [119, 120] as described in Section 3.4.1. In Section 3.4.2, we describe the influence of the wall which corresponds to the regime where the characteristic flow inertia is large and separation distance is moderate to small, $\lambda \gg \max(1, H^{-1})$. This results in invisicid flow with viscous contributions restricted to the boundary layers on probe and surfaces, as described in [118]. However, a further regime occurs when the separation distance is decreased such that the boundary layers of both surface and oscillating body becomes comparable, shown to occur when $\lambda^{-\frac{4}{3}} \lesssim H \lesssim \lambda^{-1}$ [118]. This results in a bi-phasic fluid regime with an inner lubrication flow and an outer flow that is comparable to that described in Section 3.4.2. We note that this is of relevance to high-speed AFM (see Chapter 1) and look to incorporate it into our fluid solver in future work.

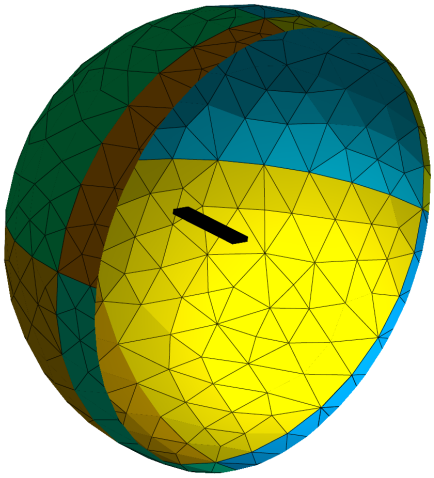

Figure 3.18: An example mesh for the case of a thin rectangular beam oscillating in 3D flow.

3.8 CONCLUSIONS

In this chapter, we have demonstrated a new FEM-based approach to calculating the hydrodynamics on an oscillating body. Our solver is versatile at handling changes to the cross-sectional geometry as well as the introduction of additional changes to the domain, such as the presence of a surface. In Section 3.4.1, we compare the calculations from our solver to previous results, such as [120] which treats the hydrodynamics of fluid around a cylindrical body, and the rectangular correction factor put forward by Sader [117]. We find good agreement with both of these methods when calculating the drag on the free body, where the relative error between these results and our own solver is less than 1% for almost all oscillatory Reynolds numbers.

The benefits of our solver are two-fold. First, the solver does not require significant adaptations in order to account for changes in the domain. For example, the mesh file that was used to calculate the influence of a wall, considered in Section 3.4.2, could also account for surface geometries to give further insight as to how the surface-sensor hydrodynamics couple during AFM measurements. Furthermore, our code is capable of being extended to account for 3D geometries, as we discuss in Section 3.7. This lays the framework for addressing existing limitations to the assumptions of the hydrodynamic theory, as described in Section 3.1.

In Section 3.4.2, we investigate the influence of a wall on the hydrodynamics of the system. We find that a rectangular body will have increased damping than that of a cylindrical body for high separation distances. This highlights that our solver is capturing the full interaction of the flow between the two boundaries and may be due to 'squeeze-film damping' effects. However, this cannot be shown conclusively without further experimental investigation as well as considerations of the contributions from length-wise fluid terms. We find that, for both geometries, the damping increases significantly when a surface is introduced, especially at low frequencies ($\mathrm{Re}(\omega) < O(1)$). Similarly, the surface causes a change in the added mass, which decreases at low fre-

quencies and increases for higher frequencies ($\mathrm{Re}(\omega) > O(1)$). We compare our results to the hydrodynamic function given in [137, 140] and find good agreement with our solver despite using a different numerical scheme (FEM, rather than BEM). We then describe how knowledge of the hydrodynamics of a body oscillating near to a surface will have implications for AFM, especially when calculating material properties using acoustic information of an AFM probe, such as contact resonance AFM (see Chapter 4 for more information). Specifically, we describe how the higher resonant modes of an AFM probe are less influenced by the hydrodynamics of the system, but that even utilisation of the higher modes will require consideration of the hydrodynamic damping when measuring phenomena such as material creep.

This work has highlighted the influence of hydrodynamic drag on an AFM oscillating near to a surface. This will motivate our choices and assumptions in later chapters. For example, in Chapter 4, we describe how to relate a shift in resonant frequency to an idealised contact stiffness which contains information about the sample properties. In this and subsequent chapters, we calculate the shift with respect to the n^{th} free and in vacuo resonant frequency of the probe so as to diminish the influence of the hydrodynamics. In Chapter 5, we demonstrate that the calculated contact stiffness is consistent across multiple modes of a soft cantilever in contact with a stiff material and use the hydrodynamic solver to calculate the viscoelasticity of a sample of stainless steel. Though the sample does not exhibit significant viscoelastic behaviour, it offers a potential avenue for the extension of this work; the measurement of viscous properties using the resonant frequencies of a soft AFM probe.

4

MODELLING A CONTACT STIFFNESS

4.1 INTRODUCTION

In this chapter, we introduce the concept of a contact stiffness, k^*, to model the contact event between a sensor and sample. We illustrate how to find the contact stiffness from a measured shift in resonant frequency of a micro–mechanical sensor, and how the inclusion of additional considerations into the model of tip-sample interaction leads to consistency of the contact stiffness across multiple modes. We note that, to the best of our knowledge, modal consistency of contact stiffness has not been previously observed across multiple higher modes when measuring 'stiff' materials, such as metals, with soft cantilevers, with low spring constant. Hence, we expect our findings to be influential within the field of contact resonance as well as motivativing work set out in later chapters, Chapter 5 and Chapter 6.

4.2 CONTACT STIFFNESS

Micro-mechanical cantilevers are increasingly being used as a characterisation tool in both material and biological sciences [162–164]. Non-destructive applications are being developed that rely on the information encoded within a cantilever's higher oscillatory modes, such as contact resonance AFM (CR-AFM), a technique that can measure the localised stiffness of a sample [66, 165]. Contact resonance techniques connect the change in resonant frequency of a probe when in contact with a surface, Δf_R, to a contact stiffness, k^*, which describes the interaction between the oscillating probe and the sample under investigation [68]. The process of using a sensor to measure the contact stiffness of a sample can be summarised into three parts:

1. Cause: The sample's material properties that couple with the sensor.
2. Model: The interaction between the sensor and the sample.
3. Effect: The response of the sensor, and the change in its behaviour when in contact.

In CR-AFM, sample information is found by measuring the shift in resonant frequency due to the tip-sample interaction [68]. The effect on the cantilever's resonant frequency is interpreted by means of a model, idealised through the introduction of a contact stiffness. The contact stiffness, which encapsulates the interaction between the sensor and sample during contact, is defined below[1].

1 This definition is further expanded upon in Chapter 5.

DEFINITION 3: **Contact Stiffness.** The contact stiffness of a sample, k^*, as measured by a probe that penetrates a total distance, δ, into a sample due to a contact force, F_N, describes the rate of change in contact force with respect to this penetration depth,

$$k^* = \frac{dF_N}{d\delta}. \tag{4.1}$$

When the contact force is applied normal to the sample, the contact stiffness will contain only the normal components in all coordinate directions. In particular, it is commonly assumed [66] that the contact stiffness can be well described by two components, $k_\perp$ and $k_\parallel$, the normal and lateral stiffness respectively.

This contact stiffness is used as a proxy to the material properties that cause the deviation in the response of the probe. In this chapter, we show how to relate the effect to a model; how a change in resonant frequency leads to a sample-specific contact stiffness. In Chapter 5, we take the further step of relating the model to a cause; namely, how an idealised contact stiffness encapsulates the material properties of the sample (such as viscoelasticity). Relating model to cause, as discussed in Chapter 5, requires confidence that the model captures a true property of the sensor-sample system. Though a relatively new technique, contact resonance techniques have been applied under different conditions to a wide range of different materials [166–169]. However, the nature of the technique requires a thorough investigation of the modelling assumptions.

We summarise the work in this chapter as follows. We begin, in Section 4.3, by introducing the contact resonace technique and framing it in the wider field of micro–mechanical sensing and atomic force microscopy. We then describe, in Section 4.4.1, the details of how to relate a shift in frequency to the contact stiffness of the sensor-sample system, as embodied by an idealised spring. In Section 4.4.2, we introduce the simplest version of the model which describes how a normal spring influences a beam that is in contact parallel to the surface. As the primary focus of this thesis is in extending the usability of contact resonance to "stiff" materials (materials with elastic modulus above or near the 100's of GPa range), we show how to relate shifts in resonant frequencies to higher regions of contact stiffness by including both normal and lateral components of the contact stiffness. Hence, we introduce the necessary modifications to this model: a beam tilted towards the surface in Section 4.4.3 and a length offset for the tip in Section 4.4.4. In Section 4.5, we demonstrate for the first time that the introduction of additional parameters to the model (the distance that the tip is offset from the free end of the probe as well as the tip height) provides a route to modal consistency of the contact stiffness, i.e. that the calculated properties of this idealised spring remains the same regardless of the sensor eigenmode used for measurement. We relate this modal consistency back to the stiffness curves described in Section 4.4.1. The theoretical descriptions outlined here are used as the foundation for Chapter 5 which relates a contact stiffness to the elastic properties of a sample.

4.3 ACOUSTIC MEASUREMENTS

4.3.1 *Scanning Acoustic Microscopy*

Since the 1970s, methods that utilise acoustic and ultrasonic waves (those that range from 100s of kHz to MHz) have been used to test material properties. One of the earliest examples used a lens that focused acoustic waves onto a surface and gained information, from the reflected waves, by inferences of the acoustic impedance (the resistance of a material to the passage of acoustic waves) of a sample [170]. These techniques continue to gain attention and application in various fields. For example, in 2015, the acoustic signal recorded from the Philae lander was used to infer material properties of the surface of a comet [171]. The landing gear of the probe was used as the sensor (with a radius of 200 mm) by which the comet surface properties were measured. However, most contact resonance methods use much smaller sensors. The advantage of a small sensor near to a sample is that the signal to noise level of acoustic measurements is increased as they become 'truer' carriers of acoustic waves (i.e. they are more flexible and compliant with lower mechanical impedence). Through microfabrication, such acoustic sensors have been made increasingly smaller with a corresponding improvement in the resolution of the measurements. For example, in 1989, a quartz tuning fork was excited over a chromium grating; the tuning fork was 2.5 mm long, 0.265 mm wide and 0.125 mm thick, yet was able to resolve the periodicity of the grating spacing which was of the order of several microns [172]. It did so by exploiting the hydrodynamic forces that act on the free end of the fork; we have examined similar hydrodynamic considerations in Chapter 3. The contact resonance of a tuning fork, with similar dimensions to that described above, was again used in 2017 to measure the oscillations of helium that caused crystallisation waves at the solid-liquid interface [173]. The advances in both contact resonance methods and metrology during the intervening time is demonstrated by the increased resolution of the measurements in [173] in comparison to [172]; the oscillation amplitudes in the later work were measured to be as small as 1 Å.

The utilisation of a scanning probe to measure surface properties acoustically has led to the combination of acoustic measurements with atomic force microscopy. These techniques, which are collectively referred to as contact resonance AFM, have found applications in both biological and material sciences,see for example [65, 164, 174]. The basic principle of contact resonance AFM has remained unchanged across these techniques: an acoustic wave is sent through either sample or probe and the change in the response of the probe is measured. The response of the AFM probe is a result of the combination of forcing, its intrinsic dynamics, and the coupled tip-sample interaction. Ultrasonic Force Microscopy (UFM) is one such method that excites the surface directly, typically at low frequencies, through a transducer fixed to the underside of the sample [175]. One of the challenges of ultrasonic actuation is separating the oscillatory behaviour caused by the sample actuation from the cantilever deflection caused by a surface artefact. This can be achieved by modulating the ultrasonic amplitude faster than the capability of the control signal but still within the detection range [176]. While this allows for simulta-

neous measurements of topography and contact resonance information, the restrictions on the ultrasonic frequency limits the range of contact resonance frequencies that can be explored [66]. Furthermore, UFM seeks to minimise damage to the tip or sample by using small contact forces that are in the order of tens of nanoNewtons. This causes the vibration of the surface to couple the viscoelastic and topographic information such that quantification of the properties becomes challenging [176].

In contrast to UFM, acoustic AFM (AFAM), originally proposed by Rabe and Arnold [177], and Ultrasonic AFM (AFM), originally proposed by Yamanaka and Nakano [178]) excite the cantilever/sample at or near to one of the cantilever's resonant frequencies. This greatly increases the sensitivity of the cantilever, as the resulting contact-resonance frequencies (the shift away from the cantilever's free resonant frequencies) are typically two to four times larger than the free resonant frequencies. The influence of exciting the sample (AFAM) or the cantilever (UAFM) has been investigated both experimentally and analytically by Rabe [66], who found that the source of excitation has no influence on the contact resonances but will alter the measured amplitudes of the coupled system [66]. Quantification of both UAFM and AFAM are possible, provided information about the cantilever is known [66, 176]. Other forms of excitation have also been investigated, such as by pulsed excitations which were found to be amenable to measurements of materials that exhibit significant adhesion [71].

Since the early conception of acoustic measurements through micro-sensors, a wide range of materials has been investigated, with Young's modulus that range over several orders of magnitude [166–169]. However, the sensitivity of the probe to the sample properties is greatly dependent on the stiffness of the respective probe and sample. For materials with elastic moduli that approach tens to hundreds of giga-Pascals, stiff probes have traditionally utilised in order to gain the appropriate sensitivity to the material properties [168, 179]. However, as we describe in Chapter 2, soft probes with low static spring constants ($k_c \sim 10^{-1}$) undergo an effective stiffening at high frequencies. Hence, the higher modes are expected to increase the sensitivity for soft cantilevers to stiff samples. This is beneficial for several reasons. First, the increased sensitivity of the probe increases the scope of materials that can be investigated [101]. Furthermore, soft cantilevers are more responsive to sample topography, such that multi-channel information is possible [6]. Finally, utilisation of soft cantilevers minimises damage to the sample under investigation, a significant aim for material testing techniques [90].

4.3.2 *Non-destructive Measurements*

The ability to measure the material properties of a sample to nano-metre resolution is highly sought after [180, 181]. One of the most popular methods for doing so is a family of techniques known collectively as nano-indentation [182]. Nano-indentation works by pressing a tip, generally made from diamond or sapphire, into the sample surface and measuring the resulting deformation. However, despite the prefix of nano-, this method does not typically operate at nano-scale resolution. The tips of nanoindentation

probes are around 100 nm to 10 µm and the stiffness maps that come from repeated nano-indentation measurements are typically tens to hundreds of micrometers apart, giving a resolution that is of the order of microns [87]. Another limitation of nano-indentation is that it cannot be repeated on a sample. Each measurement requires permanent deformation of the sample surface, causing irreversible damage. It currently forms the gold standard for the stiffness mapping on stiff materials (see, for example, [89, 183]), though the limitations of this method to material characterisation are severe. On the other hand, contact-resonance techniques are non-destructive, owing to the low normal forces imparted by the cantilevers. CR-AFM techniques have been compared to nanoindentation methods, and found to perform as well as, or better than, nanoindentation as a quantification tool with the added benefit of being entirely non-destructive [184]. Yet, CR-AFM techniques have not yet gained the same traction in material testing as nanoindentation[2]. We posit that this is partly due to the difficulties in quantifying CR-AFM measurements, as we discuss in Chapter 5, lending motivation to this work.

An advantage in the use of CR-AFM is that not only the fundamental frequency, but also higher frequencies and modes, can be used [177, 178]. In the case of quantitative elastic modulus measurements, the resonant frequency is matched to the stiffness of the sample [71]. The use of higher modes is particularly important as it allows for the utilisation of cantilevers with a low spring constant, protecting both sample and tip from damage, as well as giving a substantial decrease in the stress field when compared with nanoindentation [90] (see Chapter 1 for additional discussions on nanoindentation and Chapter 5 for a discussion of the contact area of contact-resonance measurements). While "stiff" cantilevers may lead to large forces and a stress field that covers not just the test sample area but also the material substrate and neighbouring materials, this is less of a problem for "soft" cantilevers due to the drop in force [71, 88]. Operating at the higher modes of a cantilever may lead to much more localised quantification of the residual stresses for stiff materials, though this has yet to be shown conclusively (we return to this question in Chapter 6). It is through exploiting the higher modes of the sensor that we can resolve some of the issues encountered by nanoindentation.

The importance of higher modes for contact resonance has been known since the conception of contact resonance techniques [185]. Subsequent research has highlighted the benefits of using the higher resonant frequencies, which substantially increase contrast on stiff materials, and which have increased sensitivity to surfaces with high stiffnesses [71, 164, 186]. Methods that use the higher harmonics of a cantilever have led to measurements of the elastic properties of a host of materials such as polymers, biological objects, and cellulose materials [162–164]. However, there have been relatively few attempts to use the higher modes of an AFM probe to measure stiff materials, such as steels. This is pertinant as many industries must go through costly and time-consuming testing proceedures in order to maintain quality and control of relevant system components. For example, steel that is present in nuclear reactor boilers will undergo signicant loads

2 Here, we compare to the nanoindentation paper in Ref. [182], which, at the time of writing, has been cited circa fourteen thousand times. Meanwhile, the highest cited CR-AFM paper that we are aware of [68] has circa seven hundred citations at the time of writing.

through their lifetime and it is extremely important that they are not allowed to reach failure. A means to non-destructively assess the steel components in a fast and reliable manner is highly sought after, further motivating our investigation into the effectiveness of using the higher modes of an AFM to quantify elastic properties.

4.4 METHODS

Here, we seek a means to connect the shift in resonant frequency of an oscillating cantilever (such as an AFM probe) to the material properties of a sample. Specifically, we are interested in developing the means to measure the material properties of stiff samples (such as metals) in a non-destructive manner and with nanometre resolution. We proceed as follows: First, we outline the theory that relates the shift in resonant frequency of a probe to a specific contact event (which we assume encodes information about the sample). Then, we introduce the necessary extensions required to include 'stiff' contact events, those events that occur between soft probes and samples that have elastic moduli that are above or near the 100's of GPa range. Finally, we highlight the sensitivity of various parameters and introduce a new means for parameter calculation which provides modal consistency of a contact stiffness across multiple oscillatory modes (as we show in Section 4.5).

4.4.1 *Relating a Shift in Frequency to Contact Stiffness*

We are interested in how to relate a shift in the resonant frequency of a cantilever oscillating while coupled to a sample. As we have discussed, we are primarily interested in the dynamics of a soft cantilever when it is in contact with a stiff material, a material that is many orders of magnitude stiffer than the static spring constant of the beam. Here, we describe the necessary steps needed to modify the Euler-Bernoulli model of the beam, as introduced in Chapter 2, to account for the surface.

We begin by outlining the general principle of converting shifts in frequency to a contact stiffness. First, we discuss why a shift in frequency occurs. We note that an oscillating cantilevered beam is well described by the Euler-Bernoulli beam equation for the deflection of a one dimensional flexural beam[124],

$$\frac{\partial^4 w(x^*,t)}{\partial x^{*4}} + \frac{\mu}{EI}\frac{\partial^2 w(x^*,t)}{\partial t^2} = 0, \tag{4.2}$$

where $w(x,t)$ is the displacement of the cantilever in the x-direction at time t, μ is the mass per unit length and EI is the flexural rigidity of the beam. In order to simplify calculations, we nondimensionalise the spatial variables by rescaling by the total length of the cantilever, L^*, such that $x^* = xL^*$, where asterix denotes the dimensional quantities. When seeking solutions for (4.2), we assume that they will be in the form of a harmonic standing wave,

$$\phi_n(x) = \sum_{n=1}^{\infty} A_n e^{i(\alpha_n x - \omega_n t)}, \tag{4.3}$$

where A_n is the amplitude of oscillation, ω_n is the angular resonant frequency (or eigenfrequency) of the n^{th} mode and α_n is the n^{th} (real) eigenvalue, corresponding to the spatial wavenumber of the n^{th} eigenmode, which satisfies the dispersion relation for the beam,

$$\alpha_n^4 = \frac{\mu}{EI}(2\pi f_n)^2, \tag{4.4}$$

where $f_n = \omega_n/2\pi$ is the resonant frequency of the n^{th} eigenmode. After separation of variables, the spatial solution to (4.2) will be of the form

$$w(x) = C_1 \sinh(\alpha_n x) + C_2 \cosh(\alpha_n x) + C_3 \sin(\alpha_n x) + C_4 \cos(\alpha_n x) \tag{4.5}$$

where C_i for $i = 1$ to 4, are constants found from the boundary conditions of the system. The dispersion relation, (4.4), shows that any ratio of two resonant frequencies does not explicitly depend on the physical properties of the oscillating beam, but only on the boundary conditions, since

$$\Delta f_n = \frac{f_{n,\text{contact}}}{f_{1,\text{free}}} = \left(\frac{\alpha_{n,\text{contact}}}{\alpha_{n,\text{free}}}\right)^2 = (\Delta\alpha_n)^2, \tag{4.6}$$

where we have chosen the ratio of the n^{th} resonant frequency in contact with a sample, $f_{n,\text{contact}}$, with the n^{th} free resonant frequency, $f_{n,\text{free}}$. Our reason for using the n^{th} resonant frequency, rather than the first (as is commonly done in CR-AFM methods, see for example [65]) is motivated by the work in Chapter 3. In Section 3.6, we discuss how the higher modes are less effected by considerations of the hydrodynamics of the system. Hence, utilisation of higher mode is expected to give 'truer' measurements of the sample material properties. Furthermore, we utilise the resonant frequencies *in vacuo*, found using our calibration method described in Chapter 2 to further remove the influence of hydrodynamics on the cantilever. All reference to free resonant frequencies will refer to the in vacuo calculated frequencies henceforth.

The coupling of the cantilever tip to the surface can be modelled through a suitable change in boundary conditions which, when combined with (4.2), leads to the characteristic equation of the system. This is then solved to find the wavenumbers, α_n, for a given contact stiffness. The squared ratio of the contact wavenumber to the n^{th} free wavenumber will be equivalent to the corresponding shift in frequency from the contact resonant frequency to the free resonance, provided that (4.2) continues to model the beam such that the dispersion relation, (4.4), remains unchanged [66]. Under these conditions, any shift in frequency can be related back to a contact wavenumber for a given contact stiffness introduced at the boundary (the AFM tip). We discuss these boundary changes in the subsequent sections.

4.4.2 *Parallel Cantilever*

Having described how the shift in resonant frequency will relate to a contact stiffness at the boundary, we describe how boundary conditions of the beam are adapted to include

the contact stiffness. For the simplest case, we follow [66, 177] and assume that the beam is oscillating strictly parallel to the surface and that the tip, the contact point, is located exactly at the free end of the cantilever, as shown in Figure 4.1.

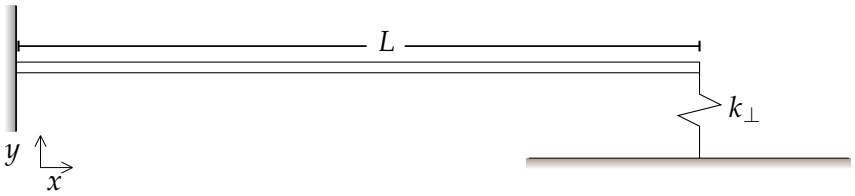

Figure 4.1: The model of an Euler-Bernoulli beam, (4.2), in parallel contact with the surface. The interaction that results from the contact between the sensor tip and surface is idealised by a spring which represents the contact stiffness, $k_\perp$.

We assume the same clamped boundary conditions at the fixed end, $x = 0$, of the cantilever as in Chapter 2,

$$w(0) = 0, \tag{4.7}$$
$$w_x(0) = 0, \tag{4.8}$$

At the end in contact with the surface, $x = L$, there is a single boundary condition that needs to be adjusted from that in Chapter 2; the shear force due to contact. This additional force is included in the third spatial derivative of the beam displacement at the free end, where contact force is introduced as a linear spring fixed normal to the surface. The contact force, described in more detail in Section 5.2 in Chapter 5, contains the normal load applied to the cantilever. The introduction of the linear spring leads to a change in the boundary conditions at the free end, $x = L$,

$$w_{xx}(L) = 0, \tag{4.9}$$
$$w_{xxx}(L) = -\left(k_\perp EI\right) w(L),. \tag{4.10}$$

Though we have introduced a means to calculate the flexural rigidity, EI, of a cantilever in Chapter 2, we note that a simplification can be made by relating the shear force to the static spring constant, defined in (2.4) and repeated here,

$$k_c = \frac{3EI}{L^3}. \tag{4.11}$$

Using (4.11), we rewrite the boundary conditions in (4.9 – 4.10) in terms of only the length of the beam, the static spring constant of the cantilever, and the normal contact spring,

$$w_{xx}(L) = 0, \tag{4.12}$$
$$w_{xxx}(L) = -\left(\frac{3k_\perp}{k_c L^3}\right) w(L), \tag{4.13}$$

Solving the spatial equation, (4.5) with boundary conditions, (4.9 – 4.10) gives the characteristic equation,

$$\left(\frac{3k_\perp}{k_c}\right)\left(\cos(\alpha_{n,\text{contact}})\sinh(\alpha_{n,\text{contact}}) - \cosh(\alpha_{n,\text{contact}})\sin(\alpha_{n,\text{contact}})\right) = \tag{4.14}$$

$$(\alpha_{n,\text{contact}})^3\left(\cos(\alpha_{n,\text{contact}})\cosh(\alpha_{n,\text{contact}}) + 1\right) \tag{4.15}$$

We can now examine how the stiffness of the contact spring will influence the resonant behaviour of the cantilever. In order to find the contact stiffness, we use the measured shift in frequency, Δf_R, to find the contact wavenumber,

$$\alpha_{n,\text{contact}} = \alpha_{n,\text{free}}\sqrt{\Delta f_n}. \tag{4.16}$$

If the spring is sufficiently weak to be considered negligible, $k_\perp \ll 1$, we return to the characteristic equation for the clamped-free beam [187],

$$\cos(\alpha_{n,\text{free}})\cosh(\alpha_{n,\text{free}}) + 1 = 0. \tag{4.17}$$

In this case, there will be no change to the resonant frequency of the beam, which is a product of the wavenumber and the material properties of the beam.

On the other hand, if the contact stiffness, represented by the linear spring, increases to that of an infinitely stiff spring then the boundary condition becomes pinned. The wavenumber will then shift to that of a clamped-pinned beam with the corresponding characteristic equation,

$$\tan(\alpha_{n,\text{pinned}}) - \tanh(\alpha_{n,\text{pinned}}) = 0. \tag{4.18}$$

More generally, a measured change in resonant frequency Δf_n gives a contact stiffness $k_\perp$, by (4.14 – 4.16). The shift in resonant frequency, found by dividing a resonant frequency when in contact by that of the free resonance, does not require direct knowledge of the cantilever's material properties, as shown in (4.6). In this way, the contact stiffness can be related directly to the change in resonant frequency due to the coupling of the tip with the sample.

It is important to consider how the wavenumber of the system varies for contact stiffnesses that fall between the limiting cases of a negligible and infinitely stiff spring. In Figure 4.2 we show how the contact stiffness varies for the first four modes of a beam, for $L = 1$, and over the range of $k_\perp/k_c = 10^0 - -10^6$. It is clear that there is a shift in wavenumber from low (the clamped-free case) to high (the clamped-pinned case) contact stiffness. However, this shift is not identical for each eigenmode of the beam. At each mode of the beam, there is an effective stiffening caused by the change in stiffness at the free end. This effective stiffness will reach a maximum such that a resonant frequency will only be able to shift to a maximum stiffness, that of a pinned constraint. The pinned constraint will reduce the amplitude of oscillation at the location of the spring. The wavenumber of the n^{th} mode of a pinned beam can be understood

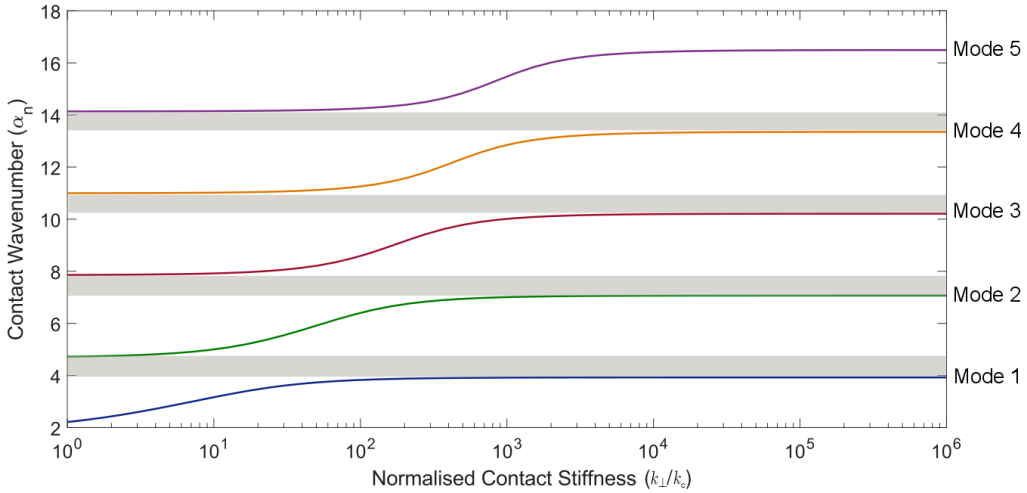

Figure 4.2: The mode-stiffness curves for increasing higher eigenmodes of the sensor. Each contact wavenumber, α_n, can be related back to a shift in frequency according to (4.6). This wavenumber relates to the normalised contact stiffness, $k_\perp/k_c$, used to model the tip-sample interaction. We note that some wavenumbers cannot be related to a contact stiffness with this model, shown as grey bands.

as creating an anti-resonance in the frequency response of the beam, a minimum in the amplitude at a frequency higher than the resonant frequency of that mode [188].

The anti-resonance of the n^{th} mode of a beam will always occur at a lower frequency than the free resonance of the $(n+1)^{\text{st}}$ mode. Higher modes will be more susceptible to larger changes in contact stiffness (as the effective stiffening of the beam increases with resonant frequency, as shown in Chapter 2) but there will be a plateau for each mode where the vibrational behaviour of the beam becomes insensitive to changes in stiffness. In the theoretical case of a beam oscillating parallel to a surface, a plateau represents an anti-resonance and a maximum shift in the resonant frequency of the beam. For the parallel case, there will be a gap between modes for which no shift in frequency is possible, shown in Figure 4.2 as grey bands between the modal stiffness curves. This gap is a result of the cantilever's motion being restricted to the x direction only.

Thus far, we have described how to relate a shift in the n^{th} resonant frequency of a parallel beam in contact with a surface to the n^{th} free resonant frequency of the beam, $\Delta f_n = f_{n,\text{contact}}/f_{n,\text{free}}$, to that of a normalised contact stiffness, $k_\perp/k_c$, by means of the contact wavenumber of the beam, $\alpha_{n,\text{contact}}$. However, we have also shown that, using this model, certain contact wavenumbers cannot be related to a normalised contact stiffness, shown as grey bands in Figure 4.2. This is not an issue if the effective stiffness of the probe is of similar magnitude to that of the sample ($k_\perp \approx k_n$), as we show in Chapter 5, but will lead to a restriction in the sensitivity of the probe for anything higher than the first few modes, shown as flat regions in Figure 4.2. Here, we are primarily concerned with measurements on stiff samples such that $k_\perp/k_c \approx 10^3$, which would require cantilevers with a high static stiffness if we were to restrict ourselves to the first mode. Instead, we utilise the sensitivity of higher modes by using soft cantilevers, $k_c \sim 2 \times 10^{-2}\,\text{N}\,\text{m}^{-1}$. This is expected to cause lower modes, such as the first and second,

to become insensitive to contact stiffnesses, as they are limited to their upper plateau in sensitivity. We demonstrate in Chapter 5 that the shift in contact stiffness actually results in contact wavenumbers that are inside the grey bands shown in Figure 4.2, such that certain shifts in resonant frequency, and hence, contact wavenumbers, cannot be related to a contact stiffness using this model. In order to include contact wavenumbers that occur beyond the plateau of lower modes, we must extend the model of the parallel beam to account for a tilt, Section 4.4.3, and an offset, Section 4.4.4.

4.4.3 *Tilted Cantilever*

We have shown that through the introduction of a normal spring modelling the tip-sample interaction, the clamped-free beam will eventually result in a clamped-pinned beam as the normal spring becomes infinitely stiff. However, the beam may also be restrained due to lateral contact forces, parallel to the surface, and modelled by a second lateral spring which is again implemented through the boundary conditions, described below. This spring induces a rotational inertia to the system. As the surface becomes infinitely stiff, without the presence of a normal spring, the system is described by a clamped-hinged constraint. If both lateral and normal spring are infinitely stiff, the system is restricted into a clamped-clamped state. The system has previously been investigated previously; see, for example [66, 189].

In order to incorporate this additional spring, we need only adapt the boundary conditions of the cantilever. The introduction of a lateral contact stiffness is a direct result of AFM probes being tilted towards the surface, as shown in Figure 4.3. This tilt introduces an additional shear force and rotary inertia that must be accounted for as well as the height of the tip, h^*, which now acts as a moment arm. The adapted model can either ignore or include changes to the tip offset (how far the tip is from the free end of the sensor) with only minor changes to the boundary conditions. We scale the tip height by the total length of the cantilever, $h^* = hL^*$. To begin with, we neglect considerations of the tip position.

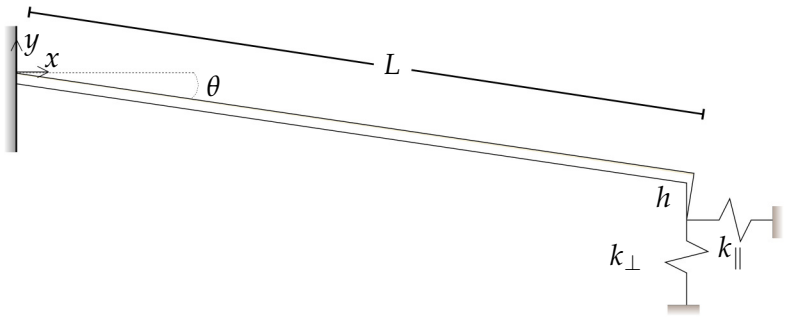

Figure 4.3: An extension to Figure 4.1, where the Euler-Bernoulli beam is now tilted with respect to the surface by an angle, θ. This tilt introduces two further parameters into the system, the tip height, h, and a lateral spring representing the lateral contact stiffness, $k_{\parallel}$, of the sensor-sample system.

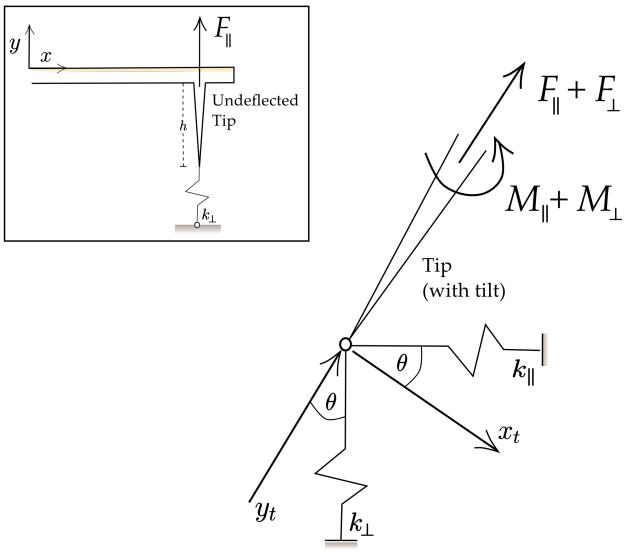

Figure 4.4: The tip, with height h, makes contact with the surface. The interaction of the tip with the surface causes a corresponding tip displacement, x_t and y_t. This displacement couples with the lateral and normal contact stiffnesses, $k_\parallel$ and $k_\perp$, represented as springs, resulting in additional moment and forces, (4.20).

The tilt of the cantilever introduces additional moment and forces at the tip. As noted by Dupas [190], the motion of the beam will cause a tip displacement, (x_t, y_t), in both x and y directions, given by

$$\begin{aligned} x_t &= hw'(x), \\ y_t &= w(x). \end{aligned} \tag{4.19}$$

The additional forces, $F_\parallel$ and $F_\perp$, and moments, $M_\parallel$ and $M_\perp$ at the tip due to lateral and normal contact stiffness springs are shown in Figure 4.4.

$$\begin{aligned} F_\parallel &= (k_\parallel EI)\,(x_t\cos(\theta) + y_t\sin(\theta))\sin(\theta) \approx (k_\parallel EI)x_t\sin(\theta) \text{ to leading order,} \\ F_\perp &= (k_\perp EI)\,(-x_t\sin(\theta) + y_t\cos(\theta))\cos(\theta) \approx (k_\perp EI)y_t \text{ to leading order,} \\ M_\parallel &= (hk_\parallel EI)\,(x_t\cos(\theta) + y_t\sin(\theta))\cos(\theta) \approx (hk_\parallel EI)x_t \text{ to leading order,} \\ M_\perp &= (hk_\perp EI)\,(x_t\sin(\theta) - y_t\cos(\theta))\sin(\theta) \approx -(hk_\perp EI)y_t\sin(\theta) \text{ to leading order.} \end{aligned} \tag{4.20}$$

The influences of these forces modify the boundary conditions at the non-clamped end of the cantilever, $x = L$. We replace EI with the known properties of the cantilever spring constant, k_c, and length, L, using (2.4). The rotary intertia becomes

$$\begin{aligned} w_{xx}(L) &= M_\parallel x + M_\perp, \\ &= \frac{3}{k_c L^3}\left[hx_t(k_\parallel\cos^2(\theta) + k_\perp\sin^2(\theta)) + hy_t\sin(\theta)\cos(\theta)(k_\parallel - k_\perp)\right] \\ &= w_x(L)Q(k_\perp, k_\parallel) + w(L)S(k_\perp, k_\parallel) \end{aligned} \tag{4.21}$$

while the shear force is

$$\begin{aligned} w_{xxx}(L) &= F_{\parallel} + F_{\perp}, \\ &= \frac{3}{k_c L^3}\left[x_t \sin(\theta)\cos(\theta)(k_{\parallel} - k_{\perp}) + y_t(k_{\parallel}\sin^2(\theta) + k_{\perp}\cos^2(\theta))\right], \\ &= w(L)S(k_{\perp}, k_{\parallel}) + w(L)T(k_{\perp}, k_{\parallel}), \end{aligned} \tag{4.22}$$

where Q, S, and T are defined to be

$$\begin{aligned} Q(k_{\perp}, k_{\parallel}) &= \frac{3h^2}{k_c L^3}\left(k_{\parallel}\cos^2(\theta) + k_{\perp}\sin^2(\theta)\right), \\ S(k_{\perp}, k_{\parallel}) &= \frac{3h}{k_c L^3}\left(\sin(\theta)\cos(\theta)(k_{\parallel} - k_{\perp})\right), \\ T(k_{\perp}, k_{\parallel}) &= \frac{3}{k_c L^3} k_{\parallel}\sin^2(\theta) + k_{\perp}\cos^2(\theta). \end{aligned} \tag{4.23}$$

The two boundary conditions, (4.21 – 4.22), show that, through the introduction of a tilt to our model of the cantilever, we must also account for the height of the tip, h. When no tilt is present, $\theta = 0$, we return to the boundary conditions for the parallel case, as given by (4.9 – 4.10).

By including consideration of the second tangential spring, we are immediately able to account for the increased sensitivity of each mode. Figure 4.5 shows how the wavenumber changes as we vary both normal and tangential spring stiffnesses. We see the existence of four plateaus. When both (normalised) stiffnesses are neglible ($k_{\perp}/k_c, k_{\parallel}/k_c \ll 1$) there is no influence of the surface on the beam and the free condition is returned at the tip. For large normal stiffness and neglible lateral stiffness ($k_{\perp}/k_c \gg 1, k_{\parallel}/k_c \ll 1$) we return the pinned condition at the tip, where the shear force is large but there is no rotary inertia. Similarly, for large lateral stiffness and neglible normal stiffness ($k_{\parallel}/k_c \gg 1, k_{\perp}/k_c \ll 1$), there is large rotary inertia but no shear force such that the beam becomes hinged at the tip. Finally, when both normal and lateral stiffnesses are large ($k_{\parallel}/k_c \gg 1, k_{\perp}/k_c \gg 1$) the rotary inertia and shear force are large enough such that no motion is possible and the beam becomes clamped at the tip.

For an oscillatory mode that is forced to a pinned boundary state by the stiffness of the contact spring, there is an additional shift in the wavenumber (and resonant frequency) due to the tangential spring. However, this shift will not surpass the free resonance of the subsequent mode, as discussed in Section 4.5. This is because of the same restriction of the anti-resonance applies, as described in Section 4.4.2. A shift in resonant frequency into the $(n+1)^{\text{st}}$ region will only occur if there exists additional modal influence on the displacement of the beam. This is caused by the tip being offset from the free end of the cantilever, as happens for many conventional AFM probes due to the manufacturing process (see, for example, Figure 2.11). We discuss a cantilever with an offset tip in Section 4.4.4.

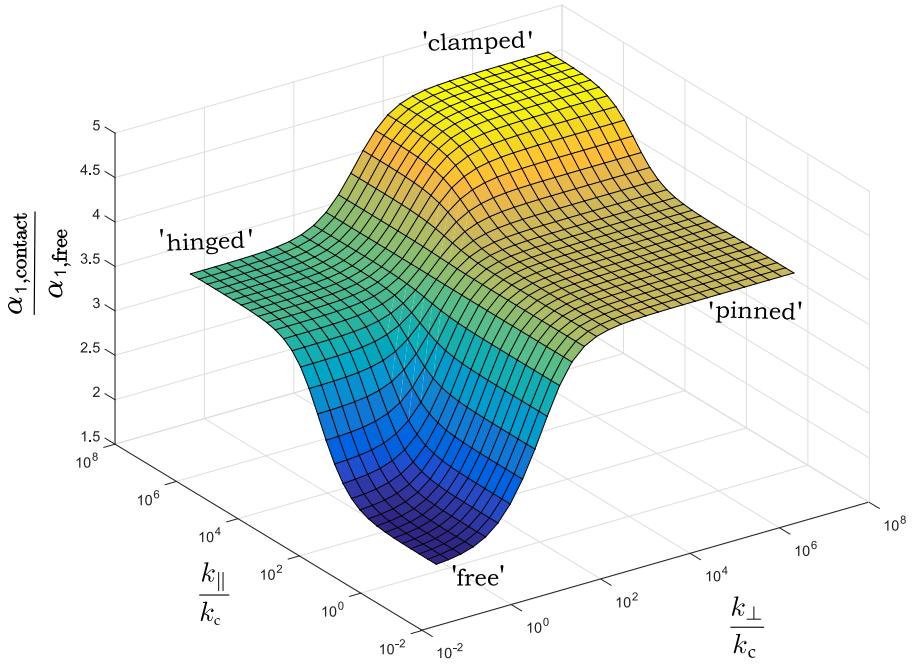

Figure 4.5: The normal and lateral stiffness space for a shift in frequency at the first mode. The four plateaus correspond to the small and large limits of the normalised contact stiffness that act in the normal, $k_{\perp}$, and lateral, $k_{\|}$, directions to the sample. These limits result in the characteristic equation (and resulting wavenumbers) being well described by specific boundary constraints: free, pinned, hinged and clamped.

4.4.4 *Cantilever with Offset Tip*

The majority of AFM probes have their tip set some distance away from the free end of the cantilever. This can be modelled by separating the cantilever into two distinct beams which are joined at the tip, as shown in Figure 4.6. We will assume that both of these beams sections have equal material properties other than their length. Each respective beam section can be thought of as having modal contributions[3] which influence the total modal response of the offset cantilever, as we discuss in Section 4.5. These modal contributions will further influence how contact wavenumbers are related to contact stiffnesses. We describe how to account for the tip offset below.

In order to model a cantilever with an offset tip, we follow [66, 190] and use two co-ordinate systems which relate to the two sections of the beam, one either side of the tip, fixed with respect to one another. The first section of the cantilever runs from the clamp to the tip, and has clamped-joined (clamp-tip) boundary conditions, while the second section has joined-free (tip-free end) boundary conditions. Additional boundary conditions are imposed at the tip, where the beams meet, which incorporate how normal and lateral contact stiffnesses influence the total two-beam system. We note that the resulting characteristic equation of the full model with tilt and offset was previously described in [190], and only summarise the calculations here with additional details.

3 The additional contributions from the offset tip influences the modal behaviour of the beam through the second and third derivative at the tip. Hence, for a tip with neglible mass on a cantilever oscillating free from a surface (as described in Chapter 2) the tip offset does not need to be accounted for.

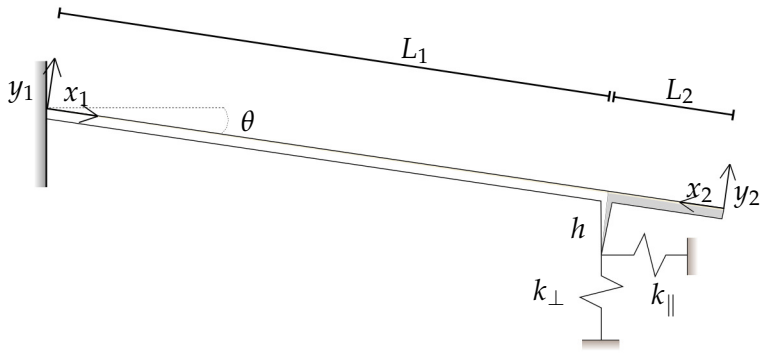

Figure 4.6: A further extension of Figure 4.1 and Figure 4.3, where the tip is now offset a distance L_2 away from the free end of the tilted beam in contact with a surface. This is required to relate a shift in resonant frequency, (4.6), to a normalised contact stiffness, $k_\perp/k_c$. This extension is modelled by separating the beam into two distinct sections, represented by the change in shading.

To account for the tip off-set, we introduce a second co-ordinate system such that spatial variables are now described by x_1^* and x_2^*. Both coordinate systems have their end at the tip off-set position, $x_1^* = L_1^*$ and $x_2^* = L_2^*$, and start from the respective ends of the total beam length; one at the clamped end, $x_1^* = 0$, and one at the free end, $x_2^* = 0$. For simplicity, we again non-dimensionalise both spatial variables, such that $x_1 = x_1^*/L_1^*$ and $x_2 = x_2^*/L_2^*$ These two coordinate systems means that each beam has a section-specific displacement function, $w_1(x_1)$ and $w_2(x_2)$. The two beam equations requires a total of eight boundary conditions: two for the clamped end, two for the free end and four transition conditions where the two beams meet. The first four are unchanged from Section 4.4.2, other than the introduction of a second coordinate system,

$$w_1(0) = 0, \qquad w_2''(0) = 0 \tag{4.24}$$
$$w_1'(0) = 0, \qquad w_2'''(0) = 0 \tag{4.25}$$

With the introduction of an additional coordinate system, we now seek the equation describing the spatial deflection of two beams, $i = 1, 2$, in the following form,

$$w_i(x) = A_{1,i}\sinh(\alpha_n x) + A_{2,i}\cosh(\alpha_n x) + A_{3,i}\sin(\alpha_n x) + A_{4,i}\cos(\alpha_n x), \tag{4.26}$$

with constants $A_{k,i}$, for $k = 1, ..., 4$. Note that α_n will still reflect the n wavenumbers of the total two-beam system owing to the joined boundary conditions introduced below. The boundary conditions, (4.24) simplify these equations to,

$$w_1(x) = A_{1,1}\left(\cosh(\alpha_n x) - \cosh(\alpha_n x)\right) + A_{2,1}\left(\sinh(\alpha_n x) - \sin(\alpha_n x)\right) \tag{4.27}$$
$$w_2(x) = A_{1,2}\left(\cosh(\alpha_n x) + \cosh(\alpha_n x)\right) + A_{2,2}\left(\sinh(\alpha_n x) + \sin(\alpha_n x)\right). \tag{4.28}$$

We now seek the remaining four transition boundary conditions that connect the two beams. First, there is continuity of displacement and slope at the tip,

$$w_1(L_1) = w_2(L_2), \tag{4.29}$$
$$-w_1'(L_1) = w_2'(L_2). \tag{4.30}$$

where the change in sign in (4.30) represents the inversion of direction in the coordinate system. In the absence of a tip, there would also be continuity of rotary inertia and shear force,

$$w_1''(L_1) = w_2''(L_2), \tag{4.31}$$
$$w_1'''(L_1) = -w_2'''(L_2). \tag{4.32}$$

In order to account for the tip forces and the tilt of the cantilever, we apply (4.21 – 4.22) together with the continuity conditions (4.29) to get [66]

$$[w'']_{\text{tip}} = w_1''(L_1) - w_2''(L_2) = -(Qw_1'(L_1) + Sw_1(L_1)), \tag{4.33}$$
$$[w''']_{\text{tip}} = w_1'''(L_1) + w_2'''(L_2) = Sw_1'(L_1) + Tw_1(L_1). \tag{4.34}$$

The boundary conditions (4.29 – 4.30) and (4.33 – 4.34) fully defines the AFM probe model including both tilt and offset. For the case where $\theta = 0, L_2 = 0$, we return to the case of the parallel beam with boundary conditions given in (4.9 – 4.10). Alternatively, for the case where $\theta = 0, L_2 = 0$, we return to the tilted case with no offset, with boundary conditions given in (4.21 – 4.22). The characteristic equation of the system then gives a means to connect a shift in frequency to a contact stiffness, through (4.6), which we calculate in Section 4.4.5.

4.4.5 *Characteristic Equation*

The characteristic equation of the tilted two-beam system is found by applying the boundary conditions (4.29 – 4.30) and (4.33 – 4.34) to (4.26). This results in the linear equation,

$$\mathbf{Ma} = \mathbf{0}. \tag{4.35}$$

where $\mathbf{a} = A_{1,1}, A_{2,1}, A_{1,2}, A_{2,2}$ are the constants to be found and $\mathbf{M}$ is the matrix encoding the boundary conditions of the system, namely

$$\mathbf{M} = \begin{bmatrix} ch_1^- & sh_1^- & -ch_2^+ & -sh_2^+ \\ \alpha_n sh_1^+ & \alpha_n ch_1^- & \alpha_n sh_2^- & \alpha_n ch_2^+ \\ d_1 & d_2 & -\alpha_n^2 ch_2^- & -\alpha_n^2 sh_2^- \\ d_3 & d_4 & \alpha_n^3 sh_2^+ & \alpha_n^3 ch_2^- \end{bmatrix}, \tag{4.36}$$

where

$$d_1 = \alpha_n^2 ch_1^+ + \alpha_n sh_1^+ Q(k_\perp, k_\parallel) + ch_1^- S(k_\perp, k_\parallel) \tag{4.37}$$
$$d_2 = \alpha_n^2 sh_1^+ + \alpha_n ch_1^- Q(k_\perp, k_\parallel) + sh_1^- S(k_\perp, k_\parallel) \tag{4.38}$$
$$d_3 = \alpha_n^3 sh_1^- - \alpha_n sh_1^+ S(k_\perp, k_\parallel) - ch_1^- T(k_\perp, k_\parallel) \tag{4.39}$$
$$d_4 = \alpha_n^3 ch_1^+ - \alpha_n ch_1^- S((k_\perp, k_\parallel) - sh_1^- T(k_\perp, k_\parallel) \tag{4.40}$$
$$ch_i^\pm = \cosh(\alpha_n L_i) \pm \cos(\alpha_n L_i) \tag{4.41}$$
$$sh_i^\pm = \sinh(\alpha_n L_i) \pm \cos(\alpha_n L_i). \tag{4.42}$$

The characteristic equation for the system is given by $|\mathbf{M}| = 0$. After some calculation, we find that

$$K_2(\alpha_n) k_\parallel^2 + K_1(\alpha_n) k_\parallel + K_0(\alpha_n) = 0, \tag{4.43}$$

with coefficients given by

$$\begin{aligned} K_2(\alpha_n) &= (3\alpha_n h)^2 (k_\perp + 1)(k_\perp + \cos(4\theta) + 1)(C_1^+ C_1^-) \\ K_1(\alpha_n) &= 6(A_2 \alpha_n^2 + A_0) \text{ where,} \\ K_0(\alpha_n) &= -8\alpha_n^6 C_1^+, \end{aligned} \tag{4.44}$$

where

$$\begin{aligned} A_2 &= 2h^2(k_\perp \cos^2\theta + \sin^2\theta)\left[C_1^- D_2^+ + D_1^+ C_2^+\right] \\ A_0 &= -2(k_\perp \sin^2\theta + \cos^2\theta)\left[C_1^+ D_2^- + D_1^- C_2^+\right] \\ C_i^+ &= \cos(\alpha_n L_i)\cosh^2(\alpha_n L_i) + 1 \\ C_i^- &= \cos(\alpha_n L_i)\cosh^2(\alpha_n L_i) - 1 \\ D_i^+ &= \cos(\alpha_n L_i)\sinh(\alpha_n L_i) + \sin(\alpha_n L_i)\cosh(\alpha_n L_i) \\ D_i^- &= \cos(\alpha_n L_i)\sinh(\alpha_n L_i) - \sin(\alpha_n L_i)\cosh(\alpha_n L_i). \end{aligned} \tag{4.45}$$

The characterstic equation, (4.43), was previously found by Rabe [66]. We have repeated the calculations in order to confirm the validity of the equation and rewritten it as a quadratic in terms of the normal contact stiffness. Given our reformulation, the solution of (4.43), $k_\parallel$, for a known contact wavenumber, $\alpha_{n,\text{contact}}$, and lateral stiffness, $k_\perp$, is

$$k_\parallel(\alpha_{n,\text{contact}}) = \frac{-K_1(\alpha_{n,\text{contact}}) \pm \sqrt{K_1(\alpha_{n,\text{contact}})^2 - 4K_0(\alpha_{n,\text{contact}})K_2(\alpha_{n,\text{contact}})}}{2K_2(\alpha_{n,\text{contact}})}. \tag{4.46}$$

Using (4.46), we are able to quickly calculate the normal contact stiffness for a given wavenumber. The positive solutions relate to the even modes while the negative solutions relate to the odd modes.

We are now in a position to find the contact stiffness for a given shift in frequency, provided that the beam has a regular rectangular geometry and that the lateral stiffness, tilt angle, tip height and length offset are known. The tilt angle is generally known to high accuracy without the need for additional measurement. The lateral stiffness, which we discuss further in Section 4.5, is assumed to be approximately equal to the normal

stiffness. However, the tip height and length offset are often not more than a few percent of the total length of the cantilever and have previously required either additional measurements to be taken of the cantilever, by e.g. SEM imaging, or by using the manufacturer values which can have significant uncertainty attached to them. Instead, we show how these tip properties can be found simultaneously with the contact stiffness such that modal consistency is introduced.

We have describe in detail how the characteristic equation of this system is found. As we show in Section 4.6, consideration of both tilt and offset causes all contact wavenumbers (and hence, all shifts in resonant frequency) to be related to a contact stiffness making their introduction important for contact resonance applied to stiff materials with soft cantilevers. However, the combination of the tip off-set with the tilted cantilever can cause the n^{th} wavenumber of the characteristic equation to cross into the region of the $(n+1)^{\text{st}}$ mode, provided that the off-set, L_2 is large enough. This is equivalent to crossing from the free-free regime into the free-clamped region of the n^{th} mode and then into the free-free region of the $(n+1)^{\text{st}}$ mode. It also results in the range of frequency shifts to be fully explored and, crucially, introduces a second parameter (the length offset) which brings modal consistency.

4.5 PARAMETER ESTIMATION

We have discussed and highlighted some of the most significant details of modelling an oscillating AFM probe that it is in contact with a sample. We have ignored any considerations of inhomogenieties, geometry, or material changes, focussing only on the position of the tip with respect to the sample. By doing so we have introduced four additional parameters required to match a shift in frequency to a contact stiffness: the height of the tip, h, the distance of the tip from the unclamped end (the offset), L_2, the lateral spring stiffness, $k_{\parallel}$, and the tilt angle of the cantilever, θ. The tilt angle will be fixed for each AFM and is generally known to high accuracy. It rarely varies by more than a few degrees so will have a known influence on the system. Here, we take the value $\theta = 0.19\,\text{rad}$[4]. We next turn to how the remaining three parameters that influence the wavenumber-stiffness curves, examples of which are shown in Figure 4.2.

We begin by considering how the lateral stiffness of the sensor-sample system will influence mode-stiffness curves. In Chapter 5, we relate the normal to the Young's modulus of a material. The lateral stiffness is a measure of the shear modulus. Previous work by Mazeran et al. [191] has found an upper and lower bound for the ratio of lateral stiffness to normal stiffness based on the maximum and minimum ratio of Young's modulus and shear modulus of materials. This was calculated to be $k_{\parallel}/k_{\perp} \approx 0.67 - 0.95$. In Figure 4.7, we demonstrate how this influences the contact wavenumber of the system using the mode-stiffness surfaces introduced in Figure 4.5. In Figure 4.7a, we show how a contact wavenumber, $\alpha_1 = 4.2$, calculated from a shift in resonant frequency by (4.6), intercepts the wavenumber-stiffness surface and in Figure 4.7b, we show a top-down

4 This is the value specified by the Cypher AFM (Asylum Research, Santa Barbara, USA), which we use in Chapter 5 and hence, use this value when calculating the normal contact stiffness from (4.46).

view of the interception with the surface. The two straight lines show the upper and lower bounds for $k_{\parallel}/k_{\perp}$, as given in [191]. The normalised contact stiffness, will vary by as much as 5% within this region, demonstrating that this contact stiffness is only weakly influenced by choice of lateral stiffness within the quoted range. As such, we choose $k_{\parallel} = 0.8k_{\perp}$ for calculations involving a tilted cantilever, which corresponds to contact with stiff materials such as metals [191].

In Figure 4.8, we consider how the gap between the mode-stiffness curves diminishes as we include further extensions to the Euler-Bernoulli beam model, as described in Section 4.4. The parallel case, shown in Figure 4.8a, will have the largest region of contact wavenumbers which cannot be related to a normal contact stiffness. These bands are problematic in practise, as they prevent certain frequency shifts from being related to a contact stiffness (and hence, a material property) when using soft cantilevers on stiff materials, as we demonstrate in Chapter 5. When the length offset is included to the parallel beam, shown in Figure 4.8b, we see that the grey bands diminish from that the of the parallel case but are still significant. However, when the tilt of the cantilever is introduced, shown in Figure 4.8c,the gaps between mode-stiffness curves become much smaller, such that almost all contact wavenumbers relate to contact stiffnesses. Even small changes in the tip height will result in increasing the sensitivity of each mode such that it covers almost all wavenumbers. This is because the boundary condition at the free end may become quasi-clamped as both normal and lateral springs become very stiff, demonstrated in Figure 4.5. When both tilt and offset are included in the model, shown in Figure 4.8d, the contact wavenumbers of high contact stiffnesses for the n^{th} mode simultaneously relate to the contact wavenumbers for very low contact stiffnesses $(n+1)^{\text{st}}$ mode such that all contact wavenumbers will relate to a, not necessarily unique, contact stiffness.

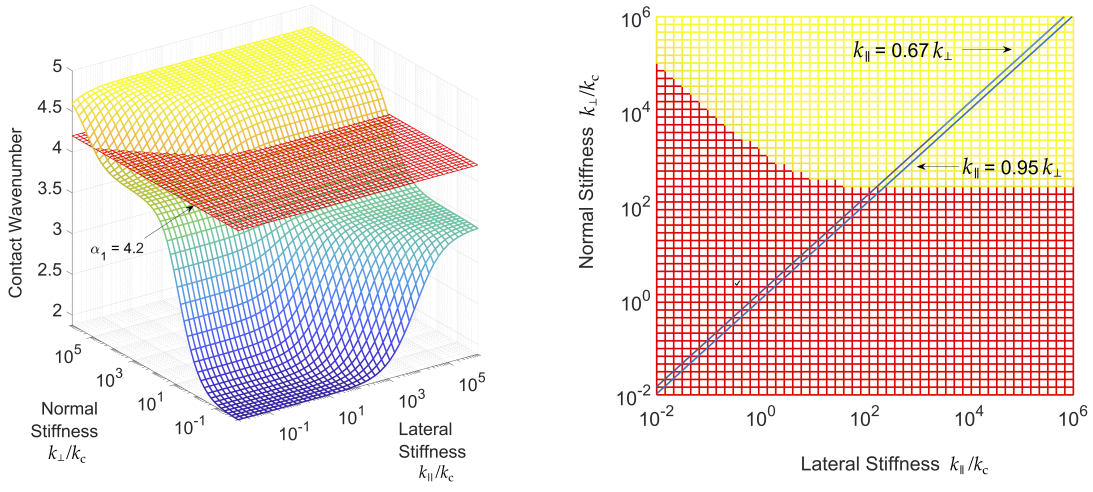

Figure 4.7: A demonstration of how a single contact wavenumber, $\alpha_1 = 4.2$, intersects one of the wavenumber-stiffness surface (a) and a top-down view that highlights the influence of the lateral stiffness on the calculated normal stiffness.

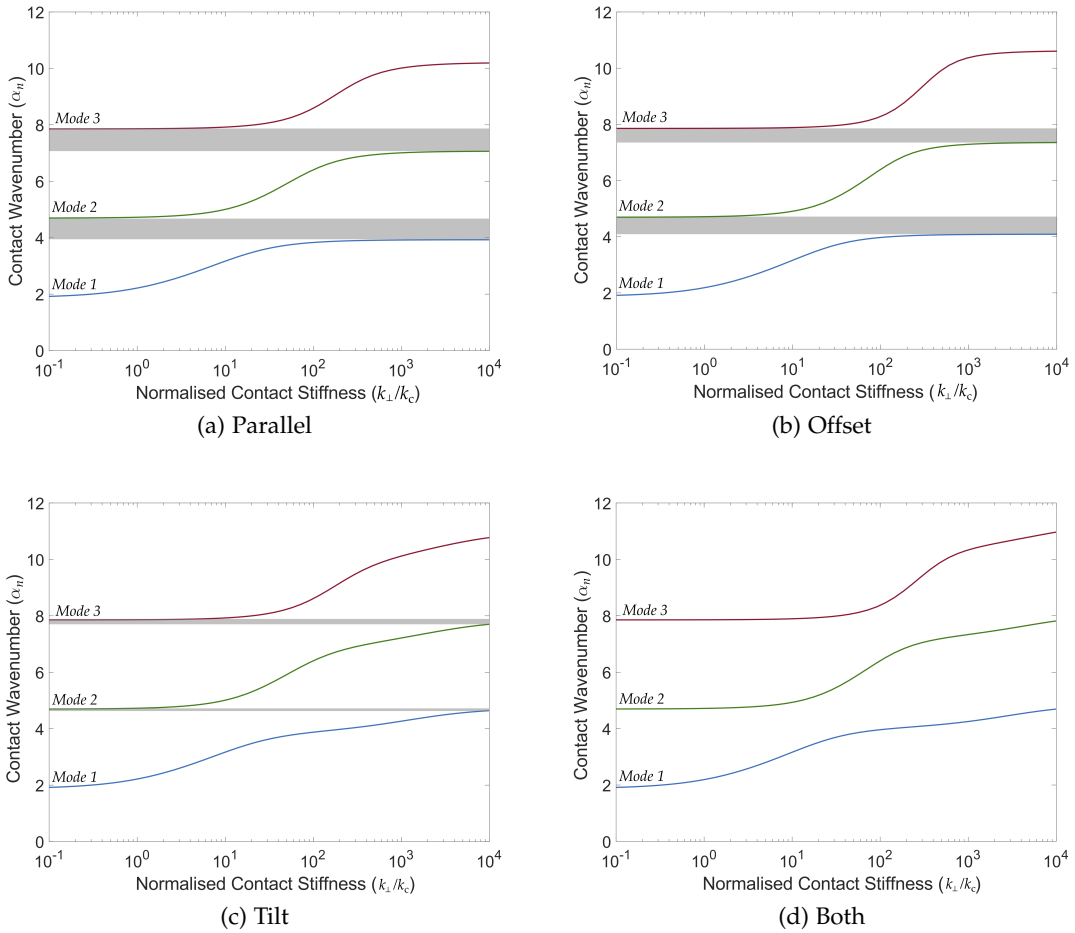

(a) Parallel (b) Offset

(c) Tilt (d) Both

Figure 4.8: We describe how the number of contact wavenumbers, α_n, (calculated from a shift in resonant frequency, Δf_n, using (4.6)) that can be related to a normalised contact stiffness, $k_\perp/k_c$, increases as we introduce both offset (b), tilt (c) and both offset and tilt (d) to the simplifed model of a parallel cantilever in contact with a surface (a). These extensions are described more fully in Section 4.4.

Figure 4.9 shows the effect of varying the tip-offset as described in Section 4.4.4. Both the typical offset and the tip height for a conventional contact mode AFM cantilever will be between 1% to 3% of the total length of the two-beam system ($L_2/L, h/L \approx$ 0.01 to 0.03, respectively). Although the change in offset does not significantly alter the calculated contact stiffness for a given contact wavenumber, it does increase the number of contact wavenumbers that are relatable to a specific stiffness (shown as a decrease in the grey bands between mode numbers in Figure 4.8). Furthermore, the increase in the range of wavenumbers that can be related to a contact stiffness also increases with mode number, demonstrated, for example, by mode 5 in Figure 4.9. However, considering only the offset still introduces a significantly limited range in wavenumbers that relate to a normalised contact stiffness. In Figure 4.10, we show how the tip height influences the cantilever. Increases in the tip height moves the second plateau such that lower normal contact stiffnesses will lead to the upper modal limit of the contact wavenumber, representing a clamped-clamped condition for that mode of the beam. As shown in Figure 4.8, this significantly increases the number of contact wavenumbers that relate to

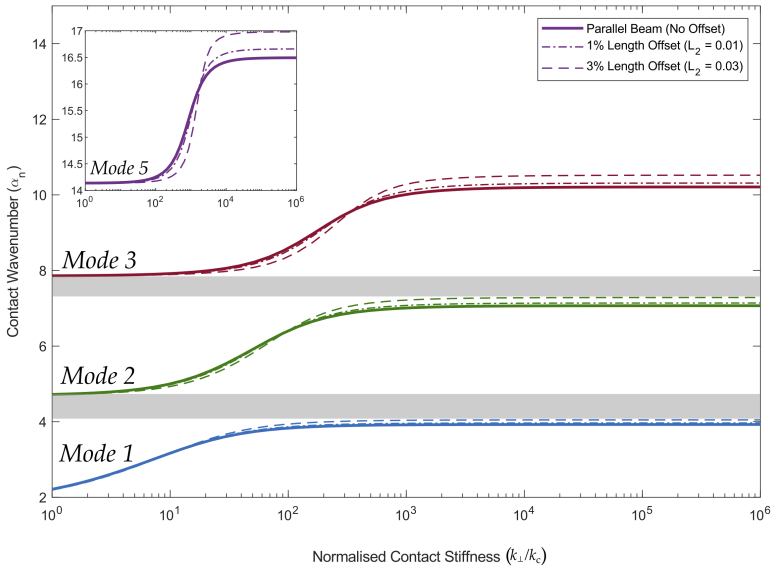

Figure 4.9: The influence of introducing a tip offset, described in Section 4.4.4. In the first panel we show the first three modes of the cantilever (blue, green, red, respectively), while we show the influence on the fifth mode (purple) in the second panel. Bands betwen modes in the first panel represent regions of contact wavenumbers that cannot be related to a normalised contact stiffness.

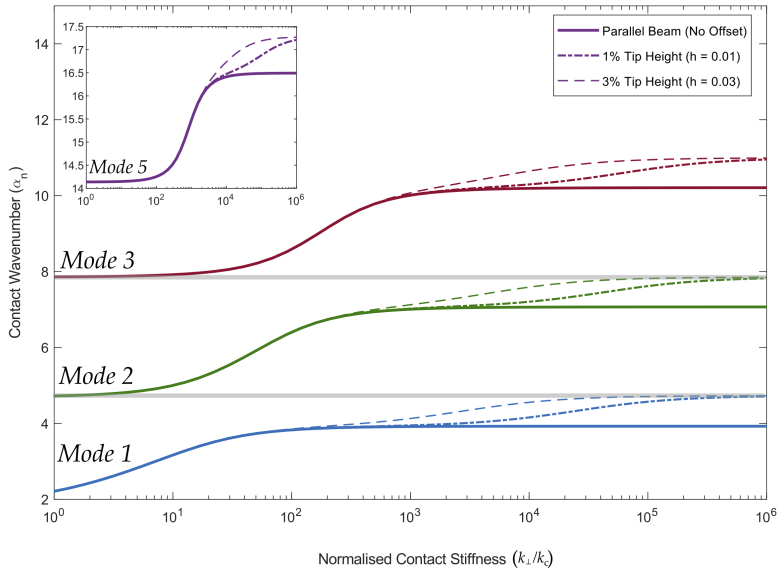

Figure 4.10: The influence of introducing a tilt to the cantilever, described in Section 4.4.3. We assume that there is no offset, a tilt angle of 0.19 rad and a lateral stiffness of $0.8k_{\perp}$. In the first panel we show the first three modes of the cantilever (blue, green, red, respectively), while we show the influence on the fifth mode (purple) in the second panel. Bands betwen modes in the first panel, representing regions of contact wavenumbers that do not relate to a normalised contact stiffness, is greatly diminished when compared with Figure 4.9.

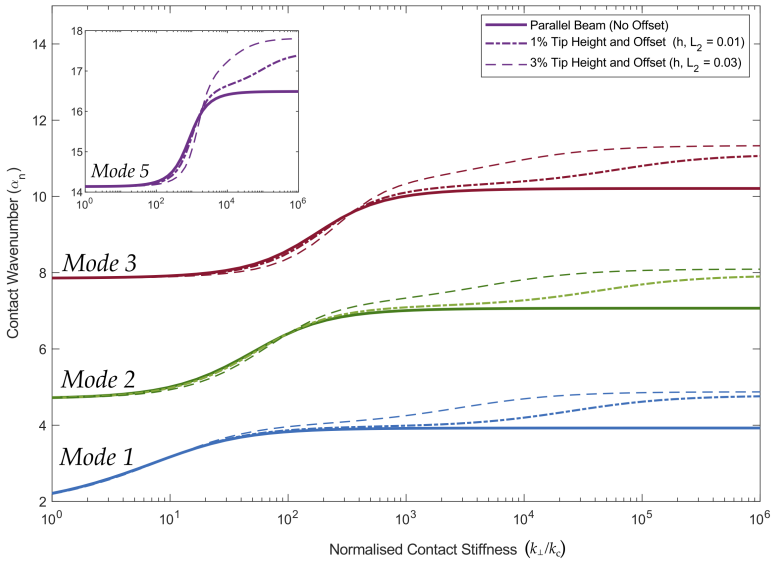

Figure 4.11: The influence of introducing a tilt and tip offset to the cantilever, described in Section 4.4.4. We assume that the both tilt and tip offset are equal, a tilt angle of 0.19 rad and a lateral stiffness of $0.8k_{\perp}$. In the first panel we show the first three modes of the cantilever (blue, green, red, respectively), while we show the influence on the fifth mode (purple) in the second panel. There are now no regions of contact wavenumbers that cannot be related to a normalised contact stiffness, however a contact stiffness is no longer uniquely related to a contact wavenumber.

a stiffness. The sensitivity of the mode-stiffness curves to the tip height is larger than that of the offset, further demonstrated by the factor of h^2 in the rotary inertia term, (4.21).

Combining both tip-offset with the tilted beam, as described in Section 4.4.4 makes further changes to the range of contact wavenumbers that can be used to recover a contact stiffness. As shown in Figure 4.11, the plateau (representing the maximum sensitivity of the n^{th} mode) moves beyond the lower region of sensitivity for the $(n+1)^{\text{st}}$ mode. This results in all contact wavenumbers being related to a normal contact stiffness. However, we no longer have uniqueness of the contact wavenumber, as some values may relate to either higher stiffnesses of the n^{th} mode or lower stiffnesses of the $(n+1)^{\text{st}}$ mode. The introduction of offset to the tilted cantilever causes the greatest change to how we relate a contact wavenumber (and, hence, a shift in frequency) to an idealised stiffness for higher modes, shown for example for mode five in Figure 4.11 (inset). We will now outline how both these parameters can be found in a self-consistent manner.

One of the advantages of including both the tip height and the tip-offset in the cantilever model is that it is possible to estimate them from their influence on experimental results, without relying on additional measurements. This has been shown previously for the tip offset in [177, 192]. However, we are unaware of any method for finding both the tip offset and height simultaneously. Previously, the tip offset was found by assuming that the contact stiffness of each mode should be equal given a value of the length offset and, hence, that the contact stiffness is modally consistent in the manner described in Section 4.4.2. Given this assumption, the characteristic equation for a cantilever that is

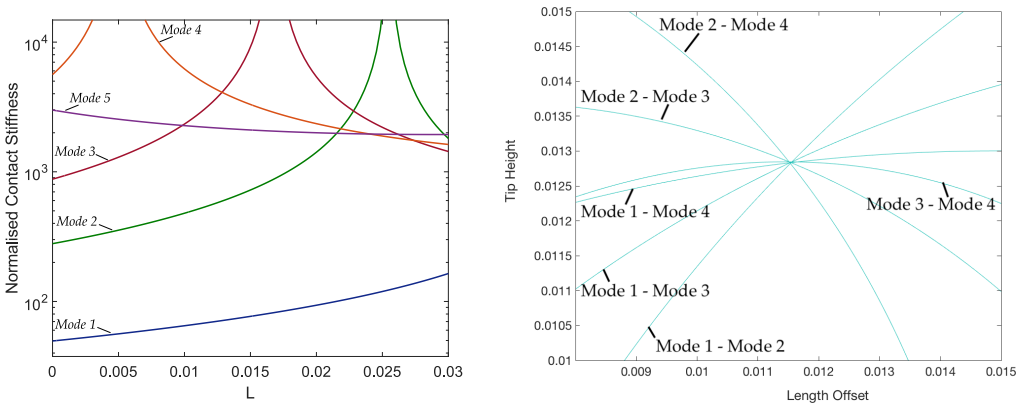

(a) Length offset using only one parameter

(b) Length offset and tip height found simultaneously

Figure 4.12: We show a comparison of the calculated contact stiffness over a range of length offsets found for modes one to five of a parallel beam. We note that there are multiple points of intersection for these contact stiffness curves. The majority of intersections occur around a length offset $L_2 = 0.012L^*$ and tip height $h = 0.013L^*$.

in contact, parallel to a surface, and with an offset tip, is solved over a range of realistic tip offsets (normalised by the total length of the cantilever) to find the contact stiffness for each mode. Plotting the contact stiffness, calculated for each possible offset, gives a set of curves for the contact stiffness of each mode. The point of intersection for all these curves is expected to uniquely identify the offset. However, we have found that does not exist a unique intersection across multiple modes in practise, as shown in Figure 4.12a.

To further restrict the characteristic equation, with the aim of reducing the number of intersection points and finding a unique contact stiffness for all modes, we repeat this method for the tilted cantilever. However, we now calculate the normal contact stiffness, (4.46), given a contact wavenumber for a realistic range of both length offsets and tip heights. By doing so, we are calculating surfaces of normalised contact stiffnesses in the parameter space of tip offset L_2 and tip height h, as shown in Figure 4.13. To find if there exists a unique point of intersection, we plot contours that show the difference between two of these surfaces equal to zero, for all pairs of modes. For example, given a measured shift in resonant frequency for the first three modes of a cantilever in contact with a sample, we calculate the difference of the contact stiffness surfaces for the first mode with that of the second and third modes equal to zero, and the differences between the second and third modes equal to zero. These contours represent points of intersection of the planes, as shown in Figure 4.13a and are expected to line up over a single point, representing the tip offset and height of the system. We show an example of such a contour plot in Figure 4.12b, which uses experimental data from the first five modes of a soft cantilever in contact with gold, described later in Chapter 5. We find a very good approximation for a modal intersection for the first four modes with a tip offset of 0.012 and a tip height of 0.013 (normalised by the total length of the cantilever) L. Additional discrepencies within this intersection are likely due to inhomogenieties in the beam or measument anomalies. Further discussion of this method of parameter estimation is given in Section 5.4.1.

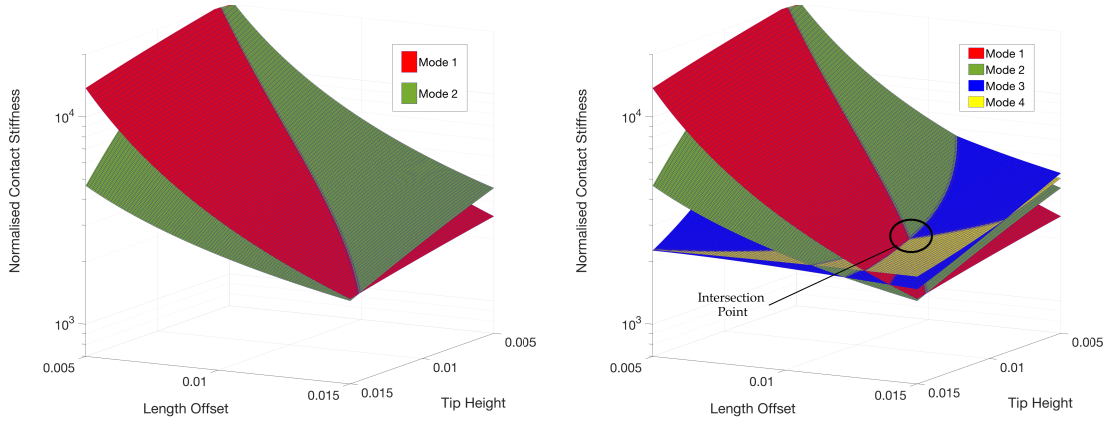

(a) Modes 1–2 (b) Modes 1–5

Figure 4.13: Demonstration of the intersection between multiple parameter surfaces, showing two modes in (a) and for five modes in (b), where the intersection point is marked. All results are shown for measurements described in Chapter 5.

4.6 CONCLUSION

In this chapter, we have investigated how the normal contact stiffness, $k_\perp$, can be calculated, how it varies with the higher modes of a cantilever, and how it is influenced by parameters of the system such as tip height, h, tip offset, L_2, and the introduction of a lateral stiffness, $k_\parallel$. We reiterate that the normal contact stiffness is an idealisation of the contact event between the AFM probe and sample. As such, we are required to know the robustness and limits of this idealisation in order to use the contact stiffness as a tool for measuring material properties at the nanoscale.

By introducing the additional details of a cantilever tilt and tip offset, we have shown that it is possible to relate any measured shift in resonant frequency to an idealised contact stiffness. Furthermore, we have shown that the introduction of these details, though making the model more complicated, also leads to a self consistent means for estimating the crucial parameters of the system, the tip height and tip offset. Specifically, information is required of the tip height and the length offset of the tip from the free end of the probe. We have introduced a method for calculating these two parameters in a straightforward manner, without the need for additional measurements such as SEM imaging. We achieve this by calculating the contact stiffness, given a shift in frequency and corresponding contact wavenumber, across multiple cantilever modes, demanding modal consistency. As shown in Figure 4.13, this leads to well-defined values for both length offset and tip height. Hence, the inclusion of a lateral stiffness ensures the existence and consistency of contact stiffness for multiple modes of a sensor. We are not aware of any previous work that has lead to these properties for an idealised contact stiffness.

Having set-out the theoretical process of relating a measured shift in resonant frequency to an idealised contact stiffness, we describe, in Chapter 5, how this is achieved in practice and describe the material properties that are contained within the contact stiffness. We illustrate how the contact stiffness becomes consistent across multiple modes of

a soft cantilever when the proper model and parameters are chosen and relate this contact stiffness to the effective stiffness of the cantilever, introduced in Chapter 2. These steps further support the higher modes of the cantilever that we utilise in Chapter 6, where we combine contact resonance techniques with high-speed AFM (HS-AFM).

5

RELATING CONTACT STIFFNESS TO ELASTIC MODULUS

The work in this chapter includes elements from collaborations with Dr Jason Killgore (Nanoscale Reliability Group, NIST, Colorado, USA) and Miss Stacy Moore (Interface Analysis Centre, Bristol, UK). Specifically, Killgore assisted with the measurements undertaken in Section 5.3. The stainless steel (SS) grade 316 (UNS S31600) sample in Section 5.3.1 is a piece of EDF Energy Cast 69431 ex service AISI Type 316H; the same sample was previously investigated by Dr Xander Warren [193][1]. It was polished and prepared by Moore.

5.1 INTRODUCTION

In previous chapters, we have investigated how to calculate the effective stiffness (Chapter 2) and the hydrodynamic loading (Chapter 3) of an AFM probe at high mode number. We have also shown that a change in the resonant frequency of the probe can be related to a contact stiffness which contains information about the material. We now turn to the process by which a contact stiffness relates to a material property. We begin by giving an overview of theories of contact mechanics, in Section 5.2, which connects an idealised contact stiffness, introduced in Chapter 4, to an elastic modulus. We then set out the experimental measurements, in Section 5.3, by which we test the relevant theory of contact mechanics that will be relied upon in Chapter 6. We measure the contact stiffness from an AFM probe in contact with samples of gold and stainless steel (SS) grade 316 (UNS S31600) as we decrease the distance between probe and sample causing a corresponding increase in the normal load. We examine a separate sample of the same SS material in Chapter 6. First, we show, in Section 5.4.1, how considerations of a lateral stiffness (as well as the tip height) are required for calculating a contact stiffness on these samples when using the lower modes of a soft cantilever. We achieve this using a new means for parameter estimation as well as the considerations of the hydrodynamics in the system, given in Chapter 3 and the resonant frequency of a beam in a vacuum, calculated using the method described in Chapter 2. In Section 5.4.2, we use our measurements of modally consistent contact stiffneses to fit models of contact mechanics, set out in Section 5.2, and find that significant uncertainties in the calculation of a reduced modulus arise when using this measurement procedure. We discuss potential causes for this uncertainty in Section 5.5 and the impact that this has on contact resonance measurements. We make our concluding remarks in Section 5.6.

1 For further details, see Section 5.3.

5.2 THE CONTACT REGION

In this chapter, we will primarily be concerned with the contact event between a cantilever and surface. This is the contact region described in Section 1.3. There are two general approaches to modelling the contact regime, depending on the assumed level of interaction between tip and sample. The first occurs when very sharp tips are used with low normal loading such that only a few atoms at the apex of the tip are in contact with the surface. This is the original formulation of the AFM [194], as described in Chapter 1. However, for cases where there are tens or hundreds of atoms, a continuum approach may be more appropriate. The use of continuum models that describe the contact mechanics have been used extensively in the contact resonance AFM community, see for example [61, 62, 68, 69, 130].

We begin by assuming a Hertzian model of contact mechanics, in which the tip is in contact with a flat plane [195]. For simplicity, we assume that the plane (which represents the surface) is entirely flat such that there is only a single region of contact and that the tip is semi-circular in cross-section, with radius R. For discussion of theories including multiple points of contact, see for example [168]. Furthermore, we assume that both bodies are non-conforming and mechanically isotropic. The hemispherical approximation of the tip has been examined in detail (see for example, [91, 196]). It is found that the approximation holds provided that there has been no tip wear.

Figure 5.1 shows a schematic of a contact event both pre- and post-contact. The tip is assumed to be hemispherical such that the cross-section of the tip is well approximated by a parabola, scaled by the tip radius of curvature. The tip begins an initial distance, d, away from the sample (Figure 5.1a) and is brought into contact (Figure 5.1b) due to an applied normal load, F_N. As the separation distance decreases, a contact zone forms

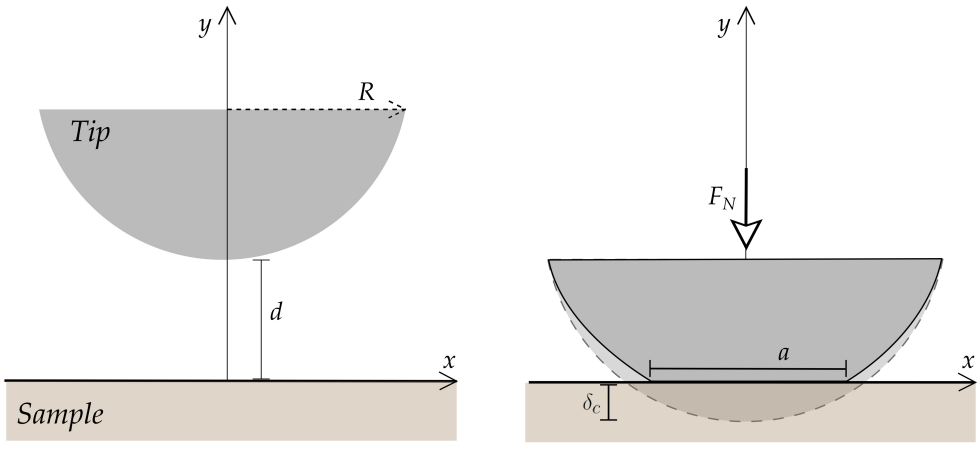

(a) Far from Surface (b) Contact Event

Figure 5.1: An AFM probe making contact with a surface, where the probe is idealised as a hemisphere with radius R, showing (a) the probe is a distance d away from the surface, and (b) after making contact with the sample causing a contact area, a, and penetration depth, $\delta_c(a)$.

which is determined by the geometry of the tip. The contact area, a, denotes the total area in which the tip has intersected with the surface. For a hemisphere under normal load, F_N, the radius of this (assumed circular) contact area is given by [195]

$$a = \sqrt[3]{3F_N R_{\text{tip}}/4E^*}, \tag{5.1}$$

where E^* is the reduced modulus of the tip-sample system. The reduced modulus is given by [69]

$$\frac{1}{E^*} = \frac{(1-\nu_s^2)}{E_s} + \frac{(1-\nu_t^2)}{E_t} = \frac{1}{M_s} + \frac{1}{M_t}. \tag{5.2}$$

and where ν refers to the Poisson ratio of the material, E is the Young's modulus of the material, and subscripts t and s refer to the tip and sample, respectively. We note that the effective modulus is also related to the indentation modulus, $M = E/(1-\nu^2)$. The maximum vertical distance that the tip has entered into the surface is the penetration depth, δ_c, which is a function of both the contact area and radius of the tip; for the assumed hemispherical geometry, it will be given by $\delta_c = \sqrt{2a}$.

Here, we have assumed that the tip will be parabolic in cross-sectional gemeotry. However, this does not always hold in practice [91]. During AFM operation, the tip may become sufficiently deformed due to the contact forces such that it more closely resembles a flat punch than a hemisphere. As outlined in [91], this can cause the exponent of (5.1) to vary from $1/3$ to 0. We shall discuss this further in Section 5.5.

Given the expression for the contact area, we seek to relate this to a contact stiffness. The contact stiffness, k^* ,modelled as a perpendicular spring, is defined in (4.1). Under adhesionless conditions, this is related to the reduced modulus and contact area according to

$$k^* = 2aE^* \tag{5.3}$$

which, when combined with (5.1), can be written in terms of the normal load, F_N, on a cantilever, the radius of the tip, R_{tip}, and the reduced modulus, E^*,

$$k^* = \sqrt[3]{6(E^*)^2 R_{\text{tip}} F_N}. \tag{5.4}$$

The final expression, (5.4), has been derived based on what is commonly referred to as the Hertzian model of contact [197]. It assumes that adhesive forces contribute a negligible amount to the total interaction potential, and that there is no deformation of either sample or tip. However, micro-mechanical cantilevers are exposed to multiple different adhesive forces which can cause deformation of the sample. We next turn to extensions to the Hertzian model of contact and how these account for adhesion and deformation.

5.2.1 *Extensions to Hertzian Contact Mechanics*

The choice on whether to include additional consideration of adhesive forces depends on whether deformation is expected to occur. If it is assumed that that no deformation

occurs, we may neglect all adhesion considerations and retain the Hertzian model of contact. Alternatively, if it is assumed that the total deformation will occur exclusively during the contact event, then we need consider only the adhesion effect of external forces. This is known as the Derjaguin, Muller and Toporov (DMT) model of contact [195]. It is valid for all forcing provided that they act on a body that is deformed by contact stress alone. For an AFM operating in ambient air, the adhesion will come from a capillary layer which causes a meniscus bridge to form between the tip and sample. This capillary layer occurs in all but ultra high vaccuum conditions, and is typically less than a nanometre in height [198].

In other cases, the influence of the adhesive interaction forces will be strong enough that the surface undergoes considerable deformation. In this case, we are within the regime modelled by Johnson, Kendall and Roberts (JKR) model [199]. This approximates all additional deformation as a flat punch, altering the expression for penetration to include the reduction in area,

$$\delta_{\text{JKR}}(a) = \delta_H(a) - \delta_{\text{adhesion}}(a), \tag{5.5}$$

where δ_H is the Hertzian penetrative distance, and the additional penetration caused by the adhesive penetration is given by

$$\delta_{\text{adhesion}}(a) = \sqrt{\frac{2\pi a w_{\text{adhesion}}}{E^*}}, \tag{5.6}$$

where w_{adhesion} is the adhesion energy. In this case, we can re-write the contact force according to,

$$F_{\text{JKR}}(a) = F_H(a) - k^*(a)\delta_{\text{adh}}(a). \tag{5.7}$$

The level of sophistication required by a model of the contact mechanics is dictated by the strength of the adhesive interaction forces relative to the deformation of the sample and the tip. In the limit of weak interactions, the contact event is well described by the DMT model which assumes that the total deformation is a result of the contact event only [195]. As the adhesive force increases, it asymptotes to the strong interaction regime, described by the JKR model, whereby adhesive forces are considered strong enough to deform the surface [199]. For cases where there are no adhesion effects, the contact mechanics are well described by the Hertzian model. Finally, for intermediary cases between the DMT and JKR models, the Maugis model [200] is used. The Maguis model considers interaction both inside and outside of the contact zone. We do not include the details of this model here and refer the reader to [201] for further details.

A single parameter, known as the Tabor parameter, can be used to identify whether a system behaves according to the DMT model, JKR model or some intermediary case [201]. The Tabor parameter is the ratio of interaction stresses, σ_0 to the contact stresses, σ_c. Rewriting the stresses in terms of the penetration depth, we have

$$\mu_T = \left(\frac{16 w_{\text{adhesion}}^2 R_{\text{tip}}}{9 E^{*2} z_0^3}\right)^{1/3} \approx \frac{\delta_{\text{adh}}}{\delta_{\text{int}}}, \tag{5.8}$$

Material	E (GPa)	E^* (GPa)	μ_c^T	$k_\perp$ (N m^{-1})	a (nm)
Au	79	60	0.01 – 0.06	72 – 334	0.5 – 2
Steel 316	198	92.5	0.01 – 0.05	132 – 620	0.5 – 1.5

Table 7: For two of the samples under consideration, we give the Young's modulus, E, reduced modulus, E^*, the modified Tabor parameter, μ_c^T, contact stiffness, $k_\perp$, and contact area, a, calculated using $R_{\text{tip}} = 10\,\text{nm}, F_N = 1 - 100\,\text{nN}$

where z_0 is the interatomic equilibrium distance for contact between two solids. We make the following observations [201]

1. For small adhesive penetration, where the adhesion energy transfer is dominated by interaction stresses ($\mu_T \ll 1$), we are within the DMT regime.
2. For large adhesive penetration, where deformations close to the contact edge dominate adhesion energy transfer ($\mu_T \gg 1$), then we are within the JKR regime.
3. For all other cases ($\mu_T \approx 1$), then we are within intermediary cases.

When a liquid meniscus is present, the capillary forces will dominate over the interatomic forces and should be considered in place of z_0. This leads to the modified Tabor parameter, where a measure of the range of capillary force, s, has replaced the atomic equilibria distance,

$$\mu_T^c = \left(\frac{16 w_{\text{adhesion}}^2 R_{\text{tip}}}{9 E^{*2} s^3} \right)^{1/3}. \tag{5.9}$$

We will exclusively be concerned with AFM probes that have tips made of silicon and with a radius of curvature that can be anywhere between tens to hundreds of nanometres depending on tip wear through contact. For a silicon tip, with an indentation modulus of 165 GPa [91], the reduced modulus of the tip-sample contact will be between $50 - 100\,\text{GPa}$ for stiff sample materials with a Young's modulus in the range of $80 - 200\,\text{GPa}$ (such as gold and stainless steel). The capillary force will extend through the height of the fluid layer which is typically a few nanometres high. For the case where capillary forces dominate, the adhesion energy is given by, $w_{\text{adhesion}} = 2\gamma_{\text{m}}$, where γ_{m} is the surface tension in the meniscus layer [201]. For water in ambient temperature (298 K), γ_{m} 0.072 N [62]. Taking these values into consideration, we find that the modified Tabor parameter will always remain much smaller than 1, shown in Table 7. Hence, we shall use the DMT model in what follows.

We now assume the following: that the dominant adhesion force is caused by a meniscus layer, such that all other adhesive influences are ignored, that the adhesive meniscus forces are weak in so far that we are within the DMT regime of contact mechanics, and that this capillary force is constant over repeated measurements. Under these assumptions, the adhesive capillary force, F_C, introduces no additional deformations to the tip-sample system. Hence, the Hertzian description of the contact event is unchanged except for the addition of the capillary force on the tip. We rewrite the contact force as

$$F_T = F_N + F_C, \tag{5.10}$$

and follow [201] in approximating the capillary force as

$$F_C = 2\pi\gamma_m R_{tip}. \tag{5.11}$$

This changes (5.4) to

$$k_\perp = \sqrt[3]{6(E^*)^2 R_{tip} F_T}, \tag{5.12}$$

where the contact force, F_T, is given by (5.10).

The contact resonance measurements, undertaken here, also give a means for estimating a, as well as the area of material that is measured by an AFM tip. In (5.3), we have a simple means for relating a contact stiffness to a contact radius given a known reduced Young's modulus. This contact radius is the lateral resolution of contact resonance measurements on the sample surface. Example contact stiffness and contact radii are given in Table 7.

Given the lateral resolution on the surface, it is natural to consider whether the acoustic measurements are able to give details of sub-surface properties. Longitudinal waves that pass through stiff materials, such as the gold and SS samples considered here, typically have a velocity of $v = 1 - 5\,\mathrm{mm\,\mu s^{-1}}$ [202]. Meanwhile, the AFM sensor is excited in the frequency range $f_n = 10\,\mathrm{kHz} - 5\,\mathrm{MHz}$, shown by our results in Chapter 2. Hence, the acoustic wavelength ranges from $\lambda = v/f_n = 5\,\mathrm{mm} - 1\,\mathrm{cm}$ [66]. The wavelength is much larger than the contact radius, such that the penetration depth will be given by the decay of the mechanical stress field rather than the distance travelled by the acoustic wave.

For Hertzian contact, the stress field is expected to be several times larger than the contact area [72], such that sub-surface features can be measured provided that they have appropriate thinness (less than 10 nm according to the contact area given in Table 7). This outlines the high spatial resolution of contact resonance measurements, which is capable of inspecting material properties over several nanometres, much smaller than the nanoindentation technique reviewed in Chapter 1. Hence, CR-AFM is theoretically well suited for non-destructive measurements at the nano-scale. However, in order to be utilised as a tool for quantification of the elastic properties of materials, it must also be amenable to robust and repeatable measurements. In this chapter, we will focus on these properties of robustness and repeatability for CR-AFM measurements.

In Section 5.3 will use (5.12) to connect a contact stiffness (calculated from shifts in resonant frequency) to the reduced modulus, (5.2), of a material. In order to test the viability of quantified contact resonance measurements on stiff materials, we take a series of measurements at multiple locations across a range of normal loads and use these measurements to test the feasibility of using the DMT model of contact mechanics for quantified stiffness measurements. In order to do so, we assume that the contact stiffness and reduced modulus follow a power-law relationship according to (5.4). As discussed, this relationship will hold provided that no changes to the tip geometry

(or manufacturing faults) have occured. In this case, the power-law relationship can be written as

$$(k^*)^3 = \bar{p}_1 F_T, \tag{5.13}$$

where k^* is the contact stiffness described in Chapter 4, $\bar{p}_1 = (6E^{*2}R_{tip})$ and F_T is the contact force combining normal load and capillary force, (5.11). Alternatively, the tip geometry may have changed such that the $1/3$ exponent is no longer valid. In this case, we rewrite this equation explicitly as a power-law with unknown exponent,

$$k^* = (\bar{p}_1 F_T)^{p_1}, \tag{5.14}$$

Taking the log of both sides of (5.14) gives,

$$\log(k^*) = p_1 \log(F_T) + p_2. \tag{5.15}$$

where $p_2 = p_1 \log(6E^{*2}R_{tip})$. This allows us to linear fit to the log-log plot of contact stiffness and contact force, where the exponent of this fit, p_1, gives insight into whether our assumption that the tip is hemispherical need hold (in which case, $p_1 = 1/3$). We can then use both gradient and intercept to calculate the reduced modulus,

$$E^* = \sqrt{\frac{\exp(p_2/p_1)}{6R_{tip}}}. \tag{5.16}$$

Alternatively, we can fit (5.13) which assumes that the tip is hemispherical. In this case, taking the log of both sides of (5.13) will give

$$3\log(k^*) = \log(F_T) + p_2, \tag{5.17}$$

$p_2 = \log(6E^{*2}R_{tip})$ such that the reduced modulus is calculated by

$$E^* = \sqrt{\frac{\exp(p_2)}{6R_{tip}}}. \tag{5.18}$$

We describe the results of these fits and calculation of the reduced modulus in Section 5.4.2.

5.3 QUANTIFIED MEASUREMENTS ON STEEL AND GOLD

In Chapter 4, we outlined how a shift in resonant frequency of the AFM probe relates to an idealised contact stiffness encoding important information about the sample. We now demonstrate how the idealised contact stiffness relates to the reduced modulus of a sample. We begin by giving experimental details before highlighting our findings in Section 5.4. We demonstrate our method for parameter estimation, as described in Section 4.5, and show that this leads to modal consistency for measurements taken on both the gold sample and the sample of SS grade 316. In Section 5.4.2, we use an

iterative procedure to attempt to relate the contact stiffness to a specific elastic modulus. We discuss uncertainties in our single point[2] measurements and highlight the impact of our findings for acoustic AFM techniques. We discuss out findings in Section 5.5.

We will be primarily interested in the ability to quantitatively measure the reduced modulus of metals in a non-destructive fashion, as motivated in Chapter 1. In order to validate the relationship between contact stiffness, k^*, and the reduced modulus of a material, E^*, we have designed an experiment that takes iterative low-resolution contact resonance measurements at a single point over a range of normal applied loads. We have collaborated with Dr. Jason Killgore at the Nanoscale Reliability Group (NIST, Colorado, USA) to take these measurements, making use of a Cypher AFM (Asylum Research, Santa Barbara, USA). The Cypher AFM excites the cantilever using the blueDrive excitation system and the z-sensor measures the displacement of the AFM probe at the tip using an optical beam deflection (OBD) detection system. The blueDrive detection system ensures that there is minimal mechanical noise imparted to the system by piezoelectric actuation. Measurements were undertaken in air at room temperature (298 K).

In order to maximise the sensitivity of higher modes and decrease damage to the sample, we use two different PPP-CONTAuD cantilevers of the same type(Nanosensors, Neuchatel, Switzerland). This cantilever model is 450 µm ± 10 µm long, 50.0 µm ± 7.5 µm wide and has a notional thickness of 2 µm ± 1 µm. Furthermore, it has a gold layer to boost the reflective signal. As these properties are similar to the cantilever investigated in Chapter 2, we assume that probe has neglible tip mass and rectangular cross-sectional area and apply our method for cantilever calibration, described in Section 2.4.3. We restrict our attention to the first five modes of the cantilever which have good signal as shown in Figure 5.2.

The measured resonant frequencies for the first five modes deviate by less than 3% when compared to the values of the resonant frequency in vacuo, calculated using the method described in Section 5.3. This strengthens our assumption that the AFM probe acts according to the stated assumptions of our calibration method and will be well modelled by the Euler-Bernoulli beam theory, utilised in Section 4.4. Using the method outlined in Section 2.4 and the measured resonant frequency and Q factor,

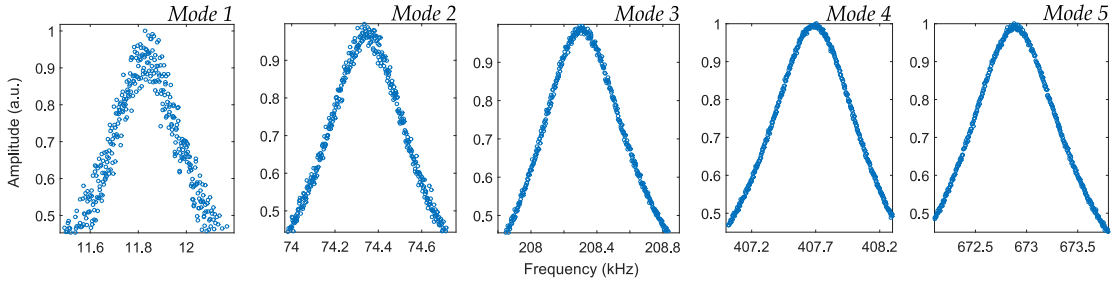

Figure 5.2: The first five free resonant peaks of the PPP-CONTAuD cantilever that was used, showing resonant frequencies of 11.8 kHz, 74.4 kHz, 208.4 kHz, 407.4 kHz, and 673 kHz.

2 We note that these measurements are a much lower resolution as the total number of position data points is far below the high pixel count of typical AFM images, especially those taken in Chapter 6.

		1	2	3	4	5
Au	$f_{n,\text{vac}}$ (kHz)	12	74	208	407	673
	k_n (N m^{-1})	0.066	2.6	20	78	214
SS	$f_{n,\text{vac}}$ (kHz)	12	76	214	419	692
	k_n (N m^{-1})	0.066	2.6	20	78	214

Table 8: The resonant frequencies (in vacuo) and effective stiffness of the two PPP-ContAUD AFM probes (Nanosensors) used during our measurements..

$f_1 = 12.1\,\text{kHz}, Q = 21$, of the first mode, we find the effective stiffness of the first five modes of the cantilever used to investigate the gold sample to be $k_1 = 0.066\,\text{N m}^{-1}, k_2 = 2.6\,\text{N m}^{-1}, k_3 = 20\,\text{N m}^{-1}, k_4 = 78\,\text{N m}^{-1}$, and $k_5 = 214\,\text{N m}^{-1}$. We also calculate the resonant fequency of the beam in vacuo for the first five modes as $f_1 = 12\,\text{kHz}, f_2 = 74\,\text{kHz}, f_3 = 208\,\text{kHz}, f_4 = 407\,\text{kHz}$, and $f_5 = 673\,\text{kHz}$. The properties of the second AFM probe (used to investigate the steel sample) were found to agree with these measurements, with the fundamental resonant frequency and Q factor as $f_1 = 11.8\,\text{kHz}, Q = 20$, the effective stiffnesses were found to be the same, and resonant frequencies in vacuo calculated as $f_1 = 12\,\text{kHz}, f_2 = 76\,\text{kHz}, f_3 = 214\,\text{kHz}, f_4 = 419\,\text{kHz}$, and $f_5 = 692\,\text{kHz}$. The effective stiffness and predicted contact stiffness, given in Table 7, implies that the fourth and fifth mode will be most sensitive for both materials. All these properties are included in Table 8.

In both this chapter and in Chapter 6, we shall calculate the contact stiffness using the ratio of the n^{th} contact resonant frequency to the n^{th} in vacuo resonant frequency, as discussed in Chapter 4. We do so in order to minimise the influence of the surrounding hydrodynamics, which we have shown to be substantial in Chapter 3. Furthermore, the means for calculating these in vacuo frequencies, given in Chapter 2, depends only on the easily measured dimensions (length and width), the resonant properties of the fundamental mode (resonant frequency and Q factor), and the fluid properties (fluid density and dynamic viscosity). Hence, we are not reliant on anomalous measurement of subsequent free resonant frequencies.

We next discuss the means by which we take contact resonance measurements on the sample. Our procedure is designed to take multiple measurements of the frequency response of a soft micro-mechanical cantilever in contact with a stiff sample. We apply the procedure to a thermally sensitised sample of SS grade 316, known to contain regions of carbides[3]. Prior to measurements on SS, we trial our procedure on a section of gold. We choose these samples as they cover a large range of elastic properties for stiff materials, as described in Section 5.2. The procedure is designed to move the cantilever towards

3 The SS grade 316 (UNS S31600) sample is a piece of EDF Energy Cast 69431 ex servic AISI Type 316H. The same sample was previously investigated by Dr Xander Warren [193]; full details of the sample are given in Warren's PhD thesis [203], and quoted here: "The ex–service +22000 hour AISI Type 316H stainless steel specimen was removed from the attachment weldment of an ex–service boiler header component (Cast 69431) from the Heysham B nuclear reactor, which during operation has been subjected to 65015 hours in the temperature range 490 °C to 530 °C, and then subjected to further thermal ageing for 22100 hours at 550 °C post service."

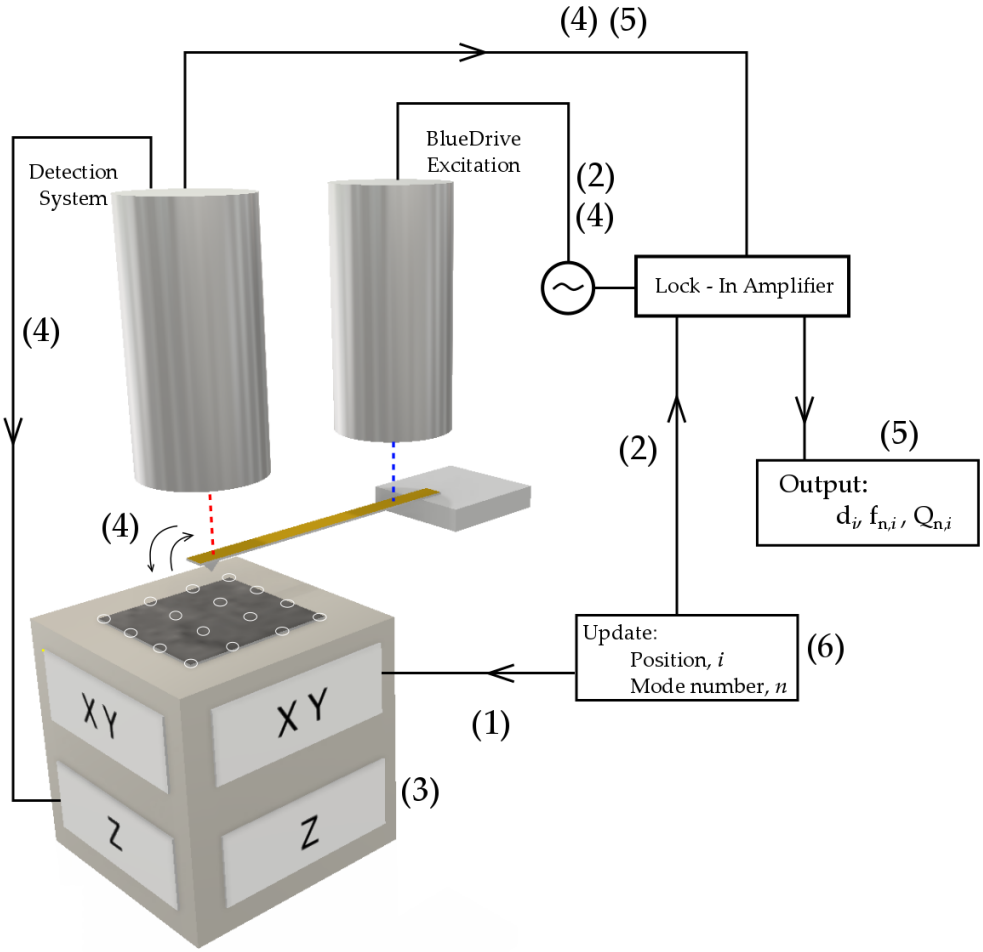

Figure 5.3: A schematic showing the experimental set-up for measurements on a single point.

the sample over a range of heights, d_i for $i = 1, ..., N$, where d_1 is the initial z distance from the set point, d_0. The distances are returned in volts, V, which is converted to a distance using the inverse optical level sensitivity, described in Chapter 1. For the gold sample, the inverse optical level sensitivity is 149 nm V^{-1} whereas for the SS sample, it is 304 nm V^{-1}. Moving the cantilever towards the sample results in a contact event where the cantilever is subjected to a normal load, $F_N = k_c d_1$. We then decrease the distance between sample and cantilever, in effect decreasing the normal load on the cantilever, and take a measurement of the resonant frequency, a contact tune, with each change in sample-sensor distance. We repeat these measurements until the stage returns to the original z-sensor set-point, at a distance d_N, and regains the free resonant frequencies, signified by returning to the original set-point of the z-sensor. The method by which we perform these measurements is included in Figure 5.3 and outlined below:

1. The cantilever is moved onto the first position on the grid through the X-Y stage but is not brought into contact.

2. The cantilever is excited near the base of the tip using the blueDrive laser in order to oscillate the cantilever, up to the higher frequencies of the first five modes.

	Position:	1	2	3	4	5	6	7	8	9	10
Au	d_i (nm)	151.95	607.8	303.9	152	30.4	24.3	18.2	12.2	–	–
	F_i (nN)	100.8	40.32	20.16	10.08	2.01	1.6	1.2	0.9	–	–
SS	d_i (nm)	770	308	154	77	46.2	30.8	15.4	12.32	9.24	6.16
	F_i (nN)	50.82	20.23	10.16	5.08	3.04	2.03	1.02	0.81	0.69	0.41

Table 9: The change in distance between sample and AFM tip, d_i, causing an increased normal load, F_N for both the gold sample (Au) and the SS grade 316 sample (SS). .

3. The cantilever is lowered onto the surface grid until it reaches a known distance from the set-point. This initial distance, d_1, represents contact with a normal loading force according to $F_N = k_c d_1$.

4. The cantilever is moved to a known distance, $d_2 > d_1$, away from the surface, causing the normal load to decrease. A contact tune is then taken. Once the cantilever motion has ceased, the procedure is repeated (at distances d_{i+1}) until the cantilever returns to the original z-sensor set-point, d_N. We record the resonant frequency and Q factor for each separation distance and mode number.

5. The free resonant frequencies of the cantilever are measured.

6. The cantilever is moved by the X-Y stage to the next location on the surface grid.

7. Steps (3) to (6) are repeated until all points on the surface grid have been measured.

At each position on, and distance from, the sample, we measure the contact resonant frequency of the cantilever, known as a contact tune, using the detection laser. We use this contact tune to calculate the shift in resonant frequency from the free resonance of the first mode at each location, and for each normal load. This is used to calculate the contact stiffness, given the shift in resonant frequency, using (4.46).

We first apply our experimental set-up to a sample of gold, shown in Figure 5.4, where we record 16 measurements over a $4 \times 4\mu$m grid. We bring the AFM cantilever into contact from the set-point distance, d_0, to an initial distance of $d_1 = 1.5\,\mu$m, corresponding to loads of 100 nN. The distance is then reduced, resulting in normal loads of 40 nN, 20 nN, 10 nN, 2 nN, 1.6 nN and 1.2 nN and 0.9 nN (calculated with $k_c = 0.066\,\mathrm{N\,m^{-1}}$). These distance and load measurements are given in Table 9.

We find that the measured resonant frequency exhibits a regime change as we increased the distance between the sensor and sample (reflected by a decrease in the normal load). This is shown in the colour maps of Figure 5.5, where the first mode shows a transition from high frequency (yellow) to low frequency (blue) where higher modes increasingly show a jump in frequency between 10 and 2 nN (5V and 0.1 V, respectively). Measurements were taken on the gold sample in order to ascertain whether the data was being properly recorded and, as such, we note that this data set is missing two components: a force-distance curve measurement at each location and position data for the iterative measurements. However, all results are included for completeness. For

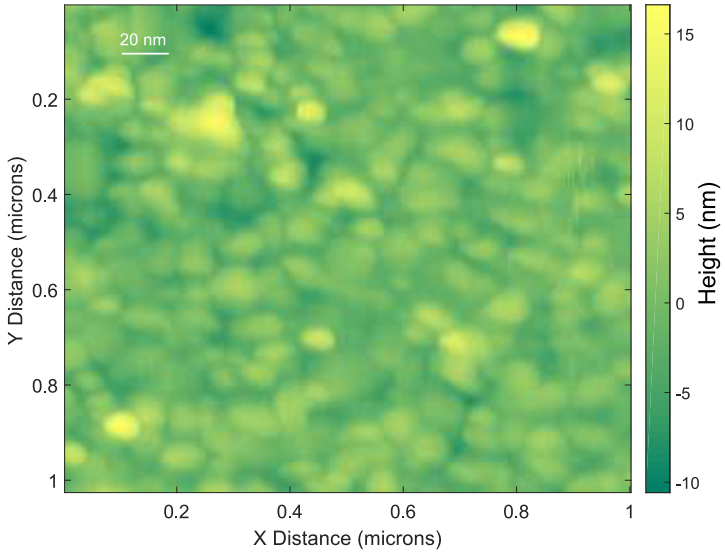

Figure 5.4: An example section of the gold sample that has been investigated. We note that the circular regions represent grain boundaries and that they vary in diameter from 5 nm to 20 nm, as indicated by the included scale bar, and up to 15 nm in height, shown by the colour bar to the right of the image.

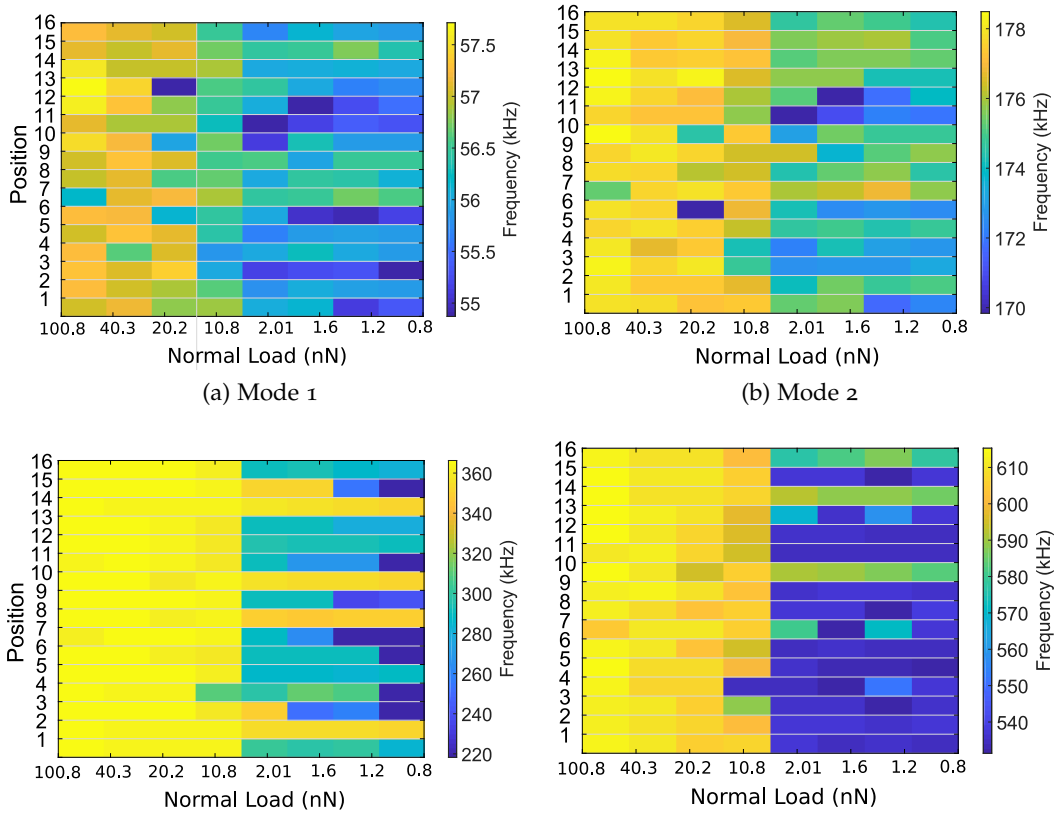

(a) Mode 1

(b) Mode 2

(c) Mode 3

(d) Mode 4

Figure 5.5: Heat maps showing the change in frequency over the 16 positions measured on the Au sample. We note that there exists a significant change in behaviour between a normal load of 10 and 0.9 nN.

subsequent measurements on the sample of SS grade 316, these components were introduced. Furthermore, the measurements on the gold sample for the fifth mode of the cantilever failed to capture the fifth resonant frequencies and have not been included in the analysis.

For the sample of SS grade 316, we have taken 25 points across a $5 \times 5\mu m$ grid, as shown topographically in Figure 5.6. This steel sample was polished and prepared by Miss Stacey Moore (Interface Analysis Centre, Bristol) and a second section of the same material is used for contact resonance on high-speed AFM (CR-HSAFM) measurements in Chapter 6. The sample of SS grade 316 contains inclusions and carbide build up, shown as low and high regions, in Figure 5.6. The carbides relate to the high regions as they are harder than the bulk steel and are less influenced by the polishing procedure. They can range from $10\,nm^2$ to $10\,\mu m^2$ in area. Each grid point position is related to a spatial position on the sample, marked as numbered circles in Figure 5.6b.

On the sample of SS 316, we bring the AFM cantilever into contact with a distance of 770 nm from the set-point, d_0. This corresponds to an initial normal load of 50.82 nN, and subsequent load and distance measurements are given in Table 9. We find that at high distances/low forces, there is a significant long-range force (potentially caused by electrostatic or van der Waals phenomena) that prevent the cantilever from fully retracting (and hence losing contact) when taking measurements on SS sample. This was addressed by adjusting the procedure to break the iterative process of decreasing the normal load when the z-sensor makes a relative change rather than previous choice to stop once the cantilever reached the set-point (step (4) above). This prevented the cantilever from snapping in and out of contact, which would result in a high number of spurious data-points being collected at low forces.

Our aim is to show that a measured contact stiffness will be consistent across modes and positions with a low amount of variation. Having calculated the contact stiffness, we seek to relate the contact stiffness to the reduced modulus of the material using (5.12) for an assumed hemispherical tip or an unknown geometry (where p_1 remains unknown). We now outline the results from our measurements, which demonstrate modal consistency of contact stiffness, and discuss, in Section 5.5, the possible causes of uncertainty in our results.

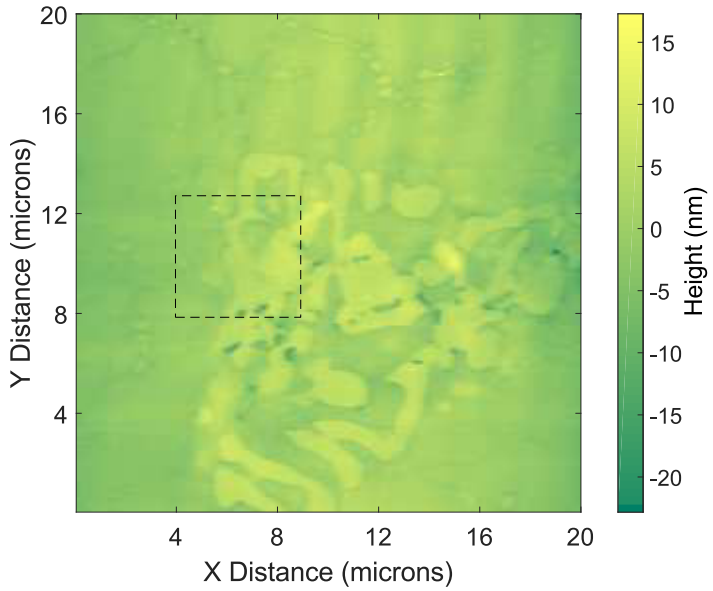

(a) Larger section of the Steel 316 sample.

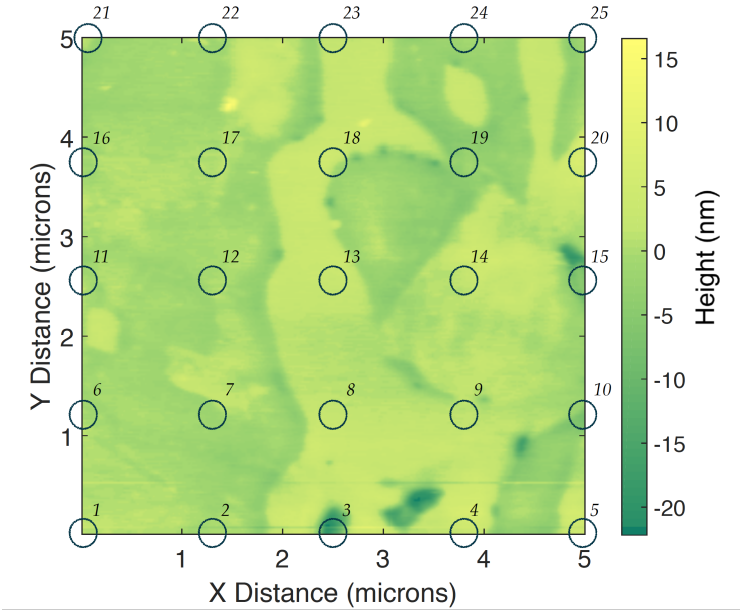

(b) Close-up of the region marked in (a).

Figure 5.6: Topographic map of the sensitised SS grade 316 sample, showing (a) larger region of the sample, demonstrating a build up of carbide across the centre region (high regions) and where we have marked the section that was investigated (b) by a dashed black box. In (b) we show a close up of this section and mark the location of the twenty five grid positions.

5.4 RESULTS

We are concerned with calculating a reduced modulus, E^*, from a shift in the frequency of an oscillating sensor in contact with a stiff material. To do so, we assume the following,

- The AFM probe is well described by the Euler-Bernoulli beam theory, (4.2).
- The idealised contact stiffness, as defined in (4.1), will have a causal relation to the contact force. The contact stiffness is found using the theory described in Chapter 4 and outlined in Section 4.4.5.
- The contact stiffness is a measure of a material property of the sample and, hence, is expected to be consistent across all modes.

We are interested in how well the calculated contact stiffness is described by the relevant contact mechanics theory outlined in Section 5.2. We investigate this by incrementally varying the normal loading force (through a change in the distance between tip and sample). We examine how the repeated measurements across multiple different locations on the gold sample and SS grade 316 sample, as described in Section 5.3, will influence the contact stiffness of the sensor-sample system. We include the unconverted values for the recorded resonant frequency at each location and tip-sample separation distance in Appendix A.

In Section 5.4.1, we calculate the necessary cantilever parameters needed to relate a shift in resonant requency to a contact stiffness using the method described in Section 4.5. We then describe how these parameters lead to modal consistency of the normal contact stiffness, over a range of normal loads (caused by a change in the tip-sample separation). Specifically, we find that the modes of an AFM probe that have an effective stiffness that most closely matches the contact stiffness of the sensor-sample system also best approximated by a parallel beam such that additional parameters (the tip height, lateral stiffness and tilt angle) can be ignored. This is not the case for the lower modes (which have reduced effective stiffness) when using a soft cantilever to measure a stiff material. Instead, the tilted cantilever model should be used. Given appropriate model selection (tilted cantilever or parallel beam), we find that the calculated contact stiffnesses are consistent across multiple modes.

Having assured ourselves of modal consistency for a contact stiffness, we examine in Section 5.4.2 how the change in calculated contact stiffness over varying normal loads can be used to fit the DMT relationship between contact stiffness and reduced modulus, (5.13) for an assumed hemispherical tip and (5.14) for a tip with unknown geometry. We find that significant variation in the calculated reduced modulus exists. We discuss potential causes for this uncertainty in Section 5.5.

5.4.1 *Modal Consistency*

We first examine whether the cantilevers parameters, estimated using the method described in Section 4.5, result in contact stiffnesses that are consistent across multiple

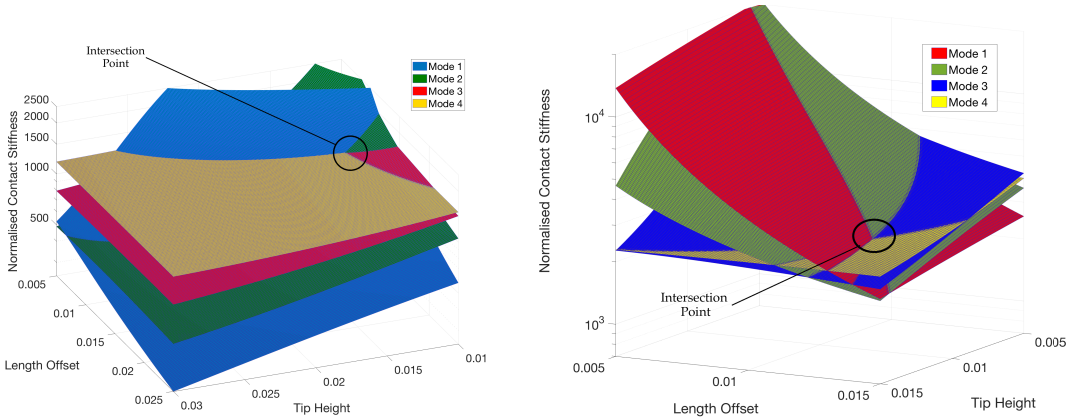

(a) SS grade 316 (b) Gold

Figure 5.7: Intersections of the parameter surfaces for measurements on Au (a) and SS grade 316 (b), leading to the calculation of calculation of two key parameters; the length offset, $L'/L = 0.012$ and tip height, $h/L = 0.013$. Note that Figure 5.7a appears earlier, in the introduction of our method for parameter estimation, Figure 4.12.

modes of the cantilever. In Figure 5.7, we show surfaces of normalised contact stiffness ($k_\perp/k_c$) for each mode over a range of tip off-set and tip height. These surfaces are found to intersect at only one location. This is an experimental validation of our method of paramater estimation that is described in Section 4.5, and is the key to gaining consistent values of a contact stiffness over multiple modes. We note that previous work assuming parallel contact (such as [138, 164, 204]) has used a similar method for calculating the length offset of the tip only. However, we have found that this method results in non-unique intersection points, such that the uncertainty around the length offset value remains. Instead, by extending the model of contact to include the cantilever tilt and simultaneously seeking a value for both the length offset and tip height, we find that a consistent contact stiffness can be calculated at the fundamental as well as at higher modes.

For all calculations, we use the ratio of the n^{th} contact frequency (the resonant frequency of the cantilever in contact with a sample) to the n^{th} free resonant frequency of the beam, calculated using the method, described in Chapter 2, due to the considerations of the hydrodynamics given in Chapter 3. We find estimates for the length offset, $L_2/L = 0.012$ and tip height, $h/L = 0.013$ for the AFM probe used on the sample of gold and length offset $L_2/L = 0.013$ and tip height, $h/L = 0.012$ for the AFM probe used on the SS sample. The tip height is slightly lower than the manufacturer value of $h/L = 0.02$–0.004, indicating possible tip damage. Information on the length-offset is not provided by the manufacturer.

The iterative procedure, outlined in Section 5.3, gives data across a range of locations and sensor-sample distances (which we relate to normal loads). In Figure 5.8, we plot the contact wavenumber as a function of the normalised contact stiffness ($k_\perp/k_c$) for each mode. We highlight the range of observed contact wavenumbers by red horizontal lines for each mode and give both the contact stiffness calculated for the model of a tilted

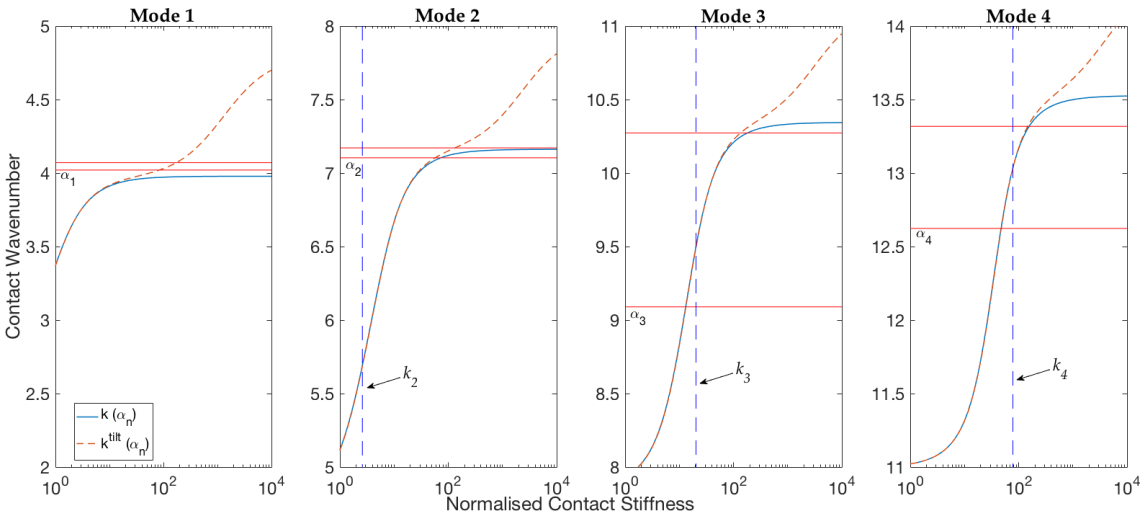

(a) Gold

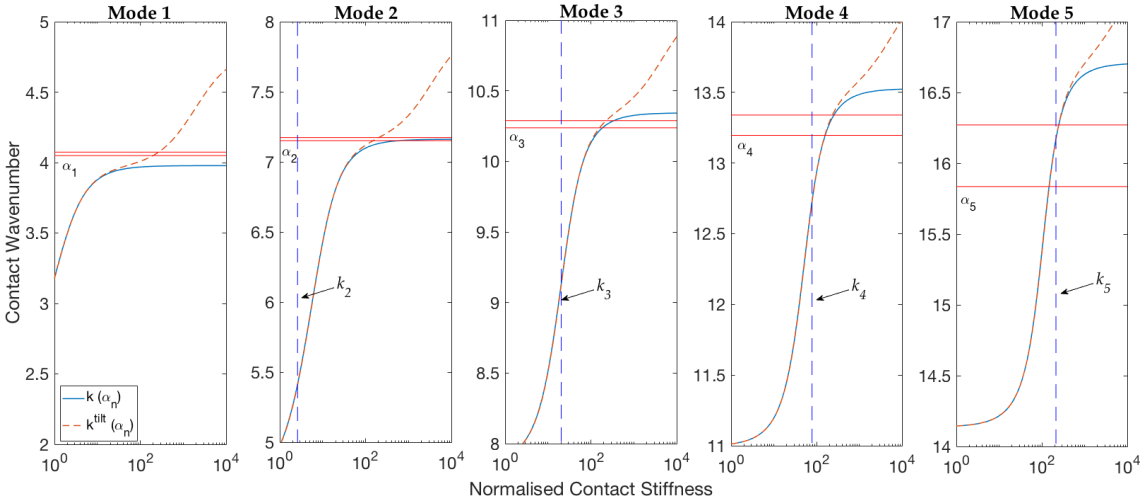

(b) Steel 316

Figure 5.8: The normalised contact stiffness, calculated using (4.46) as described in Section 4.4.5. We note that the contact stiffness calculated on the gold sample has a large standard deviation, as given in Table 10, owing to the large variation in the measured resonant frequency as shown in Figure 5.5. The sample of SS grade 316 has much lower variance, with a mean of 1948.8 ± 123.8 across all modes, with further details given in Table 11 .

beam (shown as a dashed orange line and where we assume $k_{\parallel} = 0.8$ and $\theta = 0.19$) and a parallel beam (solid blue line), as described in Chapter 4, that both have the tip offset by the values calculated above.

For the gold sample, shown in Figure 5.8a, we find that there is very large variation in the observed contact wavenumber, as reported in Table 10, and that this leads to an average normalised contact stiffness (calculated across all modes) of $k_{\perp}/k_c = 1744 \pm 843$, where the error is calculated as the standard deviation across modes. This is equal to a contact stiffness of $115\,\mathrm{N\,m^{-1}} \pm 56\,\mathrm{N\,m^{-1}}$, which agrees well with the predicted range of $k_{\perp} = 72 - 334$ given in Table 7. The variation in contact stiffness will be directly caused by the variation in the measured resonant frequency, shown in Figure 5.5, which undergoes a qualitative change when the distance between surface and sample is great (relating to low tip forces). This is particularly true for the third mode which contains a variation in α_3 of 8% but a corresponding variation in contact stiffness of 74%, as shown in Table 10.

When considering the SS sample, we find that there is much lower variation in the observed wavenumber, shown as red horizontal lines in Figure 5.8b and given in Table 11. We find that average normalised contact stiffness, calculated across all modes using the average wavenumber, is $k_{\perp}/k_c = 2187 \pm 433$, or $k_{\perp} = 144\,\mathrm{N\,m^{-1}} \pm 29\,\mathrm{N\,m^{-1}}$ which is also within the range of predicted contact stiffness, $k_{\perp} = 132 - 640$ given in Table 7. The decreased variation is further emphasised when we observe that the contact stiffnesses are largely consistent across all modes, as shown in Figure 5.8b. However, we find that the modal consistency of these contact stiffnesses requires the use of a tilted beam model for low modes, as shown in Figure 5.6b. We find that the contact wavenumbers cannot be related to a contact stiffness when using the first mode in conjunction with the model of a parallel beam with tip offset, as presented in Section 4.4.4. On the other hand, we find that the higher modes ($n = 4, 5$) are much less sensitive to lateral forces such that the difference between the contact stiffnesses calculated using the parallel beam approximation and a tilted beam (both with a length offset) is less than 1%.

Our results indicate that the higher modes of a soft cantilever (which increasingly behave as a parallel beam) are those that have an effective stiffness, as calculated using the method in Chapter 2, similar to the resulting contact stiffness. This highlights the possibility of stiffness matching for soft cantilevers in contact with stiff materials. We discuss our findings in more detail in Section 5.5. We next turn to how the values of the contact stiffness represent the theories describing contact mechanics, as outlined in Section 5.2.

5.4.2 *Calculating a Sample–Specific Elastic Modulus*

Given our iterative procedure, outlined in Section 5.3, we are able to investigate how well the theories of contact mechanics between the sample and sensor, as described in Section 5.2, are observed in practice. To do so, we consider how the normalised contact stiffness, calculated using (4.46) with the parameter choices given in Section 5.4.1, vary

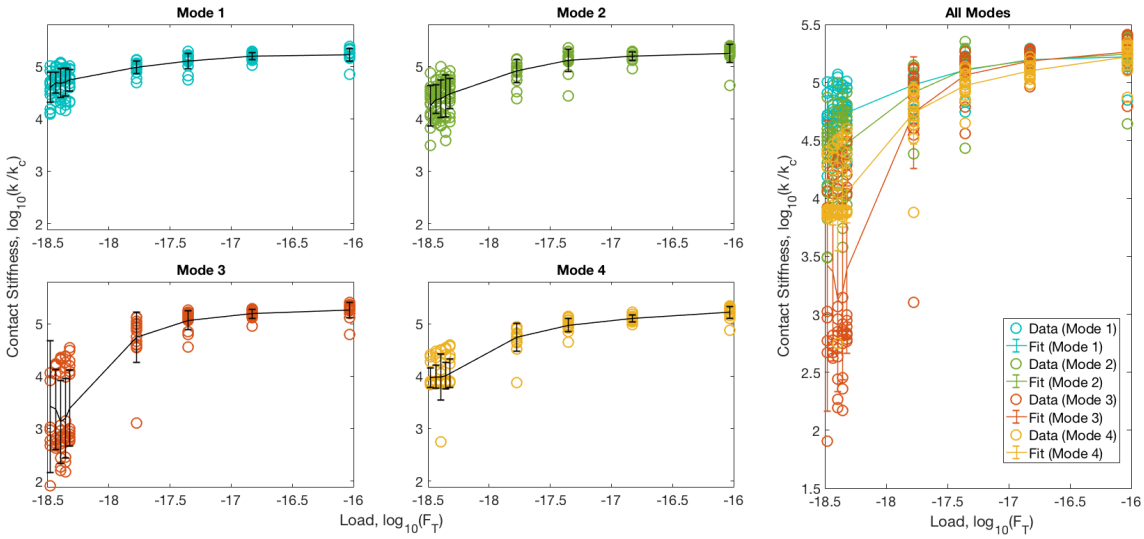

Figure 5.9: Log-log plots of the normalised contact stiffness for modes one to four for all sixteen positions, as well as the calculated normalised contact stiffness across all modes and positions, against the normal loads considered, as calculated by (5.1) for $R_{\text{tip}} = 20\,\text{nm}$. We see a significant change in the normalised contact stiffness as we move from high force to low force, most clearly signified by mode 3. Dashed lines represent lines of best fit across all data points, with errorbars drawn using the standard deviation of each normal load.

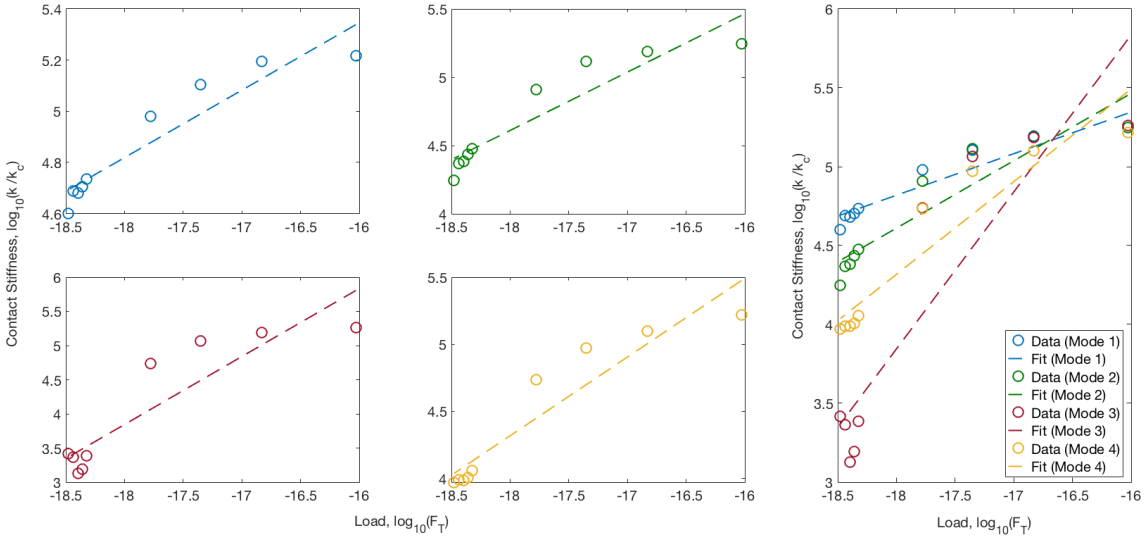

Figure 5.10: Log-log plots of the normalised contact stiffness for modes one to four for all sixteen positions, as well as the calculated normalised contact stiffness across all modes and positions, against the normal loads considered, as calculated by (5.1) for $R_{\text{tip}} = 20\,\text{nm}$. We see a significant change in the normalised contact stiffness as we move from high force to low force, most clearly signified by mode 3. Dashed lines represent a power-law fit, as described in Section 5.2.

	Contact Wavenumber		Normalised Contact Stiffness		Contact Stiffness	
	α_n	σ_α	$k_\perp/k_c$	$\sigma_{k_\perp/k_c}$	$k_\perp$	$\sigma_{k_\perp}$
Mode 1	4.093	(0.060)	2073	(576)	136	(38)
Mode 2	7.215	(0.043)	1855	(781)	122	(52)
Mode 3	9.76	(0.78)	1511	(1110)	100	(73)
Mode 4	13.02	(0.50)	1537	(818)	101	(54)

Table 10: The mean contact wavenumber, normalised contact stiffness and contact stiffness, shown with standard deviation displayed in brackets for the sample of gold (Au)

	Contact Wavenumber		Normalised Contact Stiffness		Contact Stiffness	
	α_n	σ_α	$k_\perp/k_c$	$\sigma_{k_\perp/k_c}$	$k_\perp$	$\sigma_{k_\perp}$
Mode 1	4.060	(0.014)	2344	(372)	230	(36)
Mode 2	7.163	(0.014)	2231	(382)	219	(38)
Mode 3	10.261	(0.031)	2352	(489)	231	(48)
Mode 4	13.269	(0.079)	2107	(455)	206	(44)
Mode 5	16.000	(0.297)	1894	(457)	186	(45)

Table 11: The mean contact wavenumber, normalised contact stiffness and contact stiffness, shown with standard deviation displayed in brackets for the sample of SS grade 316

over a range of positions on the sample, reflecting changes to the normal load on the cantilever. Furthermore, we are able to do so over a range of locations on a sample. This gives us an indication as to how robust these theories are to repeated measurements on a sample.

In Figure 5.9, we show log-log plots of the normalised contact stiffness calculated at each location on the sample of gold for the range of normal loads investigated. We note that there appears to be two regions of calculated contact stiffness at low forces (loads less than 10 µm), most strongly demonstrated by the increased standard deviation in measurements taken with mode three. We discuss this further in Section 5.5. Instead we consider how these values of contact stiffness reflect a material property.

We first assume that the tip is hemispherical with radius $R_{\text{tip}} = 20\,\text{nm}$. We then fit (5.17) and calculate the reduced modulus using (5.18). We calculate the mean reduced modulus across all positions to be 329 GPa ± 68 GPa, 272 GPa ± 62 GPa, 143 GPa ± 81 GPa, and 199 GPa ± 49 GPa for the first four modes (where the error is given by the standard deviation across all positions). This is significantly larger than the expected reduced modulus of 60 GPa. We then consider whether treating the exponent of the contact mechanics as an additional parameter improves calculation of the reduced modulus, representing a deviation from a hemispherical tip. These fits are calculated using the lines of best fit given in Figure 5.10, where the standard deviation across measurement positions (for each load) is used as a weight in a weighted linear regression procedure, as shown in Figure 5.9 and results given in Table 12. Each straight line represents a linear fit where the exponent is assumed to be unknown representing a tip with unknown geometry, as

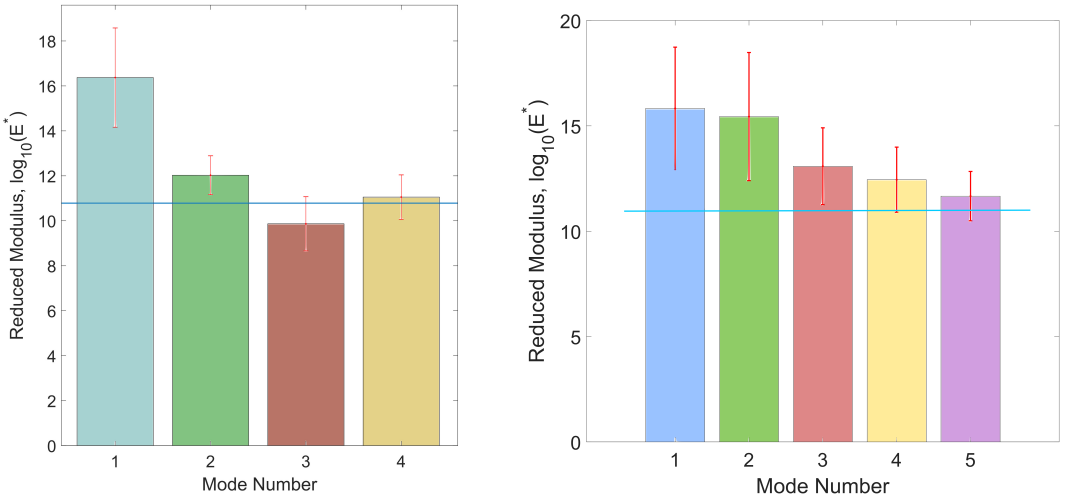

(a) Gold (b) Steel

Figure 5.11: The calculated reduced modulus,$\log_{10}(E^*)$, found using the power law fits to the data shown in Figure 5.9 (gold) and Figure 5.12 (SS 316), calculated using (5.15) described in Section 5.2. We display the log values to highlight that the difference in the reduced modulus, found using the power law fits, spans several orders of magnitude. The blue horizontal line represents the expected reduced modulus for each sample material.

described in Section 5.2. We find that the exponent of the fit varies with mode number, as 0.32 for mode 1, 0.44 for mode 2, 1.1 for mode 3 and 0.63 for mode 4.

Using these fits, it is possible to back-calculate the reduced modulus of the material. In Figure 5.11 we show the calculated reduced modulus for the gold sample for each mode. We find that the reduced modulus varies over several orders of magnitude, owing to the large difference in fitted exponents. We include these results in Table 12. The first mode number is closer to the expected reduced modulus for gold but has a standard deviation that covers over four orders of magnitude. However the standard deviation decreases with mode number, where the fourth mode has a standard deviation of one order of magnitude.

We next consider the case of repeated measurements over the SS sample. The contact stiffness for each mode over a range of forces is shown in Figure 5.12. All contact stiffnesses, as well as lines of best fit are shown in Figure 5.12, with error bars representing the standard deviation across multiple locations on the sample for each mode. The fitting procedure allows us to specify a tolerance for which we can reject measurements which do not observe a power law relation. We set a tolerance that the weighted linear regression must have RMSE > 0.95 and a p-value < 0.05, such that we reject all measurements that do not exhibit a significant linear regression relationship. Note that none of the measurements performed on the gold sample met this criteria.

We first use these lines of best fit to calculate the reduced modulus with an assumed exponent of $1/3$, representing a hemispherical tip. We find that more positions at higher modes meet the fitting criteria defined above, where the number of positions are 5, 7, 11, 17, 20 for modes one to five, respectively. The mean calculated reduced modu-

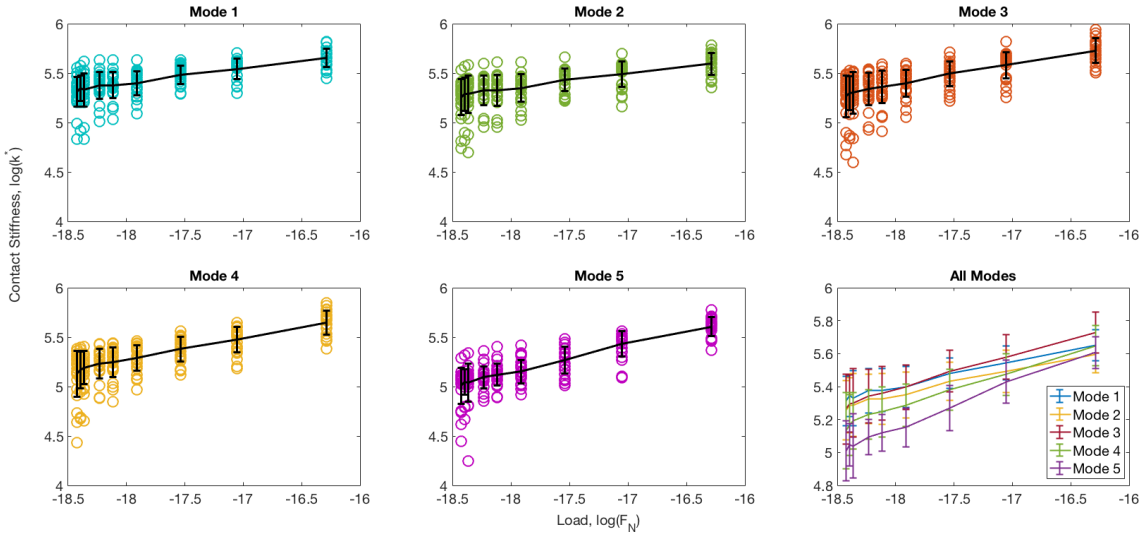

Figure 5.12: Log-log plots of the contact stiffness against the contact force across all positions on the SS grade 316 sample, shown for the first five modes as well as for all modes. Dashed lines in each frame show lines of best fit, where errorbars represent standard deviation across measurement positions.

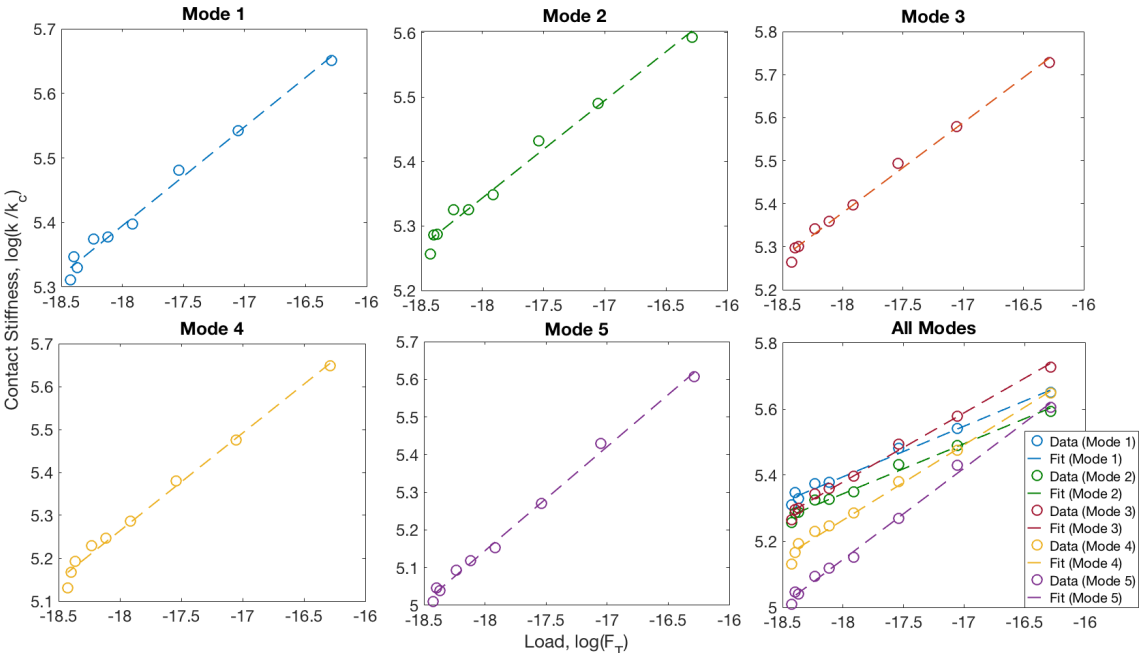

Figure 5.13: Log-log plots of the contact stiffness against the contact force across all positions on the SS grade 316 sample, shown for the first five modes as well as for all modes. Dashed lines in each frame show the results of a linear fit using the method described in Section 5.2.

lus across these positions are 657 GPa ± 157 GPa, 558 GPa ± 119 GPa, 650 GPa ± 165 GPa, 597 GPa ± 130 GPa, and 524 GPa ± 94 GPa for the first five modes (where the error is again given by the standard deviation across all considered positions). All are considerably higher than the expected reduced modulus of E^* ∼90 GPa.

We next consider how fitting with the exponent as a free parameter varies our results. First, we fit (5.15) to each of the lines of best fit given in Figure 5.12. In Figure 5.14, we give the calculated reduced modulus for the five modes that we have investigated, showing the effect of removing those positions that do not meet our fitting tolerance. Again, we find that the reduced modulus is significantly larger than expected, with results given in Table 12.

In order to investigate of the possible influence of tip wear on our measurements, we repeat these fits using three different values for tip radii to calculate the reduced modulus, R_{tip} = 20 nm, R_{tip} = 37 nm, and R_{tip} = 65 nm. We choose these values as they have been observed in [91] which investigated the contact mechanics of an AFM probe with silicon tip, with initial tip radius of R_{tip} = 7 nm, in contact with a specimen of fused quartz, with an indentation modulus of 68.4 GPa ± 1.7 GPa, and where the tip was exposed to normal forces that ranged from 0.75 µN to 45 µN. However, the spring constant of the cantilever used was 3.7 N m^{-1} and only the first mode was investigated. As we are utilising a soft cantilever and a lower force regime, we expect the tip radius to be less exposed to tip wear than those observed in [91] and treat these values as upper limits for changes to the tip radius.

We show the results of utilising different tip radius in Figure 5.15. We find that the standard deviation in reduced modulus decreases as we increase the tip radius. However, we are unable to say with confidence which tip radius is correct without further measurements such as SEM imaging. Instead, we note that when the tip radius is R_{tip} = 37 nm, the exponent most closely matches the hemispherical assumption of 1/3 for all modes, 0.21, 0.24, 0.31, 0.32 and 0.37, but that the reduced modulus at each mode is still found to vary over several orders of magnitude, though mode 4 most closely resembles the expected reduced modulus of the material, 54 GPa ± 73 GPa compared to E^* ∼ 90 GPa. Hence, we find that we are unable to quantify our measurements, and confidently relate the calculated contact stiffnesses to a material property. In Section 5.5, we discuss our findings with regards the modal consistency of the contact stiffness as well as possible causes for the uncertainty in our fitting procedure.

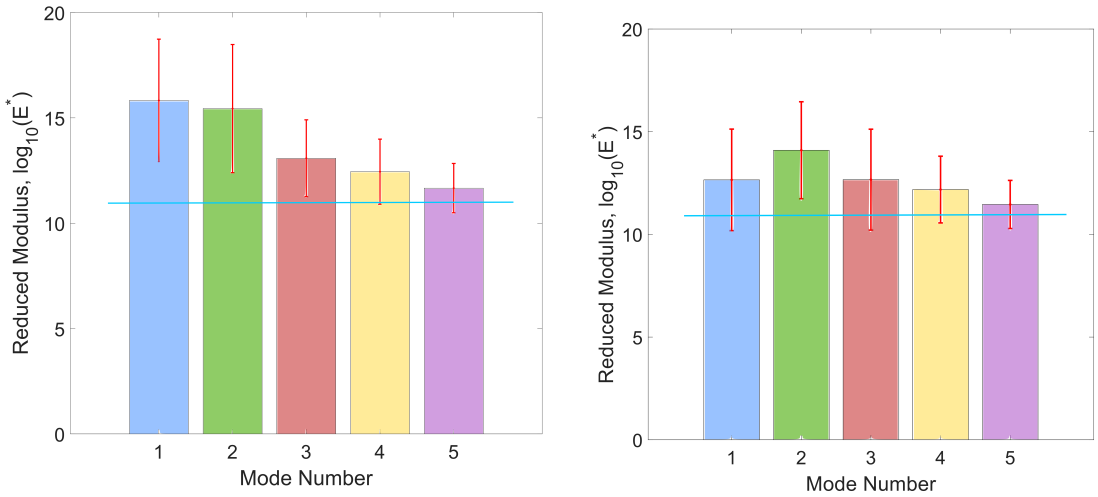

(a) (b)

Figure 5.14: By introducing a tolerance based on the goodness of fit parameters from the fitting procedure described in Section 5.2, we decrease the variation across modes in calculating the reduced modulus. We show an example comparison here, where we compare the results of the reduced modulus as calculated on the SS grade 316 sample with an assumed tip radius of 50 nm, shown without a tolerance (a) and with a tolerance (b).

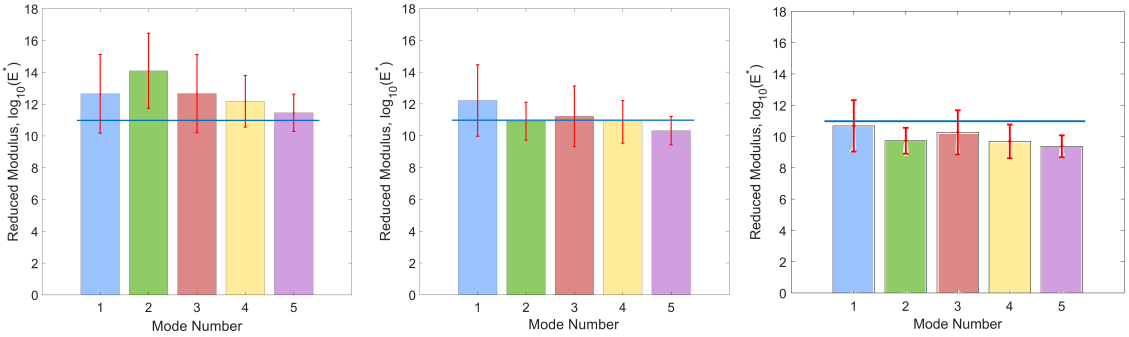

(a) R_{tip} = 20 nm (b) R_{tip} = 37 nm (c) R_{tip} = 65 nm

Figure 5.15: For the measurements on SS grade 316, we find that an increased radius results in a reduced modulus, as calculated according to (5.15) as described in Section 5.2, increasingly matches the expected reduced modulus of the sample, 95 GPa, shown as the dashed line in all figures. We expect that this is due to significant tip wear during imaging, resulting in a larger radius of the tip and a corresponding larger contact area. However, without knowledge of the tip radius, we are unable to quantify these results. Details of the measurements are included in Table 12

		Mode 1	Mode 2	Mode 3	Mode 4	Mode 5
Au	$E^*(R_{tip} = 20\,nm)$	$O(11)$	$O(10)$	$O(8)$	$O(9)$	–
SS	$E^*(R_{tip} = 20\,nm)$	$O(17)$	$O(17)$	$O(15)$	$O(14)$	$O(13)$
	$E^*(R_{tip} = 37\,nm)$	$O(13)$	$O(13)$	$O(11)$	$O(11)$	$O(10)$
	$E^*(R_{tip} = 64\,nm)$	$O(11)$	$O(11)$	$O(10)$	$O(10)$	$O(9)$
SS (tol)	$E^*_{tol}(R_{tip} = 20\,nm)$	$O(16)$	$O(15)$	$O(14)$	$O(13)$	$O(13)$
	$E^*_{tol}(R_{tip} = 37\,nm)$	$O(13)$	$O(12)$	$O(11)$	$O(11)$	$O(10)$
	$E^*_{tol}(R_{tip} = 64\,nm)$	$O(11)$	$O(10)$	$O(10)$	$O(9)$	$O(9)$

Table 12: The results of back-calculating the reduced modulus from the linear fit described in Section 5.2 for the sample of gold (Au) and SS grade 316, shown for the first four modes for gold and the first five modes for SS grade 316. We see significant variation in the reduced modulus of the material across multiple modes. For the SS grade 316, we note an improvement in the order of magnitude of the results as we increase the tip radius but note that absolute quantification is impossible without accurate knowledge of the radius. We find that the results are improved (insofar that there is lower variation in results) when we introduce a tolerance for the included results.

5.5 DISCUSSION

The work in this chapter has been focused on calculating the contact stiffness of stiff materials, considering how it varies across mode number, the relationship between contact stiffness and load, and considering whether we can fit the model of contact to low resolution load-stiffness measurements in order to calculate the reduced Young's modulus of a material. In Section 5.4.1, we have shown that modal consistency is obtained when the model of a tilted cantilever with offset tip in contact with a surface is used for the lower modes of a soft cantilever (in contact with a stiff material), while the higher modes can be approximated by the model of a parallel beam with offset tip in contact with a surface.

From our findings, we make the following observations. First, we repeat that our method for the estimation of the tip height and offset leads to contact stiffness values that are consistent across modes. This is crucial to the implementation of contact resonance methods on stiff materials using the lower modes of a soft cantilever. We note that, to the best of our knowledge, our method of parameter estimation is novel, and has not been previously implemented. In general, the lower modes of a cantilever will have improved signal-to-noise ratios due to their higher amplitudes. However, as we have discussed, their use requires knowledge of additional cantilever and system parameters. Specifically, the influence of the tip height should not be underestimated; a change in tip height of 1% will result in a change in a calculated contact stiffness by as much as 40% for low forces ($F_T < 10\,nN$). On the other hand, the higher modes of an AFM probe increasingly approximate a parallel beam which does not required knowledge of these parameters. Hence, the importance of the tip height (as well as knowledge of the lateral contact stiffness and tilt angle, though we show in Section 4.5 that these have a reduced influence in the resulting contact stiffness) highlights a trade-off for CR-AFM measurements with soft cantilevers on stiff materials; the ability of the AFM

detection system to accurately calculate the resonant frequencies of higher modes and the knowledge of a cantilever's tip height.

Second, we find that the observed contact wavenumbers on both the sample of gold and SS move closer to the first inflection point of the contact stiffness curves with higher mode number. This is particularly true of the measurements on SS (which have a reduced variation in the measured contact frequencies, demonstrated by the smaller spread in contact wavenumbers) and is the cause for the decreased sensitivity to lateral forces, such that the first inflection point is changed by introducing an offset to the position of the tip and not by a tilt to the sensor-sample system (see Section 4.5 for further discussion).

This can be further understood in terms of the effective stiffening of a cantilever with high mode number, as discussed in Chapter 2 and demonstrated by the increased proximity of the effective stiffness of the cantilever, k_n, to the observed contact wavenumbers, as shown by the vertical blue lines in Figure 5.6b. This emphasises the possibility of stiffness matching the higher modes of a soft cantilever for contact resonance measurementts on stiff materials. Hence, we find that our method for parameter estimation, along with the concept of modal consistency, motivates the utilisation of higher modes when performing contact resonance measurements on stiff materials using soft cantilevers.

Finally, we note that there can be significant variation in the observed contact wavenumber, caused by a variation in the resonant frequencies. This is observed in the qualitative change in the contact wavenumber for the sample of gold from low to high normal loads, as shown in Figure 5.5, but is also observed for certain modes and forces on the SS sample. For example, we observe a recorded contact wavenumber of 15.2 during data collection for the fifth mode on the SS sample. Though this corresponds to a decrease of 5% to the average contact wavenumber, given in Table 11, it causes a decrease in the calculated normalised contact stiffness from 1,894 (the mean value) to 885, a 50% reduction. Moreover, the difference in this calculated wavenumber from the average wavenumber corresponds to a 10% difference in the measured resonant frequency. This highlights the sensitivity of calculations of a contact stiffness to experimental conditions.

We next discuss how the contact stiffness relates to a material property. By fitting the contact stiffness calculated over a range of forces to a model of the contact mechanics, given in Section 5.2, we are able to test how well the contact stiffnesses relate to a reduced modulus (which contains information about the Young's modulus of the sample). However, as discussed in Section 5.4.2, we find that the contact mechanics models overestimates the reduced modulus when the tip is assumed to be hemispherical and that the reduced modulus can range over several orders of magnitude when the tip geometry is a fitting parameter. We now discuss possible causes for the uncertainty in our results.

First, we consider how the properties of the tip will affect our calculations of the reduced modulus. We have shown that, for both samples and across multiple locations, the fitted exponent can vary significantly from $1/3$. This implies that the tip is, in fact, subjected to considerable tip wear during our single point measurements. Furthermore, we have found that the change in tip radius will have significant influence on the calculation of the reduced modulus. A change in the tip radius will influence the adhesion

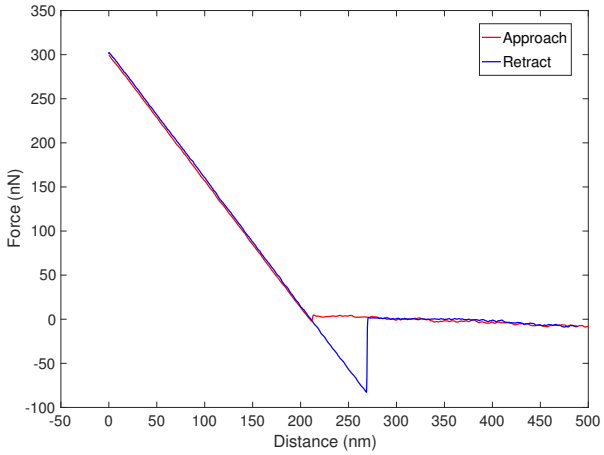

Figure 5.16: An example of the force-distance curve measured using the Cypher AFM on a position (1) on the SS grade 316 sample. The force-distance curve on all locations shows no hysterisis between the approach and retract curves, signifying that the material does not exhibit significant viscoelastic behaviour, as described in Chapter 1.

force, (5.11), with $F_c = 9\,\text{nN}$, 16 nN and 30 nN, for tip radii , $R_{\text{tip}} = 20\,\text{nm}$, 37 nm and 65 nm, respectively. This causes a change in the resulting fit parameters, increasing the exponent with increased radii. We note that our means for calculating the reduced modulus (5.16) also uses the tip radius though this is expected to have a lesser effect. As such, the tip geometry and radius are critical parameters for these single point CR-AFM measurements such that the tip properties require careful consideration both pre- and post-measurement. The influence of the tip geometry has been discussed elsewhere, see, for example, [205].

We do not have accurate information about the tip radius or tip geometry but can infer changes in the tip (or the accumulation and subsequent loss of debris) by considering any sudden changes in the calculated reduced modulus when fitting with a free exponent and infer that tip wear occurs by considering how the calculated reduced modulus varies across position number with subsequent measurements. This is shown in Figure 5.17, where it appears that substantial changes to the system occur for the first eleven positions (if position thirteen is ignored), shown by the range in reduced modulus over several orders of magnitude for these positions. On the other hand, positions fourteen onwards (as well as position twelve) appear to correspond to measurement stability as the calculated reduced moduli vary across a smaller range. We note also that the higher modes vary across a much smaller range of reduced modulus, which we posit is caused by the effective stiffening of the AFM probe, discussed in Section 5.4.1.

The tip radius will influence the level of adhesion that is incorporated into the system, as indicated by (5.11). The adhesion in the system may also play a role in the increased variation in our measurements. Our procedure operates by bringing the cantilever into contact with the surface and then reducing the separation distance between tip and surface until contact is broken. We show an example force-distance curve, similar to the schematic Figure 1.3 given in Chapter 1, in Figure 5.16. We note that there exists a region of significant adhesion which is beyond the snap-to-contact event and occurs before

the contact between sensor and sample is broken (the snap-from-contact event). Hence, for low separation distances, reflecting small normal loads, our measurements may be distorted by the influence of a meniscus layer which prevents a snap-from-contact event from occuring. Note that there is no evidence of viscoelasticity on the SS sample, shown by the lack of hysterisis in the contact regime.

This motivates a third source for potential error which is caused by the low force regime under investigation as well as the use of an AFM with OBD detection system. During data collection, we have not explicitly considered how the sample topography influences the contact event. For example, the tip may come into contact with the edge of a feature or a sample region with a large slope. In Section 5.2, we assume that the contact event initially occurs at a single point and that both tip and surface begin parallel to one another. However, if the tip comes into contact with an edge (or multiple edges), then the contact mechanics require altering to account for the subsequent change in contact area (or the simultaneous introduction of more than one contact area).

For example, the gold sample has grains, shown in Figure 5.4, that range from 5 nm to 20 nm. The radius of the tip provided by the manufacturer is given as less than 10 nm, though tip wear can lead to an increase in this, as previously discussed. Given the similarity in size between the tip radius and grain, a variety of contact events are possible; such as grazing contact or multiple asperity contact. Each would require an altered representation of the contact event, such as different configuration of contact springs (see, for example, [168]). This is more likely to occur at low normal forces, as the contact area is more sensitive to the orientation of the sample and may also occur for the SS sample, though it is less likely to be caused by the grain size of the SS sample which are typically much larger than that of gold, as shown in Figure 5.4 and Figure 5.6.

This further motivates a question on the suitability of our assumption that the contact stiffness is well approximated by a linear spring. Previous research, [185], has noted the possibility of nonlinearities in contact resonance measurements performed on stiff materials both theoretically and through direct observations. In [185], the nonlinearities are found to occur when the cantilever is forced to oscillate at large vibration amplitudes around its equilibrium condition. However, for the measurements undertaken here, we have considered small amplitude oscillations, especially when considering the higher modes of the cantilever. Hence, we do not expect the linear assumption, introduced in Chapter 4 to be the dominant cause for the uncertainty in material properties given in Section 5.4.2.

Instead, we suggest that the tip geometry, which will affect both the amount of adhesion in the system as well as the underlying contact mechanics of the system to be a significant barrier in the quantification of these contact resonance measurements. We note that we are not the first to come to this conclusion, which was previously discussed in [192, 205]. However, previous work has focussed on using only the first mode to calculate the contact stiffness (and hence, the material properties of a stiff sample) but the tilt of the cantilever was not included. As shown in Section 5.4.1, this can result in large inaccuracies in the calculated contact stiffness. Additionally, we believe that the low force regime ($F_N < 0.15\,\mu m$) investigated here are more exposed to the influence of adhesive

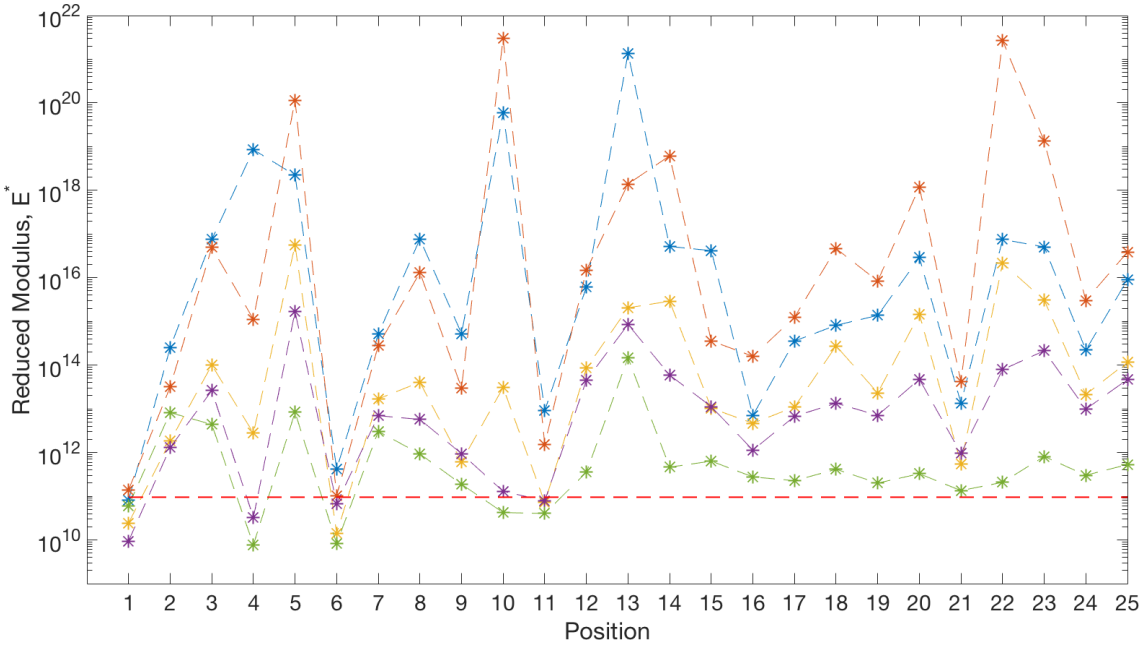

(a) All Modes

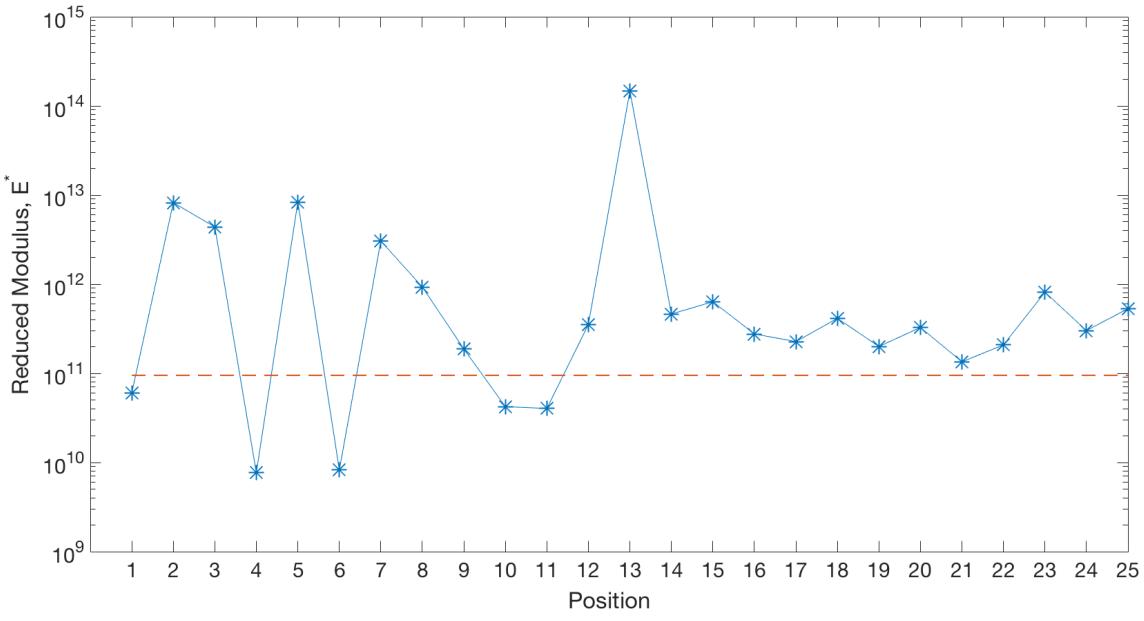

(b) Mode 5

Figure 5.17: For the measurements on SS grade 316, we find that the initial measurement positions vary significantly between each position. However, later positions (such as 14 onwards) appear to have much less variation in the reduced modulus (especially when considering the fifth mode). This supports the possibility of tip wear between sample positions. Note that data collection occured at subsequent positions, starting at position one and and continuing until position twenty five.

forces than the high force regime, shown in Figure 5.16. Therefore, our measurements motivate the use of a high normal force regime that does not cause significant tip wear during operation. This is exactly the regime operated in during high-speed AFM, introduced in Chapter 1, as the tip is 'protected' from tip wear due to a hypothesised lubrication layer, as evidenced by the stability in imaging quality over large collection periods and areas. In Chapter 6, we demonstrate the capabilities of performing contact resonance on HS-AFM (CR-HSAFM).

5.6 CONCLUSIONS

In this chapter, we have investigated how to calculate the normal contact stiffness, how it varies with the higher modes of a cantilever and to what extent there is a clear load dependence exhibited by measurements of a contact stiffness which can be related to a reduced modulus. The normal contact stiffness is an idealisation of the contact event between the AFM probe and sample. As such, we are required to know the robustness and limits of this idealisation in order to use the contact stiffness as a tool for measuring material properties at the nanoscale. To this end, we can draw the following conclusions from our investigations.

First, our results suggest that the contact stiffness is only weakly influenced by mode number of the oscillating sensor, provided that the material parameters of the probe are known. Specifically, information is required of the tip height and the length offset of the tip from the free end of the probe. We have introduced a new method for calculating these two parameters in a straightforward manner, without the need for additional measurements (e.g. by SEM imaging). We achieve this by calculating the contact stiffness, given a shift in frequency and corresponding contact wavenumber, for a range of possible values of length offset and tip height. As shown in Figure 4.12, this leads to values for both length offset and tip height which give a calculated normal contact stiffness is consistent across multiple modes. Hence, the inclusion of these two parameters ensures the existence and consistency of contact stiffness for multiple modes of a sensor.

Second, we find that our measurements do not convincingly follow the DMT theory of contact mechanics. We note that this is likely due to the low-resolution nature of the results, where repeated measurements on the cantilever may have caused significant tip wear, changing the tip radius and geometry between measurements. This highlights that contact resonance AFM, though non-destructive, is not amenable to single point measurements unless consideration is given to potential tip wear. Hence, contact resonance measurements are ideally taken under low-wear conditions. We exploit a low-wear high-force instrument in Chapter 6, where we combine the contact resonance technique with HS-AFM.

6

HIGH SPEED LARGE AREA STIFFNESS MEASUREMENTS

The stainless steel (SS) grade 316 sample (UNS S31600) used for experiments described in this chapter is a different section of the same sample as that used in Chapter 5, and was polished and prepared by Miss Stacy Moore (University of Bristol, UK). The silicon-graphene sample, used in Section 6.3, was prepared by Dr Chris Howard (University College London, UK). Additional experimental work in Section 6.3 was carried out with assistance and guidance from Dr Loren Picco (University of Bristol, UK) and Mr Freddie Russel-Pavier (University of Bristol, UK).

6.1 INTRODUCTION

We have now described the necessary knowledge required to implement acoustic measurements on an AFM. In Chapter 2, we introduced our new method for calibration of micro-mechanical cantilevers which we use to calculate the effective stiffness of an AFM probe operated at higher modes, as well as calculating the resonant frequencies of the cantilever in vacuo. We utilise this method when selecting the resonant mode of the cantilever which is expected to have the greatest sensitivity to material properties and to check the resonant frequencies of the probe in Section 6.2.1. In Chapter 3, we showed that the higher modes of a cantilever are less sensitive to the additional damping terms caused by the hydrodynamics of the surrounding fluid. In Chapter 4, we have shown how to relate a shift in resonant frequency to a contact stiffness and, in Chapter 5, we have shown that the higher modes of an AFM probe with low spring constant are more sensitive to the properties of stiff materials. The higher modes of an AFM probe also result in higher frequencies being used, making them ideal for high-speed AFM (HSAFM) which requires high frequency throughput. We now demonstrate the benefits of combining the contact resonant technique with the HS-AFM developed at the University of Bristol; that the fast scan rates of the HS-AFM allow for non-destructive measurements on a range of stiff materials and result in non-topographic feature extraction. This leads to CR-HSAFM, a tool that is capable of non-topographic non-destructive sample measurements over micron-sized areas with frame-rate capture times.

We begin this chapter by describing AFM at high speeds, and how other contact resonance techniques detect and measure the frequency response at each pixel of an AFM image. In Section 6.2, we describe our method for relating a change in amplitude, as measured using single- or dual-channel information of a lock-in amplifier, to a shift in resonant frequency. In Section 6.3, we describe measurements on two material samples, the same stainless steel (SS) grade 316 sample (UNS S31600) as examined in Chapter 5, as well as a silicon sample with deposited graphene flakes, and discuss the results of these

measurements in Section 6.4. This represents the combination of work found in all earlier chapters of this thesis, culminating in quantified stiffness mapping of stiff materials using HS-AFM. We point towards future avenues of investigation in Section 6.5. We outline and demonstrate how this achieved in this chapter.

6.1.1 *Contact Resonance Imaging Methods*

In order to combine the single point contact resonance measurements, described in Chapter 4 and Chapter 5, we require frequency information at each pixel that can be used to calculate the change in resonant frequency of an AFM probe. Since the advent of CR-FM, several methods have been introduced to achieve such frequency maps. We discuss such techniques here, before proceeding to outline two of our own methods for creating frequency maps with HS-AFM that do not make use of additional control-loops or hardware constraints.

Contact resonance techniques, as we have seen in Chapter 4, exploit the shift in the resonant frequency of an AFM probe due to sensor-sample interaction, in order to infer stiffness properties of a sample. As such, the resonant frquencies of the cantilever probe are required at each sample location where the stiffness is under investigation. One means for constructing such frequency maps is band excitation (BE) which excites and detects the response of an AFM probe across a suitable band of frequencies simultaneously [206]. The band is chosen to contain those resonant frequencies that are expected to be sensitive to sample properties. BE methods have been successful at exploring how a sample varies with time, temperature or voltage as well as under different local (as applied to the tip) or global (as applied to the sample) stimuli (see, for example, [206] for a review of BE results). This is because the data contained inside an entire frequency sweep reveals information, not just of the change in frequency but also changes to the Q factor, phase and amplitude, occuring both on and off resonance. However, BE methods result in images that are often prohibitively large, as AFM images can contain several thousands (if not tens of millions for HS-AFM) of pixels, each of which require a frequency sweep to be recorded [206]. As such, many CR-FM techniques resort to less data-intensive mechanisms.

Dual resonance frequency tracking (DRFT) [207] and dual A/C frequency tracking (DART) [130] both utilise a lock-in amplifier[1] to drive the cantilever at two frequencies, simultaneously, either side of the resonant frequency that is expected to be most sensitive to changes in material properties. DRFT considers only the change in the cantilever's oscillation frequency, as measured by differences in the amplitude at some driving frequency, due to the influence of material properties. The change in frequency is then used to calculate a shift in resonant frequency. Similarly, DART makes use of a lock-in amplifier to measure the change in amplitude, but also measures the phase at two driv-

1 See Chapter 1 for more discussion on the utilisation of a lock-in amplifiers.

ing frequencies either side of the resonant frequency. The change in both amplitude and phase (a total of four measurements) is then related to a change in frequency by [208],

$$f_R' = \sqrt{f_1 f_2 \frac{f_2 X_1 - f_1 X_2}{f_1 X_1 - f_2 X_2}}, \tag{6.1}$$

where f_R' is the shifted resonant frequency, (f_1, f_2) are the driving signal frequencies either side of the resonant peak and X_1, X_2 represent non-dimensional parameters defined to be

$$\begin{aligned} X_1 &= -\frac{1 - \text{sign}(\Phi)\sqrt{1+\Phi^2}/\Omega}{\Phi} \\ X_2 &= -\frac{1 - \text{sign}(\Phi)\Omega\sqrt{1+\Phi^2}}{\Phi}, \end{aligned} \tag{6.2}$$

where $\Phi = \tan(\phi_1' - \phi_2')$ and $\Omega = f_1 A_1' / f_2 A_2'$, for shifted amplitudes A_1', A_2' and shifted phase measurements ϕ_1', ϕ_2'.

These methods are the most popular of CR-FM imaging methods, commonly implemented in many commercial AFMs, such as the Cypher AFM used in Chapter 5. They have been able to calculate material properties of a range of materials including DNA, ferroelectric materials and viscoelastic property information [130, 208]. However, both DRFT and DART require the implementation of a control loop that keeps both amplitudes at equal height, as they are based on the symmetry of the resonant peak. This is problematic for the HS-AFM developed at the University of Bristol, as such control requires additional time-consuming protocols to be implemented which reduces the scan speed and corresponding sample throughput.

BE, DRFT, and DART all introduce limitations either through the need for additional hardware, control loops, substantial data storage capabilities or some combination of these three. Here, we describe how to implement CR-imaging on HS-AFM without recourse to one of these techniques. As such, we avoid the need for additional control loop considerations of DRFT/DART, and demonstrate how single- or dual-channel information from a lock-in amplifer can be used to rapidly estimate the resonant frequency on a per-pixel basis. We compare our technique to DART methods in Section 6.4.3, where we find that our method of dual-channel CR-HSAFM is at least as capable of existing DART methods for CR-AFM imaging, but with significantly higher pixel count. This results in a device capable of large area real-time stiffness mapping, with nanometre height resolution, and which complements existing topographic capabilities by identifying previously hidden sample features.

6.2 METHODS

When combining contact resonance techniques with HS-AFM, we make use of a lock-in amplifier to monitor the change in resonant frequency. The lock-in amplifier can be set to measure the change in amplitude or phase using one of four independent channels,

where the measured change in amplitude and phase are used to calculate shifts in the resonant frequency due to a sensor-sample contact event. Here, we describe our methods for converting single and dual channel lock-in amplifier measurements to changes in resonant frequency. We consider the restricted case of one and two channel information due to restrictions inherent in the hardware used, as described in Section 6.3.1. Once the shift in resonant frequency is calculated, we utilise the same methodology described in Chapter 4 to relate a shift in frequency to a contact stiffness and that described in Chapter 5 to further relate this contact stiffness to a material property.

6.2.1 *Single Channel Measurements*

Contact resonant information is found by setting the lock-in amplifier to give a sum of two sine waves fixed at two frequencies bracketing a resonant peak, f_1, f_2, where $f_1 < f_R < f_2$ and f_R is the resonant frequency of the peak, and subscripts represent the use of the first/second channel of the lock-in amplifier. The amplitude of each of these frequencies reflects its position on the initial measured resonant peak, as shown in Figure 6.1a. This initial resonant peak is measured when the AFM probe is in continuous contact with a bulk material property, such that the resonant peak is expected to shift only a small amount (less than if it were to shift from free to contact) causing any changes in amplitude to be more sensitive to shifts in frequency. The resonant peak will shift to the right (stiffening) or to the left (softening) as the cantilever is moved away from the bulk substrate to other material features, causing a change in the amplitude recorded by the lock-in amplifier, A_1' and A_2', which we henceforth refer to as the shifted amplitudes. When measuring with a single channel, we have access to only one of these shifted amplitudes. However, we must utilise the change in amplitude in order to calculate the change in resonant frequency. This change in frequency contains information about the contact event between sensor and sample, as discussed in Chapter 4.

In order to convert this change in amplitude to a shift in frequency, we make several assumptions. First, we assume that the resonant frequency peak as well as the shifted resonant frequency peak are well described by a damped simple harmonic oscillator (SHO), as defined in Section 2.5. We then note that a shifted resonant peak can be reconstructed from a single amplitude point only if it is assumed that there is no change in the width of the curve (the quality factor, Q). This implies that the viscous behaviour of the material is neglible, as discussed in Chapter 5 and demonstrated by the force-distance curve in Figure 5.16, or that there is little variation in the hydrodynamics of the system. This is not likely to occur in practise, as discussed in Chapter 3. However, single channel information can still be used to identify stiffness information and we outline the method for doing so below, which assumes constant Q and amplitude.

As we have assumed no change in the quality factor or height from the original resonant peak, it follows that any shift in frequency will occur by the same amount for all points on the resonant peak. Hence, we are only required to calculate the distance from the resulting amplitude of the lock-in amplifier, A_m', to the same amplitude on the

original resonant peak and where $m = 1, 2$ depending on whether the shifted amplitude relates to a reference frequency is on the left or right of the resonant frequency (relating to the first or second lock-in channel. As mentioned above, we have assumed that the resonant peak is well described by the equation for a damped simple harmonic oscillator, which gives the amplitude of the oscillator for a given frequency. In order to find the frequency for a given amplitude on the resonant peak, we note that the map from amplitude to frequency on an SHO curve has no unique inverse when the range includes frequencies greater or less than the resonant frequency. In order to create an inverse, we separate the peak to either side of the resonant frequency and fit an spline curve representing an inverse SHO for each section, $\text{SHO}^{-1}(A_1')$ for $f < f_R$ and $\text{SHO}^{-1}(A_2')$ for $f > f_R$, as demonstrated in Figure 6.1b. The change in resonant frequency is found by calculating the distance between the reference frequency and frequency given by the appropriate inverse SHO curve,

$$f_R' = \|\text{SHO}^{-1}(A_m') - f_m'\|. \tag{6.3}$$

The resonant frequency of the shifted frequency peak is then given by,

$$f_{n,\text{contact}} = f_R \pm f_R', \tag{6.4}$$

where the plus/minus refers to whether the curve has increased in frequency (+) or decreased in frequency (−).

This concludes how we relate changes in amplitude as recorded by a single channel of a lock-in amplifier to a change in resonant frequency, where we have assumed that the Q factor remains constant. However, the damping in the system is also expected to be

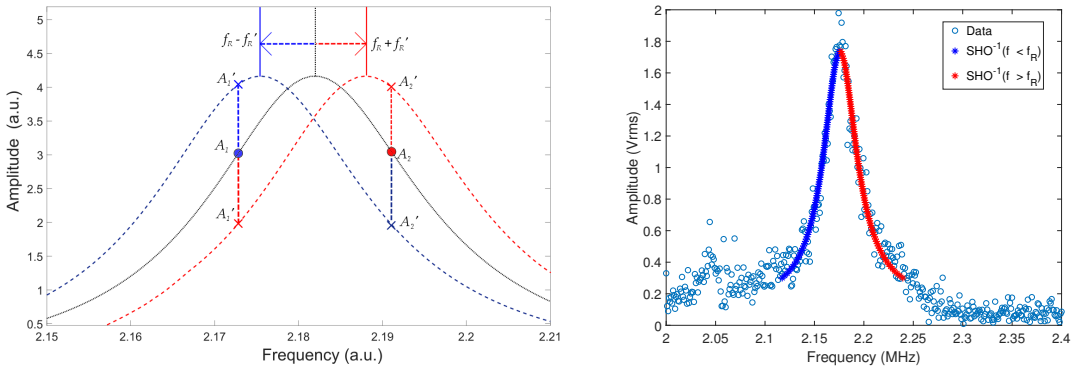

(a) (b)

Figure 6.1: (a) shows an example frequency shifts showing the change in amplitude from the reference amplitudes, A_1 and A_2 to the shifted amplitudes, A_1' and A_2' and the corresponding shift in resonant frequency to $f_R \pm f_R'$. When the AFM probe encounters a stiff material, the resonant peak is expected to increase in frequency (red), whereas for soft objects, the resonant peak is expected to decrease (blue). The shift is calculated by utilising an inverse SHO curve, see (6.3) on either side of the measured frequency peak (b), where blue represents frequency points below the resonant frequency and red represents points above the resonant frequency.

significant when the tip-sample separation distance is small, as discussed in Chapter 3. This indicates that there will be a similar increase in the Q when imaging, compared with the free case. Furthermore, imaging on a sample with topographic variation will result in changing tip-sample separation distances and subsequent changes to the hydrodynamic loading in the system. This implies that there will be a change in Q from imaging on a homogenous and significantly 'flat' (low variation in topography data) section to imaging on a section with topographic artefacts, such as the carbides we observe in Section 6.4. Under these operating conditions, we require additional information from the lock-in amplifier and utilise two channels; dual-channel measurements.

6.2.2 *Dual Channel Measurements*

To give certainty to the calculated shift in frequency, two channels of the lock-in amplifier are used to better approximate the change in resonant frequency of the oscillating AFM probe. This is achieved by continuining our assumption that the cantilever will behave as a damped harmonic oscillator near its resonance frequency, as discussed in Chapter 2. Given this, the amplitude at resonance will be a function of the driving frequency, f, resonant frequency of oscillation, f_R, and the quality factor, Q_R of the resonant peak.

With dual channel measurements, we are able to measure the amplitude at two driving frequencies either side of the resonant peak. This gives us two data points for the three unknowns, which underdetermines our system of equations. In Chapter 3, we found evidence that a cantilever oscillating near to a flat surface will experience a substantial increased in the hydrodynamic drag. As such, we expect the Q factor to be sensitive to changes in the sample topography, to a greater extent than the resonant amplitude. We note that further measurements are required to confirm this. However, we assume that the change in resonant amplitude will be small (compared to the resonant amplitude of a contact tune measured on the same sample under the sample load) in order to minimise the system unknowns. Hence, we rescale all amplitude values by the resonant amplitude value (as measured when the cantilever is in contact with the bulk material).

When imaging, we will store the amplitude recorded by each of the two channels of the lock-in amplifier at each pixel. The high throughput of the HS-AFM produces images that contain several tens of millions of pixels, such that solving the simultaneous equations at each pixel is a considerably intensive computational task. To simplify the simultaneous equations, we assume that the shift in resonant frequency is small, such that we are measuring near to the resonant peak. Given this assumption and the assumption that the change in resonant amplitude will be small, we can approximate the scaled amplitude at the n^{th} resonance by a two term Lorentzian,

$$\frac{L(f; f_R, \gamma_R)}{A_R(f \approx f_R)} = \frac{\gamma_R^2}{(f - f_R)^2 + \gamma_R^2}, \tag{6.5}$$

where $\gamma_n = f_n/Q_n$ represents the damping in the system. Hence, we use the measured amplitude value at each pixel to solve the two simultaneous nonlinear equations,

$$\begin{aligned} \frac{A_1}{A_R(f \approx f_R)} - \frac{\gamma_R^2}{(f_1 - f_R)^2 + \gamma_R^2} &= 0, \\ \frac{A_2}{A_R(f \approx f_R)} - \frac{\gamma_R^2}{(f_2 - f_R)^2 + \gamma_R^2} &= 0. \end{aligned} \tag{6.6}$$

Solving for both of these equations give us the unknown value of f_n and Q_n for each meaurement of amplitude change.

When imaging with two of the channels of the lock-in amplifier, we use (6.6) to calculate the resonant frequency, f_n which gives information on the stiffness of the material as discussed in Chapter 4, and the quality factor, Q_n which gives information about the system damping (both hydrodynamic and material viscosity), at each pixel. An increased number of lock-in channels will further characterise the resonant peak and decrease uncertainty in our measurements. For example, two additonal channels can be used to calculate the change in phase at a specific location allowing both the resonant amplitude and the drive phase to be found, (6.1) above.

Finally, we note that the use of dual channels when imaging will cause the image to invert in each of the channels; regions with high amplitude in one channel will appear low in the other and vice versa. This is because an increase in resonant frequency will cause the amplitude, A_2, relating to the higher frequency, f_2, to decrease and the amplitude, A_1, relating to the lower frequency, f_1, to increase, given two reference frequencies chosen to be either side of the resonant frequency, as discussed previously and shown in Figure 6.1. We repeat that this argument holds for small shifts in the resonant frequency, whereas for large shifts both amplitudes will see a decrease. Furthermore, this assumes that the amplitude and quality factor remain approximately constant. Hence, an observed inversion in the lock-in channel data is a good indicator that the shift in resonant frequency is small, that the quality factor and resonant amplitude have not drastically altered and that the measurements reflect a 'true' stiffness property.

6.2.3 *Converting a Shift in Frequency to an Elastic Property*

We have shown that there are several adjustments that can be made to increase confidence in contact resonance measurements. First, the higher modes of an AFM cantilever (with low spring constant) are more sensitive to changes in the stiffness of a material and less sensitive to cantilever parameters (such as the cantilever tilt, the height of the cantilever tip, and lateral forces in the system). The most sensitive mode can be found by choosing the mode that causes an effective stiffening of the cantilever, as described in Chapter 2 that most closely matches the predicted contact stiffness of the material.

Second, in Section 4.5 we have shown that multiple measurements of the resonant frequency of a cantilever in contact with a material can be used to estimate the tip height, which has the largest influence in the calculated contact stiffness. We also utilise

considerations of the hydrodynamic damping, given in Chapter 3, to recommend that the free and in vacuo resonant frequencies of the n^{th} mode are use to minimise the influence of the surrounding fluid on measurements.

In Chapter 5, we highlight potential sources of uncertainty in contact resonant measurements, where we conclude that the two main causes are changes in tip geometry (and radius) as well as the influence of adhesion forces. However, HS-AFM is thought to operate within a low wear regime caused by the lubrication of a capillary layer that exists on the surface [27]. This is demonstrated by the consistency of image quality over several hours of imaging. Hence, we expect the DMT model of contact mechanics, given in Section 5.2 to apply when carrying out CR-HSAFM. We note that, in Section 6.4.3, we compare our measurements to those taken on a different sample of the same material using the Cypher AFM, described in Chapter 5, which assumes the same model of contact mechanics.

Finally, the HS-AFM has a considerable advantage in the volume of data collection when compared with existing AFM instruments. Images taken using the HS-AFM contain 5×10^5 individual pixels, whereas commerical AFMs (such as the Cypher AFM) typically contain 5×10^4 pixels; CR-HSAFM enables a tenfold increase in data acquisition. Furthermore, this data is collected in several seconds, compared with conventional AFMs which can take minutes, if not hours.

We are now in a position to calculate the shift in resonant frequency, and, hence, the contact stiffness at each pixel of an image taken using the high-speed AFM. The process of converting a shift in frequency to an elastic property is discussed in detail in Chapter 4 and Chapter 5. We summarise the process below:

1. Measure the free resonant frequencies of the cantilever and the resonant frequencies of the cantilever when it is in contact with the sample at a single location.

2. Use the shift in resonant frequency due to sensor-sample contact to estimate the parameters of the cantilever, as described in Chapter 4.

3. Calculate the shift in frequency (using either one or two channels of the lock-in amplifier, as described in Section 6.2).

4. Calculate the contact wavenumber from a shift in resonant frequency,

$$\alpha_{n,\text{contact}} = \alpha_{n,\text{free}} \sqrt{\frac{f_{n,\text{contact}}}{f_{n,\text{free}}}}. \tag{6.7}$$

5. Calculate the contact stiffness given a contact wavenumber using (4.43), as described in Chapter 4, and with parameters found from the method described in Section 4.5.

6. Finally, relate the contact stiffness to the reduced modulus of the material using the process described in Section 5.2.

This fully captures the methodology required to relate a shift in resonant frequency to a material property when imaging with an AFM and lock-in amplifier at high-speed. We now demonstrate how to measure the reduced modulus of a material using two different samples; a sample of stainless steel (SS) (a different section of the same material as that investigated in Chapter 5) and a sample of silicon with deposited graphene flakes. We utilise the higher modes of the cantillever, providing high frequency bandwith to the HS-AFM, resulting in a non-destructive and quantifiable tool for material science that can image over micron squared areas in real time and with nano-metre height resolution.

6.3 MEASUREMENTS

6.3.1 *Experimental Procedure*

In this work, we utilise a HS-AFM system (Bristol NanoDynamics, UK), as described in [26, 31]. An example schematic of the set-up used for contact resonance HS-AFM measurements is given in Figure 6.2. The HS-AFM utilises a LDV detection system (Polytec CLB 2534) which measures the change in the cantilever's displacement. The LDV measurement system is calibrated by the speed of light to have 50 pm resolution. A camera is used to place the laser point below the tip, so as to avoid one of the cantilever nodes. When the cantilever is brought into contact with the sample, the lock-in amplifier (LIA) (Zi HS2Li) drives the cantilever at its base using one or two waveforms (depending whether the single or dual-channel method is used). The sample is mounted onto a high-speed fast-scan stage. Both X and Y stages are closed loop (using optical encoders) to 1 nm resolution. The scanning stage is open loop to allow for the passive control. The shakers are $5 \times 5 \times 1$ mm, PICMA (Physik Instrumente, UK). Just one is used for the z axis oscillation, with an expected resonant frequency to be $f_R \sim 10^6$Hz. It is shaken by approximately 1V which equates in the order of one angstrom in height.

We utilise the same cantilever model as calibrated in Chapter 2, the Bruker MSNL-B rectangular cantilever. We begin by finding the cantilever's free frequency response, as shown in Figure 6.3. We perform a frequency sweep from 0 to 1 MHz, with an additional sweep from 0 to 20 kHz to better capture the first mode and two higher sweeps to capture modes six and seven. We find the first resonant frequency at 13.99 kHz with a Q-factor of 18 and use these values to calibrate the cantilever using the method set out in Chapter 2 (also described in [93]).The resonant frequencies in vacuo are calculated and used to validate the higher resonant modes, shown as dashed red lines in Figure 6.3.

We find that the in vacuo frequencies agree to the measured frequencies with less than 3% error for the first seven resonant modes which have measured resonant frequencies of $f_1 = 13.99\,\text{kHz}$, $f_2 = 88.1\,\text{kHz}$, $f_3 = 248.1\,\text{kHz}$,$f_4 = 487.2\,\text{kHz}$, $f_5 = 807.6\,\text{kHz}$, $f_6 = 1.21\,\text{MHz}$, $f_7 = 1.69\,\text{MHz}$. The ability to identify the resonant frequencies was particularly useful where visual determination was unreliable, such as the identification of mode 2, mode 3 and mode 5, shown in Figure 6.3.

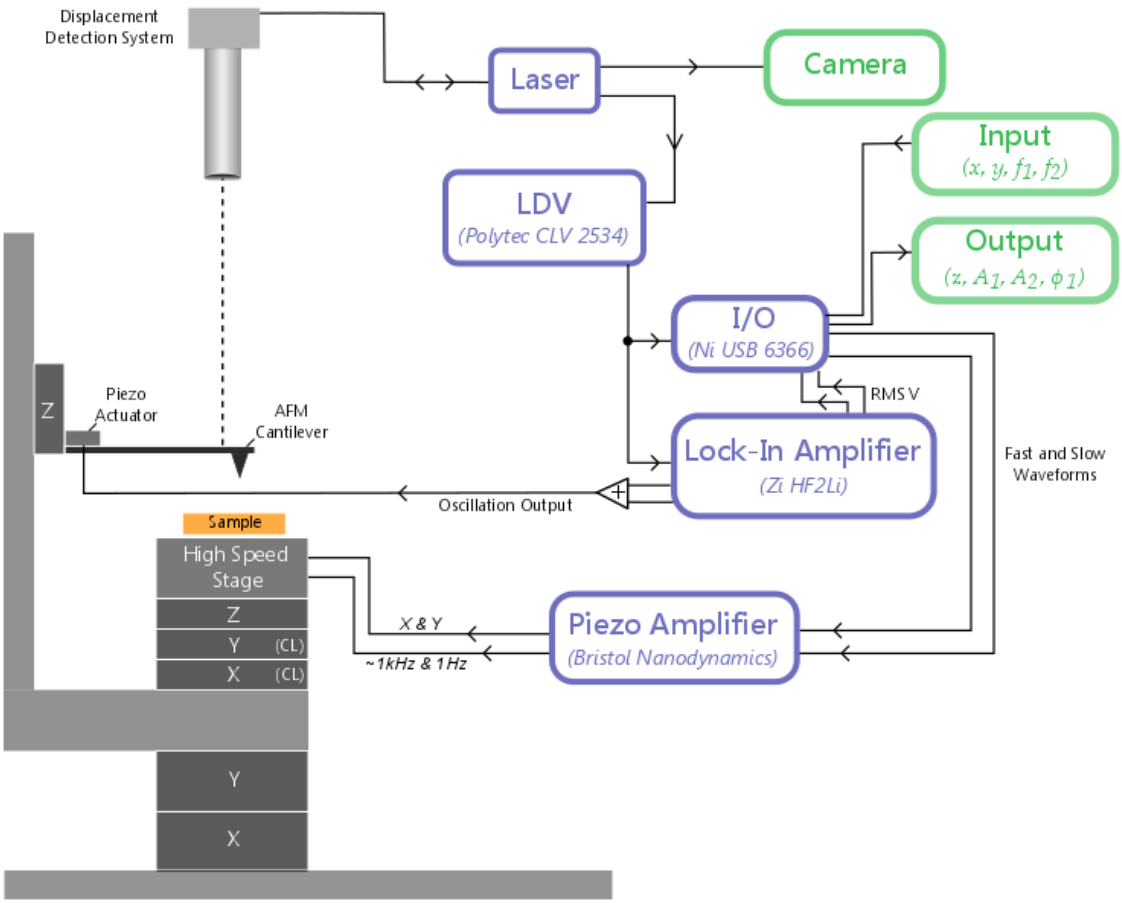

Figure 6.2: A schematic showing the experimental set-up for measurements on a single point.

We also calculate the effective stiffness, using the same calibration method set out in Chapter 2, for the first eight modes of the cantilever as $k_1 = 0.087\,\mathrm{N\,m^{-1}}$, $k_2 = 0.341\,\mathrm{N\,m^{-1}}$, $k_3 = 2.672\,\mathrm{N\,m^{-1}}$, $k_4 = 10.26\,\mathrm{N\,m^{-1}}$, $k_5 = 28.04\,\mathrm{N\,m^{-1}}$, $k_6 = 62.59\,\mathrm{N\,m^{-1}}$, $k_7 = 122.09\,\mathrm{N\,m^{-1}}$, $k_8 = 216.4\,\mathrm{N\,m^{-1}}$. This motivates the seven and eighth mode as those that are more sensitive to stiffness changes on a steel sample, as discussed in Chapter 5. These values are largely in agreement with those found in Chapter 2.

As described in Chapter 4 (Section 4.5), utilising a soft cantilever on a stiff material requires additional parameters to be known in order to confidently connect a shift in resonant frequency to a contact stiffness, which is then related to a sample-specific sample property. Two of these parameters, the height of the tip and distance that the tip is offset from the free end of the cantilever, can be found in a self consistent way by setting the intersection of multiple contact stiffness parameters surfaces equal to zero. In Figure 6.4, we show the shifts in frequency for the cantilever when it is in contact with the silicon surface. We use each of the measured shifts in frequency to calculate a contact wavenumber according to (4.6). Each of the modal contact wavenumbers are then used to find the parameters which result in a modally consistent set of contact stiffnesses. These calculated parameter values are assumed to be good estimates for the offset and tip height. In Figure 6.5, we show the intersecting parameter surfaces along with a contour plot for the difference in two parameter surfaces equal to zero.

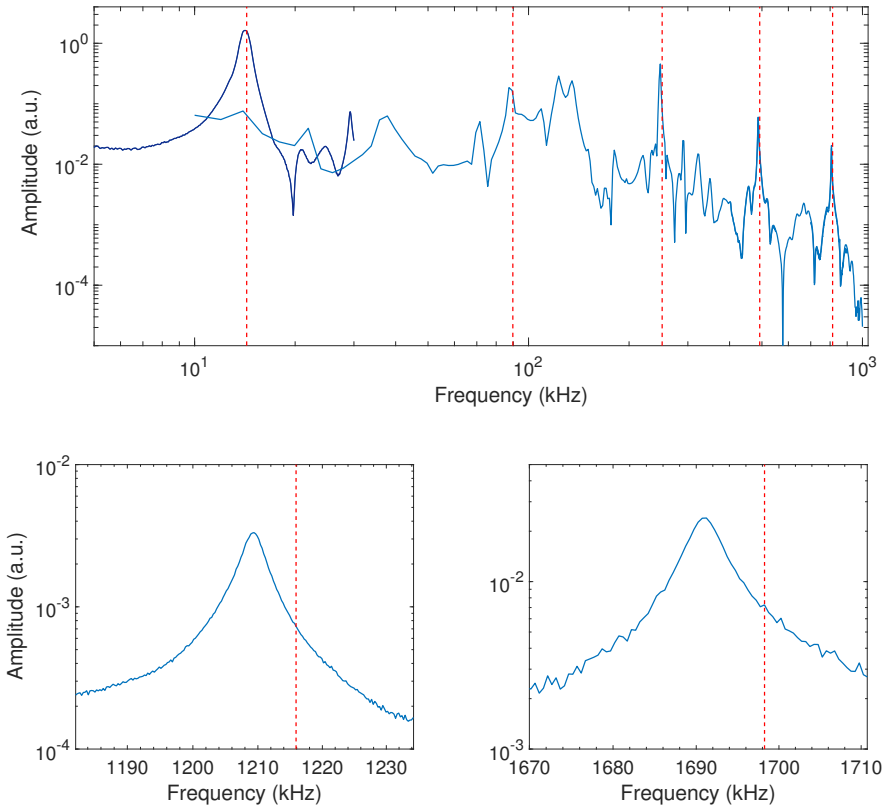

Figure 6.3: In (a) we show the region containing the fundamental resonance as well as the subsequent four modes, measured using the HS-AFM. We highlight the predicted resonant frequencies in vacuo, marked as dashed red lines and found using the calibration theory described in Chapter 2, that highlight the location of each mode. In (b) and (c), we show the sixth and seventh mode as well as the corresponding predicted resonant frequency in vacuo, marked by dashed red lines.

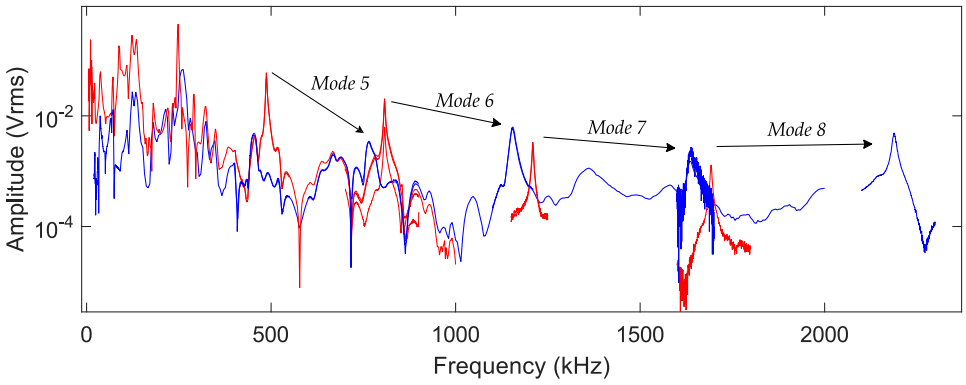

Figure 6.4: Frequency sweep showing the shift in resonant frequency at higher modes due to contact with the silicon substrate. We use the shift in resonant frequency for the fifth, sixth, seventh and eighth mode to calculate the parameters (tip offset and tip height) using the method described in Chapter 4. The lower modes were not used due to uncertainty in the contact frequency spectra.

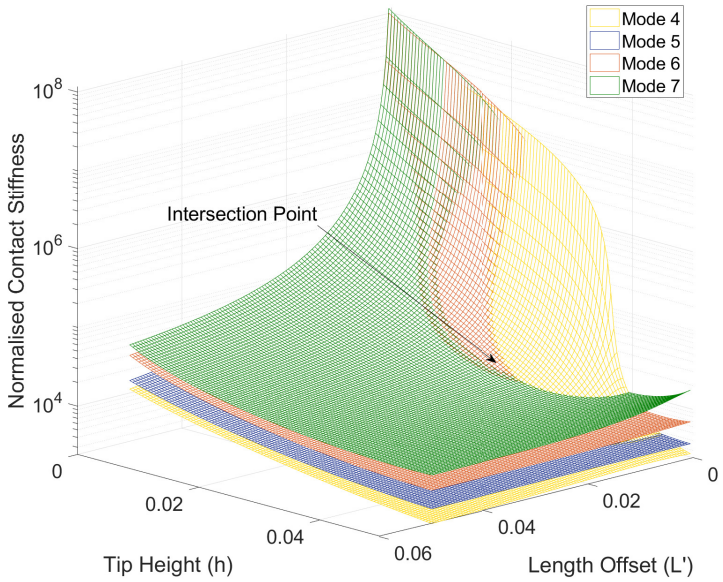

Figure 6.5: In (a) we show a contour plot for the various intersections of parameter surfaces set to zero, while in (b) we show the actual parameter surfaces. We find an intersection point at $L' = 0.01$ and $h = 0.03$, which we use in subsequent analysis.

We find that the majority of points intersect around $L_2 = 0.01$ and $h = 0.03$, which we use in subsequent analysis. Both values are in keeping with values calculated from the SEM images in Chapter 2 (from a different AFM probe of the same make and model, and hence expected to be similar) and the material properties given by the manufacturer. The tilt of the cantilever is set to 0.12 rad, preset for the HS-AFM used here, and the lateral stiffness of the sample is assumed to be $k_{\parallel} \approx 0.8 k_{\perp}$ for all samples, as discussed in Chapter 4. Using these parameters, we convert the amplitude measurements (for both the sample of SS grade 316 and of silicon with deposited graphene flakes) to frequency shifts, using (4.46) in Section 4.4.5, and then into elastic properties of the sample using the theory of contact mechanics described in Section 5.2.

In order to verify the measurements taken using the HS-AFM, we utilise the DART method with the Cypher AFM to create a stiffness map over a different sample of the same stainless steel material (SS grade 316) considered in this chapter. Initial measurements were taken using the same PP-CONTAuD cantilever as in Chapter 5. However, the soft cantilevers experienced a significant snap-down event that caused the tip to foul and image quality to reduce. Instead, a PPP-NCLAUd cantilever (Nanosensors, Switzerland) was used, which has a large thickness, $h_{\mathrm{T}} = 38 \pm 8\,\mu\mathrm{m}$ and higher spring constant, $k_c = 48 \pm 30\,\mathrm{N\,m^{-1}}$ and, hence, less influenced by long–range tip-sample interaction forces[2]. The PPP-NCLAUd cantilever has a spectrum (taken using the Cypher AFM with blueDrive excitation) is shown in Figure 6.6, where the resonant frequencies were identified using our calibration method, described in Chapter 2, whereas the spring constant is found from the manufacterers values. The second resonant mode was used.

2 See Section 1.3 in Chapter 1 for more dicussion on the long–range interaction forces.

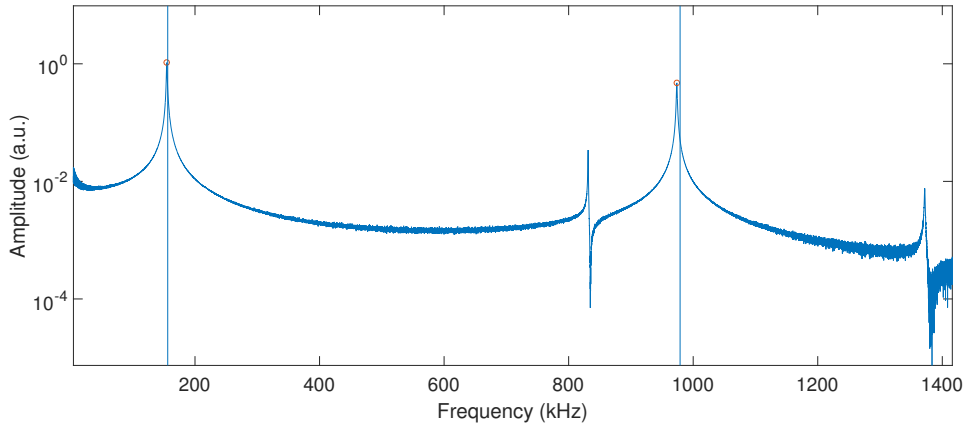

Figure 6.6: The free resonance of a PPP-NCLAUd (Nanosensors, Switzerland) AFM probe with free resonance at 157 kHz and 974 kHz, measured using a Cypher AFM with blueDrive excitation. The blue vertical lines show the predicted resonant frequency in vacuo using the method described in Chapter 2.

6.3.2 *Driving with Two Channels*

In Section 6.2.1, we discussed the means for relating a change in the measured amplitude of either one or two channels of the lock-in amplifier to a change in frequency. As we will show in Section 6.4, we find an improvement in the reliability of our measurements when using two channels. However, we are unable to drive with two channels and image simultaneously in practise due to cross-talk between the two channels. In Figure 6.7, we show examples of the beating that occurs when driving with two channels.

The beating occurs due to sine wave interference. The destruction and construction of sine waves causes an envelope wave with a frequency that is equal to the difference between both of the excitation frequencies. When the distance is small, the frequency of the envelope wave is small, such that it is theoretically possible to match the beating frequency to the the HSAFM fast-scan speed stage (1 kHz). However, this is difficult to do in practise due to differences in the internal clock of the LIA and stage inputs. The slope of interference shown in Figure 6.7 is caused by the number of waiting waveforms that are present in the fast scan direction. When there is a non-integer amount of waveforms present, the image appears distorted due to aliasing effects.

6.4 RESULTS

We discuss the results gained from measurements on a sensitised SS grade 316 sample with carbide features and a silicon sample with deposited graphene flakes and single layers. All experiments were taken with the high speed atomic force microscope (Bristol NanoDynamics, UK) and MSNL-B rectangular cantilever, the same model as that used in Chapter 2.

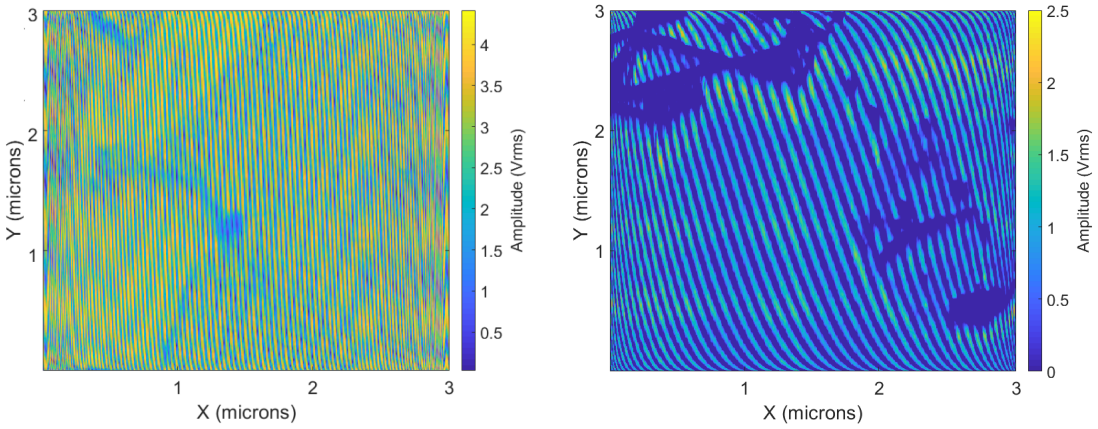

Figure 6.7: Example of beating shown on in the lock-in channel (1) of (a) the steel 316 sample and (b) the silicon-graphene sample when imaging and driving with two channels simultaneously. The beating between both channels when using two lock-in amplifier channels bracketing the resonant frequency mean that contact stiffness measurements cannot be gained.

6.4.1 *Carbides on SS grade 316*

Figure 6.8 shows a section of the SS sample that contains no grain boundaries or carbide formations. This area is thought to be representative of the bulk material as there is little variation in the topography (less than 0.5 nm, as shown in Figure 6.8a) and is used as a reference material for subsequent measurements. The frequency sweep is taken when simultaneously imaging over this section, and the change in amplitude for both lock-in amplifier channels is recorded. An example from one of the lock-in amplifier channels is shown in Figure 6.8b. We note that there appears to be discernable stiffness variation even over a section of the bulk material which appears as dark lines in the lock-in amplifier amplitude channel, highlighted by white dashed lines in Figure 6.8a. These lines may be due to surface contamination during imaging or material preparation.

As we have frequency information from both channels, we proceed to calculate the change in frequency due to contact with the bulk SS sample and use this change in frequency to calculate a normalised contact stiffness. In Figure 6.8c, we show the same section after being converted into stiffness, while in Figure 6.8d we show a histogram of the data showing the distribution of contact stiffness across the $3 \times 3\mu$m sample. We can use this distribution to calculate an estimate of the material properties of the bulk steel using the theories of contact mechanics considered in Chapter 5. The artefact is still visible but reduced when compared to the amplitude data given in Figure 6.8b, highlighting that the final stiffness values of the sample section has a reduced sensitivity compared with the raw lock-in amplitude data. It is expected that this is due to a lack of knowledge of changes in amplitude, as described in Section 6.2.1.

We next turn to sections of the SS grade 316 sample which contain sample artefacts such as carbides and grain boundaries. In Figure 6.9b, we show a topographic map of

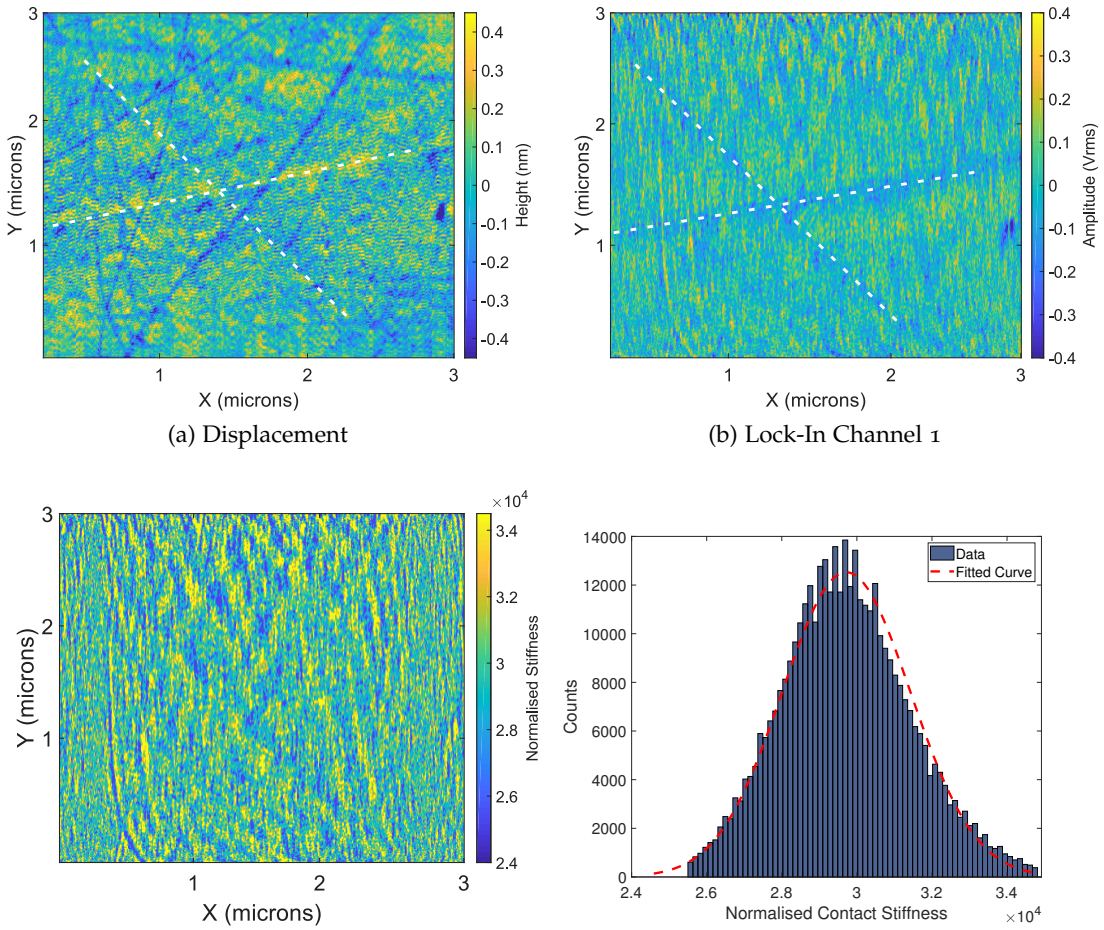

(a) Displacement

(b) Lock-In Channel 1

(c) Normalised Contact Stiffness

(d) Histogram of Contact Stiffness

Figure 6.8: (a) The topographic map of a section of bulk steel, with less than 1 nm height variation, as well as (b) the corresponding lock-in channel information of the same section and (c) the same section as normalised contact stiffness. In each of these three maps, height, amplitude and contact stiffness, we see a stiffness feature marked as dashed white lines which is not clearly identifiable using topography information alone. In (d) we show the count information for the stiffness map given in (c).

a section of the SS grade 316 which includes a large high region (maximum height is 2 nm) which is expected to be a carbide formation and significant low regions (minimum depth is 3 nm) which appears as a possible grain boundary. We make the following observations. First, the height map demonstrates the presence of three salient topographic features of SS grade 316, the bulk steel, carbide build up and the existence of a grain boundary, as observed previously in Chapter 5. The total height of the carbide is found to be approximately $2.0\,\text{nm} \pm 0.5\,\text{nm}$.

Second, we are able to use the lock-in amplifier channels to observe non-topographic feature information. In Figure 6.9c and Figure 6.9d, we show the output of two channels from the lock-in amplifier, corresponding to the reference frequencies $f_1 = 2.173\,\text{MHz}$ and $f_2 = 2.184\,\text{MHz}$, respectively. We note that the general topography of the sample section is retained. However, there now also appears an artefact in the carbide which is not present in the height map, highlighted in both Figure 6.9c and Figure 6.9d. This clearly

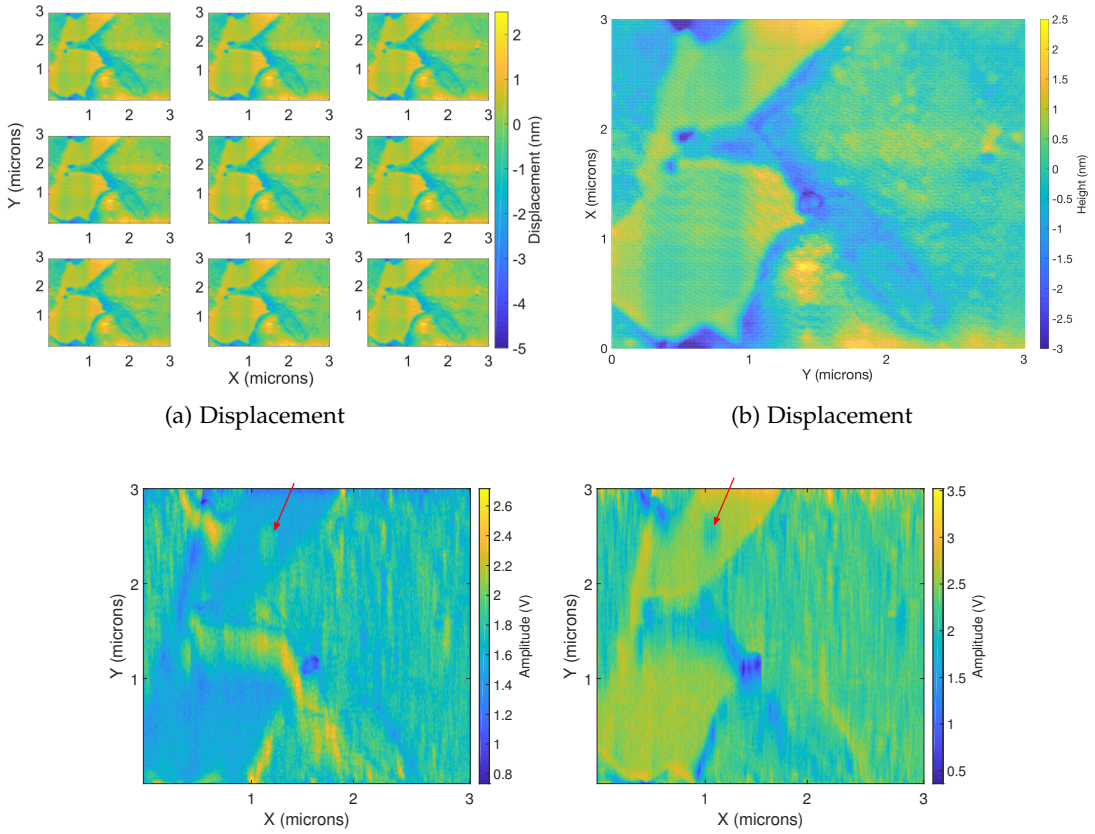

(a) Displacement

(b) Displacement

(c) Lock-in Channel 1

(d) Lock-in Channel 2

Figure 6.9: Topographic measurements (a) were taken of a single section of SS which included a carbide feature and a grain boundary. The lock-in amplifier channels showed image contrast, (c) and (d), emphasising that a true stiffness feature was detected. Note that there was little change to the frame location across multiple images. Each megapixel frame was collected in 0.5 seconds.

demonstrates that the lock-in amplifier channels, measuring a change in amplitude due to a shift in resonant frequency, are able to measure features that are non-topographic and invisible in the topographic data alone.

Third, we note that the channel data is inverted such that high amplitude regions in the first channel appear low in the second and vice versa. These observations indicate that we are correctly identifying elastic information on the sample as the amplitude of the left reference frequency will increase while the right reference frequency will decrease when a resonant frequency shift occurs. This amplitude inversion is due to a variation in the material property, as described in Section 6.2.

In order to relate the amplitude data to a shift in frequency, we implement the methodology described in Section 6.2.1, and calculate the resonant frequency of a damped harmonic oscillator using information at both channels. This requires two simultaneous equations to be solved at each pixel. In Figure 6.10a and Figure 6.10b, we show the resulting maps of quality factor and resonant frequency. As shown in Figure 6.10b, the resulting calculated frequency data retains the overall topography of the sample section, including both high region (thought to be carbide) and low region (thought to be grain

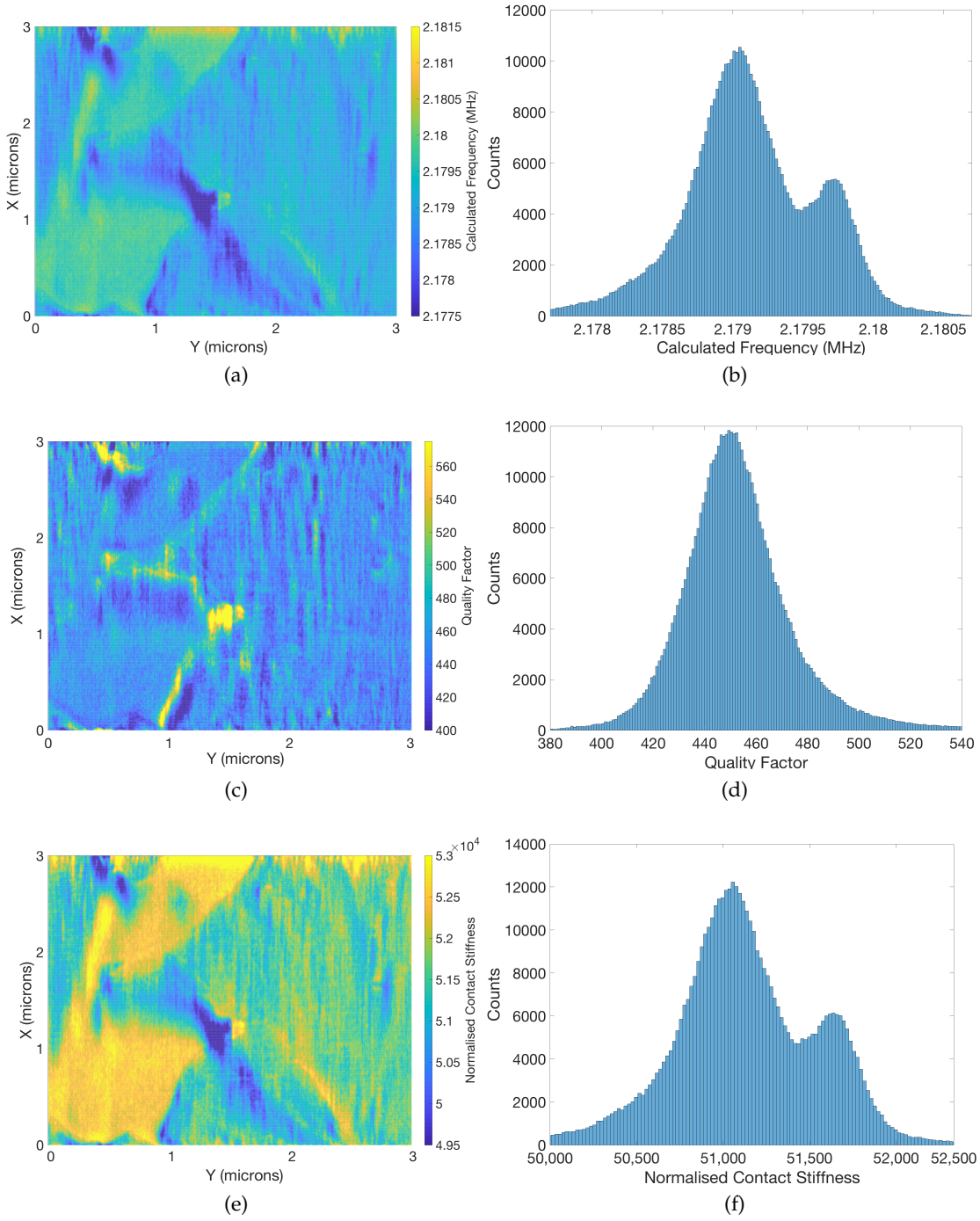

Figure 6.10: The resonant frequencies, calculated using the dual channel method described in Section 6.2.1, (a) and the observed bimodality in this data which represents the carbide and SS materials. Additional Q-factor map (b) of the same section of the sample with bimodal count information (d), which does not display significant material variation. We then show the normalised contact stiffness map (e) which continues to reflect (f) the bimodality of count data.

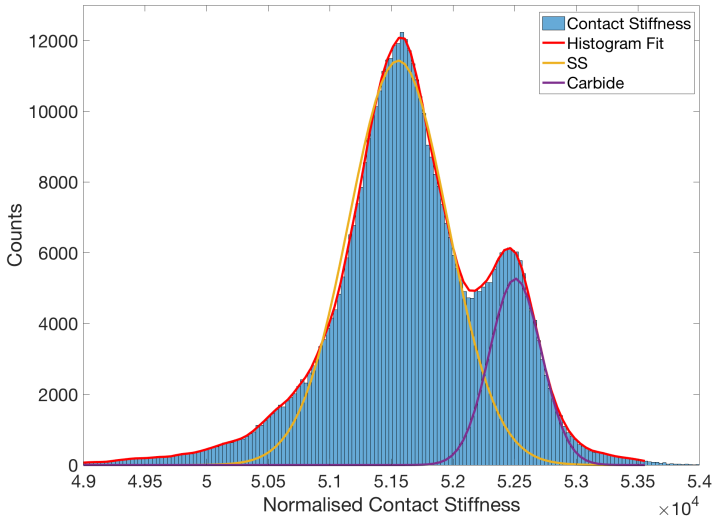

Figure 6.11: The final normalised contact stiffness can be fitted with a two term Gaussian to capture the relevant material properties. The fit parameters are $a_1 = 27,890$, $b_1 = 51,550$, $c_1 = 566$, $a_2 = 12,860$, $b_2 = 52,510$, $c_2 = 298$, where a_i is the amplitude, b_i is the centroid location (representing the mean), and c_i is the width (representing the standard deviation) of the i^{th} peak

boundary). Furthermore, when considering the distribution of calculated frequencies across the sample, we see a bimodality representing two different material properties. The calculated quality factor data also retains the overall topography, however does not appear to pick out the additional grain boundary feature. Furthermore, the distribution of Q factor data across the sample does not display the same bimodality, indicating that the two materials do not have significantly different viscous behaviour.

We use (6.7) to convert these frequencies to a contact wavenumber. Using the parameters found in Section 6.3.1 and the equation for converting contact wavenumbers to a contact stiffness, (4.46) in Section 4.4.5, we are able to calculate the normalised contact stiffness of the sample, which we show in Figure 6.10e. These represent the final (per pixel) contact stiffness for the sample. We see the same carbide region, now denoted by high contact stiffness, as well as grain boundary, denoted by low contact stiffness. The non-topographic artefact in the carbide (emphasised by the red arrow in Figure 6.9) is also retained.

As shown in Figure 6.11, we see a bimodal distribution of the contact stiffness of the frame shown in Figure 6.9, and fit a two-peak Gaussian[3], with the fit parameters of $a_1 = 27,890$, $b_1 = 51,550$, $c_1 = 566$, $a_2 = 12,860$, $b_2 = 52,510$, $c_2 = 298$, where a_i is the amplitude, b_i is the centroid location (representing the mean), and c_i is the width (representing the standard deviation) of the i^{th} peak. We assume that the higher amplitude peak (yellow) represents the bulk steel substrate and that this contact stiffness is a reflection of that material. Using the spring constant of the cantilever, we calculate a contact stiffness of $4484\,\text{N}\,\text{m}^{-1} \pm 49\,\text{N}\,\text{m}^{-1}$ for the SS sample (using b_1 and c_1 above).

3 We use the MATLAB and Curve-fitting Toolbox Release 2017b (The MathWorks, Inc., Natick, Massachusetts, United States).

This is higher than the expected contact stiffness of $132-62\,\mathrm{N\,m^{-1}}$, given in Chapter 5. Uncertainties in the tip radius and the contact force on the cantilever tip introduce difficulties in relating the contact stiffness to a material property as discussed in Chapter 5 (Section 5.5) and Section 6.5. For example, given an assumed expected reduced modulus for the SS sample of $E^* = 93\,\mathrm{GPa} \pm 2\,\mathrm{GPa}$ and a tip radius of $R = 2 - 100\,\mathrm{nm}$, this implies a contact force of $F_C \sim 10^{-3} - 10^{-5}\mathrm{N}$, significantly larger than the expected contact force of 50 nN. Hence, we will utilise the bulk material (of the SS and silicon materials) as a reference material to calculate the properties of the other topography features. We demonstrate how these contact stiffnesses reflect the elastic properties of the two materials in Section 6.4.3.

6.4.2 *Graphene Flakes on Silicon*

We now turn our attention to the contact resonance images of graphene flake on silicon. We have chosen to consider this sample in order to highlight the sensitivity of CR-HSAFM to non-topographic features, as the deposited graphene includes single layer graphene which is expected to have an effective thickness of 0.335 nm [209]. Single graphene sheets have been reported to have Young's modulus of 1 ± 0.1 TPa [209], while wrinkled graphene can have a Young's modulus of 250 GPa [209] and the Young's modulus of graphene flakes is currently an open research question. Meanwhile, silicon has a typical Young's modulus of 169 GPa [210]. The large difference in material properties, as well as the high Young's modulus of graphene is expected to enable us to identify sections of graphene even when there is low signal in the topographic data.

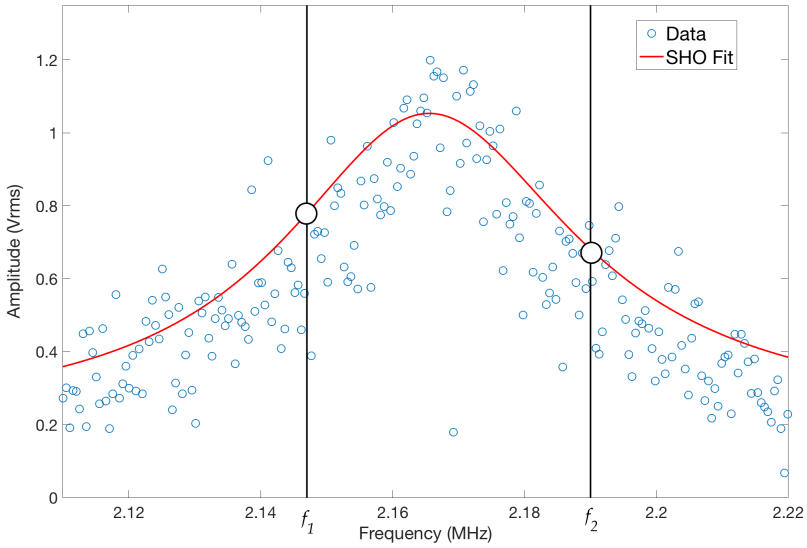

Figure 6.12: The frequency peak of the cantilever in contact with bulk silicon substrate (blue squares) which allows for a SHO curve (red dashed line) that can be used to turn amplitude information into frequency data. The chosen driving frequencies for the two channels are marked a solid circles with vertical lines.

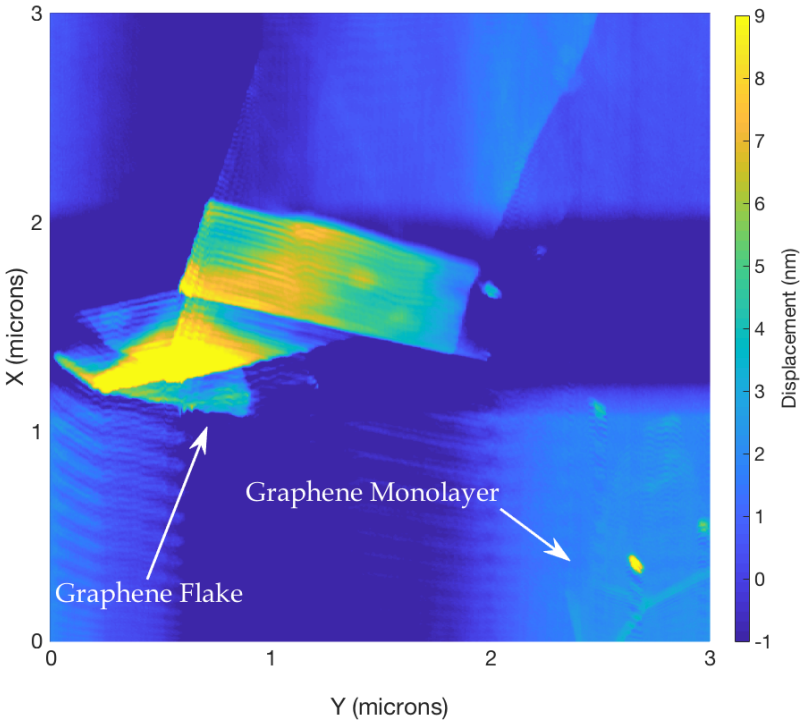

Figure 6.13: Topographic map (frame 6 in Figure 6.14), highlighting the observed graphene flake and graphene monolayer.

We repeat the same process described in Section 6.3 and first identify a clear section that is expected to be largely bulk silicon. This will form the reference material for subsequent measurements. In Figure 6.12, we show the measured frequency response of the seventh mode (blue circles) and a fitted simple harmonic oscillator to the curve (red line). This resonant peak was taken on a section of the sample that is expected to contain no graphene flakes or additional artefacts (evidenced by low variation in the topography data, not included here). Hence, we assume that it is a representative of the resonant behaviour of the beam when in contact with bulk silicon. We also highlight the position of both reference frequencies (vertical black lines), which were chosen to be $f_1 = 2.147\,\text{MHz}$ and $f_2 = 2.19\,\text{MHz}$, which bracket either side of the resonant frequency, $f_R = 2.165\,\text{MHz}$.

We focus on the ability to capture material properties while imaging and only use a single channel of the lock-in amplifier. In Figure 6.14a, we show several frames of the displacement data taken while moving across different areas of the sample, while in Figure 6.14b, we see the same regions, but taken using the first channel of the lock-in amplifier. We begin by seeing a large graphene flake that is identified in the height map of Figure 6.13. However, as the scan area moves away from this flake, we find that there also exists a single graphene layer, also identified in Figure 6.13, which is harder to clearly identify by topographic information alone. When considering the lock-in amplifier channel information, we find that the material edges allow for clear identification of different sample features. Furthermore, the single graphene layer is identifiable from the bulk silicon substrate.

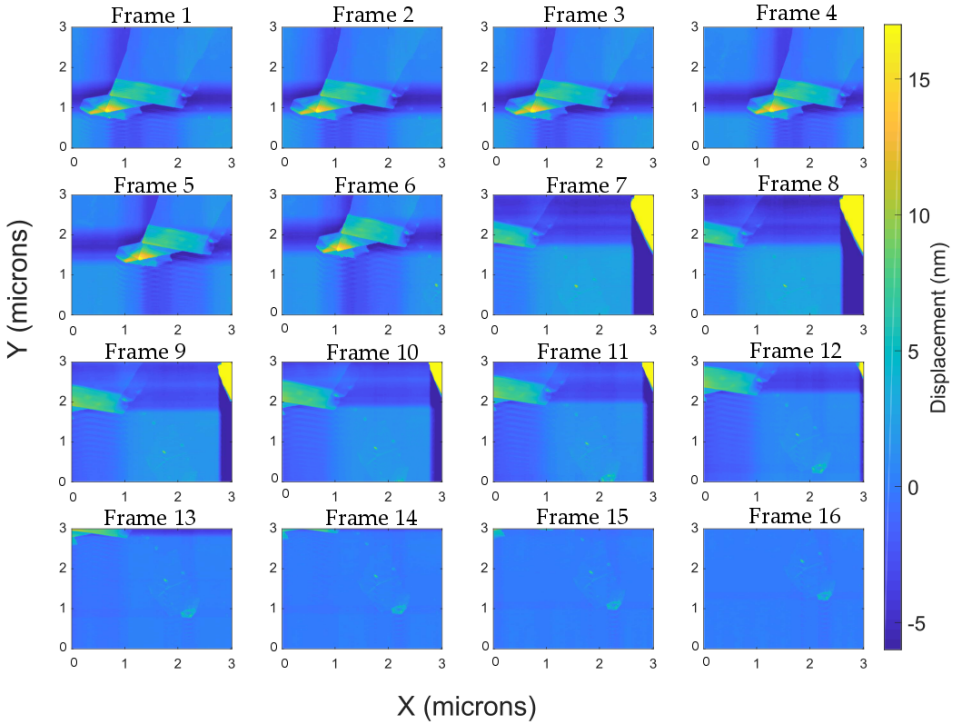

(a) Height

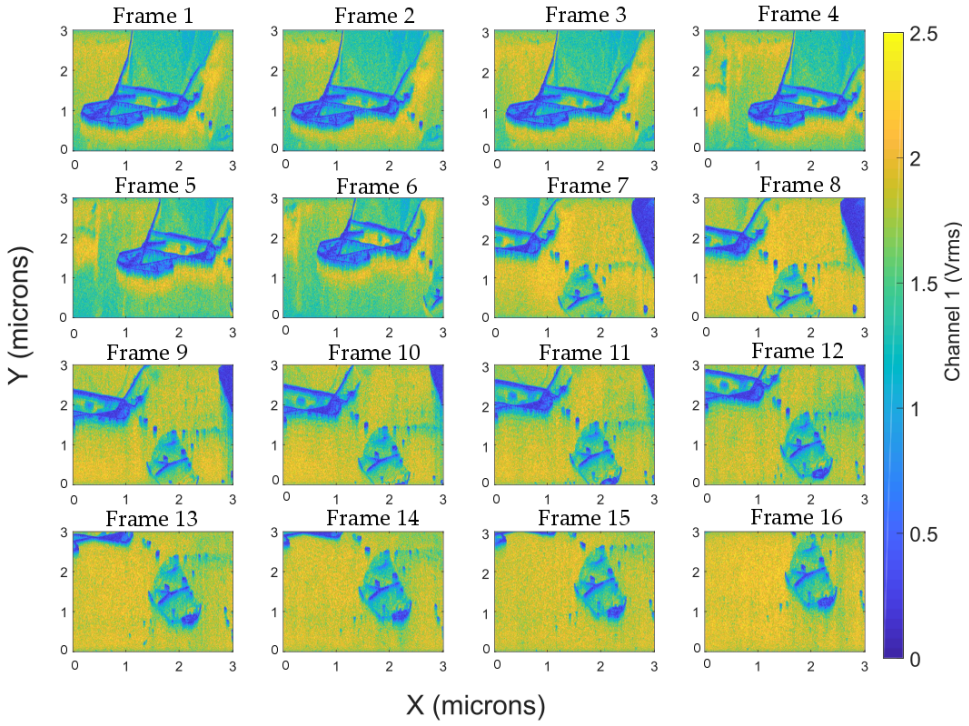

(b) Lock-in Amplifier Channel 1

Figure 6.14: The flattened height map (a) and output from the lock-in amplifier channel 1 (b) shows that the lock-in amplifier values are capable of detecting changes to the material properties such as graphene flakes and layers more clearly than the height topography. This demonstrates the benefit of combining HS-AFM with non-topographic capabalities. Data is collected at two frames per second and two million pixels per frame.

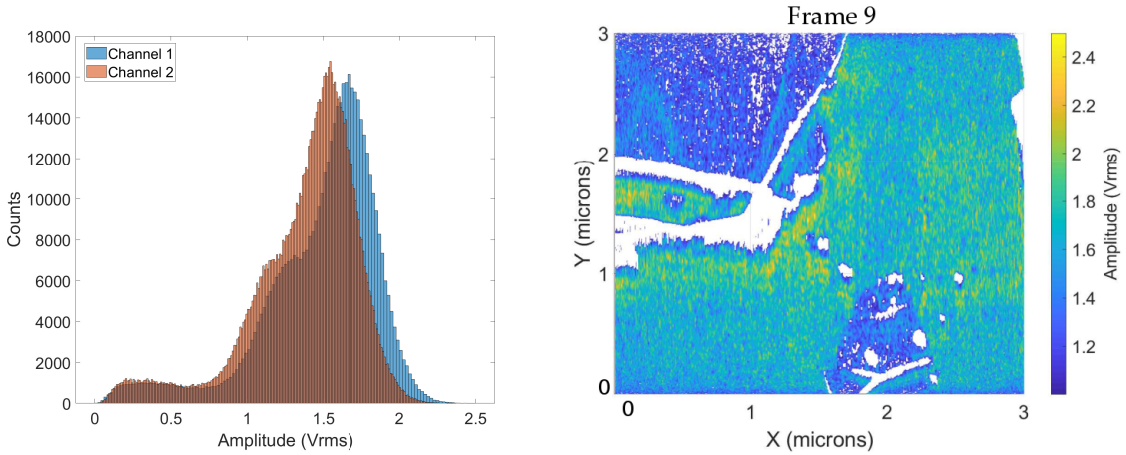

(a) (b)

Figure 6.15: A histogram of the amplitude count data (a) shows that there is a signifcant collection of low amplitude count data, which when removed (b), reflect edge effects that result in increase normalised contact stiffness and correspondingly low amplitude. The channel information shows no inversion as we are driving with one frequency.

The topographic map, shown in Figure 6.14a, records the height of the first graphene layer as being several angstroms. However, the stiffness channel, channel 1 of the lock-in amplifier, picks out additional features of the graphene layer. We proceed to improve the identification of the graphene in the lock-in channel data by considering how the amplitude varies while imaging. We first consider the edge effects, which occur due to the increased contact area when the AFM tip meets the edge of a feature. This increase in area causes a corresponding increase in the resulting tip-sample contact stiffness, known as multiple asperity contact [168]. As the edge effects have lowest amplitudes, we predict that these regions also have the highest contact stiffness. Hence, we remove all those regions that have an amplitude less than 1 Vrms, corresponding to regions that have shifted away from the bulk resonant peak. In Figure 6.15a, we demonstrate that these regions correspond with to the long tail to the left of both histogram plots in Figure 6.15, whereas in Figure 6.15b, we show the resulting graphene flake with potential edge effects removed.

The resulting images, given in Figure 6.15, show that the low amplitude regions correlate well with the regions expected to be caused by edge effects. The contrast between the substrate and the flake has increased, highlighting the difference between the two materials. The low amplitude regions remove both the edge effects around the graphene flake as well as the artefact on top of the single layer of graphene. Intuitively, the low amplitude regions correspond to those contact stiffnesses that are unrealistically produced by a single asperity contact event and are not captured by the current model. However, we note that we did not observe such contact events when imaging steel. An alternative explanation may be that the existence of adhesion effects over certain regions of the graphene, due to wrinkling. This would also result in a significant increase in the contact stiffness. The associated resonant frequency shift would have to be so far shifted to the right that the resulting fall in amplitude would be drastic. Hence, the choice to remove

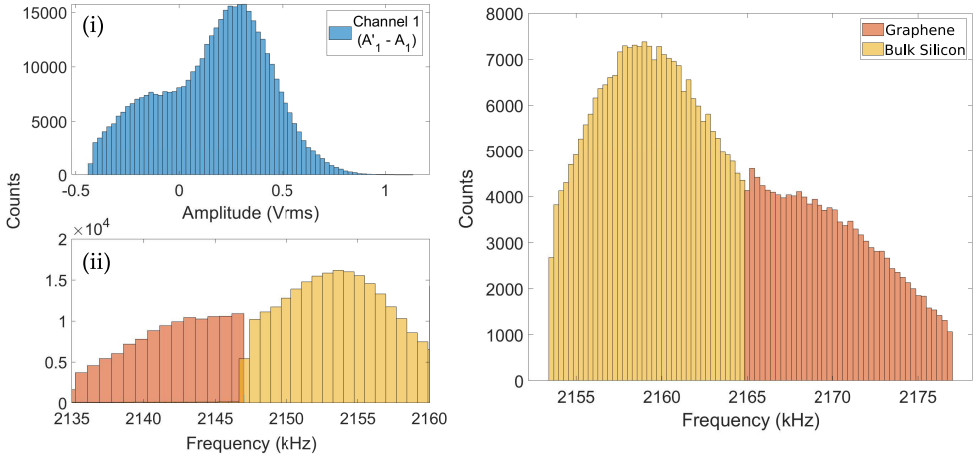

(a) (b)

Figure 6.16: We show (a) how the change in amplitude can be separated out into regions that decrease and increase in amplitude (i) reflecting higher and lower frequency shifts (ii). When combined with the initial resonant frequency (b), we see bimodal count information reflecting the two material properties, silicon and graphene.

amplitudes below a certain threshold has introduced an upper limit to the measurable contact resonance that is possible when using single channel information. The resulting images, shown in Figure 6.15a, validate that these regions are likely contact-induced anomalies, owing to their locality around the edge of the larger graphene flake.

In Figure 6.16, we demonstrate how we separate out the amplitude data and the resulting separation of the frequency data for the panel highlighted in Figure 6.14. We separate amplitude count data into regions that have increased and decreased from the initial lock-in amplifier channel denoting the left frequency point, shown in the amplitude data of Figure 6.16a, with (i) a histogram of amplitude data from the first lock-in channel (with edge-effects removed) and (ii) the resulting frequencies calculated using the inverse SHO described in Section 6.2. We explicitly separate the frequencies into two regions, where red represents all regions that have decreased in amplitude and yellow denotes an increase in amplitude. We find that the increase/decrease in amplitude reflects the bi-modality of the distribution of amplitudes. In Figure 6.16b, we show the resulting shifted resonant frequencies, $f_{n,\text{contact}}$.

We use only one channel as we are primarily concerned with the observation of non-topographic contrast whilst imaging, highlighting the sensitivity of the contact resonance with HS-AFM. However, it is not possible to image whilst using the two-channel method as discussed in Section 6.3.2. Instead, we follow the procedure, described in Section 6.2.1, to relate the results to frequency formation.

Finally, we use the frequency data to convert each pixel to a normalised contact stiffness using the theory outlined in Chapter 5. We utilise the same parameters as in Section 6.3 and calculate the contact stiffness using the first mode. The results are shown in Figure 6.17. We can clearly identify the graphene flakes that are deposited on the sample surface. We note that the expected edge sections, identified as having low am-

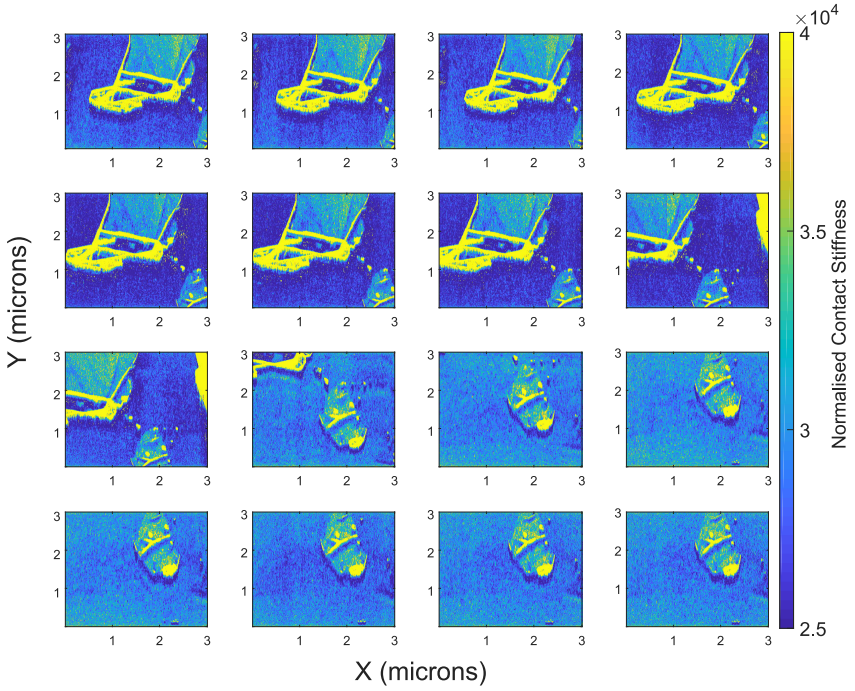

(a) With edge effects

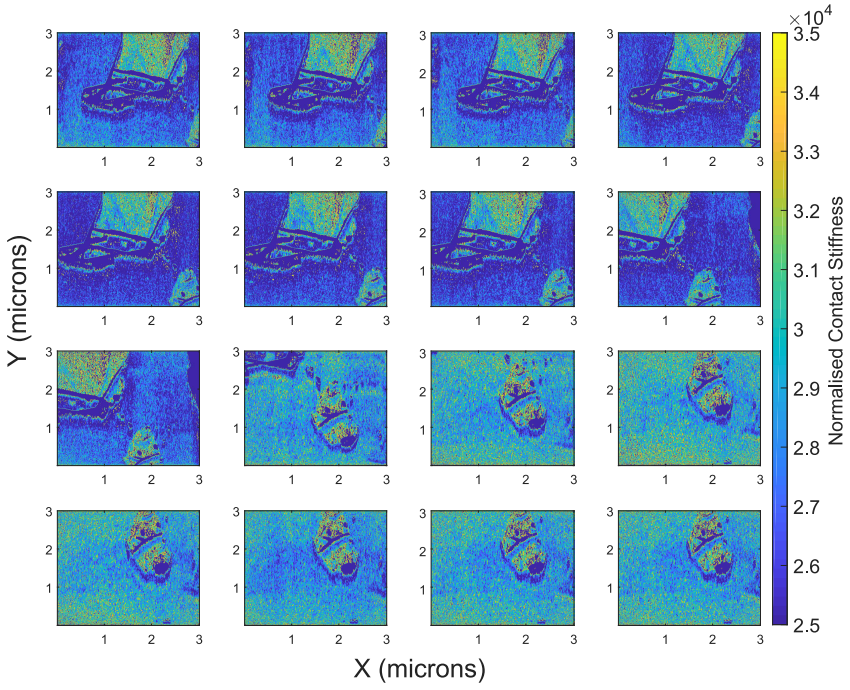

(b) Without edge effects

Figure 6.17: The contact stiffness of the bulk silicon, calculated by considering the shift in resonant frequency shown in Figure 6.16, where (a) shows the stiffness map including those regions of high contact stiffness expected to occur due to edge effects and (b) shows the same frames with edge effects removed. We see the greatest contrast between the silicon substrate and graphene features where both graphene layer and flake are present. This implies that larger material mass increases stiffness sensitivity when imaging. Data is collected at two frames per second.

plitude in Figure 6.17 result in significantly higher contact stiffness than the rest of the sample, as expected. The graphene flake has a higher contact stiffness than the bulk silicon substrate whereas the graphene layer has a more similar stiffness count. We next turn to how the contact stiffness data reflects the material properies for both steel and silicon-graphene samples.

6.4.3 *Comparing to Material Properties*

We have shown how to relate a change in amplitude on a lock-in amplifier to a stiffness measurement when imaging with HS-AFM. Our measurements have shown contrast on two different materials, carbide features on a sample of sensitised SS grade 316, and graphene flakes deposited on a silicon substrate. This demonstrates for the first time that HS-AFM can be combined with contact resonance techniques to measure non-topographic sample features, previously hidden from investigation. The direction of the frequency shifts are as expected (both graphene and carbide features are more stiff than bulk material). This is all achieved without reliance on additional control procedures which would diminish the high sample throughput of a HS-AFM.

We seek to relate the contact stiffness to material properties, which we examine in Chapter 5. Here, we outline a means for doing so in order approximate the relative change in elastic properties of different stiff materials. In order to relate the contact stiffness to a material property, we first assume that there is a adhesive but non-deformed contact event (DMT in Section 5.2) between the tip and sample [72],

$$k_{\perp} = \sqrt[3]{6R(E^*)^2 F_N}, \tag{6.8}$$

where R is the tip radius, F_N is the normal loading force, and E^* is the reduced modulus of the coupled tip-sample, as given by (5.2) in Section 5.2. Assuming a silicon tip, with a Young's modulus of 169 GPa and Poisson ratio of 0.26 [211], we expect to see the reduced modulus for the sample of gold, steel 316 and carbide sections to be approximately 60 GPa, 93 GPa, and 125 GPa, respectively. However, as discussed in Chapter 5, there are significant uncertainties in relating a contact stiffness to a reduced modulus due to changes that can occur to the tip radius (due to tip wear) and the influence of additional adhesion forces (as discussed in Chapter 1). Instead, we use (6.8), to calculate the relative difference in the tip-sample reduced modulus, according to the calculated contact stiffness. Given two contact stiffnesses (calculated using a tip of equal radius and equal normal force) the relative contact stiffness is

$$\frac{E_1^*}{E_2^*} = \left(\frac{k_{\perp,1}}{k_{\perp,2}}\right)^{\frac{3}{2}}. \tag{6.9}$$

This equation assumes that the 1/3 power law applies, such that there has not been significant tip wear and that the tip apex can be assumed to be hemi-spherical. The low tip-wear regime of HS-AFM, evidenced by the stability of image quality of several

hours, gives support for this assumption. When comparing the relative stiffness for SS sample and carbides to DART measurements, we utilise the same power law relationship in both calculations. This allows us to compare CR-HSAFM methods to existing CR-AFM methods. Our subsequent measurements on graphene are also calculated using this power law. However, the focus of the measurements on graphene was the ability to utilise contact resonance AFM whilst imaging at high speed with a single channel. Further work will look to demonstrate measurements on graphene whilst imaging using two (or more) channels to relate the lock-in amplifier data to contact stiffnesses.

In Figure 6.18, we show a comparison of the material properties of the sample normalised to the reduced modulus of steel. The reference stiffness was chosen as the mean value of the higher peak in Figure 6.11. In Figure 6.18a, we show values from our own measurements and, in Figure 6.18b, we show a comparison to values taken by the Cypher AFM (Asylum Research, Santa Barbara, USA), described in Chapter 5. We find similar values between the two measurement devices. The Cypher AFM calculates the normalised reduced modulus of the carbide feature to be $E^*_{\text{carbide}} = 1.057E^*_{\text{steel}} \pm 0.015E^*_{\text{steel}}$, whereas our own measurements give a normalised reduced modulus of $E^*_{\text{carbide}} = 1.032E^*_{\text{steel}} \pm 0.011E^*_{\text{steel}}$.

We next investigate the repeatability of our measurements over multiple frames as well as the difference in using a single channel and two channels of the lock-in amplifier. The frame shown in Figure 6.18a and subsequently analysed is one of a series of frames taken over the same section of SS grade 316. As discussed in Section 6.3.2, we are unable to drive the sample simultaneously with both channels whilst imaging due to the presence of interference across both channels. In order to circumvent this obstacle, we drive with one channel and then switch to driving with a second. This results in the inverted amplitude count data, shown in Figure 6.7. We repeat our analysis for each of the frames in this series and calculate the reduced modulus of the carbide feature for each frame.

For the nine frames, we find the normalised reduced modulus of the carbide region (as specified by the increased height of the material) to be $E^*_{\text{carbide}} = 1.059E^*_{\text{steel}} \pm 0.029E^*_{\text{steel}}$ when using the single channel data and $E^*_{\text{carbide}} = 1.032E^*_{\text{steel}} \pm 0.0047E^*_{\text{steel}}$ when using two channels. We find that the gradient matching method that utilises both channel counts gives a lower standard deviation than the single channel method. Finally, we relate the carbide material to an equivalent Youngs modulus. This has larger uncertainty owing to the anisotropic behaviour of the tip as well as the unknown poisson ratio of the carbide feature. We assume a indentation modulus of the tip of 165 GPa [69] and Poisson ratio for the carbide as 0.28 – 0.3 resulting in a calculated Young's modulus of 2173 GPa, for the normalised reduced modulus calculated using two channels of the lock-in amplifier.

We now examine how the material properties of graphene relate to the silicon substrate. In Figure 6.19, we show the contact stiffness distribution calculated at three different frames of Figure 6.20 which reflect the large graphene flake, a single graphene layer and a combination of both flake and layer. We find that the flake introduces significant change to the stiffness distribution, in a way that the single layer does not. We

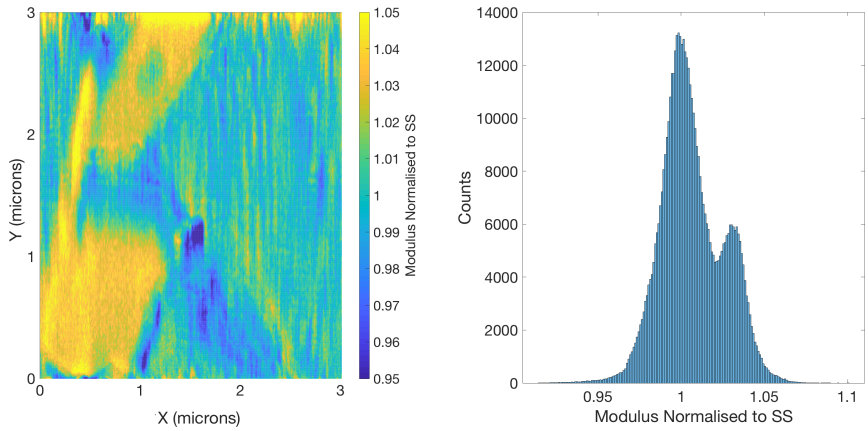

(a) CR-HSFM Measurements

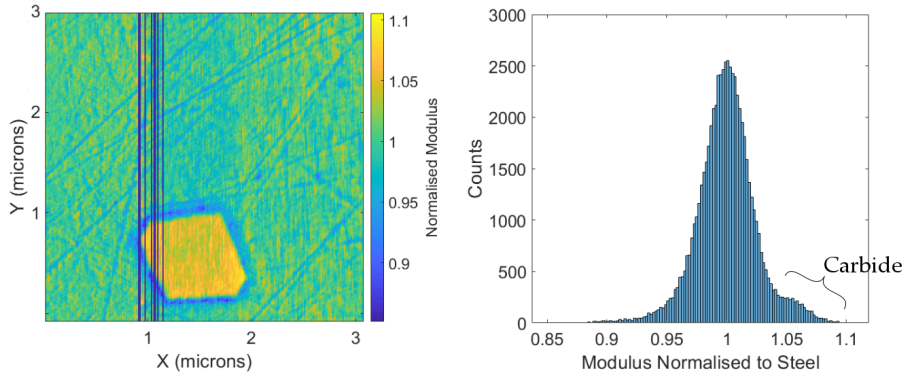

(b) DART Measurements

Figure 6.18: We show a comparison between the measured modulus normalised to that of Steel 316 taken using (a) the HS-CRFM method described here and (b) the DART method implemented on the Cypher AFM described in Chapter 5. We find very good agreement between the two measurements.

also find that the edge effects of the graphene-silicon sample are far more pronounced then similar effects on the SS sample. As we are primarily concerned with how contrast remains whilst imaging, we note that we have resticted all measurents to single channel information using the first channel. Further research will re-examine this sample using the dual channel approach (or multi-channel information), described in Section 6.2.1, which will allows us to account for changes in the quality factor as well as the resonant frequency. This will further constrain the simple harmonic oscillator equations, giving higher confidence in the calculated contact stiffness, as well as highlighting changes in the viscous properties of the two material (silicon and graphene) samples.

We now look at how the graphene material properties relate to the bulk silicon. In Figure 6.20a, we show the results of fitting a bimodal Gaussian distribution to the contact stiffness data shown in Figure 6.19, with fit parameters $a_1 = 25470, b_1 = 20890, c_1 = 1823, a_2 = 11120, b_2 = 24270, c_2 = 1967$ (where a_i is the amplitude, b_i is the centroid location (representing the mean), and c_i is the width (representing the standard deviation) of the i^{th} peak for $i = 1, 2$, see Section 6.4.1). We use the value for the contact stiffness associated with the larger peak for the reference contact stiffness and calculate the relative

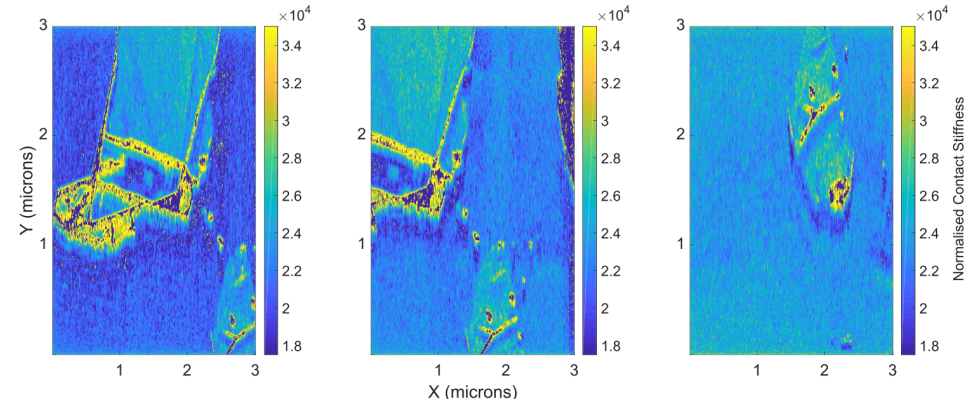

(a)

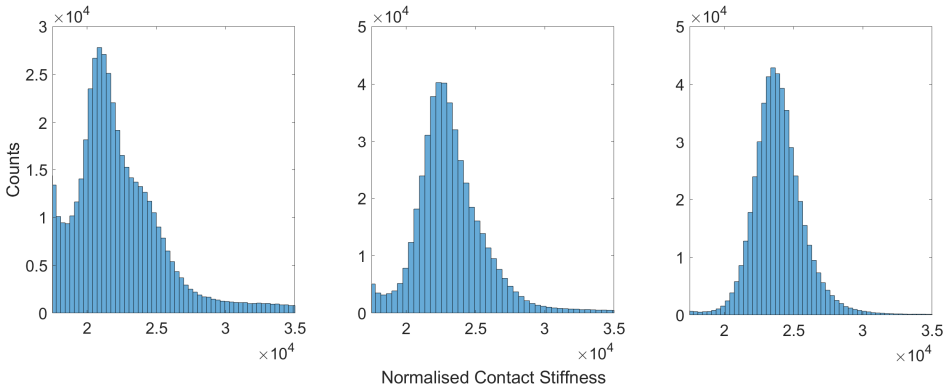

(b)

Figure 6.19: Three different sections of the silicon-graphene sample shown as (a) normalised contact stiffness images and (b) the corresponding count data. We find that the largest contrast between the silicon substrate and the graphene occurs when both flake and single layer are present, reflected in the bimodality of the first frame compared to the almost symmetrical peak of the last frame.

reduced modulus value according to (6.9), $E^* = 1.252E^*_{\text{silicon}} \pm 0.0289E^*_{\text{silicon}}$. We find that the modulus values of the graphene can only be identified in the first frame, where there is appreciable count data showing two materials. We next turn to how this value reflects a Young's modulus for the graphene material. Recall that the anisotropic nature of the silicon substrate introduces uncertainty in the Young's modulus of silicon and Poisson ratio of the graphene material is also unknown. This makes calculation of the reduced modulus of the graphene features difficult. By assuming a value of $E_{\text{Silicon}} = 169\,\text{GPa}$[4] and $\nu = 0.14 - 0.19$ according to [210, 212] and find the resulting Young's modulus of the graphene flakes to be $283\,\text{GPa} \pm 15\,\text{GPa}$, which is similar to the Young's modulus of graphene flakes (250 GPa) recorded in [209].

4 Note that the previously assumed value of the indentation modulus relates to single crystal silicon whereas this value refers to the Young's modulus of the bulk material.

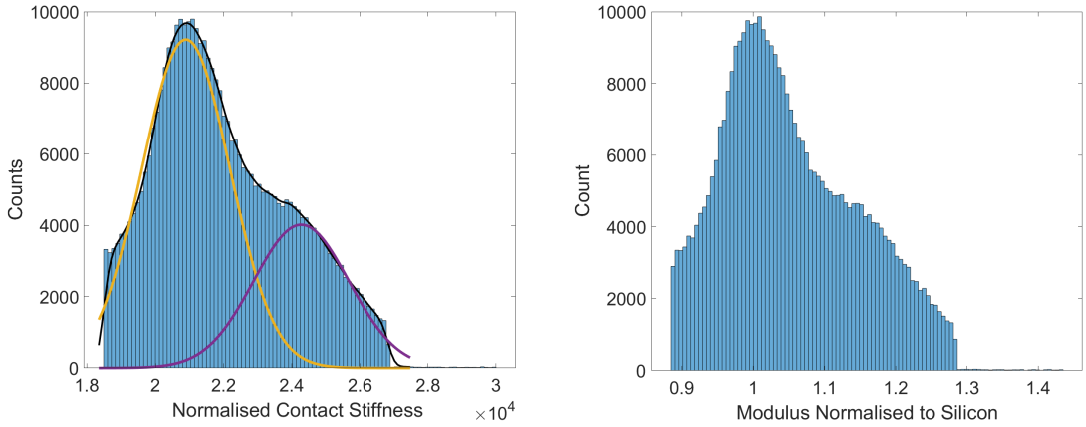

(a) (b)

Figure 6.20: Utilising the high-contrast first frame of Figure 6.19, we are able to (a) fit a two-term Gaussian, with fit parameters $a_1 = 25470, b_1 = 20890, c_1 = 1823, a_2 = 11120, b_2 = 24270, c_2 = 1967$ and where a_i is the amplitude, b_i is the centroid location (representing the mean), and c_i is the width (representing the standard deviation) of the i^{th} peak, to capture the increased stiffness of the bulk graphene material and calculate (b) the modulus normalised to the silicon substrate. We find that the graphene features are significantly stiffer than the silicon substrate, as expected.

6.5 DISCUSSIONS AND CONCLUSIONS

In this chapter, we have shown that the combination of HS-AFM with contact resonance allows for non-topographic mapping which can identify sample artefacts that do not clearly appear in the topographic data above. Furthermore, when considering the measured material properties of carbides, we find that material stiffness properties agree with the existing DART method of contact resonance as well as with literature values.

We have presented examples of how we are able to use CR-HSAFM techniques to identify features with low topographic signal when imaging. Specifically, we have demonstrated the ability to pick out graphene monolayers in the contact resonance signal when a monolayer has an expected height of 0.335 nm. This is achieved using a single channel of the lock-in amplifier which increases the difficulty in quantifying these results (due to assumptions on the amplitude and quality factor of the shifted resonant peak). Further improvements are expected when utilising two or more channels of the lock-in amplifier.

Additionally, we are able to use a single channel to quantify a surface feature when it encompasses a larger volume of the frame, such as the larger graphene flake. This indicates a sensitivity of CR-HSAFM measurements to the quantity of material that is being observed and raises questions over the interaction depth of the acoustic signal when imaging at high speed, which may be influenced by the lubrication layer that is believed to enable the HS-AFM to achieve fast scan speeds with diminished lateral forces on the AFM tip. Though this line of enquiry will be of interest for the eventual ability of CR-HSAFM to image material stiffness properties without reliance on reference materials, our results utilising CR-HSAFM will be of use for stiffness quantification of large material features such as the carbide on SS sample. However, future application of CR-

HSAFM should seek to expand the operational capabilities to measure the bulk material and additional stiffness features simultaneously without reliance on relative measurements. We describe below further experiments that may be performed to achieve such extensions.

First, we note that the theory of contact mechanics, as outlined in Chapter 5, requires the normal loading force that is applied to the cantilever to be known. In practice, the exact specifications of such a loading force is difficult to ascertain due to uncertainties as to the exact moment when the snap-down event occurs. However, this could be addressed by using an additional detection system that measures both the displacement (as is currently implemented on the HS-AFM) as well as the deflection such that the exact position of the tip is tracked, see, for example, [213]. Once the contact-event is known to occur, the distance between tip and sample can be diminished to create stiffness-loading curves at a single location, such as those seen in Chapter 5. This method would allow a single location on the bulk material to be quantified, but would be exposed to the same uncertainties of tip radius as in Chapter 5.

As the HS-AFM operates in a low-tip wear regime, it is conceivable that the iterative single point measurement methodology of Chapter 5 could be expanded to occur across multiple locations on the sample while imaging. This could be achieved such that a frame is taken of a chosen section of the sample and the distance between tip and sample is diminished on a per frame basis such that the load on the cantilevered AFM probe increases for each frame. The load dependence of the stiffness measurements across the frame would occur on a per pixel basis, such that a data volume (multiple stiffness maps, stacked across the change in load) is constructed showing how the stiffness at each pixel varies with load. While this would result in a large volume of data, it could give insight into the suitablity of existing models of contact mechanics for HS-AFM as well as the influence of the lubrication layer that occurs at high-scan speeds [31, 60].

Both approaches could give insight into the normal loading force as well as additional adhesive forces, caused by the lift-off force and lubrication effect that occurs at high-scan speeds [27], reducing one of the sources of uncertainties when relating a contact stiffness to a material property. However, there may still be significant uncertainties resulting from the material property and geometry of the tip geometry. These can be addressed through tip reconstruction methods [214] or using hard tips with known properties, such as diamond tips. However, we note that our work has successfully achieved non-destructive and non-topographic measurements using HS-AFM without such considerations.

These results present the first occurance of quantified stiffness measurements on stiff samples taken using contact resonance with HS-AFM. We find that CR-HSFM is of similar accuracy as existing CR-AFM techniques (when compared against DART performed on the Cypher AFM), but with significantly decreased data collection times and standard deviation across measurements. For example, the HS-AFM is able to collect two million pixels of topography and contact resonance data simultaneously per second, compare to approximately 100,000 data points per second for the Cypher AFM [215].

By combining contact resonance techniques with HS-AFM, we have developed a tool for stiffness measurements that operates in a non-destructive regime and with a lateral resolution of several nanometres at each pixel, as described in Section 5.2. This constitutes a significant improvement over existing techniques, such as nanoindentation (see Section 4.3), as CR-HSFM can carry out large area non-destructive material testing in real-time. We expect this to be a benefit both for industry and the wider field of material science, as set out in Chapter 1.

7

CONCLUSIONS

This thesis sets out the steps required to relate the contact-resonance measurements of a micro-mechanical AFM probe to the stiffness properties of a stiff material using a high-speed AFM (HS-AFM). Specifically, quantification of the Young's (or reduced) modulus through high-speed contact resonance AFM. Below we summarise the main contributions of our work.

1. NEW METHOD FOR HIGHER MODE CANTILEVER CALIBRATION

We have developed a new means for calibrating a micro-mechanical cantilever at high mode number. Our method utilises the hydrodynamics of the first mode to calculate the material properties of the probe that are typically hard to measure, such as the thickness of the gold layer (commonly included on AFM probes) as well as the total thickness of the beam. Once the material properties are known, two key properties of the AFM sensor can be calculated and validated experimentally: the resonant frequencies, in vacuo and oscillating far from any surface contributions, and the effective stiffnesses.

The calculated resonant frequencies, in vacuo, are used to identify the location of resonant peaks in noisy data, such as those presented in Section 2.6, Section 5.3 and Section 6.3. Separately, the effective stiffnesses describes how the probe approximates stiff materials as the oscillation frequency increases. Hence, the mode number of an AFM probe can be 'stiffness-matched' to a material to give the highest sensitivity when performing contact resonance mesaurements. We demonstrate this explicitly in the contact resonance experiments carried out in Chapter 5.

2. CALCULATION OF THE CHANGE IN HYDRODYNAMIC LOADING AT HIGH FREQUENCIES AND LOW SENSOR–SAMPLE SEPARATION DISTANCES

Considerations of the hydrodynamics, as utilised in our calibration method, highlights the sensitivity of AFM probes to environmental conditions and raises the question of how the hydrodynamics around a sensor will alter when a surface is introduced. In Chapter 3, we consider this explicitly by building our own numerical solver that simulates 2D hydrodynamics around oscillating bodies, with typical AFM cross-sectional geometry, near to a rigid surface. We consider the case where the frequency of oscillation is high and the separation distance between the body and surface is small (representing sensor-sample contact). We find that the resonant frequency of the cantilver is relatively unaffected by hydrodynamics but that the quality factor, a measure of the system damping, can increase significantly.

Our approach to calculating the hydrodynamics differs from previous results as it utilises open-source FEM methodology rather than commercial numerical packages or semi-analytic boundary element formulations. Using our numerical solver, we are able to recreate previous results with high accuracy. Given a known velocity profile of the cantilever at a given mode number, and an increase in computational power, our approach is amenable to considering 3D length-wise flow contributions. Alternatively, our results can be extended to include the bi-phasic fluid regime that has been suggested to lead to low-tip wear when scanning at high speeds [27].

3. METHOD FOR ESTIMATION OF CRUCIAL CONTACT RESONANCE PARAMETERS: TIP HEIGHT AND LENGTH OFF-SET

The utilisation of micro-mechanical cantilevers, such as AFM probes, allows for sub-micron to nanometre resolution of material properties. In Chapter 4 and Chapter 5, we have detailed and verified the theoretical steps and modelling assumptions required to relate the change in resonant frequency of an AFM probe to a material property. Importantly, we show that the assumption of parallel sensor-sample contact is not sufficient when considering stiff materials with soft cantilevers, especially at low mode number, as the shift in resonant frequency may not relate back to a contact stiffness. Instead, we show that the introduction of a tilt to the sensor-sample system creates a means for estimating two crucial parameters, the length offset as well as the tip height, which are required to calculate an idealised contact stiffness. This avoids the need for additional measurements to be taken.

4. INVESTIGATION INTO SHORTCOMINGS OF LOW RESOLUTION CONTACT RESONANCE MEASUREMENTS AS APPLIED TO STIFF MATERIALS

In Chapter 5, we verify the contact resonace technique by measuring the change in frequency of an AFM probe at multiple locations on two samples of stiff materials, gold and stainless steel, under different load conditions. These are used to test the underlying assumptions, commonly repeated within the contact resonance literature [66, 69, 71]; that the contact stiffness is related to a material property by means of a suitable theory of contact mechanics.

We give experimental validation of the sensitivity of higher modes to material stiffness when using a soft cantilever. We highlight that the use of the parallel beam approximation will lead to significant inaccuracies when the first few modes of a soft cantilever are used to measure contact stiffnesses of stiff materials, but that the higher modes are far less sensitivity to tilt parameters (such as tip height and lateral stiffnesses). By including these considerations and the method for estimation of contact resonance parameters, we are able to calculate contact stiffnesses that are consistent across all modes.

When relating the contact stiffnesses to a specific material property (the reduced modulus which contains information about the Young's modulus of both tip and sample),

we find that the calculated values can vary over several magnitudes. These results highlight the sensitivity of contact resonace measurements to experimental conditions when applied to stiff materials. Specifically, the interdependence of the tip radius and geometry to the theory of contact mechanics motivates that tip-wear is a significant obstacle in quantifying contact resonance measurements. Additionally, the presence of adhesive forces may influence the low force regime that we consider. This highlights a potential lower limit in the validity of the contact mechanics models. Further investigations are required to fully understand and differentiate between these causes.

Hence, we find that, for low-resolution contact resonance measurements on stiff materials, ongoing consideration of the tip radius and geometry is required, as well as possible changes to the modelling of the contact event (such as the influence of adhesive forces). We conclude that contact resonance measurements on stiff materials will be most robust, with lowest uncertainty and most amenable to quantification, when taken under low tip wear conditions such as using a HS-AFM.

5. DEMONSTRATION OF THE STRENGTHS OF CONTACT RESONANCE WHEN COMBINED WITH HS-AFM

The work in this thesis culminates in the combination of high speed atomic force microscopy (HS-AFM) with contact resonance (CR) measurements, as applied to stiff samples. We show that the preceding contributions allow for quantified stiffness measurements of sample artefacts on two examples of stiff materials: carbides in a sample of stainless steel (grade 316), and graphene flakes and monolayers, deposited on a buk silicon substrate. The realisation of contact resonance on stiff samples holds the following benefits over conventional contact resonance techniques:

- We demonstrate in Chapter 2 that the higher modes of an AFM probe increase its effective stiffness, allowing it to be 'stiffness matched' to stiff materials. The HS-AFM operates in a high–frequency domain in order to achieve the high scan speeds. Hence, the higher modes are easily accessed and utilised.
- The HS-AFM operates in a low tip-wear regime, emphasised by the stability of image quality over large time frames (minutes to hours). Therefore, we conclude that CR-HSAFM is not restrained by considerations of the AFM tip that we describe in Chapter 5.
- In Section 6.4, we show that CR-HSAFM is capable of non-topographic feature detection. This is significant for the area of material testing as it highlights the possibility of nanoscale stiffness measurements which cannot be achieved with existing techniques.
- By combining CR with HS-AFM, we achieve quantified stiffness maps that have a thousand–fold increase in pixel count when compared to existing methods, as shown in Figure 6.18. This results in a tool that can measure sub–nanometre stiffness variations over μm^2 areas in seconds. This is a significant improvement on the

destructive and widely used nanoindentation method that has a lower resolution of tens of nanometres across minutes to hours.

7.1 FURTHER EXTENSIONS

The versatility of AFM methods and techniques make it a rich area for scientific research. Several of the chapters in this work are amenable to extensions that would be beneficial to the wider area of AFM, as well as specifically with regards to stiffness measurement using contact resonance techniques. For example, our method of calibrating the effective stiffness of an AFM probe, given in Chapter 2, was formulated and applied to thin rectangular beams with a thin gold layer as this is one of the most common AFM cantilevers and also relied upon in Chapter 6. However, this method is equally applicable to beams with multiple composite layers or different reflective coating. Specifically, our method could be applied to AFM cantilevers that have a thin piezo or magnetic coating, or to an AFM with trapezoidal or 'stocky' (large width) geometry. However, both require careful consideration of the suitability of the Euler-Bernoulli beam model and hydrodynamics of the system.

The hydrodynamics of the system, as investigated in Chapter 3, can be considered using extensions to our FEM solver. First, the aforementioned changes to a cantilever's cross-sectional geometry, trapezoidal or stocky, can be considered using changes to the mesh files and experimental validation. Second, the solver can be extended to include three dimensional flow, which would require the inclusion of a mode-specific velocity profile for the cantilever and consideration of how the flow is treated at the clamped end. Additionally, high-performance computing is likely to be required to solve the full three dimensional system. Finally, the two dimensional case that we have presented deals with both a beam with rectangular and cylindrical cross-sectional area. However, we may alternatively consider the case of the tip–sample interaction by treating the circular geometry as an approximation for the apex of an AFM tip. Given this approximation (which requires careful treatment), an additional fluid layer situated between the 'tip' and 'sample' (the surface introduced in Section 3.4.2) could give additional insight into both the adhesive effects for regular AFM operation as well as the lubrication effect thought to occur during HS-AFM imaging.

Adhesive effects between the tip and sample (such as adhesion forces that prevent the cantilever from 'snapping from contact') are one of several sources of uncertainty during our single point measurements in Chapter 5. Repeating these experiments on similarly stiff samples using higher normal loads will reduce the effect of adhesion as we move away from effect of the snap-from-contact event. However, the tip remains a significant source of uncertainty in quantifying the material properties of a sample without recourse to other sample properties. We perform these measurements on gold and stainless steel (SS) samples which contain surface features such as grain boundaries, surface slopes, and other topographic variations. Repeatition of our procedure on a flat material with known elastic properties would aid the specification of how the tip geometry alters the

contact stiffness of a measured material and the suitability of higher modes for contact resonance measurements on stiff materials using soft cantilevers.

Ultimately, the use of soft cantilevers is beneficial for the high throughput of HS-AFM imaging. However, HS-AFM also relies on a hemispherical assumption of tip geometry. Hence, additional measurements on a flat surface with calibrated properties would aid HS-AFM as the tip is expected to experience less tip wear than measurements on a single point on a sample (due to a theorised lubrication effect). The contact stiffness measured in Chapter 6 highlights one of the most promising avenues for further investigation into contact resonance methods applied to HS-AFM; the large increase in observed contact stiffness. We note that the measured contact resonance is significantly higher than that observed when measuring at a single point. If the tip is assumed to have similar radius (as implied by the low tip wear regime), the elastic properties of the SS sample investigated in Chapter 5 and Chapter 6 are similar (where different sections of the same material were studied), and that the DMT theory of contact mechanics holds, then the total contact force is left as the only remaining parameter that could cause a significant increase in the contact stiffness.

The low tip wear regime is believed to be preceded by a 'lift-off' force that increases the tip-sample separation distance and diminishes the lateral force in the system. Hence, CR-HSAFM measurements may give a means for quantifying the magnitude of this lift-off force as well as leading to quantified stiffness measurements that are not reliant on reference material properties. Quantification of the lift-off force, possibly supported by the numerical scheme introduced in Chapter 3, would give additional evidence for and insight into the mechanism that allows the HS-AFM to achieve its several orders of improvement over other existing AFM techniques (with regards to its scanning speed, data aquisition abilities, and large area mapping) without degradation to the tip.

Even without these additional measurements, this work outlines and expands upon contact resonance applied techniques and develops their readiness for combination with HS-AFM. We expect that CR-HSAFM will greatly enhance material science due to the non-destructive, high resolution, and impressive throughput of the device and we look forward to its use in bringing further advances in material science and beyond.

A

APPENDIX

	5 V	2 V	1 V	0.5 V	0.1 V	0.08 V	0.06 V	0.04 V
Position 1	57254.9	57129.6	57037.7	56494.3	55698.7	56157.8	55965.7	55860.3
Position 2	57111.3	56970.2	57097.3	56724.1	56446.5	56507.0	56749.4	56342.8
Position 3	57556.4	56988.4	56976.8	56901.0	55988.3	56062.3	56101.5	56009.7
Position 4	57711.8	57404.2	–	56570.3	56453.1	55984.2	55632.6	55749.8
Position 5	57582.2	57280.5	56799.2	56490.0	56052.0	54871.3	55226.8	55504.6
Position 6	57111.8	56894.0	56888.1	56278.3	–	55163.8	55398.2	55281.0
Position 7	57473.2	57199.5	55948.5	56731.0	55124.4	56322.4	55885.8	55882.3
Position 8	57045.0	57304.9	57063.9	56513.9	56597.8	55965.2	56480.6	56500.5
Position 9	56976.5	57095.3	56580.5	56678.5	55986.8	56426.8	56419.6	56105.0
Position 10	56189.4	57126.0	57203.7	56877.9	56428.4	56491.5	56694.4	56570.3
Position 11	57227.7	57214.4	56138.3	56453.1	55984.2	55046.6	54929.4	55163.8
Position 12	57029.2	57280.6	57108.6	56421.9	55645.1	55862.6	55927.8	55852.8
Position 13	57249.0	56636.9	57076.6	55820.9	56000.3	56272.9	55998.3	55880.8
Position 14	57300.5	57090.3	57399.0	56008.1	55159.5	55239.9	55297.4	–
Position 15	57248.0	57019.0	56911.8	56633.7	55800.5	56064.3	55922.8	55872.2
Position 16	57024.9	57153.6	56782.6	56863.3	56068.1	56132.3	55101.9	55318.8

Table 13: Experimental data for contact resonance on sample of SS grade 316 (Mode 1)

	5 V	2 V	1 V	0.5 V	0.1 V	0.08 V	0.06 V	0.04 V
Position 1	177831	177944	177616	176481	174589	175335	174920	174430
Position 2	177915	177343	177557	176966	175582	175833	176055	175008
Position 3	178274	177362	177453	177269	175136	175543	175581	175257
Position 4	178456	177915	178281	176500	175746	175746	174239	174239
Position 5	178337	177678	177116	176010	175182	169842	171744	173939
Position 6	177636	177258	177265	175685	–	170973	172229	171978
Position 7	178489	177919	174476	177275	172954	175509	174819	174804
Position 8	177555	177982	177660	176406	176404	173678	175226	175749
Position 9	177761	177598	176162	176421	174426	175379	175773	174503
Position 10	175318	177548	177938	177379	175995	176279	176766	175746
Position 11	177872	177600	–	176751	174239	172481	172732	172481
Position 12	177663	177849	177488	176303	174666	174954	174412	174753
Position 13	178046	176604	177345	174264	172149	174268	172993	172682
Position 14	178233	177565	177977	174804	172580	172687	172682	173238
Position 15	178044	177321	177323	176709	174043	175382	174717	174985
Position 16	177845	177680	177162	177319	175315	175524	171676	172359

Table 14: Experimental data for contact resonance on sample of SS grade 316 (Mode 2)

	5 V	2 V	1 V	0.5 V	0.1 V	0.08 V	0.06 V	0.04 V
Position 1	365056	365144	364045	361334	292172	294309	286596	281469
Position 2	365539	363981	364221	362511	351530	350570	253799	218301
Position 3	365488	363795	363796	363633	357234	354884	353770	351562
Position 4	365897	365063	363724	358092	291554	290806	279218	278470
Position 5	366270	364338	363464	358054	295578	293010	292998	290965
Position 6	363660	364058	363312	358903	291937	268003	267256	218286
Position 7	366182	365065	357443	362403	356538	354498	354341	351445
Position 8	364373	365191	364414	361691	291638	291390	235899	240103
Position 9	364870	364755	360997	362694	349271	346650	348900	347999
Position 10	360389	364271	364989	363773	288751	262546	218670	218286
Position 11	365022	364917	360366	357345	291180	290806	291180	218286
Position 12	365129	364267	364600	359989	287431	286360	283567	288203
Position 13	365405	362167	363188	308871	299030	311338	306859	–
Position 14	365663	364615	364397	357284	348026	252714	257635	219408
Position 15	365221	363657	363648	362012	353140	352747	354014	352262
Position 16	365111	363699	363231	363071	302129	297406	299802	284836

Table 15: Experimental data for contact resonance on sample of SS grade 316 (Mode 3)

	5 V	2 V	1 V	0.5 V	0.1 V	0.08 V	0.06 V	0.04 V
Position 1	613052	609472	609349	601726	576818	581846	586887	578374
Position 2	614601	611106	611298	606100	537078	537115	–	536807
Position 3	614793	609807	609705	606395	592815	588413	587871	585669
Position 4	615282	612388	609904	597970	569129	536310	558686	536807
Position 5	614791	610890	606114	595786	535468	535488	534620	534822
Position 6	610454	611453	606604	594448	534321	535315	534818	534321
Position 7	615048	611154	595297	605043	590972	589836	586471	583347
Position 8	612461	613044	609769	602333	536587	537502	536949	536563
Position 9	612565	607541	603225	605190	536851	536880	–	538299
Position 10	604109	611325	610947	605969	580686	–	571118	537304
Position 11	613905	611227	602985	594489	534818	535812	534818	534818
Position 12	614066	608724	608348	599734	535625	532875	533587	532096
Position 13	613820	607325	606668	534845	535078	531408	552245	537867
Position 14	611756	610908	605839	588477	535882	535965	–	535812
Position 15	612455	609193	607268	601153	536917	536783	536212	536658
Position 16	612737	610274	605291	606386	536942	535233	535378	535313

Table 16: Experimental data for contact resonance on sample of SS grade 316 (Mode 4)

	5 V	2 V	1 V	0.5 V	0.1 V	0.08 V	0.06 V	0.04 V
Position 1	910450	887293	891936	864419	901741	902117	902276	901932
Position 2	914760	900753	900079	883324	799022	801721	–	719124
Position 3	914787	896873	895021	882414	–	850929	–	–
Position 4	916470	903408	898072	870208	902406	901787	901787	764945
Position 5	911087	898727	882162	852810	716927	733822	781893	747221
Position 6	902889	901745	882996	902709	696833	694356	689403	689403
Position 7	912527	896352	856892	879805	–	900503	837691	–
Position 8	910842	901624	896043	869999	728173	749466	760851	–
Position 9	901753	878634	877602	882287	777579	772142	–	754418
Position 10	889162	902254	896915	877196	900537	–	902406	902406
Position 11	913605	904305	887546	862159	736462	736462	745750	742034
Position 12	913917	887684	888370	858266	961495	807545	808038	–
Position 13	911191	894849	882461	780226	749594	765810	745269	753047
Position 14	893160	899088	872824	692890	779483	769192	–	738938
Position 15	899750	897773	883511	853590	–	851805	852991	–
Position 16	901734	–	877369	875903	834519	739597	741704	725944

Table 17: Experimental data for contact resonance on sample of SS grade 316 (Mode 5)

BIBLIOGRAPHY

[1] R. P. Feynman. "There is plenty of room at the bottom." In: *Miniaturization*. Vol. 29. 6. 1978, p. 282.

[2] F. J. Giessibl. "Atomic Resolution of the Silicon (111)-(7x7) Surface by Atomic Force Microscopy." In: *Science* 267.5194 (1995), pp. 68–71.

[3] S. Kitamura and M. Iwatsuki. "Observation of 7x7 Reconstructed Structure on the Silicon (111) Surface Using Ultrahigh-Vacuum Noncontact Atomic-Force Microscopy." In: *Japanese Journal of Applied Physics Part 2-Letters* 34.1B (1995), pp. 145–148.

[4] F. J. Giessibl and C. F. Quate. "Exploring the Nanoworld with Atomic Force Microscopy." In: *Physics Today* 59.12 (2006), p. 44.

[5] G. Binnig, C. F. Quate, and Ch. Gerber. *Atomic force microscope*. 1986.

[6] P. Eaton and P. West. *Atomic Force Microscopy*. 2010, pp. 1–256.

[7] A. Ruf, M. Abraham, M. Lacher, K. Mayr, and T. Zetterer. "A Miniaturised Fabry Perot AFM Sensor." In: *Solid-State Sensors and Actuators, 1995 and Eurosensors IX.. Transducers '95. The 8th International Conference on*. Vol. 1. 1995, pp. 660–663.

[8] R. S. Gates and J. R. Pratt. "Accurate and precise calibration of AFM cantilever spring constants using laser Doppler vibrometry." In: *Nanotechnology* 23.37 (2012).

[9] Z. Peng and P. West. "Crystal sensor for microscopy applications." In: *Applied Physics Letters* 86.1 (2005).

[10] M. Tortonese, Yamada. H., R. C. Barrett, and C. F. Quate. "Atomic force microscopy using a piezoresistive cantilever." In: *Solid-State Sensors and Actuators*. 1991, pp. 448–451.

[11] G. Meyer and N. M. Amer. "Novel optical approach to atomic force microscopy." In: *Applied Physics Letters* 53.12 (1988), pp. 1045–1047.

[12] C. A. J. Putman, B. G. De Grooth, N. F. Van Hulst, and J. Greve. "A detailed analysis of the optical beam deflection technique for use in atomic force microscopy." In: *Journal of Applied Physics* 72.1 (1992), pp. 6–12.

[13] M. J. Higgins, R. Proksch, J. E. Sader, M. Polcik, S. McEndoo, J. P. Cleveland, and S. P. Jarvis. "Noninvasive determination of optical lever sensitivity in atomic force microscopy." In: *Review of Scientific Instruments* 77.1 (2006), p. 013701.

[14] O. D. Payton, L. Picco, A. R. Champneys, M. E. Homer, M. J. Miles, and A. Raman. "Experimental observation of contact mode cantilever dynamics with nanosecond resolution." In: *Review of Scientific Instruments* 82.4 (2011).

[15] O. D. Payton, L. Picco, M. J. Miles, M. E. Homer, and A. R. Champneys. "Modelling oscillatory flexure modes of an atomic force microscope cantilever in contact mode whilst imaging at high speed." In: *Nanotechnology* 23.26 (2012).

[16] C. A. J. Putman, K. O. Van der Werf, B. G. De Grooth, N. F. Van Hulst, and J. Greve. "Tapping mode atomic force microscopy in liquid." In: *Applied physics letters* 64.18 (1994), pp. 2454–2456.

[17] P. K. Hansma, J. P. Cleveland, M. Radmacher, D. A. Walters, P. E. Hillner, M. Bezanilla, M. Fritz, D. Vie, et al. "Tapping mode atomic force microscopy in liquids." In: *Applied Physics Letters* 64.13 (1994), pp. 1738–1740.

[18] F. J. Giessibl and S. Morita. "Non-contact AFM." In: *Journal of Physics: Condensed Matter* 24.8 (2012).

[19] O. D. Payton, A. R. Champneys, M. E. Homer, L. Picco, and M. J. Miles. "Feedback-induced instability in tapping mode atomic force microscopy: theory and experiment." In: *Proceedings of the Royal Society A: Mathematical, Physical and Engineering Sciences* 467.2130 (2011), pp. 1801–1822.

[20] S. I. Lee, S. W. Howell, A. Raman, and R. Reifenberger. "Nonlinear dynamics of microcantilevers in tapping mode atomic force microscopy: A comparison between theory and experiment." In: *Physical Review B* 66.11 (2002), p. 115409.

[21] S. Hornstein, O. Gottlieb, and L. Ioffe. "Nonlinear Dynamics and Control of the Scan Process in Noncontacting Atomic Force Microscopy." In: *ASME 2005 International Mechanical Engineering Congress and Exposition*. American Society of Mechanical Engineers. 2005, pp. 571–581.

[22] C. A. Putman, K. O. Van der Werf, B. G. de Grooth, N. F. van Hulst, and J. Greve. "Viscoelasticity of living cells allows high resolution imaging by tapping mode atomic force microscopy." In: *Biophysical journal* 67.4 (1994), pp. 1749–1753.

[23] F. Dubourg and J. P. Aimé. "Role of the adhesion between a nanotip and a soft material in tapping mode AFM." In: *Surface Science* 466.1 (2000), pp. 137–143.

[24] Q. Zhong, D. Inniss, K. Kjoller, and V. B. Elings. "Fractured polymer/silica fiber surface studied by tapping mode atomic force microscopy." In: *Surface Science Letters* 290.1 (1993), pp. 688–692.

[25] G. Binnig, C. F. Quate, and C. Gerber. "Atomic force microscope." In: *Physical review letters* 56.9 (1986), p. 930.

[26] L. Picco, L. Bozec, A. Ulcinas, D. J. Engledew, M. Antognozzi, M. Horton, and M. J. Miles. "Breaking the speed limit with atomic force microscopy." In: *Nanotechnology* 18.4 (2007).

[27] L. M. Picco, P. G. Dunton, A. Ulcinas, D. J. Engledew, O. Hoshi, T. Ushiki, and M. J. Miles. "High-speed AFM of human chromosomes in liquid." In: *Nanotechnology* 19.38 (2008).

[28] S. B. Velegol and B. E. Logan. "Contributions of Bacterial Surface Polymers, Electrostatics, and Cell Elasticity to the Shape of AFM Force Curves." In: *Langmuir* 18.13 (2002), pp. 5256–5262.

[29] U. Maver, T. Velnar, M. Gaberšček, O. Planinšek, and M. Finšgar. "Recent progressive use of atomic force microscopy in biomedical applications." In: *TrAC Trends in Analytical Chemistry* 80 (2016), pp. 96–111.

[30] J. K. Hobbs, O. E. Farrance, and L. Kailas. "How atomic force microscopy has contributed to our understanding of polymer crystallization." In: *Polymer* 50.18 (2009), pp. 4281 –4292.

[31] O. D. Payton, L. Picco, and T. B. Scott. "High-speed atomic force microscopy for materials science." In: *International Materials Reviews* 61.8 (2016), pp. 473–494.

[32] A. D. Slattery, A. J. Blanch, V. Ejov, J. S. Quinton, and C. T. Gibson. "Spring constant calibration techniques for next-generation fast-scanning atomic force microscope cantilevers." In: *Nanotechnology* 25.33 (2014), p. 335705.

[33] T. Ando, N. Kodera, E. Takai, D. Maruyama, K. Saito, and A. Toda. "A high-speed atomic force microscope for studying biological macromolecules." In: *Proceedings of the National Academy of Sciences* 98.22 (2001), pp. 12468–12472.

[34] D. A. Walters, J. P. Cleveland, N. H. Thomson, P. K. Hansma, M. A. Wendman, G. Gurley, and V. Elings. "Short cantilevers for atomic force microscopy." In: *Review of Scientific Instruments* 67.10 (1996), pp. 3583–3590.

[35] T. E. Schaffer. "Calculation of thermal noise in an atomic force microscope with a finite optical spot size." In: *Nanotechnology* 16.6 (2005), pp. 664–670.

[36] R. V. Lapshin and O. V. Obyedkov. "Fast-acting piezoactuator and digital feedback loop for scanning tunneling microscopes." In: *Review of Scientific Instruments* 64.10 (1993), pp. 2883–2887.

[37] D. Knebel, M. Amrein, K. Voigt, and R. Reichelt. "A fast and versatile scan unit for scanning probe microscopy." In: *Scanning* 19.4 (1997), pp. 264–268.

[38] J. H. Kindt, G. E. Fantner, J. A. Cutroni, and P. K. Hansma. "Rigid design of fast scanning probe microscopes using finite element analysis." In: *Ultramicroscopy* 100.3 (2004), pp. 259–265.

[39] H. Yamashita, N. Kodera, A. Miyagi, T. Uchihashi, D. Yamamoto, and T. Ando. "Tip-sample distance control using photothermal actuation of a small cantilever for high-speed atomic force microscopy." In: *Review of Scientific Instruments* 78.8 (2007).

[40] D. Croft, G. Shedd, and S. Devasia. "Creep, Hysteresis, and Vibration Compensation for Piezpactuators: Atomic Force Microscopy Application." In: *Proceedings of the American Control Conference* 123.June (2000), pp. 23–28.

[41] A. Sebastian and S. M. Salapaka. "Design methodologies for robust nano-positioning." In: *IEEE Transactions on Control Systems Technology* 13.6 (2005), pp. 868–876.

[42] T. Ando. “Video imaging of biomolecular processes by high-speed AFM.” In: *2011 IEEE 24th International Conference on Micro Electro Mechanical Systems*. 2011, pp. 57–62.

[43] T. Ando, N. Kodera, Y. Naito, T. Kinoshita, K. Furuta, and Y. Y. Toyoshima. “A High-speed Atomic Force Microscope for Studying Biological Macromolecules in Action.” In: *ChemPhysChem* 4.11 (2003), pp. 1196–1202.

[44] Y. Hayato, T. Azuma, U. Takayuki, A. Tomoya, A. Toshio, and F. Yoshihiro. “Single-Molecule Imaging on Living Bacterial Cell Surface by High-Speed AFM.” In: *Journal of Molecular Biology* 422.2 (2012), pp. 300–309.

[45] C. Adai, C. Ignacio, B. Thomas, and S. Simon. “High-Speed Atomic Force Microscopy: Cooperative Adhesion and Dynamic Equilibrium of Junctional Microdomain Membrane Proteins.” In: *Journal of Molecular Biology* 423.2 (2012), pp. 249 –256.

[46] L. S. Shlyakhtenko, A. Y. Lushnikov, A. Miyagi, and Y. L. Lyubchenko. “Specificity of Binding of Single-Stranded DNA-Binding Protein to Its Target.” In: *Biochemistry* 51.7 (2012), pp. 1500–1509.

[47] P. E. Milhiet, D. Yamamoto, O. Berthoumieu, P. Dosset, C. Le Grimellec, J.-M. Verdier, S. Marchal, and T. Ando. “Deciphering the Structure, Growth and Assembly of Amyloid-Like Fibrils Using High-Speed Atomic Force Microscopy.” In: *PLOS ONE* 5.10 (2010), pp. 1–8.

[48] T. Ando. “High-speed AFM imaging.” In: *Current Opinion in Structural Biology* 28 (2014), pp. 63–68.

[49] T. Itani and J. J. Santillan. “In situ characterization of photoresist dissolution.” In: *Applied Physics Express* 3.6 (2010), pp. 3–6.

[50] H. Watanabe, T. Uchihashi, T. Kobashi, M. Shibata, J. Nishiyama, R. Yasuda, and R. Ando. “Wide-area scanner for high-speed atomic force microscopy.” In: *Review of Scientific Instruments* 84.5 (2013).

[51] Y. Oda, Y. Furuya, H. Noguchi, and K. Higashida. “AFM and SEM observation on mechanism of fatigue crack growth in an Fe-Si single crystal.” In: *International Journal of Fracture* 113.3 (2002), pp. 213–231.

[52] S. Moore, R. Burrows, L. Picco, T. Martin, S. Greenwell, T. Scott, and O. Payton. “A study of dynamic nanoscale corrosion initiation events by HS-AFM.” In: *Faraday Discuss.* (2018).

[53] P. Vettiger, G. Cross, M. Despont, U. Drechsler, U. Durig, B. Gotsmann, W. Haberle, M. A. Lantz, H. E. Rothuizen, et al. “The "millipede" - nanotechnology entering data storage.” In: *IEEE Transactions on Nanotechnology* 1.1 (2002), pp. 39–55.

[54] E. Eleftheriou, T. Antonakopoulos, G. K. Binnig, G. Cherubini, M. Despont, A. Dholakia, U. Durig, M. A. Lantz, H. Pozidis, et al. “Millipede - a MEMS-based scanning-probe data-storage system.” In: *IEEE Transactions on Magnetics* 39.2 (2003), pp. 938–945.

[55] M. Seong, S. Somnath, H. J. Kim, and W. P. King. "Parallel nanoimaging using an array of 30 heated microcantilevers." In: *Royal Society of Chemistry Advances* 4 (47 2014), pp. 24747–24754.

[56] S. Somnath, H. J. Kim, H. Hu, and W. P. King. "Parallel nanoimaging and nanolithography using a heated microcantilever array." In: *Nanotechnology* 25.1 (2014).

[57] S. Jackson, S. Gutschmidt, D. Roeser, and T. Sattel. "Development of a mathematical model and analytical solution of a coupled two-beam array with nonlinear tip forces for application to AFM." In: *Nonlinear Dynamics* 87.2 (2017), pp. 775–787.

[58] A. Pyne, W. Marks, L. M. Picco, P. G. Dunton, A. Ulcinas, M. E. Barbour, S. B. Jones, J. Gimzewski, and M. J. Miles. "High-speed atomic force microscopy of dental enamel dissolution in citric acid." In: *Archives of Histology and Cytology* 72.4 (2009), pp. 209–215.

[59] A. D. Warren, . I. Martinez-Ubeda A, O. D. Payton, L. Picco, and T. B. Scott. "Preparation of Stainless Steel Surfaces for Scanning Probe Microscopy." In: *Microscopy Today* 24.3 (2016), 52–55.

[60] C. C. Glover, J. P. Killgore, and R. C. Tung. "Scanning speed phenomenon in contact-resonance atomic force microscopy." In: *Beilstein Journal of Nanotechnology* 9.1 (2018), pp. 945–952.

[61] R. García and R. Perez. *Dynamic atomic force microscopy methods*. Vol. 47. 6-8. 2002, pp. 197–301.

[62] B. Cappella and G. Dietler. "Force-distance curves by atomic force microscopy." In: *Surface Science Reports* 34.1-3 (1999), pp. 1–104.

[63] F. J. Giessibl. "Advances in atomic force microscopy." In: *Reviews of Modern Physics* 75.3 (2003), p. 949.

[64] F. L. Leite, C. C. Bueno, A L. R. Da, E. C. Ziemath, and O. N. Oliveira. "Theoretical models for surface forces and adhesion and their measurement using atomic force microscopy." In: *International journal of molecular sciences* 13.10 (2012), pp. 12773–12856.

[65] J. P. Killgore, R. H. Geiss, and D. C. Hurley. "Continuous measurement of atomic force microscope tip wear by contact resonance force microscopy." In: *Small* 7.8 (2011), pp. 1018–1022.

[66] Ute Rabe. "Atomic Force Acoustic Microscopy." In: *Applied Scanning Probe Methods II: Scanning Probe Microscopy Techniques*. Ed. by B. Bhushan and Harald Fuchs. Berlin, Heidelberg: Springer Berlin Heidelberg, 2006, pp. 37–90.

[67] E. Tomasetti, R. Legras, and B. Nysten. "Quantitative approach towards the measurement of polypropylene/(ethylene-propylene) copolymer blends surface elastic properties by AFM." In: *Nanotechnology* 9.4 (1998), p. 305.

[68] U. Rabe, K. Janser, and W. Arnold. *Vibrations of free and surface-coupled atomic force microscope cantilevers: Theory and experiment*. 1996.

[69] D. C. Hurley and J. A. Turner. "Measurement of Poisson's ratio with contact-resonance atomic force microscopy." In: *Journal of Applied Physics* 102.3 (2007), pp. 1–8.

[70] J. A. Turner, S. Hirsekorn, U. Rabe, and W. Arnold. "High-frequency response of atomic-force microscope cantilevers." In: *Journal of Applied Physics* 82.3 (1997), pp. 966–979.

[71] J. P. Killgore and D. C. Hurley. "Low-force AFM nanomechanics with higher-eigenmode contact resonance spectroscopy." In: *Nanotechnology* 23.5 (2012), p. 055702.

[72] K L Johnson. *Contact Mechanics*. 1985.

[73] N. E. Dowling. *Mechanical behavior of materials: engineering methods for deformation, fracture, and fatigue*. Pearson, 2012.

[74] K. L. Murty and I. Charit. "Structural materials for Gen-IV nuclear reactors: Challenges and opportunities." In: *Journal of Nuclear Materials* 383.1-2 (2008), pp. 189–195.

[75] T. Allen, J. Busby, M. Meyer, and D. Petti. "Materials challenges for nuclear systems." In: *Materials Today* 13.12 (2010), pp. 14 –23.

[76] M. B. Anoop, K. B. Rao, and N. Lakshmanan. "Safety assessment of austenitic steel nuclear power plant pipelines against stress corrosion cracking in the presence of hybrid uncertainties." In: *International Journal of Pressure Vessels and Piping* 85.4 (2008), pp. 238 –247.

[77] A. W. Thompson and W. A. Backofen. "The effect of grain size on fatigue." In: *Acta metallurgica* 19.7 (1971), pp. 597–606.

[78] Y.H. Zhang and L. Edwards. "The effect of grain boundaries on the development of plastic deformation ahead of small fatigue cracks." In: *Scripta Metallurgica et Materialia* 26.12 (1992), pp. 1901 –1906.

[79] K. S. Chan. "Roles of microstructure in fatigue crack initiation." In: *International Journal of Fatigue* 32.9 (2010). Emerging Frontiers in Fatigue, pp. 1428 –1447.

[80] E. Arzt. "Size effects in materials due to microstructural and dimensional constraints: a comparative review." In: *Acta Materialia* 46.16 (1998), pp. 5611 –5626.

[81] R. E. Reed-Hill, R. Abbaschian, and R. Abbaschian. "Physical metallurgy principles." In: (1973).

[82] T. J. Rupert, D. S. Gianola, Y. Gan, and K. J. Hemker. "Experimental observations of stress-driven grain boundary migration." In: *Science* 326.5960 (2009), pp. 1686–1690.

[83] I. B. Timokhina, H. Beladi, X.Y. Xiong, Y. Adachi, and P.D. Hodgson. "Nanoscale microstructural characterization of a nanobainitic steel." In: *Acta Materialia* 59.14 (2011), pp. 5511 –5522.

[84] B. N. Wanjala et al. "Nanoscale Alloying, Phase-Segregation, and Core- Shell Evolution of Gold- Platinum Nanoparticles and Their Electrocatalytic Effect on Oxygen Reduction Reaction." In: *Chemistry of Materials* 22.14 (2010), pp. 4282–4294.

[85] F.-S. Pan, J.-J. Mao, X.-H. Chen, P. Jian, and J.-F. Wang. "Influence of impurities on microstructure and mechanical properties of ZK60 magnesium alloy." In: *Transactions of Nonferrous Metals Society of China* 20.7 (2010), pp. 1299–1304.

[86] K. Kim, Z. Lee, W. Regan, C. Kisielowski, M. F. Crommie, and A. Zettl. "Grain boundary mapping in polycrystalline graphene." In: *ACS nano* 5.3 (2011), pp. 2142–2146.

[87] M. Griepentrog, G. Kramer, and B. Cappella. "Comparison of nanoindentation and AFM methods for the determination of mechanical properties of polymers." In: *Polymer Testing* 32.3 (2013), pp. 155–160.

[88] R. Saha and W. D. Nix. "Effects of the substrate on the determination of thin film mechanical properties by nanoindentation." In: *Acta Materialia* 50.1 (2002), pp. 23–38.

[89] X. Li and B. Bhushan. "A review of nanoindentation continuous stiffness measurement technique and its applications." In: *Materials Characterization* 48.1 (2002), pp. 11–36.

[90] M. Kopycinska-Müller, R. H. Geiss, J. Müller, and D. C. Hurley. "Elastic-property measurements of ultrathin films using atomic force acoustic microscopy." In: *Nanotechnology* 16.6 (2005), pp. 703–709.

[91] M. Kopycinska-müller, R. H. Geiss, P. Rice, and D. C. Hurley. "Influence of Tip Wear on Atomic Force Acoustic Microscopy Experiments." In: *Materials Research* 838 (2005), pp. 1–6.

[92] C. A. Schuh. "Nanoindentation studies of materials." In: *Materials Today* 9.5 (2006), pp. 32 –40.

[93] N. R. Shatil, M. E. Homer, L. Picco, P. G. Martin, and O. D. Payton. "A calibration method for the higher modes of a micro-mechanical cantilever." In: *Applied Physics Letters* 110.22 (2017), p. 223101.

[94] S. P. Nisture. *Engineering Mechanics*. Technical Publications, 2006.

[95] D.M. Mohan, B. Mohan, and M. Das. *Structural Analysis*. PHI Learning Pvt. Ltd., 2011.

[96] J. Melcher, S. Hu, and A. Raman. "Equivalent point-mass models of continuous atomic force microscope probes." In: *Applied Physics Letters* 91.5 (2007), pp. 1–4.

[97] M. I. Younis. *MEMS Linear and Nonlinear Statics and Dynamics*. Vol. 20. Springer, 2011.

[98] G. Y. Chen, R. J. Warmack, T. Thundat, D. P. Allison, and A. Huang. "Resonance response of scanning force microscopy cantilevers." In: *Review of Scientific Instruments* 65.8 (1994), pp. 2532–2537.

[99] J. R. Lozano, D. Kiracofe, J. Melcher, R. Garcia, and A. Raman. "Calibration of higher eigenmode spring constants of atomic force microscope cantilevers." In: *Nanotechnology* 21.46 (2010).

[100] Arvind Raman, John Melcher, and Ryan Tung. "Cantilever dynamics in atomic force microscopy." In: *Nano Today* 3.1-2 (2008), pp. 20–27.

[101] J. Melcher, A. R. Champneys, and D. J. Wagg. "The impacting cantilever: modal non-convergence and the importance of stiffness matching." In: *Philosophical transactions. Series A, Mathematical, physical, and engineering sciences* 371.1993 (2013), p. 20120434.

[102] R. Raiteri, M. Grattarola, H. J. Butt, and P. Skládal. "Micromechanical cantilever-based biosensors." In: *Sensors and Actuators, B: Chemical* 79.2-3 (2001), pp. 115–126.

[103] M. L. B. Palacio and B. Bhushan. "Normal and lateral force calibration techniques for AFM cantilevers." In: *Critical Reviews in Solid State and Materials Sciences* 35.2 (2010), pp. 73–104.

[104] C. T. Gibson, B. L. Weeks, J. R I Lee, C. Abell, and T. Payment. "A nondestructive technique for determining the spring constant of atomic force microscope cantilevers." In: *Review of Scientific Instruments* 72.5 (2001), pp. 2340–2343.

[105] J D Holbery, V L Eden, M Sarikaya, and R M Fisher. "Experimental determination of scanning probe microscope cantilever spring constants utilizing a nanoindentation apparatus." In: *Review of Scientific Instruments* 71.10 (2000), pp. 3769–3776.

[106] N. A. Burnham, X. Chen, C. S. Hodges, G. A. Matei, E. J. Thoreson, C. J. Roberts, M. C. Davies, and S. J. B. Tendler. "Comparison of calibration methods for atomic-force microscopy cantilevers." In: *Nanotechnology* 14.1 (2003), pp. 1–6.

[107] A. D. Slattery, A. J. Blanch, J. S. Quinton, and C. T. Gibson. "Calibration of atomic force microscope cantilevers using standard and inverted static methods assisted by FIB-milled spatial markers." In: *Nanotechnology* 24.1 (2012).

[108] R. S. Gates and M. G. Reitsma. "Precise atomic force microscope cantilever spring constant calibration using a reference cantilever array." In: *Review of Scientific Instruments* 78.8 (2007).

[109] J. P. Cleveland, S. Manne, D. Bocek, and P. K. Hansma. "A nondestructive method for determining the spring constant of cantilevers for scanning force microscopy." In: *Review of Scientific Instruments* 64.2 (1993), pp. 403–405.

[110] A. D. Slattery, A. J. Blanch, V. Ejov, J.. S. Quinton, and C. T. Gibson. "Spring constant calibration techniques for next-generation fast-scanning atomic force microscope cantilevers." In: *Nanotechnology* 25.33 (2014), p. 335705.

[111] J. L. Hutter and J. Bechhoefer. "Calibration of atomic-force microscope tips." In: *Review of Scientific Instruments* 64.7 (1993), pp. 1868–1873.

[112] H.-J. Butt and M. Jaschke. "Calculation of thermal noise in atomic force microscopy." In: *Nanotechnology* 6.1 (1995).

[113] J. L. Hutter. "Comment on Tilt of Atomic Force Microscope Cantilevers: Effect on Spring Constant and Adhesion Measurements." In: *Langmuir* 21.6 (2005), pp. 2630–2632.

[114] J. E. Sader et al. "Spring constant calibration of atomic force microscope cantilevers of arbitrary shape." In: *Review of Scientific Instruments* 83.10 (2012).

[115] J. Laurent, A. Steinberger, and L. Bellon. "Functionalized AFM probes for force spectroscopy: eigenmode shapes and stiffness calibration through thermal noise measurements." In: *Nanotechnology* 24.22 (2013), p. 225504.

[116] R. W. Stark, T. Drobek, and W. M. Heckl. "Thermomechanical noise of a free v-shaped cantilever for atomic-force microscopy." In: *Ultramicroscopy*. Vol. 86. 1-2. 2001, pp. 207–215.

[117] J. E. Sader. "Frequency response of cantilever beams immersed in viscous fluids with applications to the atomic force microscope." In: *Journal of Applied Physics* 84.1 (1998), pp. 64–76.

[118] R. J. Clarke. "Hydrodynamics of the atomic force microscope." PhD thesis. University of Nottingham, 2005.

[119] E. O. Tuck. "Calculation of Unsteady Flows Due to Small Motions of Cylinders in a Viscous Fluid." In: *Journal of Engineering Mathematics* 3.1 (1969).

[120] M. Van Dyke. *Journal of Fluid Mechanics*. Vol. 18. 3. Oxford University Press, 1964, pp. 477–480.

[121] A. Maali, C. Hurth, R. Boisgard, C. Jai, T. Cohen-Bouhacina, and J. P. Aimé. "Hydrodynamics of oscillating atomic force microscopy cantilevers in viscous fluids." In: *Journal of Applied Physics* 97.7 (2005), p. 074907.

[122] M. S. Allen, H. Sumali, and P. C. Penegor. "DMCMN : Experimental / Analytical Evaluation of the Effect of Tip Mass on Atomic Force Microscope Cantilever Calibration." In: *Journal of Dynamic Systems, Measurement, and Control* 131.6 (2009), pp. 1–10.

[123] L. Majkut. "Free and Forced Vibrations of Timoshenko Beams Described by Single Difference Equation." In: *Journal of Theoretical and Applied Mechanics* 47.1 (2009), pp. 193–210.

[124] O. A. Bauchau and J. I. Craig. "Euler-Bernoulli beam theory." In: *Structural Analysis*. Ed. by O. A. Bauchau and J. I. Craig. Springer Netherlands, 2009, pp. 173–221.

[125] A. Khan, J. Philip, and P. Hess. "Young's modulus of silicon nitride used in scanning force microscope cantilevers." In: *Journal of Applied Physics* 95.4 (2004), pp. 1667–1672.

[126] G. W. C. Kaye and T. H. Laby. *Tables of Physical and Chemical Constants*. Longman, 1997.

[127] B. Harris. *Engineering composite materials*. Institute of Metals London, 1986.

[128] H. Frentrup and M. S Allen. "Error in dynamic spring constant calibration of atomic force microscope probes due to nonuniform cantilevers." In: *Nanotechnology* 22.29 (2011).

[129] R. J. Clarke, V. Bachtiar, T. C. Lee, J. E. Cater, and J. Minton. "Response of a fluid-immersed microcantilever close to a deformable body." In: *Journal of Applied Physics* 117.9 (2015), pp. 0–12.

[130] P. A. Yuya, D. C. Hurley, and J. A. Turner. "Contact-resonance atomic force microscopy for viscoelasticity." In: *Journal of Applied Physics* 104.7 (2008).

[131] F. J. Elmer and M. Dreier. "Eigenfrequencies of a rectangular atomic force microscope cantilever in a medium." In: *Journal of Applied Physics* 81.12 (1997), pp. 7709–7714.

[132] J. W.M. Chon, P. Mulvaney, and J. E. Sader. "Experimental validation of theoretical models for the frequency response of atomic force microscope cantilever beams immersed in fluids." In: *Journal of Applied Physics* 87.8 (2000), pp. 3978–3988.

[133] C. P. Green and J. E. Sader. "Torsional frequency response of cantilever beams immersed in viscous fluids with applications to the atomic force microscope." In: *Journal of Applied Physics* 92.10 (2002), pp. 6262–6274.

[134] J. E. Sader, J. Pacifico, C. P. Green, and P. Mulvaney. "General scaling law for stiffness measurement of small bodies with applications to the atomic force microscope." In: *Journal of Applied Physics* 97.12 (2005).

[135] J. E. Sader, R. Borgani, C. T. Gibson, D. B. Haviland, M. J. Higgins, J. I. Kilpatrick, J. Lu, P. Mulvaney, C. J. Shearer, et al. "A virtual instrument to standardise the calibration of atomic force microscope cantilevers." In: *Review of Scientific Instruments* 87.9 (2016).

[136] J. D. de Baubigny, M. Benzaquen, C. Mortagne, C. Devailly, S. Kosgodagan Acharige, J. Laurent, A. Steinberger, J.-P. Salvetat J.-P.and Aimé, and T. Ondarcuhu. "AFM study of hydrodynamics in boundary layers around micro- and nanofibers." In: *Phys. Rev. Fluids* 1 (4 2016), p. 044104.

[137] C. P. Green and J. E. Sader. "Frequency response of cantilever beams immersed in viscous fluids near a solid surface with applications to the atomic force microscope." In: *Journal of Applied Physics* 98.11 (2005).

[138] R. C. Tung, J. P. Killgore, and D. C. Hurley. "Hydrodynamic corrections to contact resonance atomic force microscopy measurements of viscoelastic loss tangent." In: *Review of Scientific Instruments* 84.7 (2013).

[139] S. Basak, A. Raman, and S. V. Garimella. "Hydrodynamic loading of microcantilevers vibrating in viscous fluids." In: *Journal of Applied Physics* 99.11 (2006).

[140] R. C. Tung, A. Jana, and A. Raman. "Hydrodynamic loading of microcantilevers oscillating near rigid walls." In: *Journal of Applied Physics* 104.11 (2008).

[141] H. Hosaka, K. Itao, and S. Kuroda. "Damping characteristics of beam-shaped micro-oscillators." In: *"Sensors and Actuators, A: Physical"* 49.1 (1995), pp. 87–95.

[142] M. H. Korayem, M. S. Sotoudegan, and N. Ebrahimi. "Effects of geometrical dimensions and liquid properties on frequency response of resonating microcantilevers in the vicinity of a surface." In: *Precision Engineering* 37.4 (2013), pp. 831–838.

[143] A. Tafuni and I. Sahin. "Non-linear hydrodynamics of thin laminae undergoing large harmonic oscillations in a viscous fluid." In: *Journal of Fluids and Structures* 52 (2015), pp. 101–117.

[144] M. Aureli, M. E. Basaran, and M. Porfiri. "Nonlinear finite amplitude vibrations of sharp-edged beams in viscous fluids." In: *Journal of Sound and Vibration* 331.7 (2012), pp. 1624–1654.

[145] C. N. Phan, M. Aureli, and M. Porfiri. "Finite amplitude vibrations of cantilevers of rectangular cross sections in viscous fluids." In: *Journal of Fluids and Structures* 40 (2013), pp. 52–69.

[146] E. Grimaldi, M. Porfiri, and L. Soria. "Finite amplitude vibrations of a sharp-edged beam immersed in a viscous fluid near a solid surface." In: *Journal of Applied Physics* 112.10 (2012).

[147] G. Falcucci, M. Aureli, S. Ubertini, and M. Porfiri. "Transverse harmonic oscillations of laminae in viscous fluids: a lattice Boltzmann study." In: *Philosophical Transactions of the Royal Society A: Mathematical, Physical and Engineering Sciences* 369.1945 (2011), pp. 2456–2466.

[148] M. S. Alnæs et al. "The FEniCS Project Version 1.5." In: *Archive of Numerical Software* 3.100 (2015).

[149] A. Logg, G. N. Wells, and J. Hake. "DOLFIN: a C++/Python Finite Element Library." In: *Automated Solution of Differential Equations by the Finite Element Method, Volume 84 of Lecture Notes in Computational Science and Engineering*. Ed. by Anders Logg, Kent-Andre Mardal, and Garth N. Wells. Springer, 2012. Chap. 10.

[150] A. Logg and G.N. Wells. "DOLFIN: Automated Finite Element Computing." In: *ACM Transactions on Mathematical Software* 37.2 (2010).

[151] M. S. Alnæs. "UFL: a Finite Element Form Language." In: *Automated Solution of Differential Equations by the Finite Element Method, Volume 84 of Lecture Notes in Computational Science and Engineering*. Ed. by Anders Logg, Kent-Andre Mardal, and Garth N. Wells. Springer, 2012. Chap. 17.

[152] R. Temam. *Navier-Stokes Equations: Theory and Numerical Analysis*. 2001.

[153] H. C. Brinkman. "A calculation of the viscous force exerted by a flowing fluid on a dense swarm of particles." In: *Flow, Turbulence and Combustion* 1.1 (1949), p. 27.

[154] M. Mota, A. Yelshin, and I. Yelshina. *Porous Media, Applications in Biotechnology*. 2010.

[155] M. Larson and F. Bengzon. *The Finite Element Method: Theory, Implementation, and Applications*. Vol. 10. 2013.

[156] G. Ramamurty. *Applied Finite Element Analysis*. I.K. International Publishing House Pvt. Limited, 2013.

[157] M.G. Larson and F. Bengzon. *The Finite Element Method: Theory, Implementation, and Applications*. Texts in Computational Science and Engineering. Springer Berlin Heidelberg, 2013.

[158] S.S. Rao. *The Finite Element Method in Engineering*. Elsevier Science, 2017.

[159] C. Geuzaine and J.-F. Remacle. "Gmsh: A 3-D Finite Element Mesh Generator with built-in Pre- and Post-Processing Facilities." In: *Int. J. Numer. Meth. Engng.* 79.11 (Sept. 2009), pp. 1309–1331.

[160] S. Basak and A. Raman. "Hydrodynamic coupling between micromechanical beams oscillating in viscous fluids." In: *Physics of Fluids* 19.1 (2007).

[161] M. Kimber, R. Lonergan, and S. V. Garimella. "Experimental study of aerodynamic damping in arrays of vibrating cantilevers." In: *Journal of Fluids and Structures* 25.8 (2009), pp. 1334–1347.

[162] R. Wagner, R. J. Moon, and A. Raman. "Mechanical properties of cellulose nanomaterials studied by contact resonance atomic force microscopy." In: *Cellulose* 23.2 (2016), pp. 1031–1041.

[163] N. Ploscariu and R. Szoszkiewicz. "A method to measure nanomechanical properties of biological objects." In: *Applied Physics Letters* 103.26 (2013).

[164] D. C. Hurley, S. E. Campbell, J. P. Killgore, L. M. Cox, and Y. Ding. "Measurement of viscoelastic loss tangent with contact resonance modes of atomic force microscopy." In: *Macromolecules* 46.23 (2013), pp. 9396–9402.

[165] K. Yamanaka and S. Nakano. "Quantitative elasticity evaluation by contact resonance in an atomic forcemicroscope." In: *Applied Physics A: Materials Science and Processing* 66.SUPPL. 1 (1998), pp. 313–317.

[166] H. Wagner, D. Bedorf, S. Küchemann, M. Schwabe, B. Zhang, W. Arnold, and K. Samwer. "Local elastic properties of a metallic glass." In: *Nature Materials* 10.6 (2011), pp. 439–442.

[167] D. G. Yablon, A. Gannepalli, R. Proksch, J. Killgore, D. C. Hurley, J. Grabowski, and A. H. Tsou. "Quantitative viscoelastic mapping of polyolefin blends with contact resonance atomic force microscopy." In: *Macromolecules* 45.10 (2012), pp. 4363–4370.

[168] G. Stan and R. F. Cook. "Mapping the elastic properties of granular Au films by contact resonance atomic force microscopy." In: *Nanotechnology* 19.23 (2008).

[169] A. B. Churnside, R. C. Tung, and J. P. Killgore. "Quantitative Contact Resonance Force Microscopy for Viscoelastic Measurement of Soft Materials at the Solid-Liquid Interface." In: *Langmuir* 31.40 (2015), pp. 11143–11149.

[170] A. Briggs. "Acoustic microscopy- a summary." In: *Reports on Progress in Physics* 55.7 (1992), pp. 851–909.

[171] C. Faber et al. "A method for inverting the touchdown shock of the Philae lander on comet 67P/Churyumov-Gerasimenko." In: *Planetary and Space Science* 106 (2015), pp. 46–55.

[172] P. Günther, U. Ch Fischer, and K. Dransfeld. "Scanning near-field acoustic microscopy." In: *Applied Physics B Photophysics and Laser Chemistry* 48.1 (1989), pp. 89–92.

[173] I. Todoshchenko, A. Savin, M. Haataja, J. P. Kaikkonen, and P. J. Hakonen. "Quartz tuning fork as a probe of surface oscillations." In: *Applied Physics Letters* 110.7 (2017).

[174] N. Gavara and R. S. Chadwick. "Noncontact microrheology at acoustic frequencies using frequency-modulated atomic force microscopy." In: *Nature Methods* 7.8 (2010), pp. 650–654.

[175] K Yamanaka, H Ogiso, and O Kolosov. "Analysis of subsurface imaging and effects of surface elasticity in the ultrasonic force microscope." In: *Japanese Journal of Applied Physics Part 1-Regular Papers Short Notes & Review Papers* 33.5B (1994), pp. 3197–3203.

[176] B. D. Huey. "AFM and Acoustics: Fast, Quantitative Nanomechanical Mapping." In: *Annual Review of Materials Research* 37.1 (2007), pp. 351–385.

[177] U. Rabe and W. Arnold. "Acoustic microscopy by atomic force microscopy." In: *Applied Physics Letters* 64.12 (1994), pp. 1493–1495.

[178] K. Yamanaka. "Ultrasonic force microscopy." In: *MRS Bulletin* 21.10 (1996), pp. 36–41.

[179] M. Kocun, A. Labuda, A. Gannepalli, and R. Proksch. "Contact resonance atomic force microscopy imaging in air and water using photothermal excitation." In: *Review of Scientific Instruments* 86.8 (2015).

[180] S. P. Shah, M. S. Konsta-Gdoutos, Z. S. Metaxa, and P. Mondal. "Nanoscale Modification of Cementitious Materials." In: *Nanotechnology in Construction 3*. Berlin, Heidelberg: Springer Berlin Heidelberg, 2009, pp. 125–130.

[181] D. G. de Oteyza et al. "Direct Imaging of Covalent Bond Structure in Signle-Molecule Chemical Reactions." In: *Science* 340.6139 (2013), pp. 1434–1437.

[182] C. Oliver and M. Pharr. *An improved technique for determining hardness and elastic modulus using load and displacement sensing indentation experiments*. 1992.

[183] B. J. Briscoe, L. Fiori, and E. Pelillo. "Nano-indentation of polymeric surfaces." In: *Journal of Physics D: Applied Physics* 31.19 (1998), pp. 2395–2405.

[184] D. C. Hurley, M. Kopycinska-Müller, A. B. Kos, and R. H. Geiss. "Quantitative elastic-property measurements at the nanoscale with atomic force acoustic microscopy." In: *Advanced Engineering Materials* 7.8 (2005), pp. 713–718.

[185] U. Rabe, E. Kester, and W. Arnold. "Probing linear and non-linear tip-sample interaction forces by atomic force acoustic microscopy." In: *Surface and Interface Analysis* 27.5-6 (1999), pp. 386–391.

[186] R. W. Stark and W. M. Heckl. "Higher harmonics imaging in tapping-mode atomic-force microscopy." In: *Review of Scientific Instruments* 74.12 (2003), pp. 5111–5114.

[187] Seon M Han, Haym Benaroya, and Timothy Wei. "Dynamics of transversely vibrating beams using four engineering theories." In: *Journal of Sound and vibration* 225.5 (1999), pp. 935–988.

[188] Z-F. Fu and J. He. *Modal Analysis*. Elsevier, 2001.

[189] O. B. Wright and N. Nishiguchi. "Vibrational dynamics of force microscopy: Effect of tip dimensions." In: *Applied Physics Letters* 71.5 (1997), pp. 626–628.

[190] E. Dupas, G. Gremaud, A. Kulik, and J.-L. Loubet. "High-frequency mechanical spectroscopy with an atomic force microscope." In: *Review of Scientific Instruments* 72.10 (2001), pp. 3891–3897.

[191] P.-E. Mazeran and J.-L. Loubet. "Normal and lateral modulation with a scanning force microscope, an analysis: implication in quantitative elastic and friction imaging." In: *Tribology Letters* 7.4 (1999), pp. 199–212.

[192] D. C. Hurley. "Contact Resonance Force Microscopy Techniques for Nanomechanical Measurements." In: *Applied Scanning Probe Methods XI*. Ed. by B. Bhushan and H. Fuchs. Springer, 2009. Chap. 5, pp. 97–138.

[193] A. D. Warren, I. J. Griffiths, and P. E. J. Flewitt. "Precipitation within localised chromium-enriched regions in a Type 316H austenitic stainless steel." In: *Journal of Materials Science* 53.8 (2018), pp. 6183–6197.

[194] F. J. Giessibl and C. F. Quate. "Exploring the nanoworld with atomic force microscopy." In: *Physics Today* 59.12 (2006), pp. 44–50.

[195] E Barthel. "Contact, Interactions, and Dynamics." In: *Acoustic Scanning Probe Microscopy*. Ed. by F. Marinello, D. Passeri, and E. Savio. Springer, 2013. Chap. 2, pp. 21–46.

[196] S. Amelio, A. V. Goldade, U. Rabe, V. Scherer, B. Bhushan, and W. Arnold. "Measurements of elastic properties of ultra-thin diamond-like carbon coatings using atomic force acoustic microscopy." In: *Thin Solid Films* 392.1 (2001), pp. 75–84.

[197] H. Hertz, D. E. Jones, and G. A. Schott. *Miscellaneous papers*. Macmillan and Company, 1896.

[198] D. Beaglehole and H. K. Christenson. "Vapor adsorption on mica and silicon: entropy effects, layering, and surface forces." In: *The Journal of Physical Chemistry* 96.8 (1992), pp. 3395–3403.

[199] K. L. Johnson, K. Kendall, and A. D. Roberts. "Surface Energy and the Contact of Elastic Solids." In: *Proceedings of the Royal Society A: Mathematical, Physical and Engineering Sciences* 324.1558 (1971), pp. 301–313.

[200] D. Maugis. "Adhesion of spheres: The JKR-DMT transition using a dugdale model." In: *Journal of Colloid And Interface Science* 150.1 (1992), pp. 243–269.

[201] D. Xu, K. M. Liechti, and K. Ravi-Chandar. "On the modified Tabor parameter for the JKR-DMT transition in the presence of a liquid meniscus." In: *Journal of Colloid and Interface Science* 315.2 (2007), pp. 772–785.

[202] G.V. Samsonov. *Handbook of the Physicochemical Properties of the Elements*. Springer USA, 2012.

[203] A. D. Warren. "The role of secondary phases in the long term degradation of stainless steels at high temperatures." PhD thesis. University of Bristol, 2015.

[204] U. Rabe, S. Amelio, E. Kester, V. Scherer, S. Hirsekorn, and W. Arnold. "Quantitative determination of contact stiffness using atomic force acoustic microscopy." In: *Ultrasonics* 38.1 (2000), pp. 430–437.

[205] M. Kopycinska-müller, R. H. Geiss, P. Rice, and D. C Hurley. "Influence of Tip Wear on Atomic Force Acoustic Microscopy Experiments." In: *Materials Research* 838 (2005), pp. 1–6.

[206] S. Jesse, R. K. Vasudevan, L. Collins, E. Strelcov, M.B. Okatan, A. Belianinov, A.P. Baddorf, R. Proksch, and S.V. Kalinin. "Band Excitation in Scanning Probe Microscopy: Recognition and Functional Imaging." In: *Annual Review of Physical Chemistry* 65.1 (2014), pp. 519–536.

[207] B. J. Rodriguez, C. Callahan, S. V. Kalinin, and R. Proksch. "Dual-frequency resonance-tracking atomic force microscopy." In: *Nanotechnology* 18.47 (2007).

[208] A. Gannepalli, D. G. Yablon, A. H. Tsou, and R. Proksch. "Mapping nanoscale elasticity and dissipation using dual frequency contact resonance AFM." In: *Nanotechnology* 22.35 (2011).

[209] D. G. Papageorgiou, I. A. Kinloch, and R. J. Young. "Mechanical properties of graphene and graphene-based nanocomposites." In: *Progress in Materials Science* 90 (2017), pp. 75–127.

[210] M. A. Hopcroft, W. D. Nix, and T. W. Kenny. "What is the Young's modulus of silicon?" In: *Journal of Microelectromechanical Systems* 19.2 (2010), pp. 229–238.

[211] J. J. Wortman and R. A. Evans. "Young's modulus, shear modulus, and poisson's ratio in silicon and germanium." In: *Journal of Applied Physics* 36.1 (1965), pp. 153–156.

[212] A. Politano and G. Chiarello. "Probing the Young's modulus and Poisson's ratio in graphene/metal interfaces and graphite: a study." In: *Nano Research* 8.6 (2015), pp. 1847–1856.

[213] N Dorozhovets, T Hausotte, N Hofmann, E Manske, and G Jäger. "Development of the interferometrical scanning probe microscope." In: vol. 6293. 2006, p. 629311.

[214] E. E. Flater, G. E. Zacharakis-Jutz, B. G. Dumba, I. A. White, and C. A. Clifford. "Towards easy and reliable AFM tip shape determination using blind tip reconstruction." In: *Ultramicroscopy* 146 (2014), pp. 130–143.

[215] A. Labuda, J. Cleveland, N. A. Geisse, M. Kocun, B. Ohler, R. Proksch, M. B. Viani, and D. Walters. "Photothermal excitation for improved cantilever drive performance in tapping mode atomic force microscopy." In: *Microscopy and Analysis28* 3 (2014), pp. 21–25.